University of Alberta

Drilling Induced Core Damages and Their Relationship to Crustal In Situ Stress States and Rock Properties

by

© Yongyi Li

A thesis submitted to the Faculty of Graduate Studies and Research in partial fulfillment of the requirements for the degree of **Doctor of Philosophy**

in

Geophysics

Department of Physics

Edmonton, Alberta

Fall, 1997

National Library of Canada
Acquisitions and Bibliographic Services
395 Wellington Street
Ottawa ON K1A 0N4
Canada

Bibliothèque nationale du Canada
Acquisitions et services bibliographiques
395, rue Wellington
Ottawa ON K1A 0N4
Canada

Your file Votre référence

Our file Notre référence

The author has granted a non-exclusive licence allowing the National Library of Canada to reproduce, loan, distribute or sell copies of this thesis in microform, paper or electronic formats.

The author retains ownership of the copyright in this thesis. Neither the thesis nor substantial extracts from it may be printed or otherwise reproduced without the author's permission.

L'auteur a accordé une licence non exclusive permettant à la Bibliothèque nationale du Canada de reproduire, prêter, distribuer ou vendre des copies de cette thèse sous la forme de microfiche/film, de reproduction sur papier ou sur format électronique.

L'auteur conserve la propriété du droit d'auteur qui protège cette thèse. Ni la thèse ni des extraits substantiels de celle-ci ne doivent être imprimés ou autrement reproduits sans son autorisation.

0-612-23018-X

Canada

UNIVERSITY OF ALBERTA

RELEASE FORM

Name of Author: Yongyi Li

Title of Thesis: Drilling Induced Core Damages and Their Relationship to Crustal In Situ Stress States and Rock Properties

Degree: Doctor of Philosophy

Year This Degree Granted: 1997

Permission is hereby granted to the University of Alberta Library to reproduce single copies of this thesis and to lend or sell such copies for private, scholarly, or scientific research purposes only.

The author reserves all other publication and other rights in association with the copyright in the thesis, and except as herein before provided neither the thesis nor any substantial portion thereof may be printed or otherwise reproduced in any material form whatever without the author's prior written permission.

Department of Physics
University of Alberta
Edmonton, Alberta
T6E 2K6

July 9, 1997

UNIVERSITY OF ALBERTA

FACULTY OF GRADUATE STUDIES AND RESEARCH

The undersigned certify that they have read, and recommend to the Faculty of Graduate Studies and Research for acceptance, a thesis entitled **DRILLING INDUCED CORE DAMAGES AND THEIR RELATIONSHIP TO CRUSTAL IN SITU STRESS STATES AND ROCK PROPERTIES** submitted by **Yongyi Li** in partial fulfillment of the requirements for the degree of **Doctor of Philosophy** in **Geophysics**.

Dr. D. R. Schmitt (Supervisor)
Department of Physics

Dr. E. Nyland
Department of Physics

Dr. M. E. Evans
Department of Physics

Dr. D. Chan
Department of Civil Engineering

Dr. D. Cruden
Department of Earth and Atmospheric Sci.

Dr. P. Meredith (External Examiner)
University College London, U.K.

Date: June 26, 1997

To my wife Ping, my daughter Nan,
my parents, and my brother.

ABSTRACT

The damage produced in cores during drilling operations is studied with the three-dimensional finite element method and laboratory experiments. A thorough investigation of the stress concentrations at the end of a wellbore under a variety of applied far-field stresses, rock properties, and cutting geometries is conducted. The consequent mechanisms producing coring-induced disking, petal, petal-centerline, and centerline fractures, and their relationship to in situ stress conditions are described. The core stub length is found to strongly influence the magnitudes of the concentrated stresses and the spacing of core fractures. The greatest tensile and shear stresses are generally located either at the drilling cut surface or at the centre of the core stub root. The increase of the tensile stress magnitudes and their eventual peak at lengths less than 40% the core diameter explain the remarkably uniform spacing of such fractures and suggest that this spacing might provide a quantitative indication of in situ stress magnitudes. Hypothetical incipient failure curves which assume the core disks are produced in tension are in good agreement with early experimental observations, a Mohr-Coulomb shear failure mechanism is inconsistent. The shapes of coring-induced fractures are modeled using a simple fracture trajectory prediction algorithm assuming they result from tension as supported by laboratory and field observations. These predicted hypothetical fracture morphologies are all observed. Moreover, relationships between the fracture morphology and in situ stress regimes suggest that the coring induced fractures can be used as independent complementary indicators in identifying crustal stress regimes. A new high pressure technique for determining the microcrack porosities and rock anisotropy resulting from microcrack damage is developed. This technique modifies differential strain analysis by accounting for the nontrivial strain of the rock's solid mineral

component and may be used to determine rock anisotropy and possibly to deduce the orientations of in situ stresses.

ACKNOWLEDGMENTS

The support of my family and friends is gratefully acknowledged. I would first like to especially thank my wife, Ping, for her understanding and patience during my graduate studies. Without her continuous support I might not have completed this work.

I am very grateful to my supervisor, Dr. Douglas R. Schmitt for his continuous support. Many invaluable critiques and constant advice from him are greatly appreciated. His financial support allowed me be able to attend or present my work at the conferences of AGU, CSEG, CSPG, and SEG. My thanks extend to Dr. Cheryl Schmitt for her hospitality during my study at the University of Alberta and her help in the preparation of this thesis.

I like to thank all my committee members, Drs. E. Nyland, M. E. Evans, D. Chan, and K. Barron for their constructive critiques and suggestions which have had significant impact on my research. I also like to thank Drs. D. Cruden, P. Meredith and D. I. Gough for joining my examination committee. Their generosity is greatly appreciated. The suggestions from the known reviewers, Drs. B. R. Kulander, J. C. Lorenz, S. L. Dean, B. Haimson, T. Engelder, L. Germanovich, and one anonymous reviewer for the published potion of this research are also greatly appreciated. Dr. Kulander deserves additional thanks for providing us with otherwise impossible to obtain contributions within the literature and for his continuing interest and advice.

Much of this work was stimulated by generous discussions with Dr. Th. Röckel when he was onsite at the KTB drillsite and also by the nearly simultaneous observations of Mr. T. Podvinsky when at PanCanadian Petroleum about some of the core fractures he had seen in material retrieved from the Western Canadian Sedimentary basin. The associated interest of Dr. D. Yale of Mobil in Dallas, TX in the core damage aspects of

the work is also noted. Although they may not know it, Drs. F. Cornet, S. Hickman, and B. Haimson provided further fodder for thought.

The help in field and laboratory from our technicians, Jay Haverstock, L. Tober, and B. Madu, and research assistant, Roger Hunt is greatly appreciated.

I like specially to acknowledge Jim MacKinnon who helped me overcome many big and small problems in everyday computer usage.

I would also like to thank my fellow graduate students Yanquan Wang, Ahmed Kebaili, Joe Molyneux, Mike Grech, Marco Mah, Youcef Bouzidi and postdoctoral fellow, Eric B. Molz, who constructed a pleasant environment for my research and study. The many small but invaluable pieces of help and interesting discussions are very much appreciated.

The help from the administration officers and secretaries, especially Lynn Chandler and Mark Henderson in the Department of Physics, and the secretary of the Institute of Geophysics, Meteorology and Space Physics, Gloria Reese, is greatly appreciated.

I would also like to thank the Society for Mining, Metallurgy, and Exploration, Inc., Journal of Geophysical Research, American Association of Petroleum Geologists, Scientific drilling, and the Geological Society who granted the permission for using their published material.

The financial support of this research by NSERC Lithoprobe Supporting Science Grant, NSERC, Mobil, and the Alberta Oil Sand Technology and Research Authority is greatly appreciated. I also like to further acknowledge the financial support in my graduate study from the Department of Physics.

TABLE OF CONTENTS

CHAPTER			PAGE
1.	INTRODUCTION		1
	1.1	Background	3
	1.2	Numerical Calculation	9
	1.3	Outline of Thesis	10
	1.4	Bibliography	14
2.	GENERAL CHARACTERISTICS OF WELLBORE BOTTOM STRESS CONCENTRATIONS		21
	2.1	Introduction	21
	2.2	Numerical Calculations	23
	2.3	Results and Observations	26
		2.3.1 Primary Stress Conditions	26
		2.3.2 Combined Stress Conditions	29
	2.3 Discussion		31
		2.4.1 Primary Stress Conditions	32
		2.4.2 Combined Stress Conditions	33
		2.4.3 Effect of Core Length on Stress Concentration	35
	2.5 Conclusions		38
	2.6 Bibliography		39
3.	INFLUENCE OF POISSON'S RATIO AND CORE STUB LENGTH ON BOTTOMHOLE STRESS CONCENTRATION		61
	3.1	Introduction	61
	3.2	Background	62
	3.3	Numerical Calculations	63
	3.4	Results	65

3.4.1 Characteristics of Primary Stress Concentrations 65
3.4.2 Peak Concentrated Stresses 68
3.4.3 Hypothetical Failure Curves 71
3.4.4 Core Stub Length and Applied Stress Magnitudes 75
3.5 Conclusions 76
3.6 Bibliography 78

4. DRILLING INDUCED FRACTURES AND IN-SITU STRESSES 98
4.1 Introduction 98
4.2 Background 100
4.3 Numerical Calculations 103
4.3.1 Finite Element Modeling 103
4.3.2 Predicting Fracture Trajectories 104
4.4 Modeling Results 105
4.4.1 Normal Fault Stress Regime 105
4.4.2 Strike-Slip Fault Stress Regime 106
4.4.3 Thrust Fault Stress Regime 106
4.4.4 Preferred Locations of Fracture Initiation 107
4.4.5 Stress State Domains of Core Fractures 108
4.5 Discussion 109
4.5.1 Comparison of Modeling Results and Observations 109
4.5.2 Additional Considerations 112
4.6 Conclusions 115
4.7 Bibliography 116

5. CONCLUSIONS AND FUTURE DIRECTIONS 133
5.1 Conclusions 133
5.2 Future Directions 137

5.2.1 Application in In-Situ Stress Determination in the Western Canadian Basin 137

5.2.2 Application to Inclined Boreholes 138

5.2.3 Application in Analysis of Wellbore Stability 139

5.2.4 Application in Analysis of Drilling Rate 139

5.3 Bibliography 140

APPENDICES:

APPENDIX 1: A HIGH-PRESSURE TECHNIQUE FOR DETERMINING THE MICROCRACK POROSITIES OF DAMAGED BRITTLE MATERIALS 143

1.1 Introduction 143

1.2 Theoretical Basis 145

1.3 Experimental Procedure 149

1.4 Results and Discussion 152

1.4.1 Compressibilities 152

1.4.2 Microcrack Strain Tensor 156

1.5 Conclusions 157

1.6 Bibliography 158

APPENDIX 2: INFLUENCE OF CORE BIT CUT GEOMETRY ON BOTTOMHOLE STRESS CONCENTRATION 167

2.1 Introduction 167

2.2 Results 168

2.2.1 General Stress Characteristics 168

2.2.2 Concentrated Stress Magnitudes and Kerf Shape 170

2.2.3 Influence of Cut Width/Core Radius Ratio 172

2.3 Conclusions 173

2.4 Bibliography 174

APPENDIX 3: PRELIMINARY MODELING OF STRESS CONCENTRATION IN AN INCLINED BOREHOLE 178

3.1 Model Description 178

3.2 Stress Concentrations Under Applied Shear Stress 180

APPENDIX 4: FRACTURE TRAJECTORY DETERMINATION METHOD 191

4.1 Fracture Tracing Algorithm 191

4.2 MATLAB Program for Fracture Tracing 194

APPENDIX 5: STRESS DATA BASE 199

5.1 Description of Stress Data Base 199

5.2 Example of ANSYS programs 204

5.3 Program for Stress Superposition 225

5.4 Program for Plotting Stress Orientations 229

LIST OF FIGURES

FIGURE		PAGE
1.1	Borehole in three dimensional in situ stress field.	20
2.1.	Examples of core disk fractures and petal fractures.	45
2.2.	Mesh of finite element model for a squared cut bottomhole.	46
2.3.	Contours of σ_3 at $\Phi = 0°$ and 90° under horizontal uniaxial stress for different core stub lengths.	47
2.4.	Orientations of principal stresses at $\Phi = 0°$ and 90° under horizontal uniaxial stress for different core stub lengths.	48
2.5.	Contours of σ_3 under overburden for different core stub lengths.	49
2.6.	Orientations of principal stresses under overburden with different core stub lengths.	50
2.7.	Contours of σ_3 under drill bit weight for different core stub lengths.	51
2.8.	Orientations of principal stresses under drill bit weight with different core stub lengths.	52
2.9.	Contours of σ_3 under wellbore fluid pressure for different core stub lengths.	53
2.10.	Orientations of principal stresses under wellbore fluid pressure for different core stub lengths.	54
2.11.	Contours of σ_3 under biaxial stress condition for different core stub lengths.	55
2.12.	Orientations of principal stresses under biaxial stress condition for different core stub lengths.	56
2.13.	Contours of σ_3 under hydrostatic stress condition for different core stub lengths.	57
2.14.	Orientations of principal stresses under hydrostatic stress condition for different core stub lengths.	58
2.15.	Orientations of principal stresses at $\Phi = 0°$ and $\Phi = 90°$ under $S_H = S_v = S_b = S_p = 20$ MPa and $S_h = 0$ for different core stub lengths.	59

2.16. The relationship between the greatest tensile and shear stresses and the normalized core stub length. 60

3.1. Examples of cup-shaped core disk fractures. 82

3.2. Details of the finite element mesh for modeling Obert and Stephenson's experiments (1965). 83

3.3. Orientations of principal stresses under S_r = 20 MPa for different core stub lengths. 84

3.4. Contours of most tensile principal stress σ_3 under S_r = 20 MPa for different core stub lengths. 85

3.5. Orientations of principal stresses under S_a = 20 MPa for different core stub lengths. 86

3.6. Contours of the most compressive principal stress σ_1 under S_a = 20 MPa for different core stub length. 87

3.7. Orientations of principal stresses under hydrostatic stress condition with $S_r = S_a$ = 20 MPa for different core stub lengths. 88

3.8. Contours of the most tensional principal stress σ_3 under hydrostatic stress condition for different core stub lengths. 89

3.9. The most tensile and compressive principal stresses along core axis. 90

3.10. Shear stresses across the surface of the kerf. 91

3.11. Peak tensile and shear stresses normalized by the applied radial stress. 92

3.12. Hypothetical tensional failure curves. 93

3.13. Mohr-Coulomb criterion in τ–σ space for the internal friction angles of a) $\phi = 25°$ and b) $\phi = 50°$. 94

3.14. Comparison of experimental data of Obert and Stephenson (1965) with calculated failure curves. 95

3.15. Hypothetical failures curves for different core stub lengths and Poisson's ratios. 96

3.16. The relationship of the core disk thickness and the in situ radial stress S_r under the in situ axial stress $S_a = 0$ and with different Poisson's ratios. 97

4.1. Examples of drilling induced cup shaped and saddle shaped core disks, petal fractures, and petal-centerline fracture. 121

4.2. Fractographic features of a fracture initiating at the center of a core and a petal fracture surface. 122

4.3. Faulting environments as characterized by Anderson (1951). 123

4.4. Details of finite element mesh for a borehole with a curved bottom cut. 124

4.5. Orientations of local principal stresses in the normal fault stress regime. 125

4.6. Predicted fracture trajectories in the normal fault stress regime. 126

4.7. Orientations of local principal stresses in the strike-slip fault stress regime. 127

4.8. Predicted fracture trajectories in the strike-slip fault stress regime. 128

4.9. Orientations of local principal stresses in the thrust fault stress regime. 129

4.10. Predicted fracture trajectories in the thrust fault stress regime. 130

4.11. The greatest tensile stresses at the inner kerf area, the root and the top of core stub in the Andersonian fault stress regimes. 131

4.12. The relationship between coring induced fractures and in situ stresses. 132

A1.1. Hypothetical linear or volumetric strain curve versus hydrostatic-confining pressure for a cracked material. 162

A1.2. Placement of nine strain gauge on cubical sample. 163

A1.3. Observed linear strains and linear crack strains versus confining pressure. 164

A1.4. Scanning electron microscope images of a section of the rock studied. 165

A1.5. Principal strains and their orientations. 166

A2.1. Normalized tensile stresses on the flat and curved cut surfaces and along borehole axis with the ratio of cut width/core radius equal to 1 under various stress conditions. 175

A2.2. Normalized greatest tensile stresses on the flat and curved cutting surfaces versus core stub length with the ratio of cut width/core radius equal to 1 under various stress conditions. 176

A2.3. Normalized greatest tensile stresses on flat cut surfaces versus core stub length with the ratios of cut width/core radius equal to 1/5, 2/5 and 1 under the various stress conditions. 177

A3.1. Inclined borehole with in situ stress field. 183

A3.2. Inclined borehole with far-field stress components. 184

A3.3. Decomposed pure shear models used for finite element modeling under (a) S_{xy}, (b) S_{xz}, and (c) S_{yz}. 185

A3.4. Finite element mesh in the vicinity of borehole bottom for the normal tractions, S_{xx}, S_{yy} and S_{zz}. 186

A3.5. Finite element mesh in the vicinity of bottomhole for the shear forces of S_{yz}. The mesh for the shear force S_{xz} is the same except a 90^{o} rotation subject to the z axis. 187

A3.6. Finite element mesh in the vicinity of borehole for the shear force S_{xy}. 188

A3.7. a) Least principal stresses (σ_3) and b) the maximum shear stresses (σ_1-σ_3)/2 at the wellbore bottom under the shear force S_{xz}. 189

A3.8. a) Least principal stresses (σ_3) and b) the maximum shear stresses (σ_1-σ_3)/2 at the wellbore bottom under the shear force S_{xy}. 190

A4.1. Description of fracture trajectory tracing process. 193

LIST OF TABLES

TABLE		PAGE
2.1	Summary of wellbore bottom stress concentrations under the primary stress conditions.	43
2.2	Summary of wellbore bottom stress concentrations under the combined stress conditions.	44
3.1	Rock physical properties and experimental results obtained in Obert and Stephenson's experiments (1965).	81
4.1	Field and experimental data of coring induced fractures.	120
A1.1	Observed linear and calculated bulk compressibilities.	161

CHAPTER 1

INTRODUCTION

Fractures and microcracks strongly affect elastic wave velocities, compressibilities, electrical conductivities and permeabilities of rock. Knowledge of the characteristics and the origins of fractures and microcracks and the crustal stress fields within which they are produced is important in analyzing geological processes, designing underground structures, in mining, in excavation, in petroleum recovery, and in seismic interpretation.

Natural fractures and microcracks are often thought to be stress-induced and result from regional tectonic activities, geothermal processes, and incompatibility between the various minerals in a stressed rock. During the drilling of a wellbore, fractures and microcracks also are created on the wellbore wall, at the bottomhole, and within the retrieved core due to the interaction of drill bit and rock, the concentration of in situ stress by the wellbore cavity, and the relief of residual in situ stresses. This damage affects wellbore stability and influences the measurement of rock physical properties. Conversely, these fractures and microcracks have the potential to carry substantial diagnostic information regarding the stress states which produced them. To date, much of this information remains mostly unused for lack of an interpretational framework. In this thesis, the stress concentrations existing at the bottomhole are studied in detail in order to determine the stress conditions under which drilling-induced core fractures and microcracks are induced and in the hope that a portion of this problem might be addressed.

Drilling induced fractures within retrieved rock cores have long been considered potentially inexpensive and easily obtained indicators of the magnitudes and orientations of crustal stresses because of their remarkably uniform shape and spacing along the core (Figures 2.1, 3.1, and 4.1-2). Great efforts have been made in the past to use these fractures in determining in situ stresses, but success has mainly been limited to

determinations of the orientation of in situ stresses. The problems basic to the localization of incipient failure, the failure mechanism, the quantitative relationships between the stress states and wellbore bottom geometries, and the morphology of these fractures remain, for the most part, unsolved. It is hoped that the present work will contribute to a better understanding of these problems and point towards a more complete usage of drilling induced fractures as both stress state indicators and perhaps as gauges of stress magnitudes.

Interest in using drilling induced fractures in constraining in situ stresses derives partly from economic considerations. If core is available, the incremental cost of analysis is only a small fraction of the expense associated with making field measurements with overcoring or hydraulic fracturing methods, for example. Large numbers of available cores suggests that substantial information could be added for use in the petroleum and mining industries. Better methods of interpreting core fractures would be a great benefit to on site drilling where the knowledge of in situ stresses may be required almost immediately. The volume and the quality of the present in situ stress database for regional geology and global tectonics (Adams and Bell, 1991; Zoback, 1992; and Coblentz and Richardson, 1996) might be supplemented greatly by the additional information that can be retrieved from the existing core repositories.

In this thesis, the core damage induced by stress concentrations at the bottom of a wellbore is studied. First, the results of a thorough investigation of bottomhole stress concentrations are described. Further studies lead to the development of the hypothetical relationship for predicting magnitudes of in situ stress from the spacings of core disks suggesting that this might be possible under certain stress conditions. Finally, the relationship between crustal in situ stress regimes and morphologies of coring induced fractures is developed. As part of this research, a newly developed method for determining the microcrack tensor within a core is also provided.

1.1 BACKGROUND

Knowledge of *in situ* state of stress is fundamentally important in designing underground structures, mining, and excavations (Hudson and Cooling, 1988). Also, information of in situ stresses plays an important role in evaluation of seismic risk, and analysis of regional and tectonic activities (Bell and Gough, 1979; Adams and Bell, 1991; and Zoback, 1992). The importance of in situ stresses to the petroleum industry, especially in the production of oil and gas, has long been recognized. The significance of in situ stress to well simulation has been emphasized by Lorenz et al. (1988) in a multiwell experiment of a low-permeability discontinuous reservoir in the Rocky Mountain region of the United States. Here, both the natural and simulated fractures trend parallel to the greatest in situ horizontal compressive stress, this indicates the importance of pre-production knowledge of in situ stress in this reservoir. In the design of production strategies the classic studies of borehole breakouts in the Western Canadian Basin by Bell and Gough (1979), Gough and Bell (1981), Bell and Babcock (1986) and Bell et al. (1994) lead to a good understanding of the relationship between in situ stresses and hydrocarbon recovery. Information of in situ stresses can be used to predict the orientation of hydraulically induced fractures, to aid in the design of inclined boreholes in a fractured reservoir, to find the tectonic signatures which may result in rock seismic anisotropy and directional permeability, and to predict the directions of hydraulic fractures.

In addition to the importance of in situ stresses in hydrocarbon production, rock anisotropy induced by in situ stresses affects seismic wave propagation and its interpretation. The relations between seismic velocities, attenuation and stress have been studied by many workers under a variety of stress state conditions (e.g., Nur and Simmons, 1969; Sayer et al., 1990, Zamora and Poirier, 1990; Yin, 1992; and Mavko et al., 1995). These studies suggested that seismic velocity and attenuation are sensitive to stress or stress-induced rock anisotropy. Studies on the influence of effective stress and pressure (Toksoz et al., 1976; Domenico, 1984; and Tatham and McCormack, 1991) and

abnormal pressure in a reservoir (Anstey, 1977) have drawn similar conclusions. Such studies indicated that knowledge of in situ stresses aid the interpretation of seismic and well logging data.

The studies of shear wave propagation in rock suggested that in situ stress-aligned pore and microcracks (extensive-dilatancy anisotropy) results in the birefringence of shear wave polarization (Roberts and Crampin, 1986; Crampin, et al., 1986; Crampin, 1987; Crampin et al., 1989; and Ass'ad et al., 1992). A direct application using the ratio of polarized shear wave components V_{S1}/V_{S2} to calculate the ratio of horizontal in situ stresses in the directions of shear wave polarization has been given by Lynn (1991). In an analysis of earthquake recording data of the Los Angeles basin and adjacent areas, Li (1996) found that the polarization direction of the fast shear wave (V_{S1}) is in good agreement with the regional north-south compression.

Many methods of measuring in situ stress have been developed, but stress determinations in the earth remain technically challenging. As there are many excellent discussions of this topic including a recently published textbook (Engelder, 1993), we will spare the reader a lengthy review. Briefly, several successful methods have been used extensively for engineering purposes, in hydrocarbon, water, and geothermal production, in site evaluation of potential high level waste repositories, or in aiding remediation efforts. These methods include hydraulic fracturing (Haimson and Fairhurst, 1967), overcoring (Leeman, 1966; Herget, 1973), differential strain analysis (Simmons et al., 1974; Schmitt and Li, 1995), anelastic strain recovery (Teufel, 1983), and optical interferometry (Bass et al., 1986; Schmitt and Li, 1996). Other methods such as wellbore breakouts (Bell and Gough, 1979), earthquake focal mechanisms (Byerly, 1955; Hodgson, 1957; Kasahara, 1981; Bossu and Grasso, 1996; Caccamo et al., 1996; and Lu et al., 1997) principally indicate stress directions. Because of the often encountered difficulties and expensive cost of using these methods, any technique which can supplement the existing knowledge at incremental expense is important.

The protocols of most of the methods described above require knowledge of the stress distribution near a wellbore and in particular the concentration of the in situ stresses by the existence of the wellbore cavity itself. Since this theme is central to the present work, it is worth reviewing briefly how stress concentrations in the vicinity of wellbores have been viewed.

In almost all cases the wellbore is assumed to be an already existing hollow cylinder of infinite extent; under this high degree of symmetry useful elastic solutions are attainable. The most famous of these was provided by Kirsch (1898) for the two dimensional plane strain formulation for a hole in a thin plate subject to a uniaxial principal stress is

$$\begin{aligned} \sigma_r &= \frac{S_H}{2}\left(1 - \frac{a^2}{r^2}\right) + \frac{S_H}{2}\left(1 + 3\frac{a^4}{r^4} - 4\frac{a^2}{r^2}\right)\cos 2\theta \\ \sigma_\theta &= \frac{S_H}{2}\left(1 + \frac{a^2}{r^2}\right) - \frac{S_H}{2}\left(1 + 3\frac{a^4}{r^4}\right)\cos 2\theta \\ \tau_{r\theta} &= \frac{S_H}{2}\left(1 - 3\frac{a^4}{r^4} + 2\frac{a^2}{r^2}\right)\sin 2\theta \end{aligned} \qquad (1.1)$$

where a is the radius of the borehole, r is the distance from the center of the borehole, and θ is measured clockwise from the direction of the compressive stress S_H. σ_θ is the concentrated circumferential or hoop stress, σ_r is the concentrated radial stress , and $\tau_{r\theta}$ is the concentrated shear stress. This solution can be incorporated into analysis of the stresses near the wellbore under the assumption that one of the principal stresses is parallel to the borehole axis. In general, the least principal stress, S_h, is nonzero, and produces a stress distribution similar to that of S_H but orthogonal to it. The straightforward superposition of the stresses produced by S_H and S_h gives the more realistic stress field in the vicinity of the borehole.

The superposition of fluid pressure, P_f, inside a borehole generates additional stresses in the rock adjacent to the borehole. Based on Lame's solution (1852) for a hollow cylinder subject to internal and external pressure, if the outer radius of the cylinder

becomes very large and the external pressure is set equal to zero, the radial, circumferential, and vertical stresses are of the form

$$\sigma_r = P_f \frac{a^2}{r^2},$$
$$\sigma_\theta = - P_f \frac{a^2}{r^2}, \qquad (1.2)$$
$$\sigma_z = 0 .$$

Superposition of such basic elastic solutions have been used to predict the orientation, shapes and dimensions of borehole breakouts (Bell and Gough, 1983; Zoback et al., 1985) and the initiation of hydraulic fractures (Hubbert and Willis, 1957; Hamison and Fairhurst, 1967). Other related, and substantial stress concentrations arise from the flow of heat or fluids into or out of the wellbore due to differences in wellbore fluid pressure and temperature (Schmitt and Zoback, 1993; Brudy, 1995) for recent discussions of these topics.

The three-dimensional solution which is often used for analyzing the stress near an inclined borehole has been given by Hiramatsu and Oka (1968), and employed in the analysis of wellbore stability by several workers (e.g., Bradley, 1979; Peska and Zoback, 1995). The solution to these stress states is given by:

$$\sigma_r = \frac{(S_{xx} + S_{yy})}{2}\left(1 - \frac{a^2}{r^2}\right) + \frac{(S_{xx} - S_{yy})}{2}\left(1 + 3\frac{a^4}{r^4} - 4\frac{a^2}{r^2}\right)\cos 2\theta$$
$$+ S_{xy}\left(1 + 3\frac{a^4}{r^4} - 4\frac{a^2}{r^2}\right)\sin 2\theta + P_f \frac{a^2}{r^2}$$
$$\sigma_\theta = \frac{(S_{xx} + S_{yy})}{2}\left(1 + \frac{a^2}{r^2}\right) - \frac{(S_{xx} - S_{yy})}{2}\left(1 + 3\frac{a^4}{r^4}\right)\cos 2\theta$$
$$- S_{xy}\left(1 + 3\frac{a^4}{r^4}\right)\sin 2\theta - P_f \frac{a^2}{r^2},$$
$$\sigma_z = S_{zz} - \upsilon\left[2(S_{xx} - S_{yy})\frac{a^2}{r^2} + 4\, S_{xy}\frac{a^2}{r^2}\sin 2\theta\right], \qquad (1.3)$$
$$\tau_{r\theta} = \frac{(S_{xx} - S_{yy})}{2}\left(1 - 3\frac{a^4}{r^4} + 2\frac{a^2}{r^2}\right)\sin 2\theta + S_{xy}\left(1 - 3\frac{a^4}{r^4} + 2\frac{a^2}{r^2}\right)\cos 2\theta ,$$
$$\tau_{z\theta} = \left(-S_{xz}\sin\theta + S_{yz}\cos\theta\right)\left(1 + \frac{a^2}{r^2}\right),$$

$$\tau_{rz} = \left(S_{xz}\ \cos\theta + S_{yz}\ \sin\theta\right)\left(1 - \frac{a^2}{r^2}\right),$$

where, S_{xx}, S_{yy}, S_{zz}, S_{xy}, S_{xz}, and S_{yz} are obtained by the coordinate transformation from (S_H, S_h, S_v) using

$$\begin{bmatrix} S_{xx} & S_{yx} & S_{zx} \\ S_{xy} & S_{yy} & S_{zy} \\ S_{xz} & S_{yz} & S_{zz} \end{bmatrix} = [A]^T \begin{bmatrix} S_1 & 0 & 0 \\ 0 & S_2 & 0 \\ 0 & 0 & S_3 \end{bmatrix} [A] \qquad (1.4)$$

in which (S_H, S_h, S_v) has been arranged as (S_1, S_2, S_3) in terms of the magnitudes and

$$[A] = \begin{bmatrix} \cos\gamma\cos\beta\cos\alpha - \sin\gamma\sin\alpha & \cos\gamma\cos\beta\sin\alpha + \sin\gamma\sin\alpha & -\cos\gamma\sin\beta \\ -\sin\gamma\cos\beta\cos\alpha - \cos\gamma\sin\alpha & \sin\gamma\cos\beta\cos\alpha + \cos\gamma\sin\alpha & \sin\gamma\sin\beta \\ \sin\beta\cos\alpha & \cos\beta\cos\alpha & \cos\beta \end{bmatrix}$$

(1.5).

The Eulerian angles α, β, γ define a sequence of three rotations necessary to rotate the coordinate system (S_H, S_h, S_v) for a vertical borehole to an inclined borehole with the axis of the borehole aligned with the z axis (Figure 1.1). Also notice that the angle θ in Equation (1.3) is in the x-y plane and relative to the x axis.

For the above solutions to hold, the section of the wellbore in question must be sufficiently removed from the wellbore bottom. If not, the stresses are influenced by the more complex but poorly understood stress concentrations at the wellbore end. The influences of bottomhole stress concentrations in drilling efficiency (Cunningham, 1959; Garnier and Lingen, 1959; Rowley, 1961; and Eckel, 1963) and drilling induced core damages (e.g., Pendexter and Rohn, 1954; Jaeger and Cook, 1963; Obert and Stephenson, 1965; and Dyke, 1989) have long been recognized. Despite this there has been little additional detailed study.

There have been many attempts to provide quantitative relationships between the geometry of drilling induced fractures and the magnitudes of in situ stresses in the past few decades. The morphology of these fractures was classified by Kulander et al. (1990) into core disking, petal, petal-centerline, and centerline fractures. Pendexter and Rohn (1954) first recognized that petal fractures may be important in retrieving information related to the drilling processes. To explore the failure mechanism of core disking fractures, Jaeger and Cook (1963), and Obert and Stephenson (1965) produced core disking fractures experimentally using stress conditions similar to a conventional rock triaxial test. Recently, Haimson and Lee (1995) produced core disking fractures under three unequal applied stresses. Earlier numerical modeling was carried out by Sugawara et al.(1978), Chang (1978), Lee (1978), GangaRao et al.(1979), and Dyke (1989). Efforts have been made to explain the failure mechanism of drilling induced fractures and to relate them to in situ stresses, but success has mostly been limited to obtaining in situ stress orientations (Friedman, 1969; Kulander et al., 1979; Plumb and Cox, 1987; Lenhoff et al., 1982; Miguez et al., 1987; Nelson et al., 1987; Paillet and Kim, 1987; Laubach, 1988; Lorenz and Finley, 1988; Maury et al., 1988; Borm et al., 1989; Natau et al., 1990; Lorenz et al., 1990; Wang and Sun, 1990; Kulander et al., 1990; Kutter, 1991; Engelder, 1993, Bankwitz and Bankwitz, 1995; and Röckel, 1996).

Part of the reason for this state of affairs is that deriving formulas for the complete three dimensional stress concentrations is very difficult even for the seemingly simple geometry at the bottomhole. The earlier exact analytic expressions (e.g. Kirsch, 1898; Hiramatsu and Oka, 1968) are able to produce relatively simple expressions for the stress concentrations along the circular wellbore. This is not possible once the bottomhole is included.

One such solution that has been developed is that of Tranter and Craggs (1945) for the stress concentrations within an infinite cylinder, the lower half of which is subject to a uniform pressure with no tractions on the upper half. High stress concentrations are

produced near z = 0 where the pressure discontinuity appears. The geometry of the situation is reminiscent of a core stub at the bottomhole. An experiment based on this solution was tested by Jaeger and Cook (1963) and as predicted core disks were produced in tension. This solution, however, only can aid in understanding the stress concentrations resulting from the discontinuous stress condition but it cannot be used to directly explain the core disking phenomenon because of the special geometry of the bottomhole cavity and the complex stress conditions. This is especially true when the progressive coring process is considered; this elastic solution cannot apply to a short core stub. As we show later, the length of a core stub at the bottomhole has a significant influence on the distribution of stress within the material. Indeed, the analytic solutions for 3D problems in elasticity can be extremely complex as may be seen by the comparisons of finite element results to analytic developments seen in a much simpler geometry than considered here (Schmitt and Li, 1996).

1.2 NUMERICAL CALCULATION

Here, the finite element method is employed in the calculations of stress concentrations as it is able to determine stress states for the asymmetric bottomhole geometry. One of the principal stresses is often vertical in regions of gentle topography (Anderson, 1951) and the calculations presented here adopt this by assuming a vertical borehole aligned with the overburden stress. More complex modeling is required once the wellbore is no longer vertical or parallel to a principal stress, this issue is addressed only briefly later on but is an important task for future study. Further, in this work the rock is taken to be a linearly elastic and isotropic material, rarely the case in reality, in order to simplify the calculations and to provide a basis from which further more complex but more realistic modeling might advance.

Several numerical modeling studies for calculating the stresses and the deformations near the wellbore bottom have been conducted for the purpose of stress measurement

related to frequently used methods in engineering such as overcoring (Crouch, 1969; Heerden, 1969; and Wang and Wong, 1987). The earliest numerical analysis which used the finite element method to study core disking fracture was conducted by Sugawara et al. (1978). Chang (1978) and Lee (1978) performed finite element calculations for modeling petal fracturing. Lenhoff et al. (1982) performed an extensive analysis of core disking using different finite element models. The most recent study employed the boundary element method (Dyke, 1989) and discussed the possible initiation locations and morphology of core disking fracture. In addition, the effect of the drill bit weight combined with horizontal far-field stress in two dimensions was studied by Lorenz et al. (1990). Several problems remain to be solved. First, the orientations of the local stresses within the material have not been provided even though they are crucial to understanding the initiation and propagation of fractures. Second, a systematic study considering the evolution of stress concentration with core stub length has not been conducted. Third, the relationship between the morphology of coring induced fractures and in situ stress has not been explored fully.

We are fortunate to be able to exploit the ready accessibility to relatively rapid computational capabilities and efficient software which was not available to the earlier researchers. The finite element package ANSYS™ was used in the modeling in this thesis. A systematic finite element modeling considering the evolution of in situ stresses, the drilling process and the bottomhole cut geometries is described in this thesis. The finite element method is now well established and will not be reviewed here.

1.3 OUTLINE OF THESIS

This paper format thesis consists of three papers in press and supplementary appendices consisting of one further published paper, some new research results, and archival material to aid the continuity for later workers. The papers in the body of the

thesis are organized chronologically; the reader may notice some progression of the research based on the order of these papers.

The first chapter provides a brief introduction and motivation for the work contained herein. This includes the importance of the knowledge of the state of in situ stress in engineering, in analysis of geological processes, and in the petroleum industry. The methods of in situ stress measurements are briefly summarized and existing analytic stress concentration solutions are provided for comparison and historical completeness.

Chapter 2, accepted for publication in the American Association of Petroleum Geology Bulletin (Li and Schmitt, 1997a), presents the results of a general 3D investigation of bottomhole stress concentrations and the potential relationship between drilling induced damage and in situ stresses. It provides a basis for understanding drilling-induced core fractures and microcrack damage at the bottomhole. The stress concentrations were studied under a variety of applied far-field in situ stress conditions including drill bit weight and wellbore fluid pressure. Further, the relationship between the core stub length and maximum tensileand shear stresses is described. Possible rock failure mechanisms and the forms of induced damage in the vicinity of the bottomhole, especially, the induced core fractures, are discussed.

Chapter 3, accepted for publication in the International Journal of Rock Mechanics and Mining Sciences and Geomechanics Abstracts (Li and Schmitt, 1997b) presents the results of a detailed study of core disking fractures in the experiments conducted by Obert and Stephenson (1965). In their tests, cylindrical samples subjected to a variety of axial and radial loads were cored and the stress levels at which core disks appeared noted. These are presently the only experimental results available with which the present modeling can be compared. The literature of the time (Obert and Stephenson 1965; Jaeger and Cook, 1963) discussed whether core disks were formed by tensional or shear compressional failures modes. The fracturing expected under each of these contrasting modes within the concentrated stress fields is determined in this study. Obert and Stephenson (1965) carried

out measurements on a wide variety of rock types which for the purposes of the present work can be characterized in terms of their Poisson's ratio as this, together with the actual geometry of the bottomhole, are the influences which control the character of the induced stress field. Consequently the dependence of the stress concentrations on Poisson's ratio is also studied. Finally, hypothetical failure curves are produced to predict the magnitudes of in situ stresses based on the thickness of core disks for the particular case of Obert and Stephenson's (1965) experimental geometry.

Chapter 4, accepted for publication in the Journal of Geophysical Research (Li and Schmitt, 1997c), describes the relationship between the morphology of drilling induced fractures and crustal in situ state of stress. A simple fracture trajectory tracing algorithm was developed in order to predict the shape of the fractures that would arise under different states of in situ stress. Interesting relationships between the shapes of the core fractures and stress states described within the Andersonian faulting regime classification are found. The shape of a core fracture can yield immediate information on the relative magnitudes of the principal in situ stresses; the shape is a simple stress indicator in its own right. Further, the existing, but extremely limited, descriptions of drilling induced fractures from laboratory experiments and field observations are compared to these theoretical results. This chapter points the way towards the more useful interpretation of drilling induced core fractures as stress state indicators.

Chapter 5 provides general conclusions and discussions for future work. It is hoped the results can be used as an interpretive tool in supplementing data in the Western Canadian Sedimentary basin and basement where numerous cores are available for study. Some preliminary results of a discussion on the influence of wellbore fluid pressure on the rate of penetration reveals one very practical aspect of this work. The initial results of a more involved finite element analysis which allows the inclusion of a shear stress (i.e. the wellbore is no longer aligned with a principal stress) are also presented in light of potential applications to drilling of deviated wells. Finally, we have not at all addressed issues

related to bottomhole stress concentrations at the wellbore wall. This is a second important area and may have implications for the interpretation of wellbore breakouts and drilling induced fractures on the wellbore wall as observed in ultrasonic and electrical imaging logs.

The result of the studies of microcracks behaviors within cores, published in the Canadian Journal of Physics (Schmitt and Li, 1995), is presented in Appendix 1. A high pressure technique developed for determining microcrack porosities of damaged brittle material is described. The characteristics of the microcrack are identified using electron scanning microscopy. The anisotropy caused by microcracks within the rock is found by precise strain measurements under a pressure up to 200 MPa. This early thesis work served as a break point in the research and provided further motivation for the main study of bottomhole stress concentrations.

One of the important aspects related to drilling induced fractures, the influence of the kerf geometries on bottomhole stress concentrations is described in Appendix 2. Comparisons of the character and magnitudes of the induced stress fields are presented in order to provide some impression of the generality of the results of Chapters 2 to 4.

The results of preliminary modeling for bottomhole stress concentrations of an inclined borehole are described in Appendix 3. The finite element model and the superposition of far-field primary normal and pure shear stresses are described in detail. The stress concentrations under two primary pure shear stress conditions are presented. The completed work provides a basis for future research in this area.

Appendix 4 describes the fracture tracing algorithm and lists the corresponding MATLAB fracture tracing program used in Chapter 4.

Finally, for archival purposes in the hopes that the data will stimulate collaborations with other workers, the stress data base generated in this research is described in Appendix 5. The corresponding programs for stress calculation (ANSYS) stress superposition (MATLAB), stress orientation plotting (MATLAB) are also listed.

1.4 BIBLIOGRAPHY

Adams, J., and J.S. Bell, Crustal stresses in Canada, in D.B. Slemmons, E.R. Engdahl, M.D. Zoback, and D.D. Blackwell, eds., Neotectonics of North America, Decade Map, *Geological Society of America*, **1**, p. 367-386, 1991.

Anderson, E.M., The Dynamics of Faulting and Dyke Formation With Applications to Britain, 2nd ed., 206 pp., Oliver and Boyd, Edinburgh, 1951.

Anstey, N.A., Seismic Interpretation: The physical aspects, International Human Resources Development Corporation, Boston, p. 2.19-2.47, 1977.

Ass'ad, J.M., R.H. Tatham, and J.A. McDonald, A physical model study of microcrack-induced anisotropy, *Geophysics*, **57**, p. 1562-1570, 1992.

Bankwitz, P., and E. Bankwitz, Fractographic features on joints of KTB drill cores (Bavaria, Germany), in M. S. Ameen, ed., Fractography: fracture topography as a tool in fracture mechanics and stress analysis, *Geological Society Special Publication*, **92**, p. 39-58, 1995.

Bass, J.D., D.R. Schmitt, and T.J. Ahrens, Holographic in situ stress measurement, *Geophys J. R. Astr. Soc.*, **85**, p. 13-41, 1986.

Bell, J.S., and D.I. Gough, Northeast-Southwest compressive stress in Alberta: evidence from oil wells, *Earth and planetary Science Letters*, **45**, p. 475-482, 1979.

Bell, J.S., and E.A. Babcock, The stress regime of the Western Canadian Basin and implications for hydrocarbon production, *Bulletin of Canadian Petroleum Geology*, **34**, p. 364-378, 1986.

Bell, J.S., P.R. Price, and P.J. McLellan, In-situ stress in the Western Canada Sedimentary Basin, Geological Atlas of the Western Canada Sedimentary Basin, Canadian Society of Petroleum Geologists and Alberta Research Council, p. 439-446, 1994.

Borm, G., C. Lempp, O. Natau, and T. Röckel, Instabilities of borehole and drillcores in crystalline rocks, with examples from the KTB pilot hole, *Scientific Drilling*, **1**, p. 105-114, 1989.

Bossu, R., and J.-R. Grasso, Stress analysis in the intreplate area of Gazli, Uzbekistan, from different sets of earthquake focal mechanisms, *J. Geophys. Res.*, **101**, p. 17645-17659, 1996.

Bradley, W.B., Failure of inclined boreholes, *Transactions of the ASME*, **101**, p. 232-239, 1979.

Brudy, M., Determination of in-situ stress magnitude and orientation to 9 km depth at the KTB site, Ph.D. Dissertation, Universität Fridericiana zu Karlsruhe, 196 p, 1995.

Byerly, P., Nature of faulting as deduced from seismograms, In crust of the earth, Geol. Soc. Am., special paper 62, p.75-85, 1955.

Caccamo, D., G. Neri, A. Sarao, and M. Wyss, Estimates of stress directions by inversion of earthquake fault-plane solutions in Sicily, *Geophys. J. Int.*, **125**, p. 857-868, 1996.

Chang, P.S., Determination of in-situ stress based on finite element modeling, MS. thesis, The West Virginia University, 92 p, 1978.

Coblentz, D.D., and R.M. Richardson, Analysis of the South American interplate stress field, *J Geophys. Res.*, **101**, p. 8643-8657, 1996.

Crampin, S, H.B. Lynn, and D.C. Booth, Shear wave VSP's: a powerful new tool for fracture and reservoir description, *JPT*, 283-288, 1989.

Crampin, S., Geological and industrial implications of extensive-dilatancy anisotropy, *Nature*, **328**, p. 491-497, 1987.

Crampin, S., I. Bush, C. Naville, and D. Taylor, Estimating the internal structure of reservoirs with shear-wave VSPs, *Geophysics, the Leading Edge of Exploration*, p. 35-39. Nov., 1986.

Crouch, S.L., A note on the stress concentrations at the bottom of a flat-ended borehole, *Journal of the South African Institute of Mining and Metallurgy*, December, p. 100-101, 1969.

Cunningham, R.A., and J.G. Eenink, Laboratory study of effect of overburden, formation and mud column pressure on drilling rate of permeable formations, *J. Pet. Tech., Trans.* **216**, p. 9-15, 1959

Domenico, S.N., Rock lithology and porosity determination from shear and compressional wave velocity, *Geophysics*, **49**, p. 1188-1195, 1984.

Dyke, C.G., Core disking: its potential as an indicator of principal in-situ stress directions, *in* V. Maury, and D. Fourmaintraux eds., Rock at Great Depth: Balkema, Rotterdam, **2**, p. 1057-1064, 1989.

Eckel, J.R., Effect of pressure on rock drillability, *Petroleum Drilling*, Reprint Series, SPE, Rechardson, TX, p. 55-60, 1963.

Engelder, T., Stress regimes in the lithosphere, Princeton University Press, p. 171-175, 1993.

Friedman, M., Structural analysis of fractures in cores from Saticoy field, Ventura Country, California, *AAPG Bulletin*, **53**, p. 367-389, 1969.

GangaRao, H.V., S.H. Advani, P. Chang, and S.C. Lee, In-situ stress determination based on fracture responses associated with coring operation, 20th Symposium on Rock Mechanics, The University of Texas at Austin, p. 683-691, 1979.

Garnier, A.J., and N.H. van Lingen, Phenomena affecting drilling rates at depth, *J. Pet. Tech. Trans.*, AIME, **217**, p. 232-239, 1959

Gough, D.I., and J.S. Bell, Stress orientations from oil-well fractures in Alberta and Texas, *Can. J. Earth Sci.*, **18**, p. 639-645, 1981.

Haimson, B.C., and M.Y. Lee, 1995, Estimating deep in-situ stresses from borehole breakouts and core disking - experimental results in granite: Proc. of the Intl.

Workshop on Rock Stress Measurement at Great Depth, 8th International Congress on Rock Mechanics, Balkema Publ., Tokyo, **3**, 1995, in press.

Haimson, B.C., and C. Fairhurst, Initiation and extension of hydraulic fractures in rock, *Society of petroleum Engineers Journal*, **7**, p. 310-18, 1967.

Heerden W.L. Van, Stress concentration factors for the flat borehole end for use in rock stress measurements, *Eng. Geol.*, **3**, p. 307-323, 1969.

Herget, G., First experiences with C.S.I.R. triaxial strain cell for stress determinations, *Int. J. Rock Mech. and Min. Sci. & Geomech. Abstr.*, **10**, p. 509-522, 1973.

Hirmatsu, Y., and Y. Oka, Determination of the stress in rock unaffected by boreholes or drifts, from measured strains or deformations, *Int. J. Rock Mech. Min. Sci.*, **5**, p.337-353, 1968.

Hodgson, J.H., Nature of faulting in large earthquakes, *Geological Society of America Bulletin*, **68**, p. 611-644, 1957.

Hodson, J.A., and C.M. Cooling, In situ rock stresses and their measurement in U.K.-part I: the current state of knowledge, *Int. J Rock Mech. Min. Sci. & Geomech. Abstr.* **25**, p. 363-370, 1988.

Hubbert, M.K., and D.G. Willis, Mechanics of hydraulic fracturing, *Trans. AIME*, **210**, p. 153-163, 1957.

Jaeger, J.C. and N.G.W. Cook, Pinching-off and disking of rocks, *J. Geophys. Res.*, **68**, p. 1759-1765, 1963.

Kasahara, K., Earthquake Mechanics, Cambridge University Press, p. 28-52, 1981.

Kirsch, G., Die theorie der elastizität und die bedürfnisse der festigkeitslehre, *Zeit. Ver. dt. Ingenieure*, **42**, p. 797-807, 1898.

Kulander, B.R., C.C. Barton, and S. L. Dean, The application of fractography to core and outcrop investigations: Technical report for U.S. Department of Energy, Contract EY-77-Y-21-1321, METC/SP-79/3, 174 p., 1979.

Kulander, B.R., S.L. Dean, and B.J. Ward, Fractured Core Analysis: AAPG Methods in Exploration Series, **8**, 88 p., 1990.

Kutter, H.K., Influence of drilling method on borehole breakout and core disking, 7th International Congress on Rock Mechanics, p. 1659-1663, 1991.

Laubach, S.E., Coring-induced fractures: indicator of hydraulic fracture propagation in a naturally fractured reservoir, *SPE* 18164, 1988.

Lee, S.-C., Investigation of stress and fracture responses associated with coring operation, M. Sc. thesis, The West Virginia University, 111 p., 1978.

Leeman, E.R., and D.J. Hayes, A technique for determining the complete state of stress in rock using a single borehole, *Proc. Ist Int. Congn. on Rock Mech.*, **2**, p. 17-24, Lisbon, 1966.

Lenhoff, T.F., T.K. Stefansson, and T.M.Wintczak, The core disking phenomenon and its relation to in-situ stress at Hanford: SD-BEI-T1-085, Rockwell Hanford Operations, Richland, Washington, 131 p., 1982.

Li, Y.Y., and D.R. Schmitt, Wellbore bottom stress concentration and induced core fractures, *AAPG bulletin*, 1997a, in press

Li, Y.Y., and D.R. Schmitt, Effect of Poisson's ratio and core stub length on bottomhole stress concentrations, *Int. J. of Rock Mech. and Min. Sci.*, 1997b, in press.

Li, Y.Y., and D.R. Schmitt, Drilling induced core fractures and in situ stresses, *J. Geophys. Res.*, 1997c, in press.

Li, Y.-G., Shear wave splitting observations and implications on stress regimes in the Los Angeles basin, California, *J. Geophys. Res.*, **101**, p. 13947-13961, 1996.

Lorenz, J.C., and S.J. Finley, Significance of drilling and coring-induced fractures in Mesaverde core, Northwestern Colorado: SAND87-1111, UC Category 92, Sandia National Laboratories, Albuquerque, New Mexico, 36 p., 1988.

Lorenz, J.C., J.F. Sharon, and N. R. Warpinski, Significance of coring-inducing fractures in Mesaverde core, Northwestern Colorado, *AAPG Bulletin*, **74**, p. 1017-1029, 1990

Lorenz, J.C., R.W. Norman, L.W. Teufel, P.T. Branagan, A.R. Sattler, and D.A. Northrop, 1988, Results of the multiwell experiment: in situ stresses, natural fractures and other geological controls on reservoirs, *Eos , Transactions, American Geophysical Union*, **35**, p. 817 & 825-826, 1988.

Lu, Z., M. Wyss, and H. Pulpan, Details of stress directions in the Alaska subduction zone from fault plane solutions, *J. Geophys. Res.*, **102**, p. 5385-5402, 1997.

Lynn, H.B., Field measurements of azimuthal anisotropy: First 60 meters, San Francisco Bay area, CA, and estimation of horizontal stresses' ration from V_{S1}/V_{S2}, *Geophysics*, **56**, p. 822-832, 1991.

Maury, V., F.J. Santarelli, and J.P. Henry, Core disking: a review, Sangorm Symposium, Rock Mechanics in Africa, Nov. p. 221-231, 1988.

Mavko, G., T. Mukerji, and N. Godfrey, Predicting stress-induced velocity anisotropy in rock, *Geophysics*, **60**, p. 1081-1087, 1995.

Miguez, R., J.P. Henry, and V. Maury, Le discage: une method indirecte d'evaluation des contraintes in-situ, Journées Universitaires de Géotechnique-St-Nazaire-28-30 Janvier, p. 353-360, 1987.

Natau, O., G. Borm, and Th. Röckel, Influence of lithology and geological structure on the stability of KTB pilot hole, *in* V. Maury & D. Fourmaintaux eds., Rock at Great Depth, Balkema, Rotterdam, **3**, p. 1487-1490, 1990.

Nelson, R. A., L.C. Lenox, and B.J. Ward Jr., Oriented core: its use, error, and uncertainty, *AAPG Bulletin*, **71**, p. 357-367, 1987.

Nur, A., and G. Simmons, Stress-induced velocity anisotropy in rock: An experimental study, *J. Geophys. Res.*, **74**, p. 6667-6674, 1969.

Obert, L., and D.E. Stephenson, Stress conditions under which core disking occurs, *SME Transactions*, **232**, p. 227-235, 1965.

Paillet, F.L. and K. Kim, Character and distribution of borehole breakouts and their relationship to in-situ stresses in deep Columbia River basalts, *J. Geophys. Res.*, **92**-B7, p. 6223-6234, 1987.

Pendexter, C., and R.E. Rohn, Fractures induced during drilling, *JPT*, March, 15& 49, 1954.

Peska, P., and M.D. Zoback, Compressive and tensile failure of inclined wellbores and determination of in situ stress and rock strength, *J. Geophys. Res.*, **100**, 12791, 1995.

Plumb, R.A. and J.W. Cox, Stress directions in Eastern North America determined to 4.5 km from borehole elongation measurements, *J. Geophys. Res.*, **92**-B6, p. 4805-4816, 1987.

Roberts, G., and S. Crampin, Shear-wave polarizations in a hot dry rock geothermal reservoir: anisotropic effect of fractures, *Int. J. Rock Mech. Min. Sci. & Geomech. Abstr.*, **23**, p. 291-302, 1986.

Röckel, Th., Der Spannungszustand in der tieferen Erdkruste am Beispiel des KTB-Programms, Ph.D. Dissertation, Universität Fridericiana zu Karlsruhe, 141 p, 1996.

Rowley, D.S., R.J. Howe, and F.H. Deily, Laboratory drilling performance of the full-scale rock bit, *J. Pet. Tech., Trans.*, AIME, **222**, p. 71-81, 1961.

Sayer, C.M., J.G. Van Munster, and M.S. King, Stress-induced ultra-sonic anisotropy in Berea Sandstine, *Int. J. Rock Mech. Sci. & Geomech. Abstr.*, **27**, p. 429-436, 1990.

Schmitt, D.R., and M.D. Zoback, Infiltration effects in the tensile rupture of thin walled cylinders of glass and granite: implications for the hydraulic fracturing breakdown equation, *Int. J. Rock Mech. Min. Sci..& Geomech. Abstr.*, **30**, 289-303, 1993.

Schmitt, D. R., and Y.Y. Li, Three dimensional stress relief displacements from drilling a blind hole, *Exp. Mech.*, **36**, p. 412-420, 1996.

Schmitt, D.R., and Y.Y. Li, A high pressure technique for determining the microcrack porosities of damaged brittle materials, *Can. J. Phys.*, **73**, p. 330-337, 1995.

Simmons, G., R.W. Siegfried, and M. Feves, Differential strain analysis: a new method of examining cracks in rocks, *J. Geophys. Res.*, **79**, p. 4383-4385, 1974.

Sugawara, K., Y. Kameoka, T. Saito, Y. Oka, and Y. Hiramatsu, A study on core disking of rock: *Journal of Japanese Association of Mining*, **94**, p. 19-25, 1978.

Tatham, R.H., and M.D. McCormack, Multicomponent Seismology in Petroleum Exploration, Society of Exploration Geophysicists, p. 66-71, 1991.

Teufel, L.W., Determination of in situ stress from anelastic strain recovery measurements of oriented cores, *SPE* 11649, presented at 1983 SPE/DOE Symposium Low Permeability Reservoir, Denver, Colorado, March, p. 14-16, 1983.

Toksoz, M.N., C.H. Cheng, and A. Timur, Velocities of seismic waves in porous rocks, *Geophysics*, **41**, p. 621-645, 1976.

Tranter, C.J., and J.W. Craggs, The stress distribution in a long circular cylinder when a discontinuous pressure is applied to the curved surface, *Phil. Mag.*, **36**, p. 241-250, 1945.

Wang, Y., and T.-F. Wong, Finite element analysis of two overcoring techniques for in situ stress measurement, *Int. J. Mech. Min. Sci. & Geomech. Abstr.*, **24**, p. 41-52, 1987.

Wang, C.Y., and Y. Sun, Oriented microfractures in Cajon Pass drill cores: stress field near the San Andreas fault, *J. Geophys. Res.*, **95**, p. 11135-11142, 1990.

Yin, H., Acoustic velocity and attenuation of rocks: Isotropy intrinsic anisotropy, and stress-induced anisotropy, Ph. D. thesis, Stanford University, 1992.

Zamora, M., and J.P. Poirier, Experimental study of acoustic anisotropy and birefringence in dry and saturated Fontainebleau Sandstone, *Geophysics*, **55**, p. 1455-1465, 1990.

Zoback, M.D., D. Moos, and L. Mastin, 1985, Well bore breakouts and in situ stress, *J. Geophys. Res.*, **90**, p. 5523-5530, 1985.

Zoback, M.L., First- and secondary-order patterns of stress in the lithosphere: the world stress map project, *J. Geophys. Res.*, **97**, p. 11703-11728, 1992.

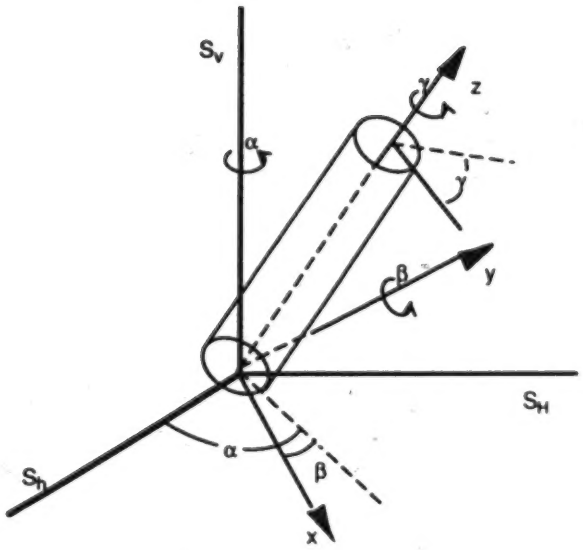

Figure 1.1. Borehole in three dimensional in situ stress field.

CHAPTER 2

GENERAL CHARACTERISTICS OF WELLBORE BOTTOM STRESS CONCENTRATION

2.1 INTRODUCTION

Drilling into the earth results in a redistribution, or concentration, of stress in the vicinity of the wellbore. These concentrated stresses affect drill bit penetration, create wellbore wall breakouts, produce inadvertent hydraulic fractures, and damage cores. Elegant solutions for the stresses concentrated near a wellbore with circular cross-section are well known (Kirsch, 1898; Hiramatsu and Oka, 1962) and have been crucial in predicting the initiation of hydraulic fractures (Hubbert and Willis, 1957) and breakouts (Gough and Bell, 1981). But near the bottomhole, these solutions do not apply. The bottomhole passes each point in the final wellbore during drilling. Thus the bottomhole stress concentrations have the first opportunity to influence the rock. Most particularly, the bottomhole stress concentrations produce drilling induced core fractures which may contain substantial information about the state of in situ stress. Since any information on in situ stress states that can be gleaned from core or well logs is useful in production development, it is important that the bottomhole stress concentrations be well understood for the interpretation of observed core fractures.

Visible drilling-induced core fractures take shapes commonly known as disking, petal, and petal-centerline fractures (Kulander et al., 1979; Kulander et al. 1990) (Figure 2.1). The creation of these fractures is attributed to the concentration of the in situ stress by the wellbore cavity (Figure 2.2). Along a core, these fractures are often of

---

A version of this chapter has been accepted for publication, January 1997, American Association of Petroleum Geologists Bulletin.

uniform shape and spacing, and they have long been considered to be indicators of both far field in situ stress magnitudes and directions. There have been many attempts to provide quantitative relationships between the geometry of these fractures and the magnitudes of in situ stresses (Jaeger and Cook, 1963; Leeman, 1964; Obert and Stephenson, 1965; Durelli et al., 1965; Sugawara et al., 1978; GangaRao et al., 1979; Stacey, 1982; Miquez et al., 1987; Maury et al., 1988; Borm et al., 1989; Perreau, 1989; Dyke, 1989; Haimson & Lee, 1995; and Röeckel, 1996). But, success has mostly been limited to obtaining in situ stress orientations using oriented core (Friedman, 1969; Kulander et al., 1979; Plumb and Cox, 1987; Lenhoff et al., 1982; Nelson et al., 1987; Paillet and Kim, 1987; Laubach, 1988; Lorenz and Finley, 1988; Natau and et al., 1990; Lorenz et al., 1990; Wang and Sun, 1990; Kulander et al., 1990; Kutter, 1991; Engelder, 1993, and Bankwitz and Bankwitz, 1995) based on the empirical observation that the core fractures strike in the direction of the greatest horizontal principal compression. Problems basic to the localization of incipient failure, the failure mechanism, the quantitative relationship between the state of stress and rock physical properties, the geometry of wellbore bottom, and the geometry of these fractures remain unsolved because the stress concentrations in the vicintiy of the wellbore have not been obtained. Determination of the far field in situ stress magnitudes (i.e. those existing in the earth prior to the drilling of the wellbore and remaining outside the zone of stress concentration at the bottomhole) from the geometry of the induced core fractures is not yet practical.

Part of the reason for this state of affairs is that deriving formulas for the complete three dimensional stress concentrations is very difficult even for the seemingly simple geometry at the bottomhole and has not been carried out. The earlier expressions (e.g. Kirsch, 1898) are able to exploit geometric symmetries to produce relatively simple expressions for the stress concentrations along a circular wellbore. This is not possible once the bottomhole is included. As a result, aside from Jaeger and Cook's (1963) analysis of core disking which employed the expressions of Tranter and Craggs (1945) workers have mostly employed

numerical calculations to estimate stress concentrations (Chang, 1978; Sugawara et al., 1978; Lorenz and Finley, 1988; and Dyke, 1989). The results of these studies suggest that failure generally initiates in tension at the root or the side of the core. However, these earlier studies did not provide indications of the orientations of the concentrated stress within the core. The orientations are crucial to understanding the interactions between the far-field in situ stresses, the drill bit weight, and the wellbore fluid pressure. Further, a systematic study considering in detail the evolution of the stress concentration with core stub length has not been published.

This study builds on the earlier numerical results with a systematic 3-D finite element modeling of the stress concentrations produced by the principal components of the far-field in situ stresses, the drill bit weight, and the wellbore fluid pressure. These applied forces are hereafter referred to as the primary stress conditions; more complex states of stress are obtained by superposing the primary results. In order that the results will be of use to other workers, the calculated stress concentrations are first described in some detail. A nearly continuous measure of the changes in stress concentration with core length is also provided for the different primary stress conditions. The implications of the calculations are then discussed especially with regards to the creation of core petal, petal-centreline, and disking fractures.

2.2 NUMERICAL CALCULATION

Here, the finite element method is employed in the calculations because it is able to determine stress states for the asymmetric bottomhole geometry. Four primary stress conditions are considered: 1) the greatest compressive horizontal principal stress S_H directed along the x direction at the azimuth of $\Phi = 0^o$; 2) the vertical principal lithostatic stress (overburden) S_v directed parallel to the wellbore axis; 3) the drill string weight S_b vertically applied uniformly at the bottom of the kerf (i.e. the cut of the core bit); and 4) the wellbore fluid pressure S_p applied perpendicularly to all the free surfaces of the wellbore.

Note that in these calculations the principal tectonic stresses are orthogonal to the vertical wellbore with the remaining and least compressive horizontal principal stress S_h directed in the y direction along an azimuth of $\Phi = 90^\circ$ (Figure 2.2). The stress concentrations produced by S_h can be obtained by an appropriate rotation of the solutions for S_H and individual calculations are not necessary.

The model core bit has a 100 mm ID and 140 mm OD with a flat kerf bottom. Since the wellbore axis is the vertical, symmetry considerations allow the calculations over only one quadrant of the wellbore allowing use of more and smaller elements in the near vicinity of the wellbore cavity where the stress concentrations are most rapidly changing. This quadrant has dimensions of 100 cm x 100 cm x 150 cm in the x, y and z directions, respectively, and contains 4220 elements and 5432 nodes. The bottom of the vertical borehole is in the center of the model 75 cm below the top surface. The external boundaries are well removed from this point so boundary effects are ignored. Displacements on the surfaces at $\Phi = 0^\circ$ and at $\Phi = 90^\circ$ and at the base of the model are constrained in the normal direction as expected from the model symmetry.

Details of the finite element mesh are shown in Figure 2.2. The finite element package ANSYS™ was used in the modeling. We refer to the inner and outer corners of the kerf as the corners of the cut adjacent to the core stub (which remains completely attached to the rock mass) and the wellbore wall, respectively. The size of the elements is kept as small as possible close to the corners of the kerf where the greatest stress concentrations appear. Higher resolutions are obtained by using 20 node elements near the kerf inner corner. The coring process is modeled by adding new layers of elements to the top of the existing core stub in each successive calculation. Note that this is not the same as the actual physical act of coring in a real situation, but what is important from the perspective of the stress concentations is the geometry and which in the calculations does not differ whether the core stub is built up by adding successive layers or by deepening the bottomhole cavity. This procedure has the advantage that the elements at the wellbore bottom remain the same in all

the calculations, and guarantees that the resolution of the modeling is not affected by the increase of core stub length. In total, twelve calculations were carried out for each primary stress case to simulate the coring process with the core stub length, l, increasing from zero to the core diameter, d (Figure 2.2); the stress concentrations did not substantially change for larger core stub lengths. Smaller increments of core length were employed for short core stubs where the stress concentrations most rapidly evolved.

The rock medium is assumed to have a Young's modulus of 20 GPa and a Poisson's ratio of 0.25. A value of 20 MPa (2900 psi) was chosen for the magnitude of the primary applied stresses. This value is typical of the lithostatic vertical stress at depths near 1000 m in sedimentary basins. The geometry, the applied stresses, and the Young's modulus could all be presented more generally in dimensionless form; but the scales chosen are typical of those encountered in practical situations.

Because the medium is linearly elastic and isotropic, the stress concentrations produced by a more complex state of in situ stress are obtained by scaling and superposing those obtained for the primary conditions. This process is carried out to provide further insight into the patterns of stress concentration for biaxial horizontal far-field stress ($S_H = S_h$), for hydrostatic far-field stress ($S_H = S_h = S_v$), and for a more complex case ($S_H = S_v = S_p = S_b$, $S_h = 0$).

Illustration of the complete tensor information for the multitude of three dimensional calculations (84 in all) is impractical; and consequently only a limited number of our calculations are presented in graphical form. The results are reported in terms of the magnitudes and directions of the principal concentrated stresses in vertical planes at $\Phi = 0^o$ and 90^o. Comparison of the tensile and shear stress magnitudes suggests that the former is most responsible for core fracturing (Dyke, 1989; Haimson and Lee, 1995) and only the most tensile principal stress is contoured. The magnitude of the other principal stress and the maximum shear stress $(\sigma_1 - \sigma_3)/2$ (hereafter referred to as shear stress) may be inferred from the corresponding plots of the principal concentrated stress orientations. Tensional

stress contours and principal stress orientations are shown only for core lengths of 0.0, 1.0, 2.5, and 5.0 cm.

2.3 RESULTS AND OBSERVATIONS

2.3.1 Primary Stress Conditions

As described, stress concentrations were individually calculated for the four separate applied primary stress conditions. In this section, features of the resulting concentrated stress fields are noted but their implications are deferred to later sections. The concentrated stress magnitudes and their orientations and type of core fracture expected are summarized in Table 2.1. Stress directions are reported by their angle from core axis (z direction). The orientations given for the maximum shear stresses are those for the corresponding minimum or maximum principal compressive stress oriented at 45° difference to the maximum shear stress $(\sigma_1 - \sigma_3)/2$. The stress sign convention used in rock mechanics is applied here with compression positive and tension negative.

1). Uniaxial horizontal stress (S_H = 20 MPa, $S_h = S_v = S_p = S_b = 0$)

Contours of the least compressive stress σ_3 at $\Phi = 0°$ and 90° are shown in Figure 2.3. The largest positive and negative stress magnitudes are found at these azimuths and fractures are most likely to originate from points within the vertical planes so oriented. The less extreme stress concentrations at other azimuths are therefore not shown.

At $\Phi = 0°$ a small tensional concentration of 5% to 15% of S_H appears inside the core. A large tensile stress zone with stress magnitudes nearly that of S_H appears on the wellbore wall a distance approximately one core diameter above the wellbore bottom (Figure 2.3). This stress concentration agrees with the well known plane strain solution of Kirsch (1898) (see Timoshenko and Goodier, 1970) for a hole in an infinite plate. Two other tensional zones are on the sides of the core and these grow with core stub length. The top of the core is also under weak tension.

At $\Phi = 90°$ the wellbore wall stresses removed from the wellbore bottom agree with Kirsch's plane strain solution (1898). Tension exists at the inner corners of the kerf (Figure 2.3). These tensional zones extend towards the core root with the core stub lengthening. The magnitude of this tensile stress is only 10% of S_H when there is no core stub, but rapidly increases to 125% of S_H at core length of 4 cm.

Corresponding stress orientations for the core lengths of 0, 1.0 and 2.5 cm are given in Figure 2.4. Here, the principal stress orientations are given by the directions and the magnitudes are represented by the proportional length of the lines. Thin solid lines represent compression; and thick solid lines represent tension. In Figure 2.4, compression dominates at $\Phi = 0°$. These compressive stresses are mainly horizontal but deviate at the corners of the kerf where the greatest compressive stresses are located. Weak tensions at the core side and top are directed parallel to the surface. The greatest shear stresses at this azimuth are also at the corners of the kerf; they increase from about 75% to 175% the magnitude of the applied far-field S_H with core length. In contrast, at $\Phi = 90°$ the stress regime is predominantly tensional (Figure 2.4). The tensile stresses deviate towards the inner corners of the kerf where they reach a maximum of 120% of S_H.

The existence of a core stub strongly influences the state of stress at the wellbore bottom. Initially at $\Phi = 0°$, the dominant stresses on the wellbore surface are horizontal and compressive (Figure 2.4). These stresses increase when the core stub forms. At $\Phi = 90°$, the surface stresses are horizontal and tensile. When no core stub exists, tension increases towards the wellbore wall. The tensile stresses increase substantially as the core stub grows, especially near the kerf.

2).Overburden ($S_v = 20$ MPa, $S_H = S_h = S_p = S_b = 0$)

For this primary applied stress condition, a large concentrated tension with a magnitude 0.6 S_v exists before forming the core stub (Figure 2.5). This tension migrates to the inner corner of the kerf and its peak magnitude increases to 2 S_v with increasing core stub. The

greatest shear stress is located at the outer corner of the kerf; it remains relatively constant at 1.25 S_v regardless of the core length.

The orientations of the tensile stresses at and in the vicinity of the inner kerf corner are similar (Figure 2.6) to those of the uniaxial case at $\Phi = 90°$ but the magnitudes are greater. There are high compressive stresses at the outer corner of the kerf but their magnitudes and orientations remain nearly constant.

The concentrated stresses at the wellbore bottom are essentially horizontal and tensional (Figure 2.6). When no core stub exists, the magnitudes of these tensile stresses are almost uniform until very near the wellbore wall. The greatest tensile stress exists at the inner corner when the core stub is produced.

3). Weight on drill bit (S_b = 20 MPa, $S_H = S_h = S_v = S_p = 0$)

A uniform compressive traction of 20 MPa is applied only over the area of the base of the kerf to simulate the drill bit weight. This produces compression immediately beneath the drill bit and tension at the inner and outer corners of the kerf (Figures 2.7 and 8). The magnitude of the tensile stress at the inner corner increases to 12 MPa as the core length grows to 4 cm and remains almost constant for longer lengths. A tensile stress of 24 MPa exists at the outer kerf corner. This stress is also nearly independent of core length. The tensile stresses at the inner kerf corner are oriented in a direction similar to those observed in the previous two cases (uniaxial case at $\Phi = 90°$). Tensile stresses exist only in a small area near the kerf corners. Little stress concentration is produced within the core stub indicating that the drill bit weight does not significantly influence material in the body of the core.

4). Wellbore fluid pressure (S_p = 20 MPa, $S_H = S_h = S_v = S_b = 0$)

A uniform wellbore pressure of 20 MPa was applied to model the effect of fluid pressure on stress concentrations. The contours of σ_3 are shown in Figure 2.9. A tensile

stress of 20 MPa is produced on the wellbore wall approximately one core diameter above the wellbore bottom. This is predicted from Lamé's solution for a hole in an infinite plane under an internal pressure (Timoshenko and Goodier, 1970). In addition, tension appears near the outer corners of the kerf where a very large tensile stress with a magnitude 300% of S_p and independent of core length results. Compression dominates inside the core but these stresses decrease from the top towards the root of the core.

High tensile stresses at the outer kerf corner are oriented about 45° from the horizontal (Figure 2.10). Small tensile stresses at the bottom of the kerf are horizontally directed. The orientations of the tensile stresses at the inner kerf corner are again similar to the previous three cases (uniaxial case at $\Phi = 90°$). The orientations of compressive principal stresses indicate that the upper part of the core is almost in a state of hydrostatic compression.

From the fluid pressure all stresses oriented normal to the cutting surface are compressive (Figure 2.10). When no core stub yet exists, the horizontal stresses at the bottom change from compression to tension from the borehole axis to its outer wall. Once the core stub is produced, tension is observed at the base of the kerf.

In practice during coring an additional 8 meter (25 foot) long column of rock may rest on the top of the core stub within the core barrel. The additional stresses added to the top of the core stub by this column are quite small in comparison to the primary stress conditions described. For example, an 8 meter column of dense limestone, with density of approximately 2.6 g/cm^3 results in an additional vertical load of only 0.21 MPa (30.4 psi) and as a result has been ignored for the present.

2.3.2 Combined Stress Conditions.

The stress concentrations resulting from each of the primary stress conditions are instructive when considered in isolation. However, such stress conditions are rarely, if ever, encountered in real situations. To explore more realistic conditions, the primary stress concentrations may be appropriately scaled relative to each other and superposed by simply

adding the corresponding stress components at the nodal points. New principal stress magnitudes and orientations are then easily determined using standard methods (Timoshenko and Goodier, 1970). Three illustrative examples of: 1) a horizontal biaxial stress condition ($S_H = S_h$), 2) an hydrostatic stress condition ($S_H = S_h = S_v$), and 3) a combination of primary tractions ($S_H = S_v = S_p = S_b$, $S_h = 0$) are presented in the following sections. The first two cases are symmetric with respect to the borehole axis. The last case represents a highly anisotropic stress condition as $S_h = 0$. Important observations on peak stress locations for these cases are compiled in Table 2.2.

1). Horizontal biaxial stress ($S_H = S_h = 20$ MPa, $S_v = S_p = S_b = 0$)

This stress condition is the same as if a uniform horizontal radial stress were applied to the model boundary. Figure 2.11 shows the contours of σ_3 for a variety of core lengths. Two tensional zones appear with increasing core length. The most prominent is at the root and the other is directed circumferentially around the core. The tensile stresses at the root increase initially but then decline once the core is longer than 2.5 cm. The tensile stresses on the core side increase until a core length of 7 cm is reached. High shear stresses are located at both the inner and outer corners of the kerf. At the inner kerf corner, the shear stresses increase when the core length is less than 2 cm and essentially remain constant at 28.2 MPa past this point.

The tensile principal stresses are oriented nearly vertically (Figure 2.12). High compression at and below the kerf is aligned almost horizontally but deviates close to the kerf corners. The stresses within cutting surface are horizontally compressive.

2). Hydrostatic stress condition ($S_H = S_h = S_v = 20$ MPa, $S_p = S_b = 0$)

A hydrostatic stress condition is formed by superposing the overburden and the biaxial stress cases. Contours of σ_3 and the orientations of principal stresses are given in Figures 2.13 and 14, respectively. High tension appears circumferentially around the core once a

core stub is formed. The greatest tensile stress in this region increases to 12 MPa with the core lengths to 7 cm. The tensional zone also expands in volume. Relatively high tension is observed at the very top of the core, but compression is seen towards the root. A nearly tension free zone is initially located at the wellbore bottom. This zone persists and expands at the root of short core stubs (< 2.5 cm length). It diminishes and moves upward with longer core (5 cm).

The orientations of maximum principal stress, σ_3, for both the biaxial and hydrostatic cases are similar. The greatest tensile stresses are on the surface of the core. The greatest compressive stresses converge at the outer kerf corner. On the cutting surface, horizontal compressive stresses dominate.

3). Effect of bit weight and wellbore fluid pressure

An example which superposes both fluid pressure and drill bit weight with the overburden and uniaxial stress is considered. The applied confining stresses are $S_H = S_v = S_b = S_p = 20$ MPa and $S_h = 0$. The applied stress normal to the cutting surface is doubled due to the superposition of both S_b and S_p.

The orientations with magnitudes are shown in Figure 2.15. At $\Phi = 90°$, high tension exists below the cut. The greatest tension originally located at the outer corners migrates to the inner corners when a core stub is formed. The greatest tensile stress at the inner corner reaches a very high (and realistically unattainable) maximum of 80.5 MPa at core length of 3.0 cm. This magnitude is twice as large as the magnitude of the tensile stresses on the wellbore wall at $\Phi = 0°$. Compressive stresses dominate at $\Phi = 0°$ and the greatest shear stress at the outer kerf corner has a magnitude of 22 MPa.

2.4 DISCUSSION

In the previous sections, the stress concentrations for four primary and three illustrative combined stress conditions are described. High stress concentrations appear near the

wellbore bottom in nearly all the cases. A drilling induced fracture is expected if this tensile stress exceeds the strength of the rock. In the following section, possible failure modes are discussed in light of the calculated stress concentrations. Modes of failure favored by the primary stress cases will be discussed first in order to evaluate the effectiveness of each stress condition in favoring certain kinds of fracture. Various criteria for fracture could be employed, but for the preliminary analysis here we take the simplest and assume that Mode I (tensile) fractures open in the direction of the greatest tension and propagate perpendicular to it.

2.4.1 Primary Stress Conditions

For the uniaxial stress case (Figures 2.3 and 4), two important points arise with respect to failure of the rock at the wellbore bottom. First, even though the magnitudes of the greatest tensile stress at $\Phi = 90°$ (0.05 to 1.25 S_H) are less than that of the greatest shear stresses at $\Phi = 0°$ (0.75 to 1.75 S_H), tensile failure is more likely because the tensile strength of rock is generally small relative to the compressive strength. As a result, tensional failure is expected to initiate at the inner corners at $\Phi = 90°$. Second, initially the fracture would propagate downward at an angle 0° to 40° from the horizontal away from the inner kerf corners (normal to the direction of the maximum tensile stress) towards the root of the core. The tensile stress orientations at the bottom of wellbore at $\Phi = 0°$ in Figure 2.4 suggest that the continued propagation is subhorizontal. This is consistent with saddle-shaped core disking.

In the case with only overburden, S_V, the orientations of the tensile stresses at and in the vicinity of the inner kerf corner (Figure 2.6) are similar to those of the uniaxial case at $\Phi = 90°$ (Figure 2.4). In this case, a tensile fracture would follow a path downwards into the rock mass below the wellbore bottom along a trajectory expected for petal fractures. This suggests that a large overburden stress may be a necessary requirement for the production of these types of fractures. Alternatively, the horizontally directed tension at the

top surface of a short core stub might induce centerline fracturing.

It has been suggested that the weight on the drill bit produces petal fracturing (Lorenz and Finley, 1988; Kulander et al., 1990). This was based on the observation (Lorenz and Finley, 1988) that the trajectory of the greatest compressive stress determined from a finite element model is similar to the shape of the petal fractures. The results here indicate that less than 1 cm away from the inner kerf corner and into the body of the core stub the concentrated stresses produced by the drill bit weight are all compressive. These stresses would retard any further advance of a tensile fracture into the body of the core. An increase in the magnitude of the drill bit weight is not expected to significantly change this scenario as the concentrated compressions so generated are also proportionally magnified. Near the inner kerf corner, however, and under bit weights of 1000 kg to 10000 kg, tensions are generated with magnitudes ranging from 0.76 MPa to 7.6 MPa. This suggests that the drill string weight might aid or result in the incipient fracture initiation at the inner corner but would not promote additional propagation into the core. In isolation from any other primary stress conditions, the drill bit weight would first promote tensile failure into the borehole wall from the outer kerf corner.

Wellbore fluid pressure similarly produces high tensile stresses at the outer kerf corner and suggests that this stress condition is fayorable to tensional fracturing into the borehole wall. An inner corner tension would aid initiation of fracture but as the stresses soon become compressive it would not assist fracture propagation. The intrusion of pressured fluid along the surface of the crack, however, is not considered here and could influence propagation.

2.4.2 Combined Stress Conditions

The results of the present calculations of biaxial stress conditions are consistent with those of Sugawara et al. (1978), who found high tension at the root of the core and a magnitude of the greatest tensile stresses of about 0.25 that of the applied stress. In this

study, it can be seen that the orientations of the principal tensile stresses remain vertical along the core axis. Away from the core axis, they are still nearly vertical and this stress condition could be responsible for cup-shaped core disking. This axisymmetric stress distribution is in good agreement with the morphology of the fractures produced in the "pinching" experiments of Jaeger and Cook (1963), where cylinders of rock were subject to a uniform radial compression.

The hydrostatic case is a superposition of the biaxial and the overburden cases, and illustrates the competing influences of these two stress conditions. Along and near the core axis the vertical components of the stresses for the biaxial case are tensional, but compressive for the overburden case. Consequently, their superposition diminishes the tensions inside and at the root of the core. For example, for a core length less than 1/4 the core diameter, the region at the root of the core is nearly free of tension due to the competing influences of the vertical and horizontal stresses.

This stress interaction between the biaxial and overburden cases may also explain qualitatively the core disking experiments of Obert and Stephenson (1965). Their experiments began at a trial radial pressure, S_{ro}, applied uniformly to intact cylinders of rock. These cylinders were then axially cored under stress. If no core fracturing was observed, the radial stress on the sample was increased and the procedure repeated until core disking occurred. Further experiments were carried out under the application of compression parallel to the axis of the cylinder. Numerous trials showed that for a variety of sedimentary and igneous rocks, the critical applied stresses at which core disking occurred could be described by a linear relation $S_r = S_{ro} + k\ S_v$ or $\Delta S_r = k\ S_v$, where k was a constant with a value less than 1. This is in agreement with a simple criteria that failure occurs once the stress concentrations reach the tensile strength of the material, and with the observations from Figures 2.11 and 13 that an increase in S_v requires a corresponding increase in S_r to result in core disking.

For the final complex case with a combination of all the stresses (Figure 2.15), the core

stub is everywhere in compression at $\Phi = 0°$. At $\Phi = 90°$, however, substantial horizontal tension is produced at the wellbore bottom prior to formation of the core stub and stress orientations shown might promote centerline fracturing. Once a core stub exists, high tensile stresses are produced at the inner kerf corner at $\Phi = 90°$, more suggestive of a petal fracture which would become a petal-centreline fracture with continued propagation.

In the real earth, the state of stress is not so clear as in the above illustrative examples. The far-field stress states will generally be anisotropic ($S_H \neq S_h \neq S_v$). Wellbore fluid pressure will depend on drilling fluid density. Drill bit weights can change drastically with the removal of the drill string during core bit replacement. It is difficult to outline here all the potential combinations which might arise as this needs to be done case by case. This task is further complicated by the observation that the applied stresses result in competing stress concentrations which can cancel each other. This is most apparent in Figure 2.14 where the tension at the core root generated by the uniform biaxial far-field compression as shown in Figure 2.12 is eliminated by the addition of the vertical overburden stress S_v whose effects are shown in Figure 2.6.

A number of general observations from the above results are important. First, it appears that petal or petal-centreline fractures can only exist in the presence of a substantial overburden stress S_v. Second, the consistent strikes of saddle shaped disk and petal fractures observed in the field (e.g. Kulander et al., 1990) are, as expected, related to differences in the magnitudes of the horizontal stresses. The strikes of these fractures will be parallel to S_H. Finally, the points of initiation of drilling-induced core fractures also depend on the stress state as suggested by fractographic observations in core (e.g. Bankwitz and Bankwitz, 1995).

2.4.3 Effect of Core Length on Stress Concentration

The effects of core stub length on stress concentration have been shown in previous sections to be significant. The reason for this is that the redistribution of the far-field

stresses depends on the bottomhole geometry. Thinking of the stresses as areally distributed forces, the very existence of the core stub constrains the displacements of the materials due to applications of the stresses. Since the material is continuous, a push or a pull generated at one spot within the material will influence the motion of adjacent points. Consequently, a change in the geometry of the bottomhole due to growth of the core stub with drilling must result in a different distribution of the stress within the material. Here, the implications of these changing stress concentrations with core stub length are considered.

The magnitudes of the greatest tensile and shear stresses generated by the primary stress conditions at the inner kerf corner are plotted versus core stub length in Figure 2.16. The overburden produces the greatest tensile stress with a magnitude of about 2 S_v (Figure 2.16a). This is followed by the uniaxial stress case with a magnitude about 1.25 S_H also at $\Phi = 90°$. The weight on the drill bit and the fluid pressure produce tensile stresses with smaller magnitudes near 0.6 S_b or 0.6 S_p.

The curves for the overburden S_v and drill bit weight S_b increase monotonically with core stub length, reaching a limit once the core length is 0.4 the core diameter; although most of the change occurs before the core stub length reaches 0.25 the core diameter. In contrast, the curves for the uniaxial S_H and wellbore fluid pressure S_p cases reach a maximum prior to leveling off. The stress peak for the uniaxial case is at a core length of 0.4 the core diameter, and for fluid pressure is at a core length of 0.15 the core diameter. Under these two stress conditions, if tensional failure occurs the spacing of core fractures is limited to the length of the core stub at which these maximum tensions occur. If the rock has not failed in tension before these core lengths are reached then core fractures are not expected. Under the overburden S_v and drill bit weight S_b conditions tensional failure may occur at any core stub length, although most of the increase in stress concentration occurs for core stubs shorter than 0.25 the core diameter.

For the uniaxial stress condition S_H, the stress concentrations at $\Phi = 0°$ have the highest

shear stresses with a magnitude about 1.75 S_H (Figure 2.16b). Overburden, S_v, and fluid pressure S_p produce shear stresses with magnitudes about 0.75 the applied stress. As with Figure 2.16a, the greatest shear stresses of the overburden, S_v, and the weight on drill bit, S_b, increase monotonically. The greatest shear stresses of the uniaxial stress, S_H, and the fluid pressure, S_p, cases have a maximum value.

The greatest tensile and shear stresses versus core length for the three combined stress conditions are shown in Figure 2.16c and 16d. The locations of the greatest tensile stresses are the root of the core for the biaxial case, the side surface of the core for the hydrostatic case, and the inner kerf corner for the case with all primary applied stresses.

For the biaxial horizontal stress condition the concentrated tensile stresses increase rapidly while the core stub length is less than 2.5 cm, and then decline past this length. The highest value of tensile stress with a magnitude about 0.25 S_H is at the core length of 2.5 cm. This relation suggests that the most severe tensional fracture damage may occur at core stub lengths 25% of the core diameter. If this tensional damage initiates core disking, the disks would occur at a spacing of no more than 1/4 the core diameter. This is in accord with laboratory experiments (e.g. Obert and Stephenson, 1965) and field observations.

For the hydrostatic case, the greatest tension appears around the core side. In general, the tensile stress increases monotonically with core length. The highest value of the tensile stress is about 55% of the applied hydrostatic stress condition. The relationship between the peak tensile stress and the core length is complicated for lengths less than 1 cm, displaying an initial local maximum for a 0.2 cm stub which decays to a minimum at 1 cm. The relatively high tensile stresses at this location should not produce large fractures because they are confined to a very small region (Figure 2.13).

The greatest tensile and shear stresses for the case with all of the primary stresses are shown in a 1/4 scale in Figures 2.16c and 16d in order to emphasize the larger magnitudes relative to those for the biaxial and hydrostatic cases. This case yields the largest tensile stress of all the superposed examples with a magnitude of 80.5 MPa, a value which easily

exceeds the tensional strength of any rock. The character of the stress field (Figure 2.15) is consistent with petal fracturing; the peak tensile stress is reached near a core length of 3.0 cm and suggests that petal fracture spacing produced under such a state of stress would be not more than 30% of the core diameter.

The shear stresses for the three combined cases increase monotonically with core length (Figure 2.16d). The largest increase occurs within 2.0 cm or 20% of the core diameter. These stresses are essentially constant for longer core stubs and their magnitudes are unlikely to result in shear failure except in the weakest of rocks.

2.5 CONCLUSIONS

Decomposition of the in situ state of stress into primary confining stress conditions provides insights into the stress concentrations of wellbore bottom which are crucial to the understanding of the formation and propagation of drilling induced core fractures. More complex and realistic stress conditions are easily determined by superposing the solutions obtained by three dimensional finite element modeling. The locations at which failures initiate and the consequent paths along which core fractures are likely to propagate are indicated by the orientations and magnitudes of the concentrated stresses.

The results of this modeling indicate possible stress concentrations which favor disking fractures, petal fractures, and petal-centerline fractures. The large tensions generated suggest that core fractures are tensile features. Saddle-shaped disk fractures are produced by uniaxial horizontal stress condition. Cup-shaped disk fractures are promoted by the biaxial horizontal stress condition and initiate at the root of the core away from the cut. Petal fractures may be produced at the inner kerf corner and most likely under a high overburden stress. Drill bit weight and wellbore fluid pressure may aid in the initiation of core fracturing but place the interior of the core in compression and would not be expected to contribute to continued fracture propagation. Centerline fracturing may be produced for a short core stub under a high overburden stress. Saddle shaped core disks are more

complex but given their asymmetric geometry they probably initiate at the inner corner of the kerf at an azimuth of 90° from the greatest horizontal compression or at the root of the core stub. Both petal and saddle-shaped disk fractures strike in the direction of the greatest horizontal compression.

Core length has a significant effect on stress concentrations. Further understanding of the relation between these concentrated stresses and the rock strength may lead to quantitative prediction of core fracture trajectories and the magnitudes of in situ stresses. This might allow use of the spacing and shape of the drilling induced fractures as indicators of the three dimensional in situ state of stress in the rock mass.

The results presented here are derived for a flat wellbore bottom with square corners. The sharpness of the corners here leads to higher magnitudes for the concentrated stresses than might be obtained for a more realistic wellbore bottom. However, ongoing modeling with more realizable wellbore bottom geometries suggests that present results are indicative of the style of stress concentration produced regardless of core bit shape or related kerf width. Nonlinear effects, fluid infiltration into the rock mass and fractures, the torsional stress caused by drill bit rotation, and variances in rock properties such as Poisson's ratio have not yet been taken into account. These are important in certain situations. Further work involving these factors, the effects of boundary shear stresses, and the determination of the propagation paths of the tensile fractures is presently underway.

2.6 BIBLIOGRAPHY

Bankwitz, P. and E. Bankwitz, 1995, Fractographic features on joints of KTB drill cores (Bavaria, Germany), in M. S. Ameen, ed., Fractography: fracture topography as a tool in fracture mechanics and stress analysis: Geological Society Special Publication, No. 92, p. 39-58.

Borm, G., C. Lempp, O. Natau, and T. Röckel, 1989, Instabilities of borehole and drillcores in crystalline rocks, with examples from the KTB pilot hole: Scientific Drilling, v. 1, p. 105-114.

Chang, P. S., 1978, Determination of in-situ stress based on finite element modeling: Ms. thesis, The West Virginia University, 92 p.

Durelli, A. J., L. Obert, and V. J. Parks, 1965, Stress required to initiate core disking: Trans. Soc. Min. Eng., AIME, v. 241, p. 269-275.

Dyke, C. G., 1989, Core disking: its potential as an indicator of principal in-situ stress directions, *in* V. Maury, and D. Fourmaintraux eds., Rock at Great Depth: Balkema, Rotterdam, v. 2, p. 1057-1064.

Engelder, T., 1993, Stress regimes in the lithosphere: Princeton University Press, p. 171-175.

Friedman, M., 1969, Structural analysis of fractures in cores from Saticoy field, Ventura Country, California: AAPG Bulletin, v. 53, p. 367-389.

GangaRao, H. V., S. H. Advani, P. Chang, and S. C. Lee, 1979, In-situ stress determination based on fracture responses associated with coring operation: 20th Symposium on Rock Mechanics, The University of Texas at Austin, p. 683-691.

Gough, D. I. and J.S. Bell, J. S., 1981, Stress orientations from oil-well fractures in Alberta and Texas: Canadian Journal of Earth Sciences, v. 18, p. 638-645.

Haimson, B. C. and M. Y. Lee, 1995, Estimating deep in-situ stresses from borehole breakouts and core disking - experimental results in granite: Proc. of the Intl. Workshop on Rock Stress Measurement at Great Depth, 8th International Congress on Rock Mechanics, Balkema Publ., Tokyo, v. 3 (in press).

Hiramatsu, Y. and Y. Oka, 1962, Stress around a shaft or level excavated in ground with a three-dimensional stress state: Memoirs of the Faculty of Engineering, Kyoto University. v. 24, p. 56-76.

Hubbert, M. K. and D. G. Willis, 1957, Mechanics of hydraulic fracturing: Trans. AIME, v. 210, p. 153-163.

Jaeger, J. C. and N. G. W. Cook, 1963, Pinching-off and disking of rocks: Journal of Geophysical Research, v. 68, p. 1759-1765.

Kirsch, G., 1898, Die theorie der elastizität und die bedürfnisse der festigkeitslehre: Zeit. Ver. dt. Ingenieure, v. 42, p. 797-807.

Kulander, B. R., C. C. Barton, and S. L. Dean, 1979, The application of fractography to core and outcrop investigations: Technical report for U.S. Department of Energy, Contract EY-77-Y-21-1321, METC/SP-79/3, 174 p.

Kulander, B. R., S. L. Dean, and B. J. Ward, 1990, Fractured Core Analysis: AAPG Methods in Exploration Series, 8, 88 p.

Kutter, H. K., 1991, Influence of drilling method on borehole breakout and core disking: 7th International Congress on Rock Mechanics, p. 1659-1663.

Laubach, S. E., 1988, Coring-induced fractures: indicator of hydraulic fracture propagation in a naturally fractured reservoir: SPE 18164.

Leeman, E. R., 1964, The measurement of stress in rock, Part 1: Journal of the South African Institute of Mining and Metallurgy, Sept., p. 76-80.

Lenhoff, T. F., T. K. Stefansson, and T. M.Wintczak, 1982, The core disking phenomenon and its relation to in-situ stress at Hanford: SD-BEI-T1-085, Rockwell Hanford Operations, Richland, Washington, 131 p.

Lorenz, J. C., and S. J. Finley, 1988. Significance of drilling and coring-induced fractures in Mesaverde core, Northwestern Colorado: SAND87-1111, UC Category 92, Sandia National Laboratories, Albuquerque, New Mexico, 36 p..

Lorenz, J. C., J. F. Sharon, and N. R. Warpinski, 1990, Significance of coring-inducing fractures in Mesaverde core, Northwestern Colorado: AAPG Bulletin, v. 74, p. 1017-1029.

Maury, V., F. J. Santarelli, and J. P. Henry, 1988, Core disking: a review, Sangorm Symposium: Rock Mechanics in Africa, Nov., p. 221-231.

Miguez, R., J. P. Henry, and V. Maury, 1987, Le discage: une method indirecte d'evaluation des contraintes in-situ, Journées Universitaires de Géotechnique - St - Nazaire-28-30 Janvier, p. 353-360.

Natau, O., G. Borm, and Th. Röckel, 1990, Influence of lithology and geological structure on the stability of KTB pilot hole, *in* V. Maury & D. Fourmaintaux eds., Rock at Great Depth: Balkema, Rotterdam, v. 3, p. 1487-1490.

Nelson, R. A., L. C. Lenox, and B. J. Ward Jr., 1987, Oriented core: its use, error, and uncertainty: AAPG Bulletin, v. 71, p. 357-367.

Obert, L. and D. E. Stephenson, 1965, Stress conditions under which core disking occurs: SME Transactions, v. 232, p. 227-235.

Paillet, F. L. and K. Kim, 1987, Character and distribution of borehole breakouts and their relationship to in-situ stresses in deep Columbia River basalts: Journal of Geophysical Research, v. 92-B7, p. 6223-6234.

Perreau, P. J., 1989, Tests of ASR, DSCA, and core disking analyses to evaluate in-situ stresses: SPE 17960, p. 325-336.

Plumb, R. A. and J. W. Cox, 1987, Stress directions in Eastern North America determined to 4.5 km from borehole elongation measurements: Journal of Geophysical Research, v. 92-B6, p. 4805-4816.

Röckel, Th., 1996, Der Spannungszustand in der tieferen Erdkruste am Beispiel des KTB-Programms, Ph.D. Dissertation, Universität Fridericiana zu Karlsruhe, 141 p.

Stacey, T. R., 1982, Contribution to the mechanics of core disking: Journal of the South African Institute of Mining and Metallurgy, Sept., p. 269-275.

Sugawara, K., Y. Kameoka, T. Saito, Y. Oka, and Y. Hiramatsu, 1978, A study on core disking of rock: Journal of Japanese Association of Mining v. 94, p. 19-25.

Timoshenko, S. P., and J. N. Goodier, 1970, Theory of Elasticity: MaGraw-Hill, 567 p.

Tranter, C. J. and J. W. Craggs, 1945, The stress distribution in a long circular cylinder when a discontinuous pressure is applied to the curved surface: Phil. Mag., v. 36, p. 241-250.

Wang, C. Y., Y. Sun, 1990, Oriented microfractures in Cajon Pass drill cores: stress field near the San Andreas fault: Journal of Geophysical Research, v. 95, p. 11135-11142.

Zoback, M. D., D. Moos, and L. Mastin, 1985, Well bore breakouts and in situ stress: Journal of Geophysical Research, v. 90, p. 5523-5530.

Table 2. 1. Summary of wellbore bottom stress concentrations under the primary stress conditions

stress concentration / applied stress condition	greatest tensional stresses		greatest shear stresses		fracture produced
	location	magnitude and direction	location	magnitude and direction	
horizontal uniaxial, S_H = 20 MPa (2900 psi)	$\Phi = 0°$ core side $\Phi = 90°$ inner corner	9 MPa (1305 psi), 110° 25 MPa (3625 psi), 130°	$\Phi = 0°$ inner corner $\Phi = 90°$ outer corner	35.5MPa (5147 psi),125° 31 MPa (4495 psi), 75°	saddle-shaped disking, originating at inner kerf corner at $\Phi = 90°$
overburden, S_v=20 MPa (2900 psi)	inner corner	41 MPa (5945 psi), 135°	inner corner outer corner	15.5 MPa (2247 psi) 18.5 MPa (2682 psi), 20°	petal fracturing, originating from inner kerf corner; centreline fracture possible for short core stub
weight on drill bit, S_b = 20MPa (2900 psi)	inner corner outer corner	11.5 MPa (1667 psi),140° 16 MPa (2320 psi), 35°	outer corner	6 MPa (870 psi), 18°	tensional failure at inner corner aids fracture initiation but not propagation
fluid pressure, S_p = 20MPa (2900 psi)	inner corner outer corner	11.5 MPa,(1667 psi), 110° 60 MPa, (8700 psi), 50°	inner corner	14 MPa (2030 psi), 20°	tensional failure at inner corner may aid fracture initiation but not propagation into core

Table 2.2. Summary of stress concentrations under the combined stress conditions

stress concentration / applied stress condition	greatest tensional stresses		greatest shear stresses		fracture produced
	location	magnitude and direction	location	magnitude and direction	
biaxial, $S_H = S_h$ = 20 MPa (2900 psi)	root of core side surface	5.2 MPa (754 psi), 0° 8.5 MPa (1232 psi), 35°	inner corner outer corner	28.2MPa (4089 psi),120° 25 MPa (3625 psi), 75°	cup-shapped disking fracture initiating at the root of the core; small fracturing into core from side
hydrostatic, $S_H = S_h = S_v$ = 20 MPa (2900 psi)	side surface top surface	11 MPa (1595 psi), 15° 8.5 MPa, (1232 psi), 90°	outer corner	32 MPa (4640 psi), 50°	fracture initiating above inner kerf corner
$S_H = S_v$ = $S_b = S_p$ = 20MPa (2900 psi)	Φ = 90°: inner corner outer corner	80.5 MPa (1167 psi),120° 42 MPa (6090 psi), 90°	Φ = 0° outer corner Φ = 90° inner corner	22MPa (3190 psi), 110° 41 MPa (5945 psi)	petal or petal-centerline fracturing originating from inner kerf corner

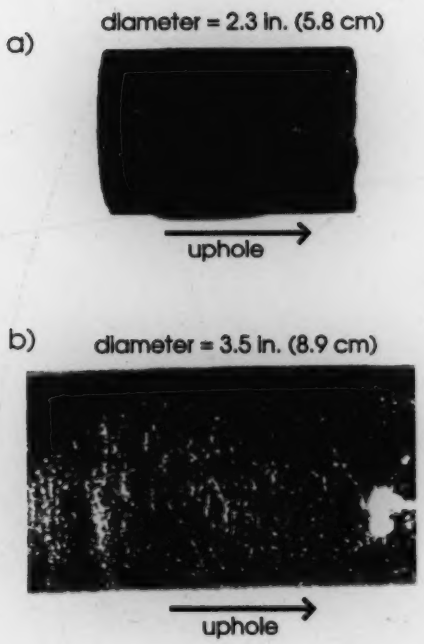

Figure 2.1. a) Core disk fractures in a massive sulphide core of diameter 2.3 in. (5.8 cm), and b) petal fractures in a granite core of diameter 3.5 in.(8.9 cm).

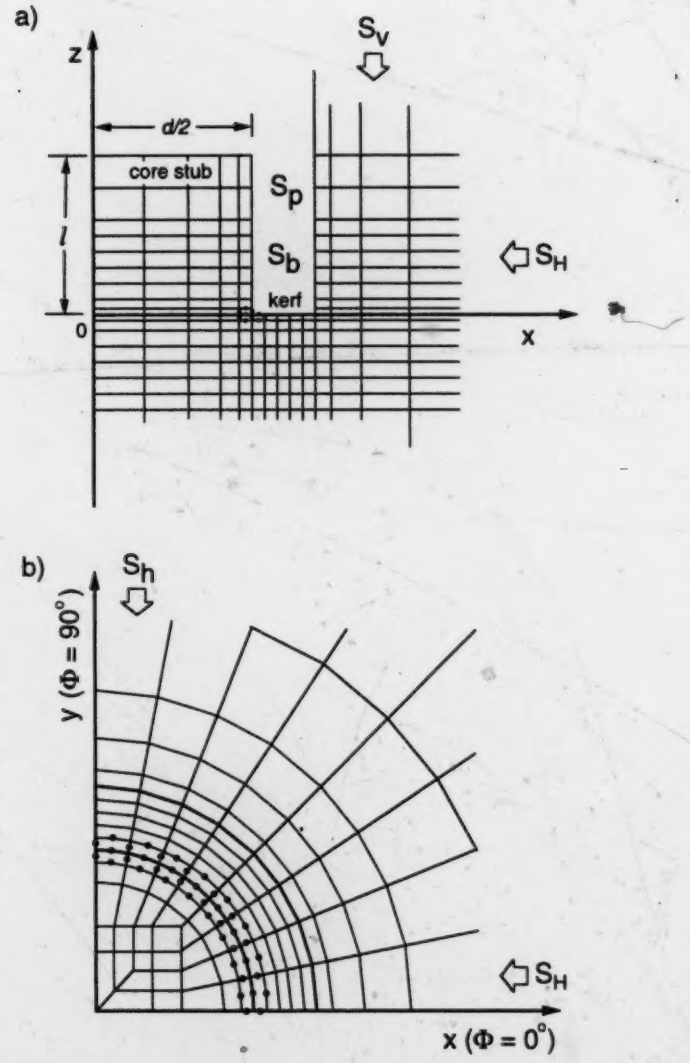

Figure 2.2. Mesh of finite element model: a) side view; b) top view. The stresses applied are the greatest horizontal stress, S_H; the least horizontal stress, S_h; the overburden, S_v; wellbore fluid pressure, S_p; and weight of drill bit, S_b.

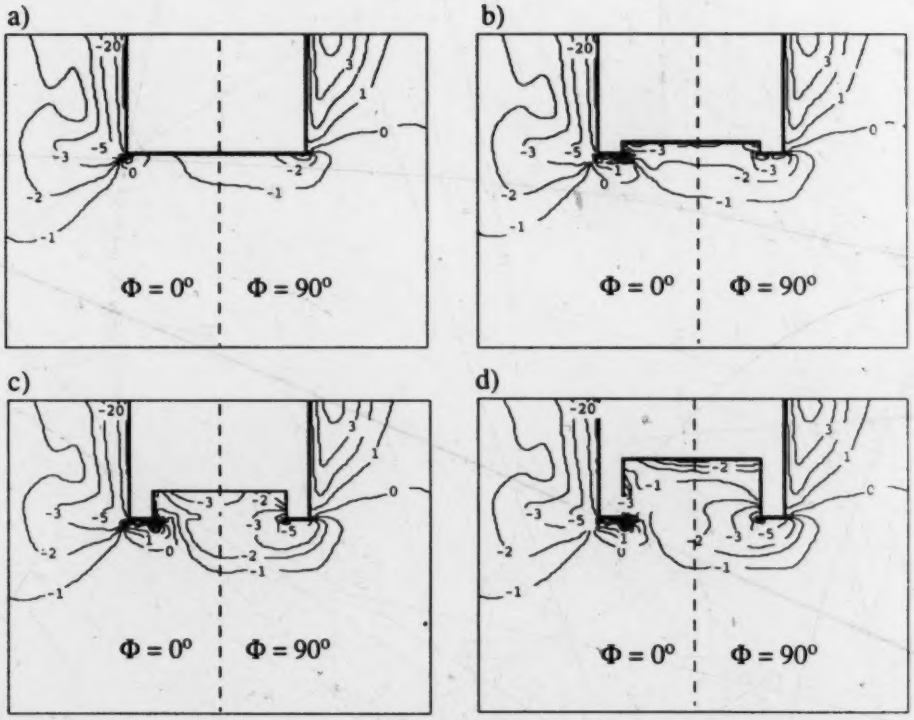

Figure 2.3. Contours (MPa) of the least compressive principal stress σ_3 at $\Phi = 0°$ and 90° under horizontal uniaxial stress $S_H = 20$ MPa for core stub lengths of a) 0 cm, b) 1 cm, c) 2.5 cm, and d) 5.0 cm.

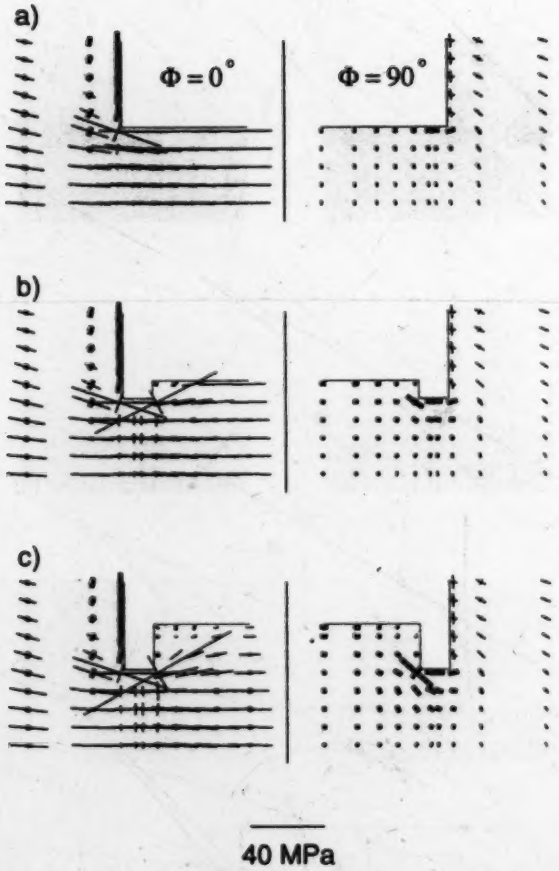

Figure 2.4. Orientations of principal stresses at $\Phi = 0°$ and 90° under horizontal uniaxial stress $S_H = 20$ MPa for core stub lengths of a) 0 cm, b) 1 cm, and c) 2.5 cm. Thin solid lines represent compression, and thick solid lines represent tension.

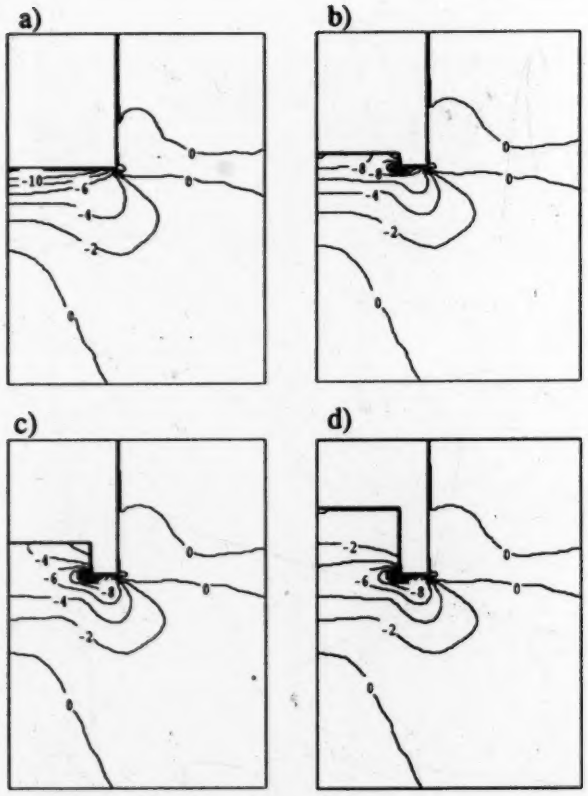

Figure 2.5. Contours (MPa) of σ_3 under overburden S_v = 20 MPa for core stub lengths of a) 0 cm, b) 1 cm, c) 2.5 cm, and d) 5.0 cm.

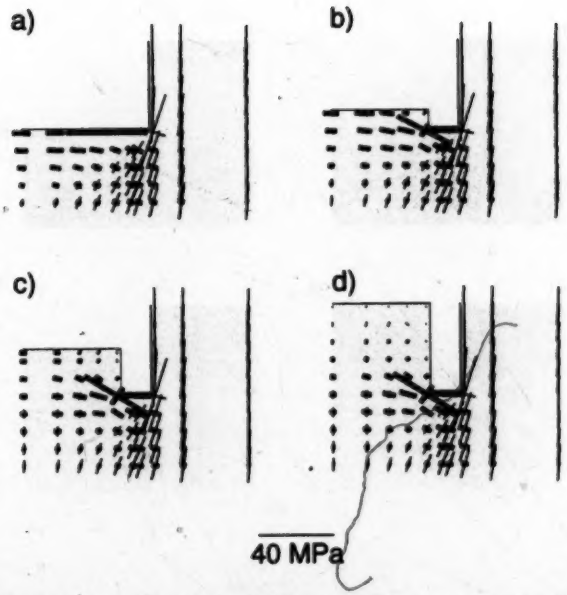

Figure 2.6. Orientations of principal stresses under overburden S_v = 20 MPa for core stub lengths of a) 0 cm, b) 1 cm, c) 2.5 cm, and d) 5.0 cm. Thin solid lines represent compression, and thick solid lines represent tension.

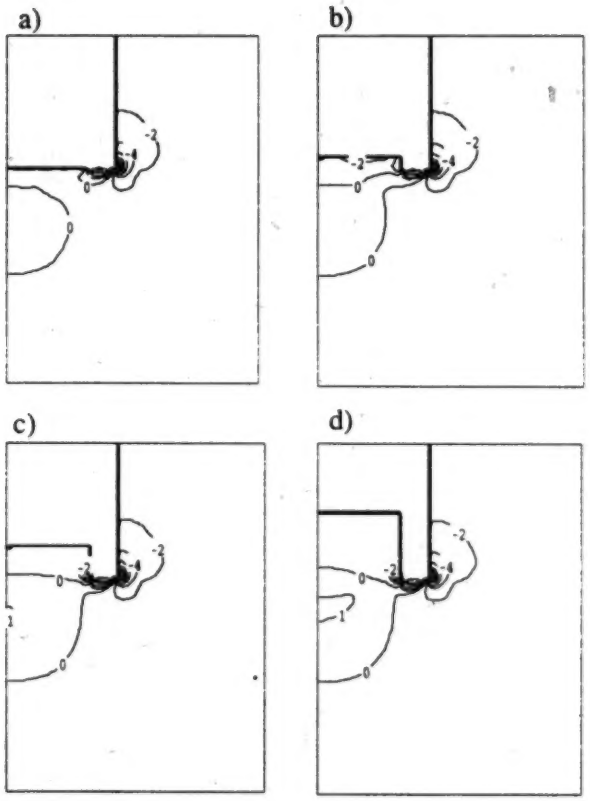

Figure 2.7. Contours (MPa) of σ_3 under drill bit weight S_b = 20 MPa for core stub lengths of a) 0 cm, b) 1 cm, c) 2.5 cm, and d) 5.0 cm.

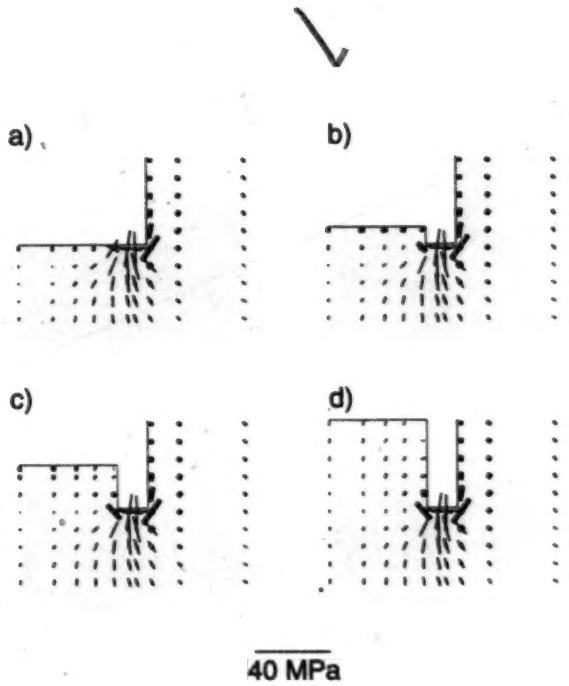

Figure 2.8. Orientations of principal stresses under drill bit weight S_b = 20 MPa for core stub lengths of a) 0 cm, b) 1 cm, c) 2.5 cm, and d) 5.0 cm. Thin solid lines represent compression, and thick solid lines represent tension.

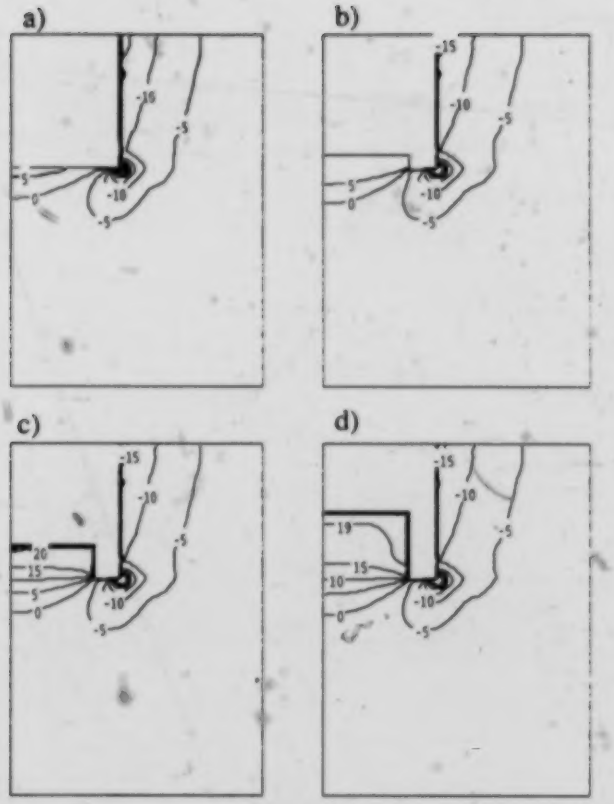

Figure 2.9. Contours (MPa) of σ_3 under wellbore fluid pressure S_p = 20 MPa for core stub lengths of a) 0 cm, b) 1 cm, c) 2.5 cm, and d) 5.0 cm.

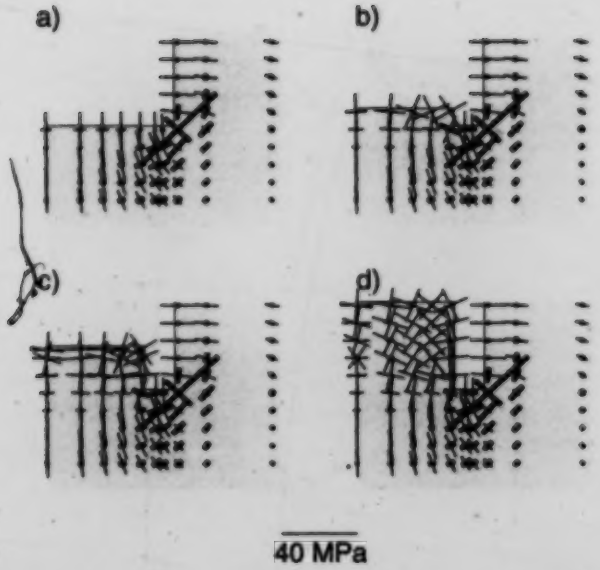

Figure 2.10. Orientations of principal stresses under wellbore fluid pressure S_p = 20 MPa for core stub lengths of a) 0 cm, b) 1 cm, c) 2.5 cm, and d) 5.0 cm. Thin solid lines represent compression, and thick solid lines represent tension.

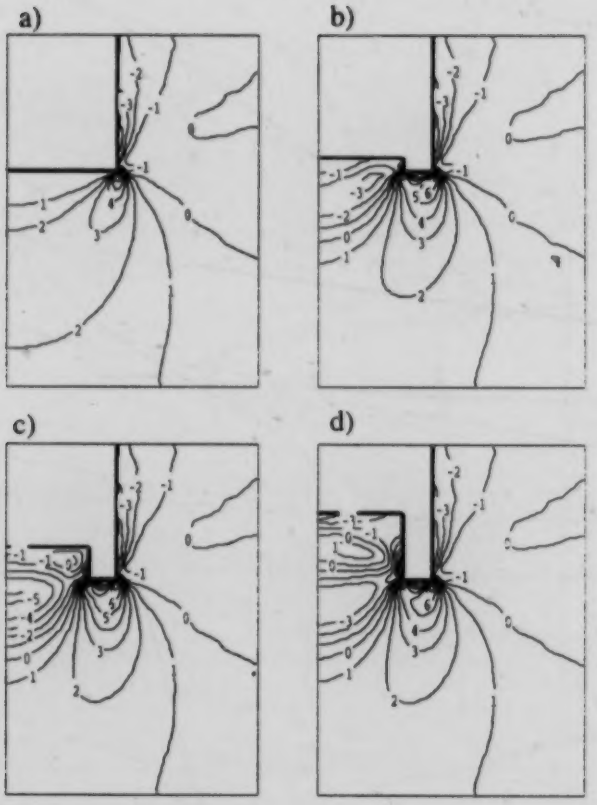

Figure 2.11. Contours (MPa) of σ_3 under biaxial stress condition $S_H = S_h = 20$ MPa for core stub lengths of a) 0 cm, b) 1 cm, c) 2.5 cm, and d) 5.0 cm.

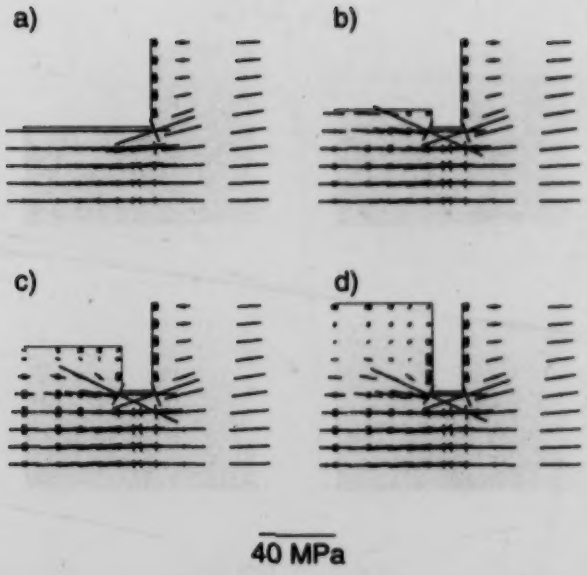

Figure 2.12. Orientations of principal stresses under biaxial stress condition $S_H = S_h$ = 20 MPa for core stub lengths of a) 0 cm, b) 1 cm, c) 2.5 cm, and d) 5.0 cm. Thin solid lines represent compression, and thick solid lines represent tension.

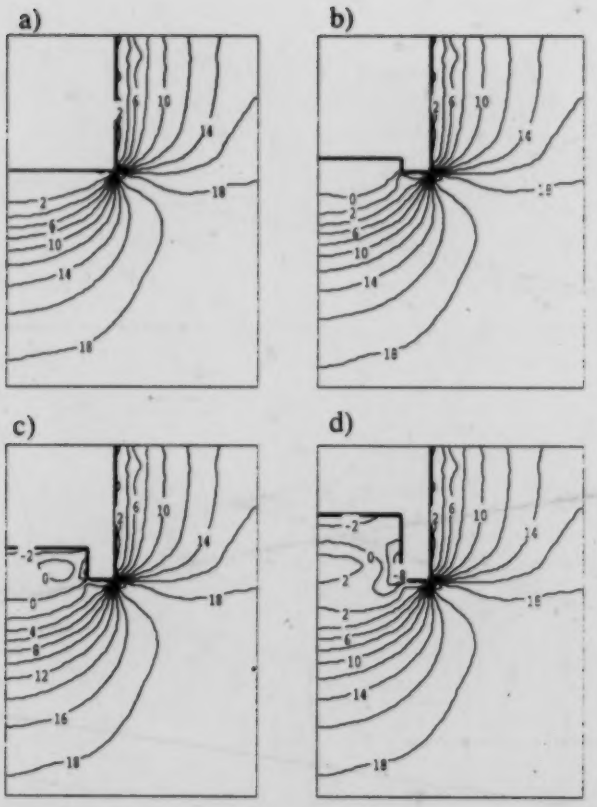

Figure 2.13. Contours (MPa) of σ_3 under hydrostatic stress condition $S_H = S_h = S_v$ = 20 MPa for core stub lengths of a) 0 cm, b) 1 cm, c) 2.5 cm, and d) 5.0 cm.

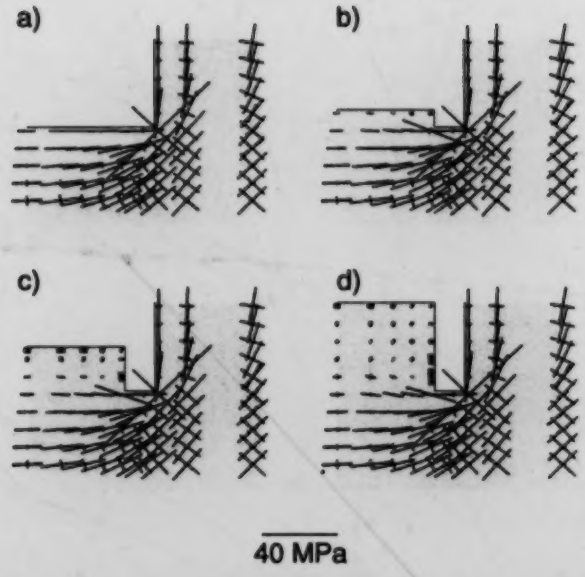

Figure 2.14. Orientations of principal stresses under hydrostatic stress condition S_H = S_h = S_v = 20 MPa for core stub lengths of a) 0 cm, b) 1 cm, c) 2.5 cm, and d) 5.0 cm. Thin solid lines represent compression, and thick solid lines represent tension.

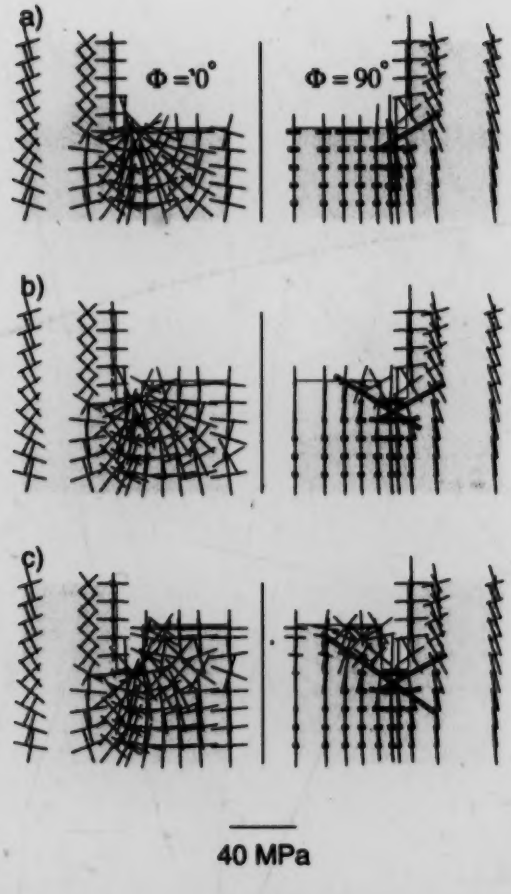

Figure 2.15. Orientations of principal stresses at $\Phi = 0°$ and $\Phi = 90°$ under $S_H = S_v = S_b = S_p = 20$ MPa and $S_h = 0$ for core stub lengths of a) 0 cm, b) 1 cm, and c) 2.5 cm. Thin solid lines represent compression, and thick solid lines represent tension.

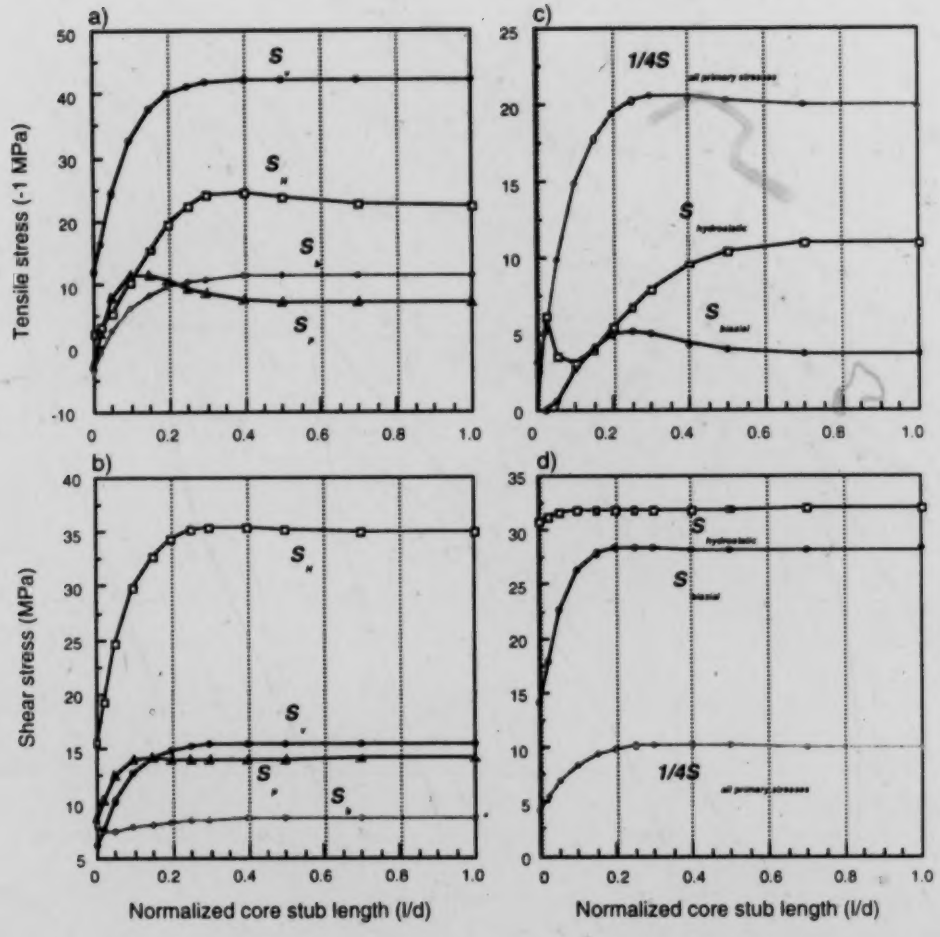

Figure 2.16. The relationship between the greatest tensile and shear stresses and the normalized core stub length (l/d): a) and b) tensile and shear stresses under the greatest horizontal stress S_H = 20 MPa, overburden S_v = 20 MPa, wellbore fluid pressure S_p = 20 MPa, and the weight of drill bit S_b = 20 MPa; c) and d) tensile and shear stresses under biaxial stress condition $S_H = S_h$ = 20 MPa, hydrostatic stress condition $S_H = S_h = S_v$ = 20 MPa, and all primary stress condition $S_H = S_v = S_p = S_b$ = 20 MPa. Note that the stress concentrations values shown for the last case are scaled by a factor of 0.25 from their larger true values to fit on the plot.

CHAPTER 3

INFLUENCE OF POISSON'S RATIO AND CORE STUB LENGTH ON BOTTOMHOLE STRESS CONCENTRATIONS

3.1 INTRODUCTION

The measurement of the in situ stress tensor in deep wellbores is often restricted by economic or technical considerations. As a result, any information about the state of stress that can be gleaned from geophysical logs or core material is important.

Retrieved cores are often used to provide information on in situ stress states. Some core stress indicators which are perhaps not well understood but commonly used include differential strain analysis, anelastic strain recovery, ultrasonic velocity anisotropy, and drilling induced core fractures. Of these, the drilling induced fractures can provide an indication of in situ stress directions from oriented core. The uniform spacing and morphology of these core fractures further hint that they contain substantial additional information about the state of stress at the point in the earth from where they were obtained. However, little is known about the in situ stress conditions leading to this core fracturing; and tempting as this may be, there are no published relationships allowing estimation of stress magnitudes from core fracture observations.

Drilling induced core fractures are produced by concentrations of the in situ stresses at the wellbore bottom. Here, these concentrated stresses are calculated using numerical methods for a particular in situ "far-field" state of stress. The results are used to better understand the mode of failure and the relationship between the core fracture morphology and the magnitudes of the applied stresses. The effect of variation in elastic properties and

---

A version of this chapter has been accepted for publication, December, 1996, International Journal of Rock and Mining Sciences & Geomechanics Abstracts.

core stub length for this stress state are studied in detail. Finally, relationships between the spacing of core disk fractures and stress magnitudes are developed with a view towards potential future use in the estimation of stress magnitudes.

3.2 BACKGROUND

Retrieved core often fractures into nearly identical disk-like slices. The uniform thicknesses and orientation of saddle-shaped fractures have long been recognized as stress direction indicators, and have motivated explorations for a quantitative relationship between stress magnitudes and core disk thickness and shape. Such studies have been carried out by many workers (e.g., Jaeger and Cook, 1963; Obert and Stephenson, 1965; Durelli et al., 1965; Sugawara et al., 1978; Stacey, 1982; Miguez et al., 1987; Maury et al., 1988; Dyke, 1989; and Haimson and Lee, 1995).

The failure mechanism responsible for creating disk fractures remains in dispute and different criteria have been used to explain them. Obert and Stephenson (1965) suggested that shear failure was responsible on the basis of their experiments in which rock cylinders were subject to varying states of radial S_r and axial S_a compression. Other workers have indicated that tensional fracture is important (e.g., Jaeger and Cook, 1963; Sugawara et al., 1978; Dyke, 1989; Haimson, 1995; and Panet, 1969). Jaeger and Cook (1963) produced cup-shaped fractures in simple laboratory tests which were produced under tension (Figure 3.1a). Using finite element modeling of the bottomhole stress concentrations, Sugawara et al. (1978) found that core disking fractures probably initiate in tension at the root of the core stub and provided a relationship describing the critical stress conditions for incipient core disking. Dyke (1989) concluded from boundary element modeling that tensional failure plays the major role as the shear stress magnitudes are insufficient to cause failure. Most recently, Haimson and Lee (1995) did not detect evidence for shear displacement in the microscopic examination of core disk fracture surfaces created in the laboratory, and indicated on this basis that core disks are tensional fractures.

Core disks are manifestations of the fracturing produced by concentration of the in situ stresses by the bottom-hole cavity. Analytic solutions to these stress concentrations do not exist in three dimensions, and would in any case be highly restrictive in terms of the geometry of the bottomhole and core stub (e.g., Tranter and Craggs, 1945). This lack of knowledge of the stress concentrations at the bottomhole has both delayed description of the failure mode and impeded attempts to utilize core fractures in quantitative estimation of in situ stress magnitudes.

The geometry of wellbore bottom, the in situ stress conditions, and the rock physical properties influence the localization and mode of failure and are here studied numerically for a given bottomhole kerf (cut) shape. The finite element method is employed under the assumption that the earth material is linearly elastic and isotropic. This is rarely true but the present results may serve as a basis for further work. In order to explore the mechanism of core disking, the calculations were carried out to allow direct comparison to the laboratory experiments conducted on cylinders of rock by Obert and Stephenson (1965); some of the core disks produced in their experiments are illustrated in Figure 3.1b.

The coring process is modeled almost continuously with a core stub which lengthens from zero to the core diameter. Knowledge of the influence of the core stub length on the stress concentrations is used to explain the relationship between the core disk thicknesses and the in situ stress magnitudes. In this study, the effect of Poisson's ratio on the distribution of stress concentrations is of particular interest. Its influence has been recognized in earlier numerical modeling of overcoring (Crouch, 1969; Heerden, 1969; and Wang and Wong, 1987) where variations in Poisson's ratio result in changes of the stress concentration factors by up to 20%.

3.3 NUMERICAL CALCULATIONS

The two primary applied stresses here are a uniform biaxial radial and a wellbore-axis parallel uniaxial compression denoted by S_r and S_a, respectively. In Figure 3.2, z is the

distance from the borehole bottom, r is the radial distance from the borehole axis, D and d are the borehole and the core diameters, respectively, and l is the core stub length.

The finite element package ANSYS™ was used in the modeling. The coring bit has 2.54 cm (1.0-in.) ID and 3.01 cm (1-3/16-in.) OD as used in the experiments of Obert and Stephenson (1965). The ratio of the kerf width to the core diameter is about 0.185. As the wellbore axis is parallel to the applied axial stress S_a, symmetry considerations allow the calculation to be carried out using only a 90° segment of the whole model and the results obtained for any vertical plane apply at all azimuths. The use of three dimensional analysis is based on the consideration that the intermediate principal stress may have an effect on the failure of the rock. The exsiting criterion (Mogi, 1972) for considering the effect of intermediate prinsipal stress requirs that all principal stresses are compressive. This prevents from conducting the analysis of rock failure using intermediate principal stress because high tension is generated in the vicinity of bottomhole.

The cylindrical specimens used in Obert and Stephenson's experiments (1965) had two different outside diameters of 10.16 cm (4-in.) and 14.28 cm (5-5/8-in.) with corresponding axial lengths of 20.32 cm (8-in.) and 26.67 cm (10-1/2-in.), respectively. Here, the smaller specimen with the diameter of 10.16 cm is chosen for the modeling as the effect of boundary conditions is expected to be more significant. The borehole has a depth of 10.16 cm. The stress magnitudes calculated from this model are 2% and 5% higher than those obtained in the larger 14.28 cm diameter cylinder and in an "infinite" block, respectively.

The model contains 4220 elements and 5432 nodes. The finite element mesh for this model is shown in Figure 3.2. High stress concentration is expected at the sharp square corners of the kerf, and to ameliorate this problem the sizes of elements in close proximity to the corner were reduced. Higher resolution is further obtained by employing 20 node elements at the inner kerf corners. The bottom of the model was constrained in the normal direction with zero displacement.

The coring process is modeled by adding layers a single element thick to the top of the existing core stub after each calculation. The advantage of this procedure is that all the elements at the wellbore bottom remain unchanged. Twelve separate calculations were designed to complete a coring process with core length increasing from zero to the core diameter. Calculations for greater core lengths were not carried out as the stress concentrations change very little for longer core stubs. Smaller core length increments were employed for short core stubs where the stress concentration fields would most rapidly evolve. The stress sign convention used in rock mechanics is applied here with compression positive and tension negative. The calculations were carried out with a Young's modulus of 20 GPa and Poisson's ratios of 0.05, 0.15, 0.25, 0.35 and 0.45.

The stress concentrations produced by the applied radial S_r and the axial S_a stresses were calculated individually. This allows a better understanding of the differing contribution of each. The concentrated stresses resulting from any combination of these two primary stress conditions are then easily determined by linear superposition and recalculation of the new stress tensor at each nodal point.

3.4 RESULTS

3.4.1 Characteristics of Primary Stress Concentrations

The results of the modeling are first reported in terms of the magnitudes and orientations of the concentrated principal stresses for the two cases of pure S_r and S_a only. These primary stress concentrations are then superposed with $S_r = S_a$ as a further example. The magnitudes of the maximum shear stress $(\sigma_1 - \sigma_3)/2$ (hereafter referred to as shear stress) may be inferred from the plots of principal stress orientations. For brevity, contours of principal stresses and the corresponding orientation plots are given only for core lengths of l/d = 0.0, 1/10, 1/4, and 1/2. In the derivation of the figures, the magnitude of the applied compression is 20 MPa although the results could also be presented in dimensionless

form. The results shown are for a Poisson's ratio of 0.25 but complete calculations have been carried out over the range of Poisson's ratio from 0.05 to 0.45.

1) Radial compression (S_r = 20 MPa).

The magnitudes and the orientations of the principal stresses under S_r = 20 MPa for a variety of core lengths are shown in Figure 3.3. In the principal stress orientation plots, thick solid lines represent the directions and magnitudes of the principal tensile stresses and the thin solid lines represent compressive stresses. The tensile stresses are mostly oriented parallel to the core axis. In contrast, the greatest compressive stresses are nearly horizontal. They rotate counterclockwise towards the outer corner and clockwise towards the inner corner of the kerf. Along the axis of the borehole, the magnitudes of the tensile stresses increase towards the root of the core stub.

There are three zones of concentrated tension produced by the radial compression, S_r. The first is on the borehole wall near the bottomhole. It is affected little by the change of the core length. At the higher levels along the wellbore wall this tension disappears to be replaced by the overall stress state predicted in Lamé's (Timoshenko and Goodier, 1970) hollow cylinder formulation. A second, and more prominent tension is produced at the root of the core. The peak magnitude of the tensile stress lies along the core axis and increases with core lengths to 1/4 of the core diameter. This is consistent with the calculations of Sugawara et al. (1978). The third tensional zone is at the surface of the core with tension oriented vertically along the side and horizontally along the top.

High shear stresses are located at and near the kerf and have their greatest magnitude on the surface of the cut. The greatest magnitude increases rapidly for short core lengths but remain almost constant past a core stub length of 1/5 the core diameter.

Figure 3.4 shows the corresponding contours of the most tensile principal stresses σ_3. Before there is a core stub, tension exists only on the wellbore wall. Tensional zones

emerge at the root, the side, and the top of the core once the stub is formed. The tension at the root attains its greatest magnitude when l/d = 0.25 (Figure 3.4c) but then declines slightly for longer core stubs. A tensional zone on the side of the core expands with increasing core length. A large tension becomes apparent at the top of the core stub for a core length equal to 1/2 the core diameter (Figure 3.4d).

2). Axial compression (S_a = 20 MPa).

The orientations of the principal stresses for this case (Figure 3.5) are nearly opposite those for the applied radial stress above. Tensional stresses are oriented nearly horizontal, and they rotate clockwise towards the inner corner of the kerf where the greatest tension is found. Tension exists throughout the core extending to its root and below the kerf. Greater compressive stresses are nearly vertically oriented with magnitudes which decrease towards the core axis. Along the core axis, the least tensile principal stresses (σ_1) are compressive and parallel to the core axis.

The contours of σ_1 under the applied axial stress S_a are shown for a variety of core lengths in Figure 3.6. The magnitudes of compressive stresses decrease gradually towards the top of the core stub, and the greatest compression appears at the wellbore wall near the kerf.

The similarity of the orientations for the most tensile stress σ_3 for a pure application of S_r and for the most compressive stress σ_1 for a pure application of S_a demonstrates their counteracting influence on the stress concentrations.

3). Hydrostatic compression ($S_r = S_a$ = 20 MPa).

The superposition of the radial and axial primary stress cases both with the same magnitude produces a hydrostatic stress condition. The orientations of the most tensile principal stresses are similar to those of the radial stress cases but their magnitudes are substantially diminished (Figure 3.7). Small tensile stresses exist within the body of the

core and they converge towards the inner corner of the kerf and at the center of the top of the core stub. The most compressive stresses at the root are oriented nearly horizontal.

Contours of σ_3 under this stress condition are shown in Figure 3.8. The only substantial tension observed is on the side of the core and at the top of the core stub. A nearly tension free zone is located at the wellbore bottom when there is no core stub. It moves to the root of the core stub and expands in volume as l/d increases to 1/4 (Figure 3.8c). This tension free zone migrates upwards in the core for longer core stubs (Figure 3.8d).

Under a hydrostatic stress condition the already described competing effects of the applied radial stress,S_r, and axial stress, S_a, reduce the magnitude of the tension. Tension produced by S_r at the root of the core and on the wellbore wall is more than nullified by the concentrated compression from S_a. The tension at the inner corner and in the area below the kerf produced by S_a is also canceled by the compression produced by S_r.

3.4.2 Peak Concentrated Stresses.

The results can be compared to the experimental core disking observations of Obert and Stephenson (1965) and some discussion of their experiments on a number of different rock types is necessary. In each of their tests, trial axial S_a and radial S_r stresses were first applied to a rock cylinder which was then cored under this stress state. If no core disking was observed from the retrieved core plug, then S_r was increased under the same S_a and the experiment continued until core disks were finally produced. This same experiment was then iterated at higher levels of S_r and S_a. The final results were presented as plots of the applied critical radial stress at which failure producing core disking occurred versus the applied axial stress.

We assume that fractures initiate at the locations where the tensile or the shear stresses obtain their greatest magnitudes; consequently the tensile stress concentrations at the root of the core and the shear stress concentrations on the surface of the kerf are studied in detail.

As an example, profiles of the greatest tensile stress σ_3 along the core axis induced by an applied radial stress, S_r = 1 MPa, are shown in Figure 3.9a, and similar profiles of the least tensional stress σ_1 under the applied axial stress S_a = 1 MPa are shown in Figure 3.9b. The curves shown are for a variety of l/d ratios and material with a Poisson's ratio of 0.25. The horizontal axis represents the distance, z, from the wellbore bottom, which is normalized by the core diameter d. Under S_r alone, the highest tensile stress exists at the root. The magnitude of this stress increases for core stub l/d ≤ 1/4 but then declines for longer stubs. Under the applied axial stress S_a, σ_1 is compressive and monotonically decreases towards the top of the core stub where it nearly vanishes (Figure 3.9b).

Along the core axis the σ_3 produced by S_r and the σ_1 produced under S_a align in the same orientation, and the degree of tension or compression finally existing depends on which dominates. The σ_3 existing under hydrostatic applied stresses with $S_r = S_a$ = 1 MPa is shown in Figure 3.9c. Compared to the results in Figure 3.9a, the magnitude of the highest tensile stress at the root of the core has been reduced substantially from 0.255 MPa to 0.07 MPa.

Figure 3.9d is an example for the superposition with S_a = 1 MPa and S_r = 2 MPa. This shows that the radial stress must almost double to regain the peak tensions similar to the case with no applied axial stress. These examples illustrate that multiplying S_r increases tension at the root of the core while S_a has the opposite effect.

In contrast, the largest shear stresses exist on the surface of the kerf, and the shear stresses across the kerf surface are shown in Figure 3.10. Figure 3.10a and 3.10b share the same applied stress conditions as Figure 3.9a and 3.9d, respectively. The ratio r/d is the normalized radial distance from the core axis. At each core length, there are two shear stress peaks on the surface of the kerf (except for l/d < 0.05). A doubling in the magnitude of the applied S_r also nearly doubles the magnitudes of the peak concentrated shear stresses. This suggests that the peak shear stresses are dependent primarily on the applied radial stress S_r and influenced little by the applied axial stress S_a.

The peak tensile and shear stresses, as shown in Figures 3.9a and 10, respectively, are important in failure initiation, and their relation to core stub length is of special interest. These peak stresses are plotted as a function of the core stub length in Figure 3.11 for two cases with $S_a/S_r = 0$ and $S_a/S_r = 1/2$ and for the full range Poisson's ratio. All stresses in Figure 3.11 are normalized by the applied radial stress S_r.

In Figure 3.11a and 3.11b, the tensile stresses increase rapidly at short core lengths, and then reach a peak. When $S_a/S_r = 0$, the tensile stresses are maximum at $l/d = 0.25$ for all values of υ (Figure 3.11a). For the second case of $S_a/S_r = 1/2$, the tensile stresses reach their greatest magnitude at $l/d = 0.25$ for $\upsilon = 0.05$ and at $l/d = 0.20$ for $\upsilon = 0.15$ to 0.45 (Figure 3.11b). Four observations are apparent from the results shown in Figure 3.11a and 3.11b. First, if disking occurs the spacing between the disk fractures or the disk thickness can be no more than 25% of the core diameter. Second, higher concentrated stresses produce thinner core disks. Third, if the core stub does not fail even at the peak tensile stress then there can be no core disking and the core remains intact. And, fourth, Poisson's ratio, υ, has a large influence on the magnitudes of the concentrated tensile stresses. The reduction in tension caused by the applied axial stress is also apparent in Figure 3.11b.

Figure 3.11c and 3.11d show the relationship of the normalized greatest shear stresses versus l/d for the two different cases. The largest increase of the shear stresses occurs when $l/d \leq 0.2$. Past this point, the concentrated shear stresses increase only marginally with core stub length. Further, the peak concentrated shear stress magnitudes are only slightly influenced by application of the axial stress indicating that this stress only weakly influences the shear stress. An additional important observation is that no peak concentrated shear stress exists suggesting that if shear stresses were responsible for core disking then core disks could have any thickness.

This last theoretical suggestion contrasts with field and laboratory observations where core disk thicknesses ranging from 1/5 to 1/4 the core diameter have been mostly observed (Jaeger and Cook, 1963; Leeman, 1964; Obert and Stephenson, 1965; Sugawara et al.,

1978; Stacey, 1982; Zhu and Wang, 1985; Born et al., 1989; Haimson and Lee, 1995; and Ishida and Saito, 1995). For example, in the statistical analysis of a large number of 3.88 cm and 8.18 cm diameter core disks at the engineering site of a hydropower station by Zhu et al. (1985), the average core disk thicknesses are 1.07 cm (27.5% of diameter) and 2.09 cm (25.5% of diameter), respectively. In Obert and Stephenson's tests the l/d ratios ranged from 0.18 to 0.25. These observations are consistent with a tensile failure mechanism for core disking but do not by themselves exclude a shear mechanism.

The competing effects of tension from S_r and compression from S_a are consistent with the experiments carried out by Jaeger and Cook (1963) who found that the core disking is inhibited by axial stress. They further suggested that core disking is least likely when drilling is in the direction of the greatest principal compressive stress.

3.4.3 Hypothetical Failure Curves

Hypothetical failure curves are derived from the results of the modeling in order to allow direct comparison to the experimental observations of Obert and Stephenson (1965). Their final result was a series of empirically derived linear relations between S_a and S_r of the form

$$S_r = k_1 + k_2 S_a \tag{3.1}$$

where S_r is the critical radial stress at which core disking initiates for a given axial stress S_a, k_1 is the intercept which represents the magnitude of S_r when $S_a = 0$, and k_2 is the slope. This relation was assumed by Obert and Stephenson (1965) to describe the stress conditions under which core disks were first produced. This empirical relation delineates the boundary between disking and no disking, and as a result the strength of rock is intrinsic to the formulation and reflected in the intercept k_1. The slope k_2 contains information on the balance of the stress concentrations produced by both S_r and S_a.

It must be remembered that their empirical curves result from a simple linear regression fit to the data. This appears to describe the observations relatively well, but further investigation is warranted. This is especially true if core disks are to be used as indication of stress magnitudes.

The rock type, the shear strength (cohesion) S_o, the angle of internal friction ϕ, the Brazilian tensile strength T_o, and the observed k_1 and slope k_2 from Obert and Stephenson (1965) are listed in Table 3.1.

In Obert and Stephenson's experiments (1965), two processes produced changes in the stress concentrations. One was the increasing magnitudes of the applied compressive S_a and S_r. The other was changes in geometry due to coring. As shown in Figure 3.11, increasing the applied radial stress S_r results in a proportional increase of the tensile and shear stresses; with progressive coring, the core stub grows in length and the stress concentrations also evolve. Core disking initiates if the greatest tensile or shear stress attains the value of the rock strength.

Assuming that the tensile stress peaks in Figure 3.11 have the same magnitude as the tensional strength, hypothetical core disking S_r vs. S_a curves were calculated from the results of the finite element analysis using a procedure that mimics Obert and Stephenson's experiments (1965). For each set of calculations, a S_a is first given and then S_r is increased gradually. When the magnitude of the peak tensile stress reaches the tensional strength, both S_a and S_r were recorded. This calculation was repeated with an increased level of S_a to produce the hypothetical failure curves as shown in Figure 3.12a.

These tensional failure curves are not perfectly linear as the local slope k_2 decreases slightly with increasing S_a (Figure 3.12b). In addition, k_2 depends on Poisson's ratio υ and varies from 0.75 to 1.42 over the range of Poisson's ratios from 0.05 to 0.45 (Figure 3.12b). As the tensional strength is assumed uniform for all υ, a greater magnitude of S_r is required to produce core disking for a large υ. Despite this, the curves are still nearly linear with only minor changes in the local slope, which otherwise depends much more

strongly on υ. It is doubtful that the subtle changes in slope could be resolved in the experiments of Obert and Stephensen (1965); this justifies their use of a linear least squares fit to their data.

Hypothetical shear failure curves were similarly obtained but using the Mohr-Coulomb criterion of the form (e.g., Fjaer et al, 1992)

$$\sigma_1 = 2S_0 \frac{\cos\phi}{1 - \sin\phi} + \sigma_3 \frac{1 + \sin\phi}{1 - \sin\phi}. \qquad (3.2)$$

Shear failure is assumed to initiate on the surface of the kerf. For the calculations, extreme internal friction angles of 25° and 50° were chosen to place bounds on the hypothetical shear failure curves. These friction angles bound those given in Table 3.1 and also the normally observed range between 30° to 45° as suggested by Byerlee (1978). In Eq. 3.2, the only unknown is the shear strength S_0. It was determined from the magnitudes of σ_1 and σ_3 corresponding to the greatest shear stress on the surface of the kerf for a given ϕ when $S_a = 0$. In the calculation, the normalized core length used was 0.25 based on the observation that the greatest shear stress remains nearly constant for longer core stubs (Figure 3.11c).

As S_a has a small effect on the greatest shear stress on the surface of the kerf, the radius of the Mohr-circle (i.e. the magnitude of the shear stress) is mostly controlled by S_r. In the determination of the hypothetical shear failure curves, values of S_a and S_r were first arbitrarily chosen and the resulting concentrated σ_1 and σ_3 used to derive the descriptive Mohr-circle. Incipient shear failure was assumed when this Mohr-circle first became tangent to the failure envelope of Eq. 3.2 whereupon the corresponding S_a and S_r magnitudes were recorded.

The hypothetical shear failure curves show that S_r at which shear failure occurs actually decreases as S_a becomes larger (Figure 3.12c). This decrease is most apparent for large ϕ.

For $\phi = 25^o$ and 50^o, the local slope k_2 ranges from -0.05 to -0.28, and -0.32 to -0.67, respectively (Figure 3.12d).

For the purpose of further illustration, two sets of Mohr-circles corresponding to $\phi = 25^o$ and 50^o for normalized S_a increasing from zero to 1.0 with an increment of 0.1 and for $\upsilon = 0.25$ are shown in Figure 3.13. The failure shear stress τ varies little. Basically, the critical Mohr-circles shift from the right to the left, and their radii are reduced as S_a increases. This is more apparent for the case with $\phi = 50^o$.

The results of Figure 3.12a and 3.12c and the experimental data from Obert and Stephenson (1965), normalized by S_r when $S_a = 0$, are summarized in Figure 3.14. The hypothetical tensional and shear failure curves are widely separated with positive and negative slopes, respectively. The experimental data is generally in good agreement with the tensional failure curves. Of the five types of rocks, the observed failure level for the Georgia granite, the Maryland marble, and the Vermont marble fall within the tensional failure region. The data for the Nova Scotia sandstone and the Indiana limestone have nearly the same positive trend but lie just outside the predicted region.

The reason for this discrepancy is not known and there is insufficient information on the physical properties of these rocks to provide a complete explanation. It may be due to the use of different coolants in the Obert and Stephenson's experiments (1965). For the Georgia granite, the Maryland marble, and the Vermont marble, water was the coolant whereas air was employed in the coring of the Nova Scotia sandstone and the Indiana limestone. This may suggest that these latter samples were weaker because of the damage caused by drilling on the cut surface . Consequently, core disking is then more likely at lower values of S_r resulting in a smaller k_2.

The hypothetical shear failure curves are not in agreement with the experimental data. The applied radial stress S_r may be less than the applied axial stress S_a if shear failure occurs according to Mohr-Coulomb criteria. This result contradicts both experiments and observations which suggest that core disks are produced under a stress condition in which

the applied or the in situ stress perpendicular to core axis must be greater than the stress applied in the direction of core axis (Jaeger and Cook, 1963; Obert and Stephenson, 1965; and Haimson and Lee, 1995).

3.4.4 Core Stub Length And Applied Stress Magnitudes

The thickness of a core disk is here taken to be the length of core stub which can withstand the concentrated stress. If the tensile strength of rock is constant, Figure 3.11 indicates that a thinner core disk is obtained by increasing S_r. As such, and in reference to Figure 3.11, the spacing of the core disking fractures has the potential to provide some simple indication of in situ stress magnitudes. This is observed experimentally. Jaeger and Cook (1963) first confirmed that the ratio of the thickness of core disks to the core diameter decreases as the applied stress is increased. This was further observed by Haimson and Lee (1995) in their experiments using Lac du Bonnet Granite. In the field, Leeman (1964) and Perreau et al. (1989) have described thin core disks with l/d ratios of 0.1 and 0.12, respectively.

Obert and Stephenson's (1965) empirical failure curves are for optimal disk thickness; and different relationships are to be expected for thinner core disks. Such hypothetical failure curves for a range of the normalized core stub length l/d are derived from the results of the finite element modeling and shown for different Poisson's ratios in Figure 3.15. The curves in Figure 3.15 for normalized core lengths of 0.25 are those shown in Figure 3.12a. As the core stubs become thinner, the radial stress required to effect failure increases dramatically and for convenience in viewing Figure 3.15 is plotted logarithmically.

There is little sensitivity to the applied stresses for core stub lengths between 0.2 and 0.25 and their curves are nearly identical in the logarithmic plot for all Poisson's ratios. In contrast, creating a core disk with a normalized thickness of 0.1 requires a doubling of the radial compression in some cases. Consequently, and as also suggested in Figure 3.11a

and 11b, there is substantial sensitivity of the core stub thickness to the applied radial stress in the range of the normalized core stub lengths between 0.1 and 0.2.

According to the calculations, shorter core stubs are even more dependent on the magnitude of the applied radial stress. Indeed, the applied radial stress necessary to cause tensile failure is approximately inversely proportional to the core stub length as indicated by the example plot (Figure 3.16).

The hypothetical failure curves in Figure 3.15a-d show that the thickness of the core disks produced could be used as estimators of the relative magnitudes between the radial and axial stresses. To do this, both Poisson's ratio and either S_a or S_r must be known or assumed. For example, in a vertical borehole, the axial stress could be determined from integration of the density log in an area of mild surface topography then used in Figure 3.15 to estimate the biaxial horizontal stresses. Conversely, in the same vertical borehole, the radial stress might be given from hydraulic fracturing measurements allowing estimation of the axial vertical stress.

3.5 CONCLUSIONS

Finite element modeling indicates that both Poisson's ratio and core stub length influence the bottomhole concentration of farfield in situ stresses. Alone, a biaxial compression normal to the wellbore axis generates a substantial tension in the root of the core stub as has been noted by other workers (Sugawara et al, 1978; Dyke, 1989). In contrast, far-field axial compression produces a counteracting compression at the core root which inhibits tensile core disking. The two calculated stress concentration fields are scaled and superposed to derive hypothetical relationships between the radial and axial compressions at incipient core disking. These curves assumed either tensile or compressive shear failure was responsible in the formation of the core disks. Only the curves which assume a tensile mechanism are consistent with the laboratory results of Obert and Stephenson (1965).

The concentrated stresses display substantial dependence on core stub lengths less than l/d = 0.25. A peak tension exists near l/d = 0.25 and as a result core disks thicker than this are not expected in homogeneous materials. The concentrated tension produced by the radial stress is nearly inversely proportional to the core stub length and the radial stresses required for tensile failure increase dramatically for core stub lengths shorter than l/d = 0.1. This suggests that very thin core disks could provide a measure of the stress magnitudes, but whether such accuracy could be achieved in practice is doubtful as large uncertainties will exist in the measurement of core disk thicknesses. It is, however, interesting to note that very thin bottom hole chips have been observed from coring in a region of high stress at the Underground Research Laboratory near Pinawa, Manitoba (Martin, 1994).

Poisson's ratio influences core disking substantially. Concentrated tensions diminish with larger values of Poisson's ratio. Under a uniform stress state core disks are more easily produced in rocks with smaller υ. This suggests that the existence or non existence of core disking may also indicate changes in rock properties under an otherwise uniform stress state near the wellbore. Care should be taken not to assume that the rapid appearance and disappearance of core disks is due to stress heterogeneity although other factors such as drill string weight may play a factor in initiating core disk fractures (Li and Schmitt, 1997).

It is important to reiterate that the relationships between core disk thickness and applied loads derived here may be used to predict the magnitudes of in situ stresses only if core disks have a radially symmetric cup shaped fracturing surface such as observed by Jaeger and Cook (1963) and as shown in Figure 3.1. That is, the results derived here apply in the case where the wellbore aligns with a principal stress with axis-perpendicular biaxial stress. They should not be used to infer stresses in more complex stress regimes (Li and Schmitt, 1997) where saddle shaped or petal fractures are likely.

Ongoing research includes consideration of the influence of the bottomhole geometry. The calculated stress concentrations seen here at the sharp kerf corner are greater than those

possible in a more rounded and realistic kerf. However, for this case the largest tensile stresses are produced at points along the wellbore axis at the core root at a point well removed from the kerf corners. Consequently, according to St. Venant's principle the influence of the square kerf on the calculated stress magnitudes at the core root is expected to be minimal.

The present study has assumed simple failure criteria. More sophisticated analyses are required to determine the growth of the fracture and consequent core disk shape. The shape itself probably contains substantial additional information on the in situ stresses existing prior to the drilling of the wellbore. Prediction of the fracture growth and trajectory may, however, be influenced by the fracturing dynamics and mixed-mode fracturing. Other effects such as pore pressure, nonlinear elasticity of rock, and yielding have not been considered and may be of interest under field conditions. However, the present modeling agrees well with the laboratory testing and field observations.

Fracture mechanics studies have not been applied. For example, it may be of interest to know whether fractures originating at the centre of the core root grow stably. If they do, then an apparently undamaged core may in fact contain internal fractures which would spuriously influence laboratory tests of rock strength, permeability, and elasticity.

3.6 BIBLIOGRAPHY

Borm G., Lempp C., Natau O. & Rockel T., Instabilities of borehole and drillcores in crystalline rocks, with examples from the KTB pilot hole, *Scientific Drilling*, **1**, 105-114 (1989).

Byerlee J. D., Friction of rocks, *Pure and Applied Geophysics*, **116**, 615-625 (1978).

Crouch S. L., A note on the stress concentrations at the bottom of a flat-ended borehole, *Journal of the South African Institute of Mining and Metallurgy*, December, 100-101 (1969).

Durelli A. J., Obert L. & Parks V. J., Stress required to initiate core disking, *Trans. Soc. Min. Eng. AIME*, **241** 269-275 (1965).

Dyke C. G., Core disking : Its potential as an indicator of principal in situ stress directions, *Rock at Great Depth*, Maury V. Fourmaintraux D. (eds.), **2**, 1057-1064 (1989).

Fjaer E., Holt R. M., Horsrud P., Raaen A. M. & Risnes R., *Petroleum related rock mechanics*, Elsevier (1992).

Haimson B. C. & Lee M. Y., Estimating deep in situ stresses from borehole breakouts and core disking- experimental results in granite, *Proceedings of the International Workshop on Rock Stress Measurement at Great Depth*, The 8th International Congress on Rock Mechanics, Balkema Publ., Tokyo, **3**, (1995), (in press).

Heerden W. L. Van, Stress concentration factors for the flat borehole end for use in rock stress measurements, *Eng. Geol.*, **3**, 307-323 (1969).

Ishida T. & Saito T., Observation of core discing and in situ stress measurements: stress criteria causing core discing, *Rock Mechanics and Rock Engineering*, **28** (3), 167-182 (1995).

Jaeger J. C.& Cook N. G. W., Pinching-Off and disking of rocks, *Journal of Geophysical Research*, **68**, 1759-1765 (1963).

Leeman E. R., The measurement of stress in rock-Part I, *Journal of the South African Institute of Mining and Metallurgy*, September, 76-80 (1964).

Li Y. Y. & Schmitt D. R., Wellbore bottom stress concentration and induced core fractures, *AAPG Bulletin* (1996), in press.

Martin C. D., Quantifying drilling-induced damage in samples of Lac du Bonnet granite, *Rock Mechanics*, Proceedings of the 1st North American Rock Mechanics symposium, A. A. Balkema, 419-426 (1994).

Maury V., Santarelli F. J. & Henry J. P., Core disking: A review, Sangorm Symposium, *Rock Mechanics in Africa*, November, 221-231 (1988).

Miguez R., Henry J. P. & Maury V., Le discage: une method indirecte d'evaluation des contraintes in-situ, *Journées Universitaires de Géotechnique* - St - Nazaire-28-30 Janvier, 353-360 (1987).

Mogi K., Fracture and flow of rocks, *Tectonophysics*, 541-568 (1972).

Obert L. & Stephenson D. E., Stress conditions under which core disking occurs, *SME Transactions*, **232**, September, 227-235 (1965).

Panet M., Quelques problèmes de mecanique des roches posés par le tunnel du Mont-Blanc, *Annales de l'Institut Technique du bâtiment et des travaux publics*, **264**, 1968-1979 (1969).

Perreau P. J., Tests of ASR, DSCA, and core disking analyses to evaluate in-situ stresses, *SPE 17960*, 325-336 (1989).

Stacey T. R., Contribution to the mechanics of core disking, *Journal of the South African Institute of Mining and Metallurgy*, September, 269-275 (1982).

Sugawara K., Kameoka Y., Saito T., Oka Y. & Hiramatsu Y., A study on core disking of rock, *Journal of Japanese Association of Mining*, **94**, 19-25 (1978).

Timoshenko S.P. & Goodier J. N., *Theory of Elasticity*, Third edition, MaGraw-Hill (1970).

Tranter C. J.& Craggs J. W., The stress distribution in a long circular cylinder when a discontinuous pressure is applied to the curved surface. *Phil. Mag.*, **36**, 241-250 (1945).

Wang Y.& Wong T.-F., Finite element Analysis of two overcoring techniques for in situ stress measurement, *Int. J. Mech. Min. Sci. & Geomech. Abstr.*, **24**, 41-52 (1987).

Zhu W., Li G. & Wang K., Analysis of disking phenomenon and stress field in the region of an underground powerhouse, *Rock Mechanics and Rock Engineering*, **18**, 1-15 (1985).

Table 3.1. Rock physical properties and experimental results (Obert and Stephenson, 1965)

	Intercept	Slope	Internal friction angle	Cohesion	Brazilian tensional strength
	k_1 (MPa)	k_2	ϕ(degree)	S_o(MPa)	T_o(MPa)
Indiana limestone	40.4	0.64	24	8.2	6.0
Vermont marble	53.1	0.68	36	13.8	6.5
Nova Scotia sandstone	57.8	0.59	45	17.6	5.6
Georgia granite	66.5	0.84	52	22.7	9.1
Maryland marble	77.9	0.89	46	27.6	9.9

(a) (b)

Figure 3.1. a) Cup-shaped core disk fracture produced in the laboratory (Jaeger and Cook, 1963). b) Core disks produced in the laboratory (Obert and Stephenson, 1965).

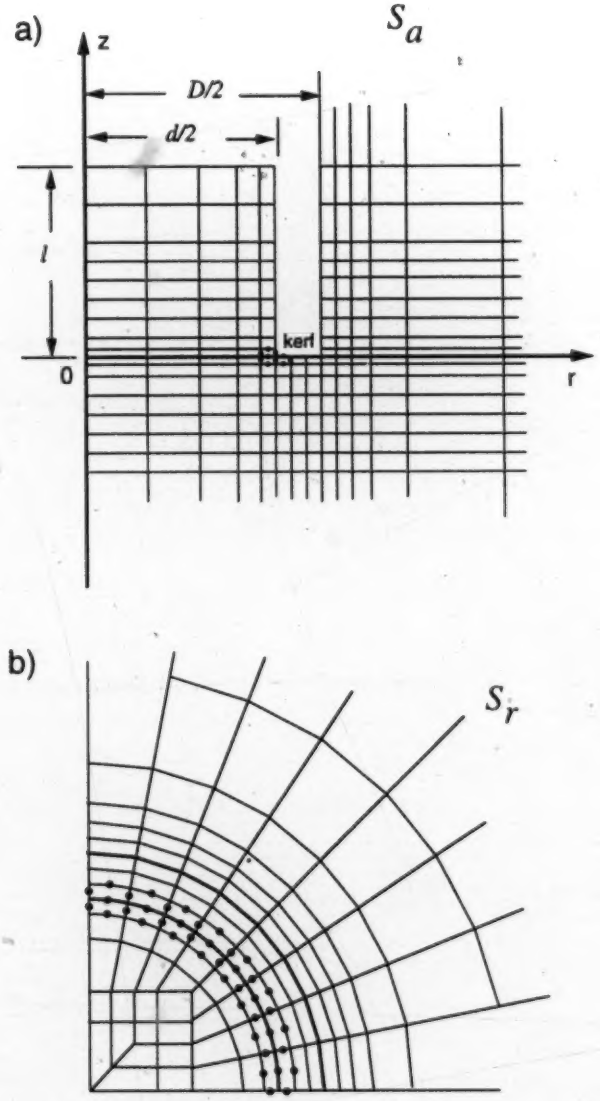

Figure 3.2 Details of finite element mesh of a) side view and b) top view in the vicinity of the borehole. S_r and S_a represent the uniform biaxial radial and the wellbore-axis parallel uniaxial compression, respectively.

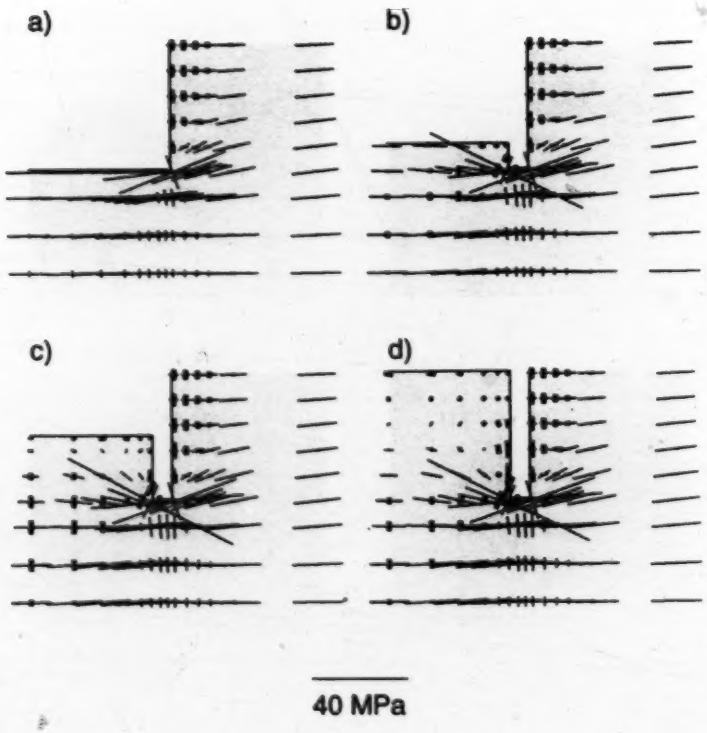

Figure 3.3. Orientations of principal stresses under S_r = 20 MPa for core lengths of a) l/d = 0, b) l/d = 0.1, c) l/d = 0.25, and d) l/d = 0.5.

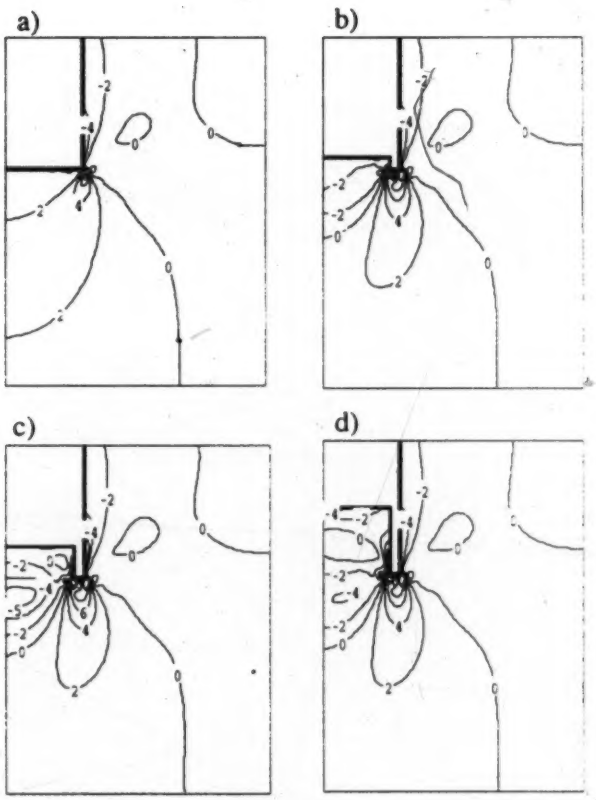

Figure 3.4. Contours (in MPa) of most tensile principal stress σ_3 under $S_r = 20$ MPa for core lengths of a) l/d = 0, b) l/d = 0.1, c) l/d = 0.25, and d) l/d = 0.5.

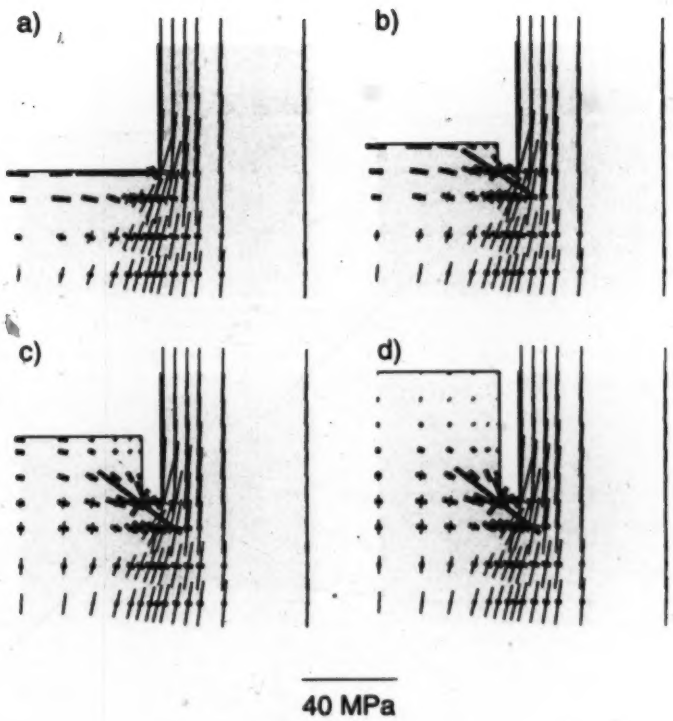

Figure 3.5. Orientations of principal stresses under S_a = 20 MPa for core lengths of a) l/d = 0, b) l/d = 0.1, c) l/d= 0.25, and d) l/d = 0.5.

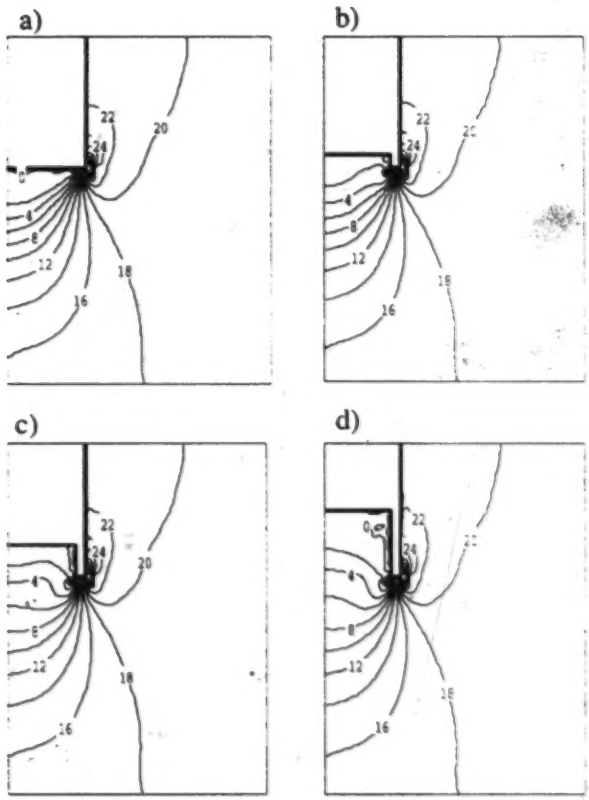

Figure 3.6. Contours (in MPa) of the most compressive principal stress σ_1 under S_a = 20 MPa for core lengths of a) l/d = 0, b) l/d = 0.1, c) l/d = 0.25, and d) l/d = 0.5.

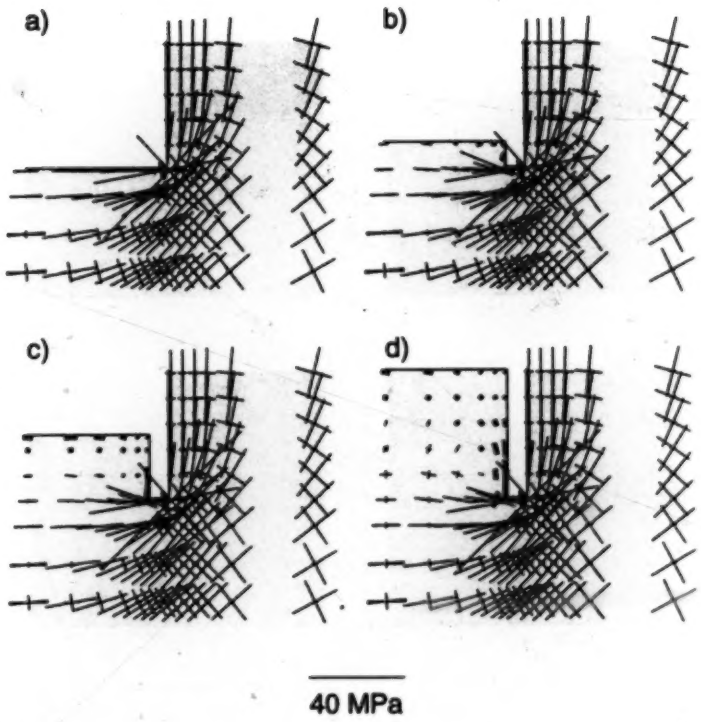

Figure 3.7. Orientations of principal stresses under hydrostatic stress condition with $S_r = S_a = 20$ MPa for core lengths of a) l/d = 0, b) l/d = 0.1, c) l/d = 0.25, and d) l/d = 0.5.

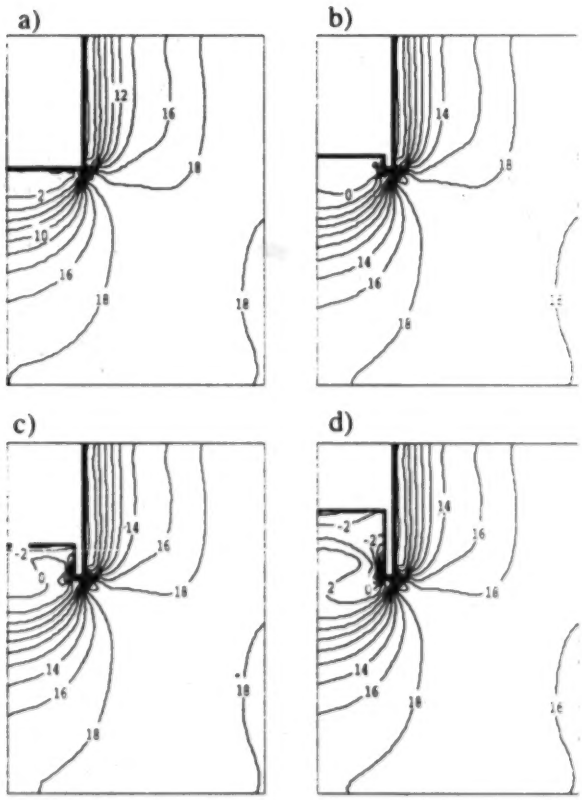

Figure 3.8. Contours (in MPa) of the most tensional principal stress σ_3 under hydrostatic stress condition with $S_r = S_a = 20$ MPa for core lengths of a) l/d = 0, b) l/d = 0.1, c) l/d = 0.25, and d) l/d = 0.5.

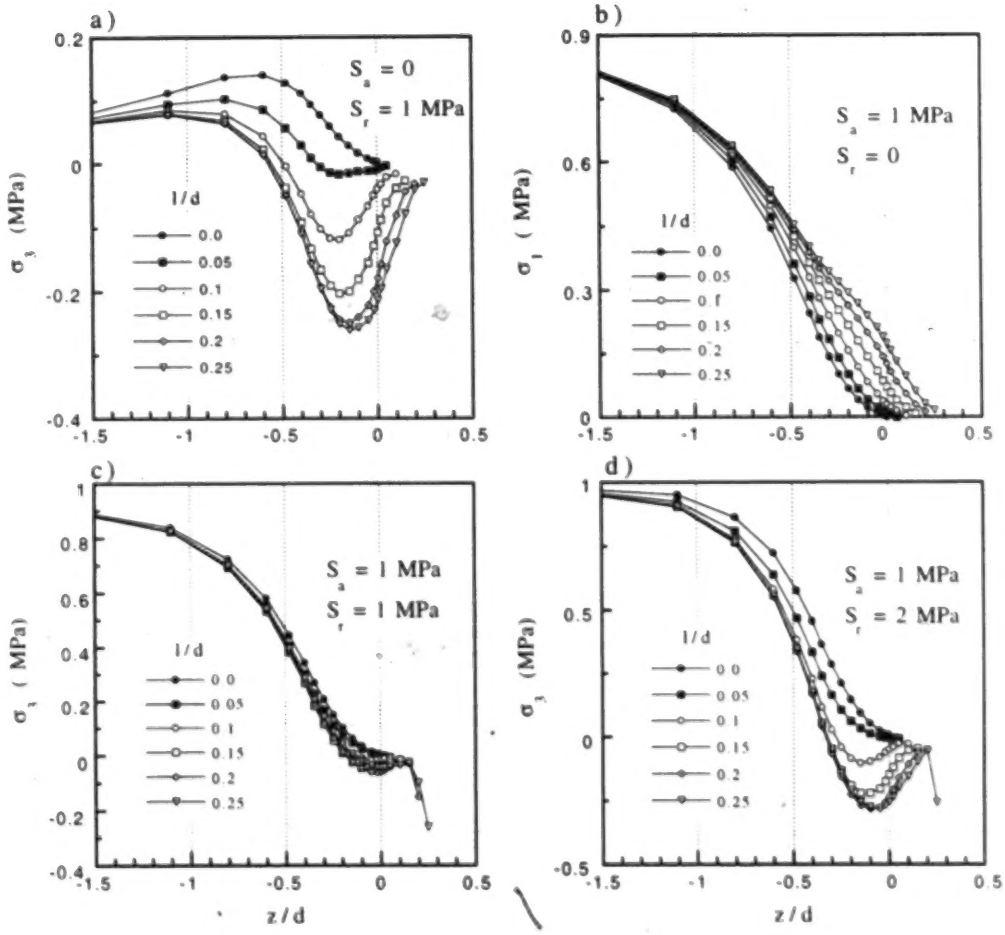

Figure 3.9. Stresses along core axis. a) The most tensile principal stress σ_3 under S_r = 1 MPa, b) The most compressive principal stress σ_1 under S_a = 1 MPa, c) The most tensile principal stress σ_3 under $S_r = S_a$ = 1 MPa, and d) the most tensile principal stress σ_3 under S_r = 2 MPa and S_a = 1 MPa.

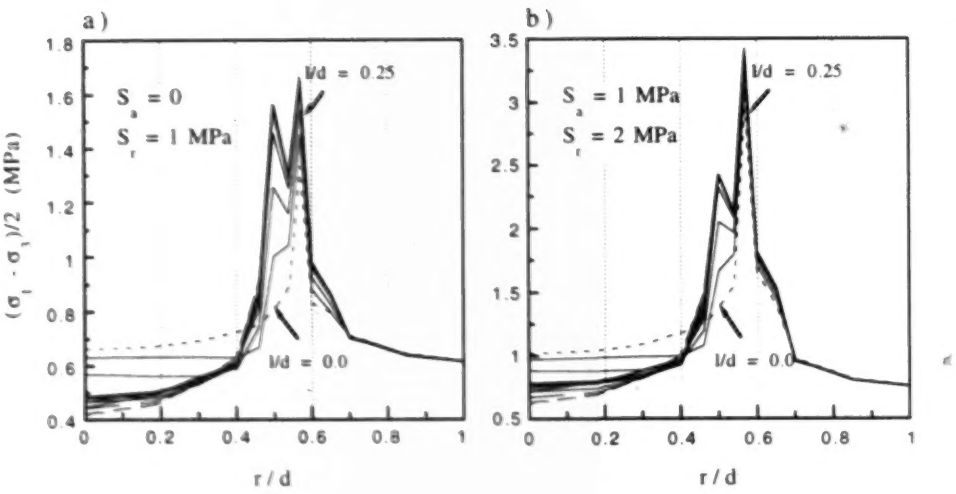

Figure 3.10. Shear stresses across the surface of the kerf. a) S_r = 1 MPa, and b) S_r = 2 MPa and S_a = 1 MPa.

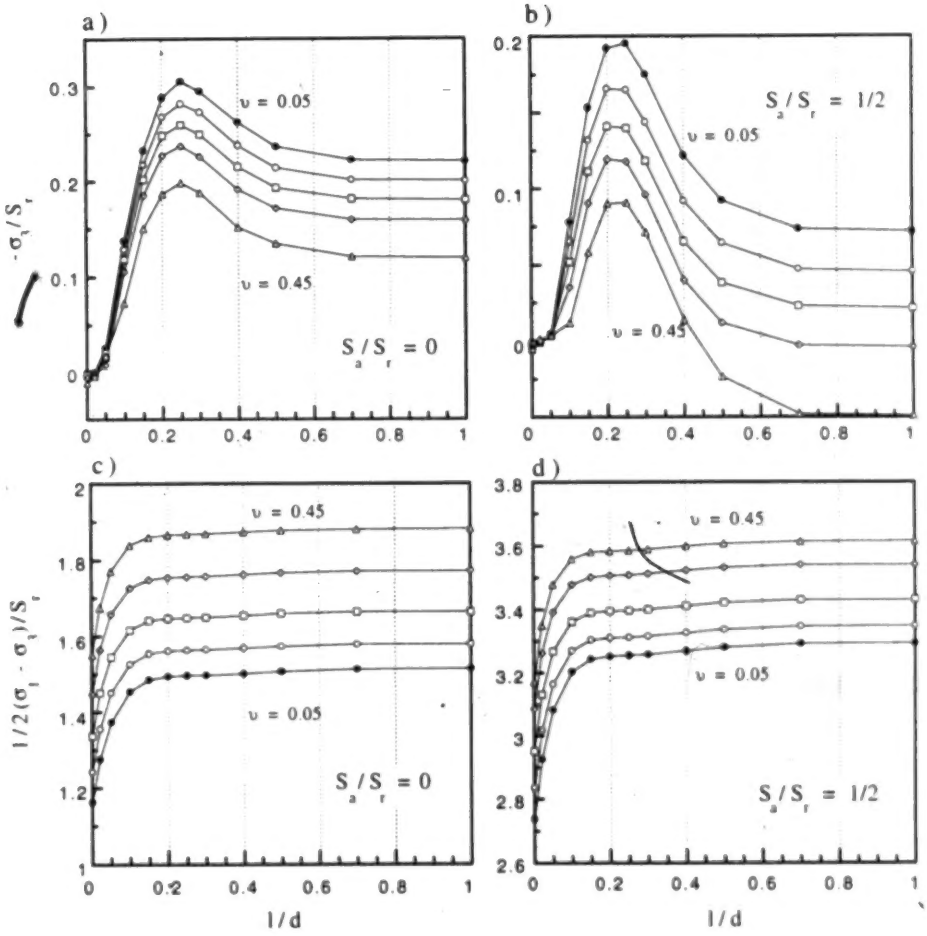

Figure 3.11. Dependence of the peak tensile and shear stresses on core stub length. a) Tensional stresses under $S_a/S_r = 0$, b) tensile stresses under $S_a/S_r = 1/2$, c) shear stresses under $S_a/S_r = 0$, and d) shear stresses under $S_a/S_r = 1/2$. All stresses are normalized by the applied radial stress S_r.

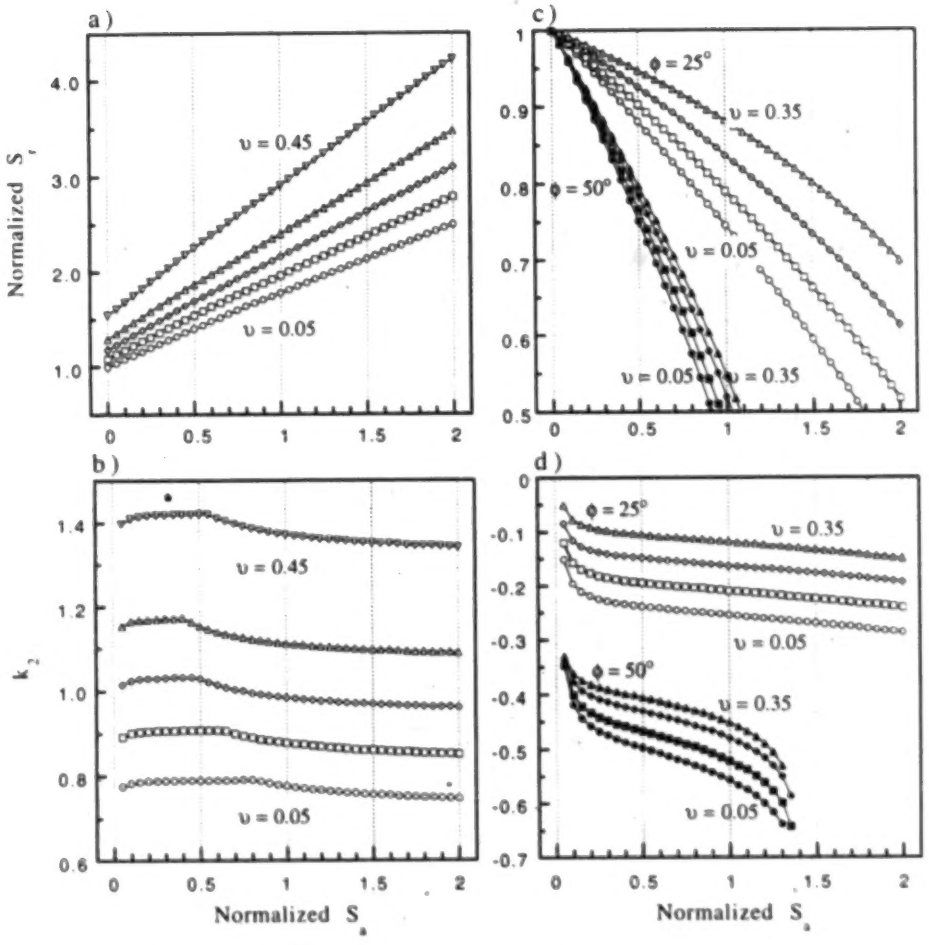

Figure 3.12. a) Hypothetical tensional failure curves, b) local slope k_2 of tensional failure curves, c) hypothetical shear failure curves, and d) local slope k_2 of shear failure curves. The applied stresses are normalized by the S_r under $S_a = 0$ for the case with Poisson's ratio = 0.05.

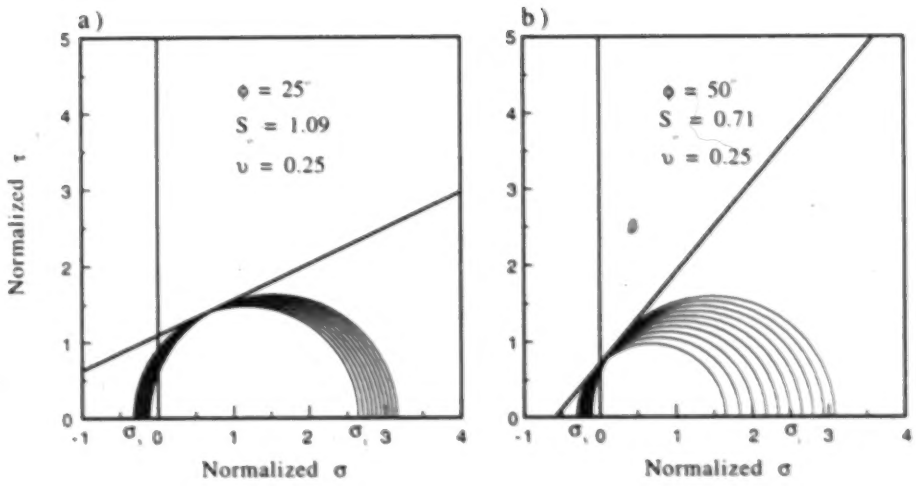

Figure 3.13. Mohr-Coulomb criterion in τ–σ space for the internal friction angles of a) ϕ = 25° and b) ϕ = 50°.

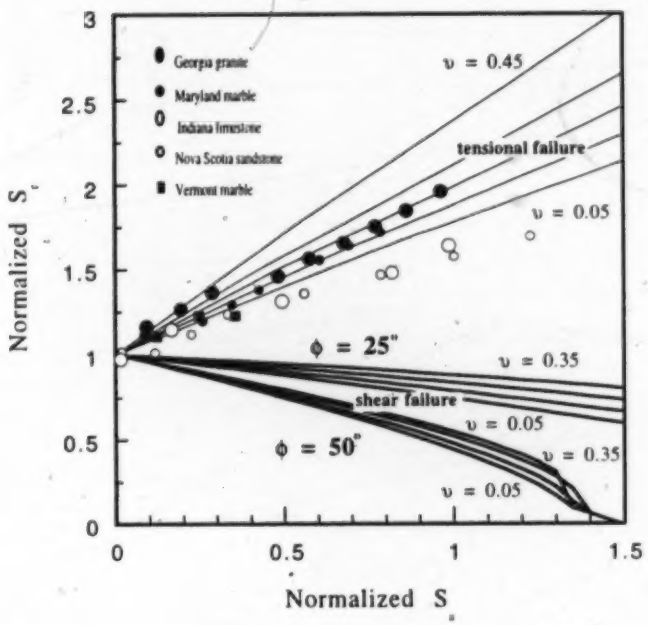

Figure 3.14. Comparison of experimental data of Obert and Stephenson (1965) with calculated failure curves. Normalized by the magnitude of the applied radial stress required for tensile failure under no axial compression.

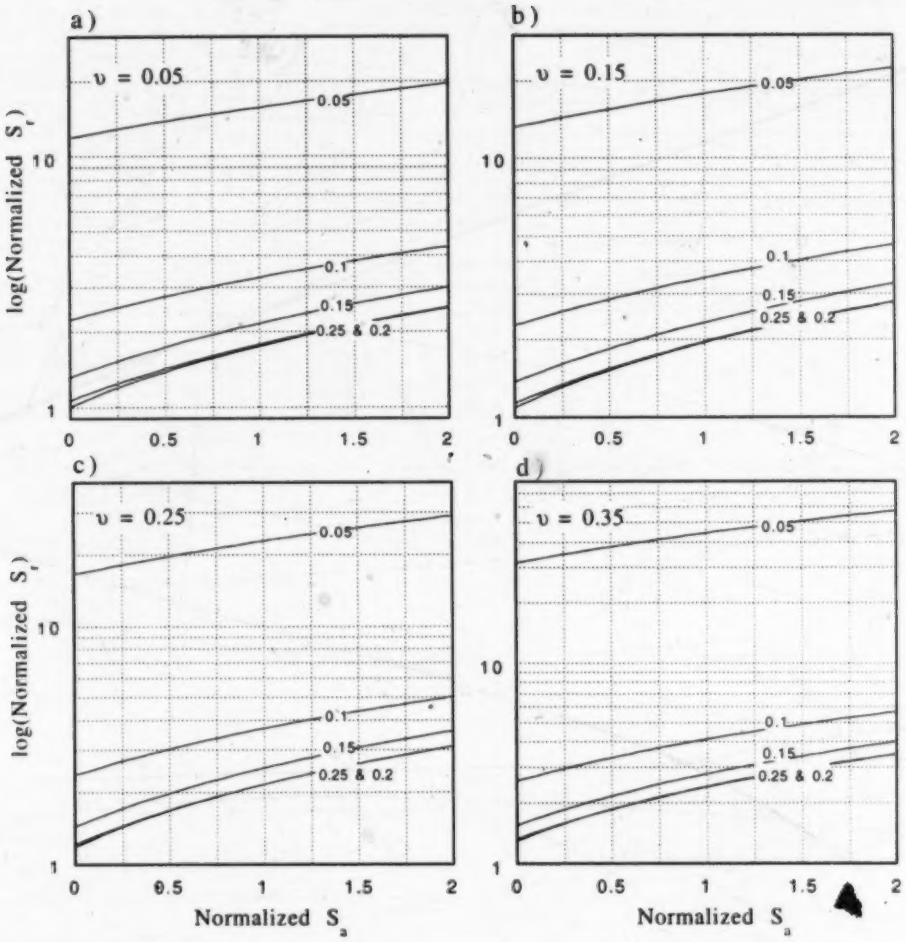

Figure 3.15. Hypothetical failures curves for different core stub lengths for a) υ = 0.05, b) υ = 0.15, c) υ = 0.25, and d) υ = 0.35. The applied stresses, S_r and S_a are normalized by the S_r at $S_a = 0$ for the case with Poisson's ratio = 0.05.

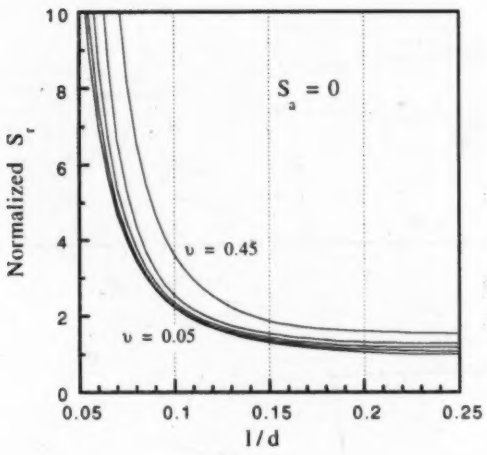

Figure 3.16. The relationship of the core disk thickness and the in situ radial stress S_r under the in situ axial stress $S_a = 0$ and with Poisson's ratios of 0.05 to 0.45. The applied radial stress, S_r, is normalized by the S_r at l/d = 0.25 for the case with Poisson's ratio = 0.05.

CHAPTER 4

DRILLING INDUCED CORE FRACTURES AND IN-SITU STRESSES

4.1 INTRODUCTION

Drilling-induced core fractures appear in different shapes and are classified on this basis as disking, petal, and petal-centreline fractures. A number of examples of these differing fractures are given in Figure 4.1. The uniform spacings and shapes and the consistent strike orientations of these drilling induced fractures suggest that their morphologies are related to the stress conditions within the earth. Indeed, it is well known empirically that the strike directions of these fractures coincide with the direction of the greatest horizontal compression. However, despite the obvious differences in the shapes between a disk and a petal fracture, little is known about the conditions under which these fractures form. Further study of these fractures is warranted as they potentially contain much information on in situ stresses and may in some cases be the only information that can be obtained, especially in deep drilling of the crust.

Many workers have been involved in the observation and study of these fractures (e.g., Pendexter and Rohn, 1954; Leeman, 1964; Jaeger and Cook, 1963; Obert and Stephenson, 1965; Durelli et al., 1965; Sugawara et al., 1978; GangaRao et al., 1979; Stacey, 1982; Miguez et al., 1987; Maury et al., 1988; Borm et, al, 1989; Perreau, 1989; Dyke, 1989; Lorenz et al. 1990, Kulander et al., 1990; Haimson & Lee, 1995, Bankwitz and Bankwitz, 1995; and Li and Schmitt, 1997a, 1997b), but the relationship between the fracture morphology and in situ stresses remains to be determined.

A version of this chapter has been accepted for publication, April, 1997, Journal of Geophysical Research.

This state of affairs arises in part due to theoretical difficulties associated with determining the stresses in the vicinity of the bottomhole. Drilling-induced core fractures result in part from the concentration of the in situ stress in proximity to the wellbore bottom. As the bottomhole geometry is only axisymmetric, it does not lend itself to a closed-form analytic solution for the stress concentrations comparable to that given, for example, by Kirsch (1898) for a circular hole in a plate and employed in describing incipient wellbore breakouts and hydraulic fractures. Consequently, numerical modeling has in the past been employed on case by case for core disking fractures (e.g., Sugawara et al., 1978; Dyke, 1989) or for petal fractures (GangaRao et al., 1979; Lorenz et al., 1990). The earliest attempt at modeling the morphology of coring induced fractures was carried out by Chang (1975) who assumed shear failue according to Mohr-Coulomb theory and used strain energy densities (Shih, 1973) to predict fracture trajectories. In contrast, Stacey and Harte (1989) and Dyke (1989) used mappings of extensional strain to suggest possible fracture trajectories.

Another reason for the lack of information about coring induced fractures is difficulties in applying complex stresses to a rock specimen in the laboratory. In the early laboratory experiments (Jaeger and Cook, 1963; Obert and Stephenson, 1965) conventional triaxial rock tests with only a radial confining pressure and an axial load were applied to cylindrical samples. Only recently were Haimson and Lee (1995) able to apply complete poly-axial states of stress to cubical samples which were then cored under load. Even so, no petal, petal-centerline, or centerline fractures have been produced in a laboratory.

In this contribution, we calculate the stress concentrations produced at the bottom of a vertical wellbore containing the stub of a core being drilled into different in situ stress states here classified into faulting regimes by Anderson (1951). We find that the predicted trajectories of the tensile fractures created in such concentrated stress fields are in good agreement with observed core fractures, consequently making apparent the relationships

between the fracture shapes and their points of origin with the state of in situ stress. These fracture trajectories are compared to core fractures observed in the existing, but limited, cases in the literature where stress states have been quantitatively measured by alternative means. Although these relationships are in need of laboratory validation, they suggest that the fracture morphology provides a simple and direct indicator of the relative magnitudes of the principal stresses.

4.2 BACKGROUND

It is first important to discuss the morphology, the fractographic observations, and the assumed failure mechanism of drilling induced core fractures; the reader is also directed to the reviews of Kulander et al. (1990) and Engelder (1993).

A collection of different drilling induced core fractures is shown in Figure 4.1. These include the core disks with cupped and flat fracture surfaces in Georgia granite from the early experiments of Obert and Stephenson (1965) (Figure 4.1a), saddle shaped core disking fractures in metabasites from the KTB drill site at a depth 3582 m (Borm et al., 1989) (Figure 4.1b), petal fractures in a metamorphic core from the Alberta Basement (Figure 4.1c), and a petal-centerline fracture from Pendexter and Rohn (1954) (Figure 4.1d). Fracture here taken describes where the core actually separates into two distinct pieces (e.g. Figure 4.1a, b and d) and where the core remains intact but with a visible and well developed deformation zone along the fracture trace (e.g. Figure 4.1c). Obert and Stephenson (1965) preferred to distinguish this difference by referring to the latter case as a rupture, whether this long and thin zone of deformation can be described as process zones (e.g. Atkinson, 1987) is not clear.

As shown in Figure 4.1, core disking fractures have a variety of shapes and are uniformly spaced. On the basis of field observations, laboratory experiments and numerical modeling, the thickness of core disks often ranges from 1/5 to 1/4 of the core diameter (e.g., Jaeger and Cook, 1963; Leeman, 1964; Obert and Stephenson, 1965; Zhu and et al.,

1985; Borm et al., 1989; Ishida et al., 1995; and Li and Schmitt, 1996b). The other major characteristic is that the trough of saddle shaped core disking fractures is aligned with the direction of the greatest horizontal compressive stress S_H (e.g., Kulander et al., 1990; Haimson and Lee 1994).

Petal fractures are often also uniformly spaced but the upper limit is greater than that of core disks. Random spacing is often observed. Chang (1975) measured a large number of petal fractures and found the dip angles of the fracture surface range from 30° to 45°. Petal-centerline fractures (Figure 4.1d) which finally propagate in the direction of the core axis may be considered as special cases of petal fractures. Kulander et al. (1979) divided the surface of petal centerline fracture into two morphological sections. The initial section near core boundary dips from 30° to 75° and the second has vertical inclination. The strike of the fracture surface is aligned with the direction of the greatest horizontal stress S_H for both petal and petal-centerline fractures

Fractographic features on the fracture surfaces contain further information. Figure 4.2 shows two typical examples of coring-induced fracture surfaces. In Figure 4.2a, the hackle structures indicate that the fracture originates at the center of the core along the wellbore axis (Bankwitz and Bankwitz, 1995). Such internally generated fractures have also been observed by Zanon (Maury et al.; 1988) in x-ray examinations of what appear to be otherwise intact cores. This contrasts with the fractures in Figure 4.1b which originate from outside the core. Core disking fractures can initiate either near the boundary of the core or at its interior; the point of fracture initiation depends on the state of stress and this can also be used as a stress indicator. This is because the point at which the greatest concentrated tension is found migrates from the kerf (cut) of the core root depending on the stress conditions.

The fracture morphology and the fractographic features in Figure 4.1c-d and Figure 4.2b indicate that both petal and petal-centerline fractures originate outside the core or near its boundary. The downward curved arrest lines in Figure 4.2b suggest that petal and

petal-centerline fractures propagate downwards into the core with slow progress possibly controlled by the drilling (Kulander et al., 1990). A gradual evolution of core fracture morphology that begins from saddle shaped core disks to petal fractures and finally to petal-centerline fractures, dependent upon the in situ stress, may exist.

In compressional stress regimes substantial tensions are generated in the vicinity of the bottomhole. Drilling-induced core fractures appear to result primarily from tensional failure of the material as suggested by field observations, laboratory experiments, and numerical modeling. Jaeger and Cook (1963) conducted a series of experiments and suggested that the core disking fractures are produced under tension because the fracture surface always appears clear and unsheared. Panet (1969) suggested core disking may initiate where tensile stress appears and, noting that rock tensile strength always is much smaller than its compressive strength, applied a tensile strength criterion to the experimental results of Obert and Stephenson (1965). This was supported by the numerical modelling of Sugawara et al. (1978), Dyke (1989), and Li and Schmitt (1997a) which indicated that large tensions were generated in the vicinity of the bottomhole drilled into compressional stress states. A Mohr-Coloumb shear failure criteria is not consistent with the Obert and Stephenson's (1965) experimentally observed failure curves (Li and Schmitt, 1997b). Finally, in recent tests Haimson and Lee (1995) found no evidence for shear failure in the microscopic examination of the surfaces of core disking fractures produced in the laboratory as did Durham's (1993) profilometry of core disking surfaces from the KTB wellbore. These are important points; and in the analyses below it is assumed that the drilling induced core fractures are tensile.

In this study the in situ stress states are discussed in terms of faulting environment stress regimes (Anderson, 1951). This Andersonian classification arranges the overburden S_v, the greatest compressive horizontal principal stress S_H and the least compressive horizontal principal stress S_h relative to the three major types of faulting in the lithosphere

(Figure 4.3). The characterizations are: 1) in the normal fault regime, $S_v > S_H > S_h$, 2) in the strike-slip fault regime, $S_H > S_v > S_h$, and 3) in the thrust fault regime, $S_H > S_h > S_v$.

4.3 NUMERICAL CALCULATIONS

4.3.1 Finite Element Modeling

A description of the finite element modelling procedures may be found in Li and Schmitt (1997a). Briefly, however, details of a small portion of the finite element mesh near the wellbore across the borehole axis are shown in Figure 4.4 with a ratio of core diameter d to wellbore diameter D is 1/2. The curved kerf (cut) was assumed as a semi-circle with a radius of 1/2 the width of the kerf. The size of the elements near the corners of the kerf where the greatest stress concentrations appear are reduced. To obtain a higher resolution, 20 node isoparametric elements were used at the inner corner of the kerf. To effectively remove the influence of the model boundaries, the nearest external surface was removed a distance of 15d from the bottomhole. In all calculations, the medium was assumed linearly elastic and isotropic and a Poisson's ratio of 0.25 and a Young's modulus of 20 GPa were used. The modeling here assumes the wellbore is vertical and is parallel to a principal far-field stress which within the context of the discussion is obviously S_v.

Because the medium is linearly elastic and isotropic, the local stress tensor at each point within the grid was calculated by superposing the stress concentrations resulting individually from the three, appropriately scaled, principal in situ stresses S_v, S_H and S_h applied in the far field of the wellbore (Li and Schmitt, 1997a). Although the bottomhole geometry modeled in this previous study differs from that here the general characteristics of the concentrated stress fields for both are similar and the stress concentrations generated by these individual far field stresses will not be presented here.

The length of the core stub influences the stress concentrations (Li and Schmitt, 1997b). Based on this earlier modelling a core stub length $l = d/4$ was chosen for use here

as for a given state of applied far-field stress the greatest concentrated tensions are produced near this length.

4.3.2 Predicting Fracture Trajectories

The most often employed theories of fracture initiation include the maximum tensile stress theory, the maximum energy release rate theory, the minimum strain energy theory (Minguez, 1993), and Griffith's theory (Griffith, 1921). In this study, the maximum tensile stress theory is used. The fracture (Mode I) initiates at the point of the greatest local tensile stress opening parallel to the tension and σ_3 propagating perpendicular to it once the material tensile strength is exceeded. As the fracture propagates, its orientation is controlled by the local direction of the tension, superb examples of this effect are given in Lawn and Wilshaw (1975). In a finite element modeling of rock fracturing, Ingraffea and Heuze (1980) compared the first three theories, and found that the fracture trajectories predicted by the first two theories are in good agreement with their experimental observations.

An automatic program for the fracture tracing was developed based on the maximum tensile stress theory. The details of the algorithm are given in the Appendix 4. Its procedure is summarized as the following: First, the orientations and magnitudes of the most tensional local principal stresses (σ_3) are interpolated from the finite element mesh into finer and regular grids. A search is conducted to find the greatest tensile stress. The fracture is assumed to initiate from this point and then to proceed within the grids in the direction normal to σ_3. This procedure is carried out only in the 2D cross-sectional planes which pass through the wellbore axis and are aligned parallel ($\Phi = 0°$) and perpendicular ($\Phi = 90°$) to the direction of the greatest compressive horizontal principal stress S_H. Although the analysis requires a full 3-D calculation, the extremum stress magnitudes always occur within these two planes.

4.4 MODELING RESULTS

Stress concentrations were calculated under various states of far-field stress and are displayed in the form of stick diagrams: thin and thick sticks show the orientations of the compressional and tensile local principal stresses at their center points, respectively. Their length is directly proportional to the magnitude. The stresses are all presented in dimensionless form normalized by the magnitude of the greatest far-field compression. Predicted fracture trajectories are shown in separate figures for a variety of stress conditions, in each figure the point of fracture initiation is indicated by an asterisk. These stress state descriptions are followed in sequence by the corresponding predicted fracture trajectories.

4.4.1 Normal Fault Stress Regime ($S_v > S_H > S_h$)

With high overburden stress and under highly anisotropic horizontal stresses (Figure 4.5a) large tensions parallel to the surface exist at the inner side of the kerf and at the top of the core stub at $\Phi = 90°$. The tension is reduced substantially with increasing S_h, and only a small tension remains at the kerf when $S_h = S_H$ (Figure 4.5c).

The shapes of the predicted fracture trajectories evolve with the relative magnitudes between the horizontal stresses (Figure 4.6). In all cases of $S_H > S_h$, the fracture is expected to initiate at the kerf and at azimuths of $\Phi = 90°$. When $S_H = S_h$, the fracture may initiate at any azimuth at the kerf. Fracture trajectories resembling steeply dipping petal fracture shapes are seen while the horizontal stresses remain anisotropic but as S_h becomes larger this evolves to the angle shallows and the trajectories appear to pass through stages very similar to petal-centreline fractures and eventually disking fractures. These disk-like shapes are primarily concave for smaller horizontal stress (Figure 4.6) but convex shapes appear at the cases with increased magnitude of the greatest horizontal stress (Figure 4.6b).

In addition, the strikes of the petal and the petal-centerline fractures and the direction of the deeper trough of the core disking fractures coincide with the direction of

S_H. This is in agreement with the empirical field observations and indicate the utility of the core fractures as indicators of stress directions when oriented core is available (e.g., Kulander et al., 1990).

4.4.2 Strike-Slip Fault Stress Regime ($S_H > S_v > S_h$)

The principal stress orientations and magnitudes under strike-slip faulting conditions (Figure 4.7) are similar to those seen above under normal faulting. The greatest tensions appear at the surface of the inner side of the kerf at $\Phi = 90°$ or immediately at the top of the core stub. Tensional stresses progressively attenuate as S_h increases.

Under strike-slip conditions the greatest tension and presumed fracture initiation point always occurs at the kerf at $\Phi = 90°$ (Figure 4.8). In many ways, the fracture trajectories are similar to those for the normal faulting case. Trajectories similar to petal fracture appear for highly anisotropic horizontal stresses while these pass through a petal-centreline stage and to a disk shape finally. Concave saddle shapes appear possible as indicated by the trajectories when $S_h = 0.25$ with the high points of the saddle at $\Phi = 90°$ and the trough aligned with S_H. Convex (Figure 4.8a) and nearly flat (Figure 4.8b) are also seen. Fracturing local to the core surface may result under high and uniform values of Sh and S_v (Figure 4.8b).

4.4.3 Thrust Fault Stress Regime ($S_H > S_h > S_v$)

Concentrated stresses for a selected variety of conditions found within the thrust faulting regime are shown in Figure 4.9 and these suggest a differing behavior of core fracturing than in the other faulting regimes. In Figure 4.9a, the lone uniaxial horizontal compression generates relatively large tensions at and directed parallel to the inner surface of the kerf at $\Phi = 90°$. However, once the least horizontal stress is increased, the location of the greatest tension migrates to the axis of the wellbore into the material at the root of the core (Figures 4.9 b-d). Inclusion of a vertical overburden load counteracts the axially

directed and located tensions produced by the horizontal stresses (compare Figures 4.9c-d).

Only disk-like fracture trajectories appear under thrust faulting conditions (Figure 4.10). A saddle shaped disk may be indicative of highly anisotropic horizontal stress conditions (Figure 4.10a). Essentially flat trajectories result for more uniform horizontal stresses but the trajectories become convex once a substantial vertical stress exists (Figure 4.10b). Another important observation is that, in most of the cases, the greatest tension exists not at the kerf but at the core axis. This is a crucial difference as the core fracture is expected to initiate within the rock mass and not on the wellbore surface; a fracture initiation point on the core axis indicates thrust faulting stress conditions.

4.4.4 Preferred Locations of Fracture Initiation

The results above give only an indication of the styles of fracture trajectories possible and the points of fracture initiation. A more thorough study of the latter is worthwhile as the results suggest that where the fracture initiates is a valuable additional piece of information. The magnitudes of the peak concentrated tensile stresses at points either at the kerf, the top of the core stub, or at its root are shown in normalized form in Figure 4.11. In these plots, the preferred position of the fracture initiation for a given stress state occurs at that point subject to the greatest tension.

Under normal faulting conditions where the vertical far-field stress is the most compressive, the largest tensions exist either at the kerf or at the top surface of the core (Figure 4.11a). While S_h remains small relative to S_v, the greatest tensions are concentrated at the kerf. It is worth noting that the absolute value of the magnitude of this concentrated tension is greater than that for the overburden S_v with small S_h. At increased values of S_h, however, the tensions at the kerf or at the top of the core are very close indicating that the fracture initiation point could change easily between these two locations.

The near equivalence of these tensions possibly explains the continued propagation of centreline fractures down the core.

In the strike-slip faulting regime, tensions exist at both the kerf and within the root of the core (Figure 4.11b). The tension at the kerf is substantially greater in almost all stress conditions suggesting that the resulting drilling induced core fractures will initiate at the kerf.

In contrast, the preferred fracture initiation location under thrust faulting is nearly always at the core root (Figure 4.11c). Initiation at the kerf may be preferred under highly anisotropic stress states with a relative large magnitude for S_v.

4.4.5 Stress State Domains of Core Fractures

Information on the preferred fracture initiation points plus the predicted fracture trajectories of Figures 4.5 to 4.10 and numerous additional trajectory tracings not shown are summarized in Figure 4.12. Here the type of fracture (petal or disk) and the fracture initiation point (kerf or root) are displayed as fields over a graph of S_v/S_H versus S_h/S_H. This mapping allows direct comparison of all the faulting regimes. The area covered by the normal faulting regime and lying above the horizontal line defined by $S_v/S_H = 1$ in this mapping is essentially infinite. The strike-slip field covers the area below this horizontal line but above the diagonal line defined by $S_v = S_h$ which extends from the origin. Finally, the area describing thrust faulting stress conditions lies below this diagonal. Most in situ stress regimes encountered in practice will lie within the confines of Figure 4.12, only those cases with very high S_v magnitudes cannot be shown but all will be characterized by petal fracturing.

The advantage of the mapping is that the evolution of the different styles of the drilling induced core fractures is apparent (Figure 4.12). This progression begins under thrust faulting conditions with only core disks most of which initiate at the core root, through core disks all of which initiate at the kerf and generally associated with more

uniform horizontal farfield stresses under both normal and strike-slip faulting, to finally petal fractures when more anisotropic horizontal stresses are encountered. Conversely, a description of a drilling-induced core fracture might quickly indicate the approximate state of stress under which the core fracture was created.

Derivation of the boundary lines between the different core fracturing behaviors is straightforward. The boundary between kerf and axis fracture initiation for core disks derives directly from the result of Figure 4.11. The boundary between petal and disk fractures is delineated by finding the points at which the fracture trajectories discontinuously shift from vertical (indicative of petal-centreline fractures) to horizontal (indicating disk fractures). No other fracture trajectory dips were found at the wellbore axis.

4.5 DISCUSSION

4.5.1 Comparison of Modeling Results and Observations

Very broadly, the fracture trajectories predicted above are consistent with the shapes of drilling induced core fractures (Figure 4.1) either produced in early laboratory experiments (Jaeger and Cook, 1963; Obert and Stephenson, 1965; and Haimson and Lee, 1995) or from field observations (e.g., Pendexter and Rohn, 1951; Leeman, 1964; Stacey, 1982; Maury et al., 1988; Borm et al., 1989; Perreau, 1989; Kulander et al. 1990; and Bankwitz and Bankwitz, 1995). Further, orientations of the strikes and high points on these fractures relative to in situ stress directions agree fully with observation. Although this agreement is encouraging, if the theoretical relationships between drilling induced core fracture morphology and in situ stress state are to be useful, more quantitative comparisons are required. A comprehensive set of laboratory experiments to test the result of Figure 4.12 is not yet available although Haimson and his coworkers (Haimson and Lee, 1995; Song and Haimson 1996) have recently made substantial progress in this direction.

Here, we compare observed core fractures with the states of stress from which they were recovered. However, there are, unfortunately, few studies where simultaneously both good descriptions of the core fractures exist and in situ stresses have been quantitatively measured. Most often in the literature, descriptions of core fractures are only anecdotal and their existence is justly taken by the authors to indicate high levels of in situ stress. The comparisons available to us, and summarized in Table 4.1, stem from both laboratory experiments and field drilling projects in which hydraulic fracturing measurements had been carried out; these will be discussed on a case by case basis in the context of the results of Figure 4.12. We note further that field stress measurements as conducted by the hydraulic fracturing method are still not perfect and although determinations of S_h by a variety of methods (Engelder, 1993) are reliable, estimates of magnitude of S_H can be influenced by numerous material and pressurization rate dependent factors (e.g. Schmitt and Zoback, 1993) and are more prone to error.

Obert and Stephenson's (1965) experiments have been previously discussed in detail (Li and Schmitt, 1997b). These cored cylindrical samples of a variety of rock types under progressively compressive radial and axial loads until core disking was observed. Their loading conditions fall entirely within the thrust fault regime but, as uniform radial stress exists, limited only to the extreme right hand boundary of the graph where $S_H = S_h$. The fact that they observed core disks is consistent with Figure 4.12; they did not provide additional details on the morphology of their disks but the photographs as reproduced in Figure 4.1a indicate relatively flat disking surfaces which would be consistent with a state of uniform horizontal compression (Figure 4.10a). No information on fracture initiation points was given nor can this information be unambiguously extracted from their photographs.

Jaeger and Cook (1963) carried out simple experiments in which they subjected cylindrical test pieces, already centrally cored and containing an intact core stub, to an approximately radial uniform compression with no axial stress. They provide an example

of one such resulting core disk fracture in a photograph. This fracture is nearly flat and is again consistent with the suggested core disking. Again, no information on where the fracture initiated was provided although the uniform radial symmetry of the fracture and the fact that it extended to beneath the kerf suggests the fracture initiated at the core root.

Numerous experiments have recently been carried out by Haimson and Lee (1995) and Song and Haimson (1996) over a broader range of stress conditions (Table 4.1). They report that saddle shaped core disking fractures which originated in the vicinity of the kerf were produced. The box shown in Figure 4.12 describes only the reported ranges of loads (Haimson and Lee, 1995) applied to their samples, details of which individual stress states were used are not yet available.

We have access to only two published examples where both in situ stresses have been quantitatively measured and the core disks have been observed and sufficiently described.

The earlier of these studies consists of hydraulic fracturing tests in wellbores near depths of 1000 m in the Columbia River basalts, Washington State by Paillet and Kim (1987). Horizontal principal stresses were measured with hydraulic fracturing method (Table 4.1) and the predicted stress conditions lie immediately below to the thrust /strike-slip faulting boundary and near the proposed root/kerf fracture initiation border. They observed extensive core disking again broadly consistent with Figure 4.12. One photograph shows a typical saddle-shaped core disk. The fracture initiation point of which appears to be near or outside the core in agreement with what might be expected. However, another photograph in their paper shows numerous core disks which may have flat fracture surfaces. No descriptions of additional core disks were provided and it is unknown whether disks with fractures initiating at the root were observed since some of their reported stress conditions fall within this region. Regardless, the observation of core disking is in agreement with Figure 4.12.

The next set of pertinent observations come from the recently completed KTB wellbore and include the descriptions of the drilling induced core fractures (Röckel, 1995), and the quantitative estimates of in situ stress from hydraulic fracturing measurements (Baumgärtner et al, 1990) in the KTB-VB pilot wellbore and from a combined stress analysis in the KTB-HB main wellbore (Brudy, 1995). The hydraulic fracturing results to 3 km depth (Röckel and Natau, 1993; Brudy, 1995) are summarized in Table 4.1 and plotted in Figure 4.12 but the quantitative studies indicate strike-slip faulting conditions exist to depths of almost 7 km. Röckel (1995) observes a few saddle shaped disking fractures above the depth of 3500 m in the pilot hole but numerous core disking fractures occur below depths of 3560 m the high points of which were used as indicators of the direction of S_h. These core fractures are in good agreement with that expected in Figure 4.12. However, it must be noted that Röckel (1995) also describes a few isolated appearances of petal and centreline fractures. The petal fractures are not in agreement with the general results of Figure 4.12, although some of these fractures may be related to the foliations of the metamorphic rocks cored.

4.5.2 Additional Considerations

A number of other factors which possibly influence the morphology of the core disks have to this point been purposely ignored in order that the dependencies of the drilling-induced core fractures on the in situ stress state are clear. Some additional complications which will not be discussed here but will influence stress field in the core and near the bottomhole arise due to the nonlinear elastic behavior and yielding of rock, to torque loading imposed by friction forces of the rotating core barrel, to anisotropy of the elastic properties or of the tensile strength (foliation or bedding plane), to deviation of the wellbore axis from a principal stress direction, to hydraulically driven fracture propagation by pressurized wellbore fluid, and to thermoelastic and poroelastic stresses resulting from

contact and transfer of drilling fluid with the rock mass. We address some of the more general influences below.

If the medium is not homogeneous, the core disking fracture may not initiate at the center or the boundary of the core. Stresses are additionally locally concentrated by inclusions with differing elastic properties (e.g., Tapponier and Brace, 1976); additional tensile stresses could consequently be generated very near these inclusions from which fracturing might originate. One such example, in Devonian shale core from Appalachian basin, Kentucky, is given by Kulander et al. (1990) in which a core disking fracture originates at a pyrite nodule which is neither at the axis or near the core boundary. Bankwitz and Bankwitz (1995) give a further example from the KTB wellbore where the disking fracture initiated at an inclusion midway between the core axis and boundary.

The loads imposed by the weight of the drill string and from the pressure of the wellbore fluid (i.e. drill mud weight) have been previously described in a simpler, but less realistic, square bottomhole geometry (Li and Schmitt, 1997a). Substantial concentrated tension is generated at the square inner corner of the kerf for both of these loads; but this tension remains highly localized to a small region near the kerf. The concentrated stresses within the rock mass which will become the core are largely compressive.

Although such induced tension could promote fracture initiation from the kerf, the states of stress concentrated by these loads should not assist continued propagation. Common anecdotal descriptions of the existence of core disking depending on the rate of penetration (i.e. on which drill crew was employed) may be related to a potential trigger effect here; speculatively, a higher rate of penetration requires a greater bit load generating a greater local tension at the kerf making fracture initiation more likely. In the more realistic geometry used in the present finite element modelling (Figure 4.4) with the loads distributed over a smoothly curving surface, these concentrated tensions will be even more attenuated. However, these effect of drill bit weight should not be immediately dismissed;

it may result in a shift of the hypothetical boundaries between the different types of petal and disk fractures in Figure 4.12.

Pore pressure is an important consideration in the brittle failure of rock. Under quasi-static loading conditions the influence of pore pressure in promoting tensile failure is described by the relationship first described by Terzaghi (Schmitt and Zoback, 1992):

$$S + (T - P_p) < 0 \tag{4.1}$$

where S is the most tensional principal stress at the point of failure, T is the material dependent tensile strength, and P_p is the pore pressure at the point of failure. Inclusion of a pore pressure serves here only to diminish the compression in the material, the shapes and fracture initiation points (assuming uniform pore pressures) remain dependent on the concentrated total stresses.

The effects of changing the geometry of the bottomhole by use of a core bit of different dimensions or by varying the length of the core stub is of obvious importance here. Both will influence the concentrated stress field (Li and Schmitt, 1997a, b). As regards the former, the relative core and wellbore diameter is an important parameter. Some modelling carried out by us to test this indicates that this ratio does not have a large influence on the character or the magnitudes of the stresses concentrated near the core for a reasonable range of relative kerf thicknesses.

In contrast, the length of the core stub has considerably more influence on the stress concentrations. The length used here (Figure 4.4) conforms to that for the greatest spacing between incipient core disking fractures. Smaller spacings between the fractures will occur at higher stress levels whereas no macroscopic core fracturing is expected for greater spacings in homogenous rock (Li and Schmitt, 1997b). Interpretation of core disk fractures in light of the results given in Figure 4.12 should account for this.

In this study, only the general evolution of the morphology of the drilling induced fractures with in situ stresses has been explored. The above figures suggest, however, that considerably more information might be extracted from the core fracture shape. For example, whether the core fracture is concave or convex is additional information not exploited in Figure 12 which might allow for more detailed classification of the stress conditions. This further subdivision of the regimes of fracture shape will be the subject of future studies.

4.6 CONCLUSIONS

A simple model of tensile fracture propagation within the concentrated stress field produced at the bottomhole is developed. The calculated fracture trajectories resemble well the morphology of observed drilling induced petal, petal-centreline, and disking fractures. This agreement suggests that the shapes of the core fractures contain substantial information on the relative magnitudes of the in situ states of stress. The point at which the fracture initiates, whether at the core axis or near its outside boundary, is an additional piece of information. Further, there is a gradual, stress state dependent, evolution of the fracture morphology made apparent by the mapping of Figure 4.12 from petal fractures to petal-centreline fractures to disking fractures.

The modelling here also confirms field and laboratory observations related to the orientation of the drilling induced core fractures. The strike of the fractures is parallel to that for the greatest horizontal compression whereas the azimuth of the high points on petal and saddle-shaped disks indicates the direction of the least compressive horizontal principal stress.

The relationships between in situ faulting environments and core fracture shape are promising and indicate that the core fractures can provide important complementary qualitative information to more quantitative methods such as hydraulic fracturing and overcoring. The spacings of the core fractures are known to depend on stress magnitudes,

and detailed relationships between stress magnitudes and fracture spacings are possible when the applied stress conditions are known (Li and Schmitt, 1997b). However, carrying out this procedure for more complex shaped core fractures produced under anisotropic stress conditions and in consideration of the influence of geometry would be tedious; some type of interactive modelling of the core fractures in which the variety of controlling parameters can be rapidly changed and the resulting core fractures calculated would be useful in this regard and forms part of the basis for future work.

The above results, although in relatively good agreement with the limited observations, remain theoretical; both additional experimental tests and comparisons with field observations in light of these results are necessary.

4.7 BIBLIOGRAPHY

Anderson, E.M., *The Dynamics of Faulting and Dyke Formation With Applications to Britain*, 2nd ed., 206 pp., Oliver and Boyd, Edinburgh, 1951.

Atkinson, B. K. (Ed.), *Fracture Mechanics of Rock*, 534 pp., Academic Press, New York, 1987.

Bankwitz, P. and E. Bankwitz, Fractographic features on joints of KTB drill cores (Bavaria, Germany), in M. S. Ameen, ed., *Fractography: fracture topography as a tool in fracture mechanics and stress analysis*, Geological Society Special Publication, 92, 39-58, 1995.

Baumgärtner, J., F. Rummel, and M.D. Zoback, Hydraulic fracturing in situ stress measurements to 3 km depth in the KTB pilot hole VB, in Bram, K, J.K. Draxler, W. Kessels, and G.Zoth, eds. *KTB Report 90-6a*, 353-399, 1990.

Borm, G., C. Lempp, O. Natau, and T. Rockel, Instabilities of borehole and drillcores in crystalline rocks, with examples from the KTB pilot hole, *Scientific Drilling*, 1, 105-114, 1989.

Brudy, M., *Determination of in-situ stress magnitude and orientation to 9 km depth at the KTB site*, Ph.D. Dissertation, Univ. Karlsruhe, 196 pp., 1995.

Chang, P. S., *Determination of in-situ stress based on finite element modeling*, Ms. Thesis, 92 pp., The West Virginia University, 1978.

Durelli, A.J., L. Obert, and V.J. Parks, Stress required to initiate core disking, *Trans. Soc. Min. Eng.*, AIME, 241, 269-275, 1965.

Durham, W.B., Topographic measurement of disking fractures from the KTB pilot hole, depth 3606 m, in *KTB Report 93-2*, Emmermann, R., J. Lauterjung, and T. Umsonst, eds., 219-222, 1993.

Dyke, C.G., Core disking : Its potential as an indicator of principal in situ stress directions, *Rock at Great Depth*, Maury, V. and D. Fourmaintraux (eds.), 2, 1057-1064, 1989.

Engelder, T., *Stress regimes in the lithosphere*, Princeton University Press, 171-175, 1993.

GanRao, H.V., S.H. Advani, P. Chang, and S.C. Lee, In-Situ stress determination based on fracture responses associated with coring operation, *20th Symposium on Rock Mechanics*, The University of Texas at Austin, 683-691, 1979.

Griffith, A.A., The phenomena of rupture and flow in solids, *Phil. Trans. Roy. Soc.*, A221, 163-198, 1921.

Haimson, B.C, and M.Y. Lee, Borehole breakouts and core disking and their complementary roles as in situ stress indicators - an initial laboratory study, *EOS Trans.*, AGU 75, 677, 1994.

Haimson, B.C. & M.Y. Lee, Estimating deep in situ stresses from borehole breakouts and core disking- experimental results in granite, *Proceedings of the International Workshop on Rock Stress Measurement at Great Depth*, The 8th International Congress on Rock Mechanics, Balkema Publ., Tokyo, 3, in press, 1995.

Ingraffea, A.R., and F.E. Heuze, Finite element models for rock fracture mechanics, *Int. J. for Numerical and Analytical Methods on Geomech.*, 4, 25-43, 1980.

Ishida, T., and T. Saito, Observation of core discing and in situ stress measurements; stress criteria causing core discing, *Rock Mechanics and Rock Engineering*, 28 (3), 167-182, 1995.

Jaeger, J.C., and N.G.W. Cook, Pinching-Off and disking of rocks, *J. of Geophys. Res.*, 68, 1759-1765, 1963.

Kulander, B. R., C.C. Barton, and S.L. Dean, The application of fractography to core and outcrop investigation, *Thechnical report for U.S. Department of Energy*, Contract EY-77-Y-21-1321, METC/SP-79/3, 174 pp., 1979

Kulander, B. R., S.L. Dean, and B.J. Ward, *Fractured Core Analysis*, AAPG Methods in Exploration Sèries, 8, 88 pp., 1990.

Lawn, B.R., and T.R. Wilshaw, *Fracture of Brittle Solids*, 204 pp., Cambridge Univ. Press, 1975.

Leeman, E.R., The measurement of stress in rock-Part I, *Journal of the South African Institute of Mining and Metallurgy*, September, 76-80, 1964.

Li, Y.Y., and D.R. Schmitt, Wellbore bottom stress concentration and induced core fractures, *AAPG Bulletin* , in press, 1997a.

Li, Y.Y., and D.R. Schmitt, Influence of Poisson's ratio on bottomhole stress concentrations, *Int. J. Mech. Min. Sci. & Geomech. Abstr*, in press, 1997b.

Lorenz, J. C., J. F. Sharon, and N. R. Warpinski, Significance of coring-inducing fractures in Mesaverde core, Northwestern Colorado, *AAPG Bulletin*, 74, 1017-1029, 1990.

Maury, V., F.J. Santarelli, and J.P. Henry, Core disking: A review, *Sangorm Symposium, Rock Mechanics in Africa*, November, 221-231, 1988.

Miguez, R., J.P. Henry, and V. Maury, Le discage: une method indirecte d'evaluation des contraintes in-situ, *de Journal Universitaires de Geotechnique* - St - Nazaire-28-30 Janvier, 353-360, 1987.

Minguez, J.M., Strength theories in Fracture mechanics, *Engineering Fracture Mechanics*, 44, 335-340, 1993.

Natau, O., G. Borm, and Th. Rockel, Influence of lithology and geological structure on the stability of the KTB pilot hole, *Rock at Great Depth*, Maury, V. and D. Fourmaintraux (eds.), 3, 1487-1490, 1990.

Obert, L., and D.E. Stephenson, Stress conditions under which core disking occurs, *SME Transactions*, 232, September, 227-235, 1965.

Paillet, F.L. and K. Kim, Character and distribution of borehole breakouts and their relationship to in-situ stresses in deep Columbia River basalts, *J. of Geophys. Res.*, 92-B7, 6223-6234, 1987.

Panet, M., Quelques peoblemes de mecanique des roches poses par le tunnel du Mont-Blanc, *Annales de l'Institute Technoque du batiment et des travaux publics*, 264, 1968-1979, 1969.

Pendexter, C, and R.E. Rohn, Fractures induced during drilling, *JPT*, March, 15 &49, 1954.

Perreau, P.J., Tests of ASR, DSCA, and core disking analyses to evaluate in-situ stresses, *SPE* 17960, 325-336, 1989.

Röckel, Th., *Der Spannungsustand in der tieferen Erdkruste am Beispiel des KTB-Programms*, D.Ing Dissertation , Univ. Fridericiana zu Karlsruhe, 141 pp., 1995.

Röeckel, Th. and O. Natau, Estimation of the maximum horizontal stress magnitude from drilling induced fractures and centerline fractures at the KTB drill site, in Emmermann, R., J. Lauterjung, and T. Umsonst, eds., *KTB Report 93-2*, 203-209, 1993.

Schmitt, D.R. and M.D. Zoback, Diminished pore pressure in low porosity crystalline rock under tensional failure: apparent elastic dilatant strengthening, *J. Geophys. Res.*, 97, 273-288, 1992.

Schmitt, D.R. and M. D. Zoback, Infiltration effects in the tensile rupture of thin walled cylinders of glass and granite: Implications for the hydraulic fracturing breakdown equation, *Int. J. Rock Mech. Mining Sci. & Geomech. Abstr.*, 30, 289-303, 1993.

Shih, G.C., *Methods of Analysis and Solution of Crack Problems*, Noordhoff International Pub., Leyden, 1, XXIII-XLIV, 1973.

Song, I., and B.C. Haimson, Core disking in Westerley granite as a potential indicator of tectonic stress - A laboratory study, *EOS Trans.*, AGU, 77, F694, 1996.

Stacey, T.R., Contribution to the mechanics of core disking, *Journal of the South African Institute of Mining and Metallurgy*, September, 269-275, 1982.

Stacey, T.R, and N.D. Harte, Deep level raise boring - Prediciotn of rock problems, *Rock at Great Depth*, Maury, V. and D. Fourmaintraux (eds.), 2, 583-589, 1989.

Sugawara, K., Y. Kameoka, T. Saito, Y. Oka, and Y. Hiramatsu, A study on core disking of rock, *Journal of Japanese Association of Mining*, 94, 19-25, 1978.

Tapponier, P., and W.F. Brace, Development of stress-induced microcracks in Westerly granite, *Int. J. Rock Mech. Mining. Sci. & Geomech. Abstr.*, 13, 103-112, 1976.

Zhu, W., G. Li, and K. Wang, Analysis of disking phenomenon and stress field in the region of an underground powerhouse, *Rock Mechanics and Rock Engineering*, 18, 1-15, 1985.

Table 4.1. Field and experimental data of coring induced fractures

Source of Data	Rock Type	S_H (MPa)	S_h (MPa)	S_v (MPa)	S_h/S_H	S_v/S_H	Type of Fracture
Obert and Stephenson (1965)	Geogia granite	66.5~137.9	66.5~137.9	0~82.0	1.0	0~0.59	Core disking fracture
	Nova Scotia sandstone	57.8~106.8	57.8~106.8	0~82.0	1.0	0~0.77	
	Vermont marble	55.1~ 68.9	55.1~ 68.9	0~20.7	1.0	0~0.30	
	Indiana limestone	41.4~ 68.9	41.1~ 68.9	0~41.1	1.0	0~0.60	
	Maryland marble	89.6~137.9	89.6~137.9	0~68.9	1.0	0~0.50	
Jaeger and Cook (1963)	Rand quartzite	120.0	120.0	0.0	1.0	0.0	Core disking fracture
	Wombeyan marble	48.0	48.0	0.0	1.0	0.0	
	Dolerite	110	110	0.0	1.0	0.0	
Haimson and Lee (1995)	Lac du Bonnet granite	92.5~231.2	20.0~50.0	25.0~60.0	0.10~0.54	0.10~0.65	Core disking fracture
Brudy (1995)	KTB pilot hole (805 m ~ 3011 m)	25.0 ~ 48.7	49.4 ~ 98.7	22.5 ~ 84.3	0.49 ~ 0.51	0.46 ~ 0.93	Core disking fracture
Röeckel and Natau (1993)	KTB pilot hole (3582 m)	102.4	48.8	102.0	0.48	0.99	Core disking fracture
Paillet and Kim (1987)	Borehole DC-4: basalts	59.9	30.8	24.4	0.51	0.41	Core disking fracture
	Borehole DC-12: basalts	61.2±6.8	34.8±2.7	26.2±0.4	0.56±0.10	0.43±0.03	
	Borehole RLL-2: basalts	60.6±5.3	34.5±2.7	26.3±3.1	0.57±0.08	0.43±0.07	
	Borehole RLL-6: basalts	61.6±5.4	33.0±2.4	27.8±1.9	0.54±0.08	0.45±0.05	

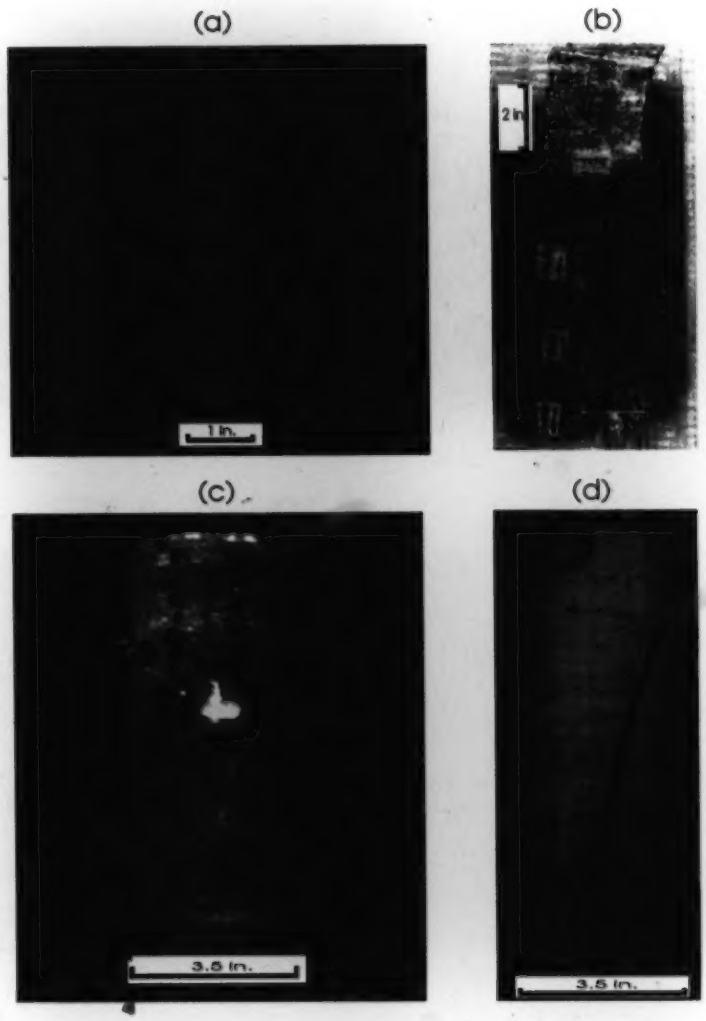

Figure 4.1. Examples of drilling induced core fractures. a) Cup shaped core disks (after Obert and Stephenson, 1965), b) saddle shaped core disks (after Borm et al., 1989), c) petal fractures, and d) petal-centerline fracture (after Pendenter and Rohn, 1954).

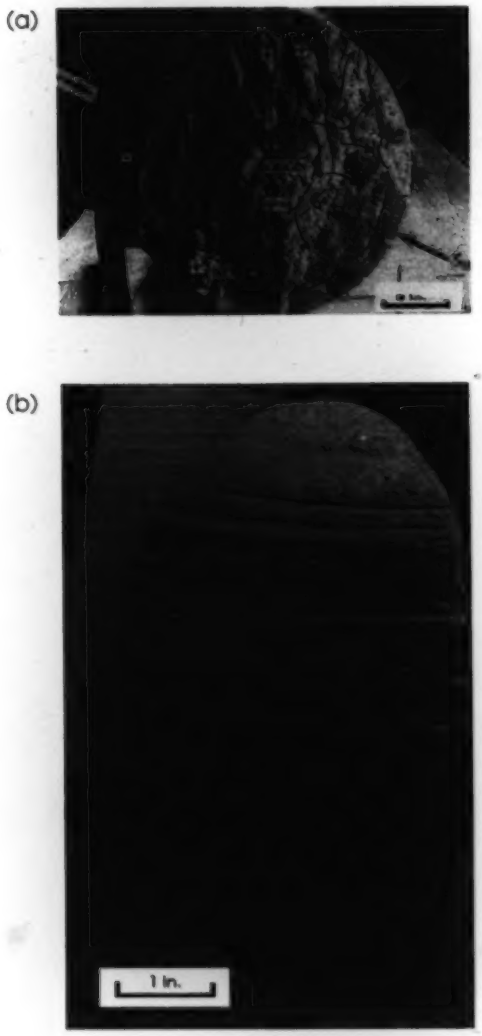

Figure 4.2. Fractographic features of a) a fracture initiating at the center of a core (after Bankwitz and Bankwitz, 1995) and b) a petal fracture surface (after Kulander et al., 1990).

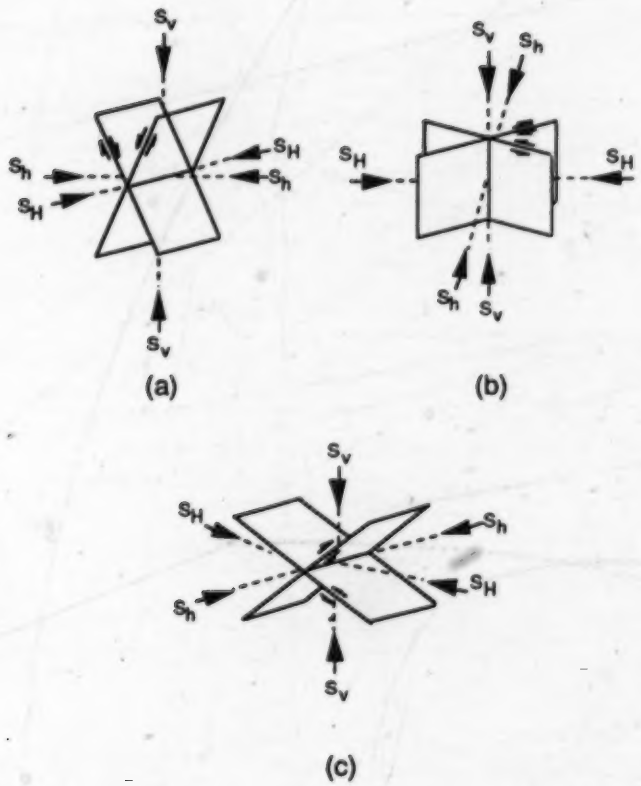

Figure 4.3. Faulting environments as characterized by Anderson (1951): a) the normal fault stress regime ($S_v > S_H > S_h$), b) the strike-slip fault stress regime ($S_H > S_v > S_h$), and c) the thrust fault stress regime ($S_H > S_h > S_v$).

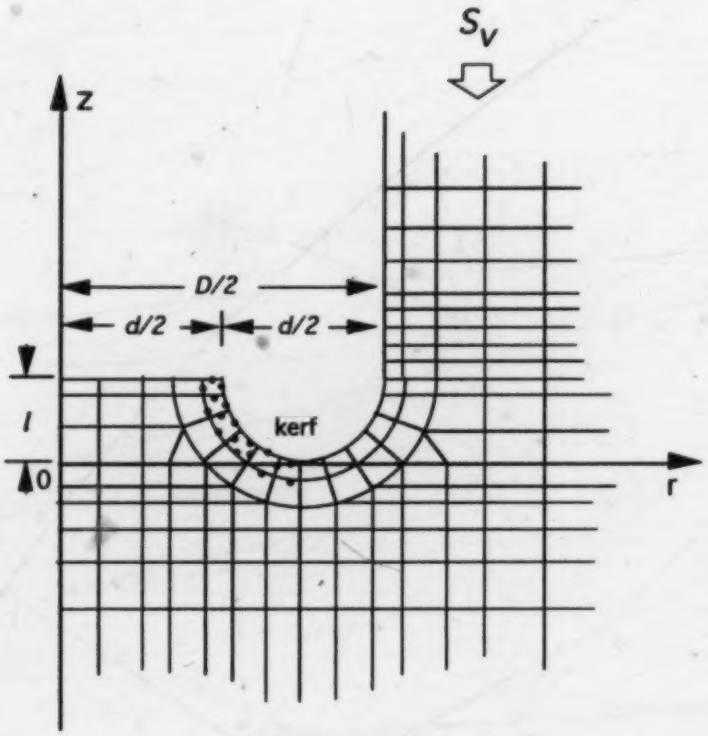

Figure 4.4. Details of finite element mesh in the vicinity of the bottomhole.

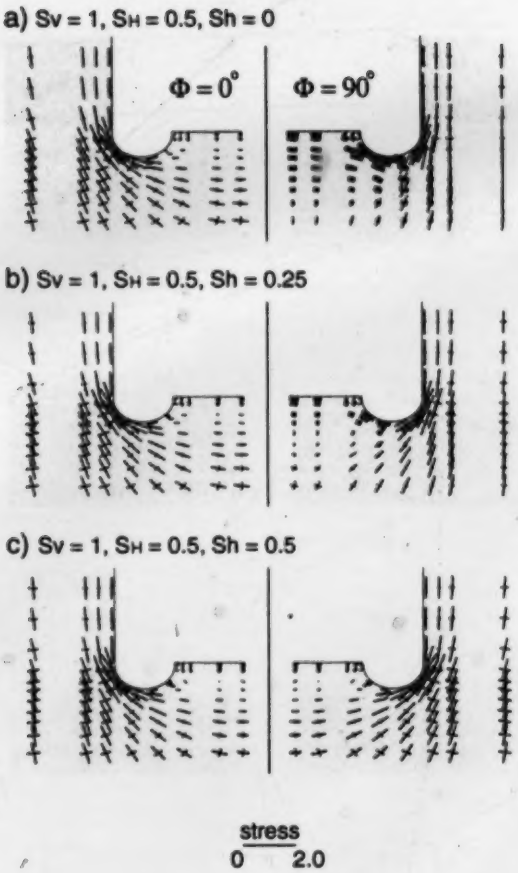

Figure 4.5. Orientations of local principal stresses in the normal fault stress regime with $S_v = 1$, $S_H = 0.5$ and a) $S_h = 0.0$, b) Sh = 0.25 and c) Sh = 0.5.

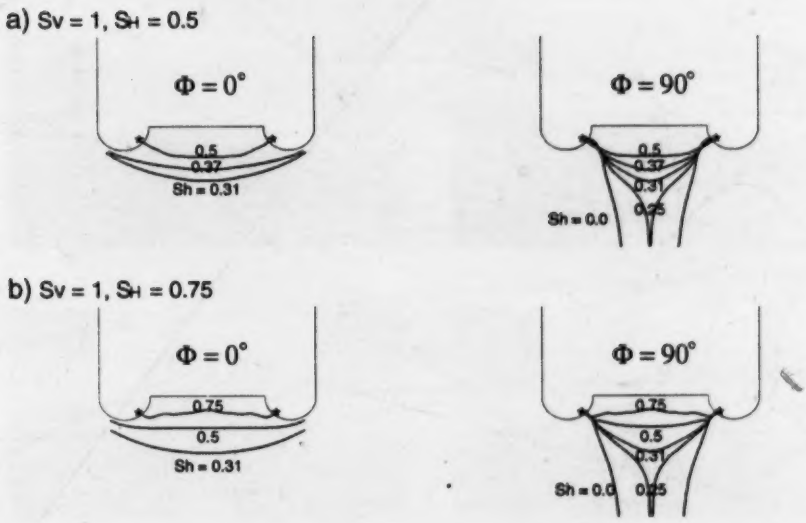

Figure 4.6. a) Predicted fracture trajectories in the normal fault stress regime with S_v = 1, S_H = 0.5, and $0.0 \leq S_h \leq 0.5$ within planes at $\Phi = 0°$ and 90°, and b) with $S_v = 1$, S_H = 0.75, and $0.0 \leq S_h \leq 0.75$ within planes at $\Phi = 0°$ and 90°.

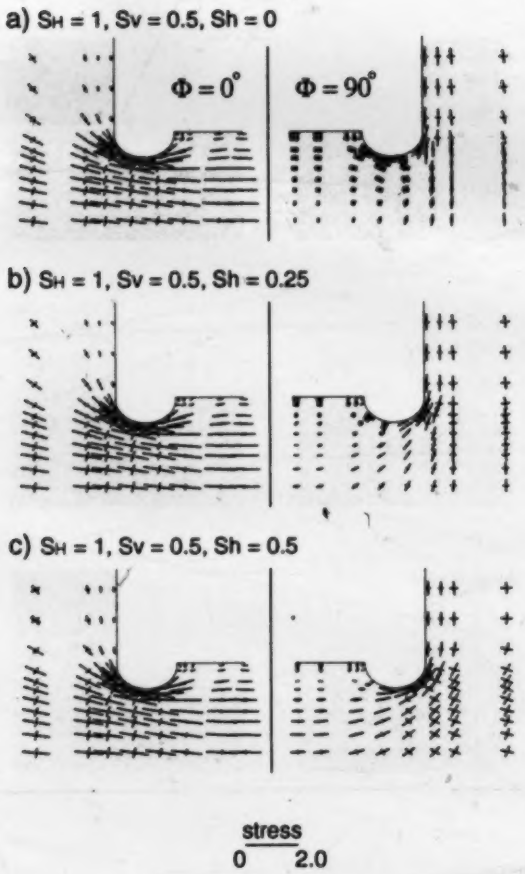

Figure 4.7. Orientations of local principal stresses in the strike-slip fault stress regime with $S_H = 1$, $S_v = 0.5$, and a) $S_h = 0.0$, b) Sh = 0.25 and c) Sh = 0.5.

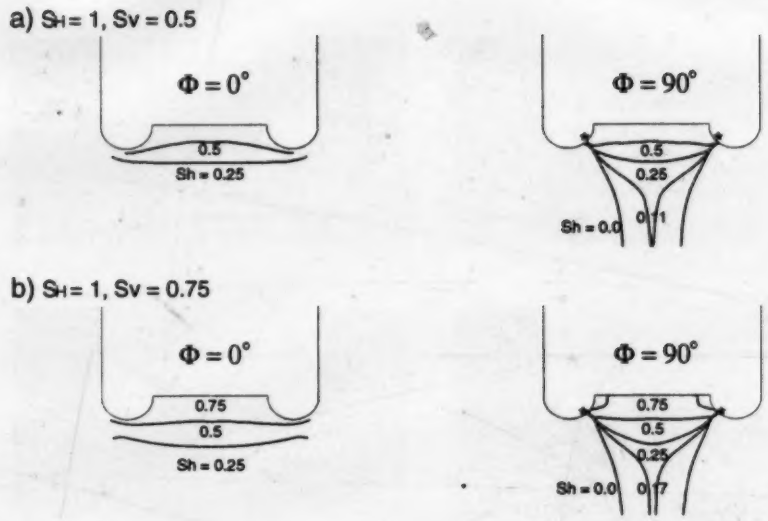

Figure 4.8. a) Predicted fracture trajectories in the strike-slip fault stress regime with S_H = 1, S_v = 0.5, and $0.0 \leq S_h \leq 0.5$ at $\Phi = 0°$ and 90°, and b) with S_H = 1, S_v = 0.75, and $0.0 \leq S_h \leq 0.75$ at $\Phi = 0°$ and 90°

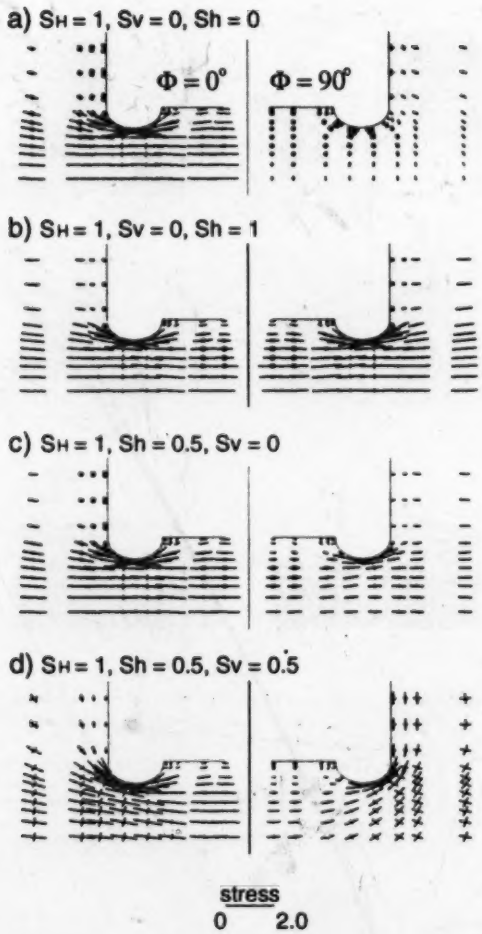

Figure 4.9. Orientations of local principal stresses in the thrust fault stress regime for S_H = 1, S_v = 0 with a) S_h = 0 and b) S_h = 1, and for S_h = 0.5 with c) S_v = 0 and d) Sv = 0.5.

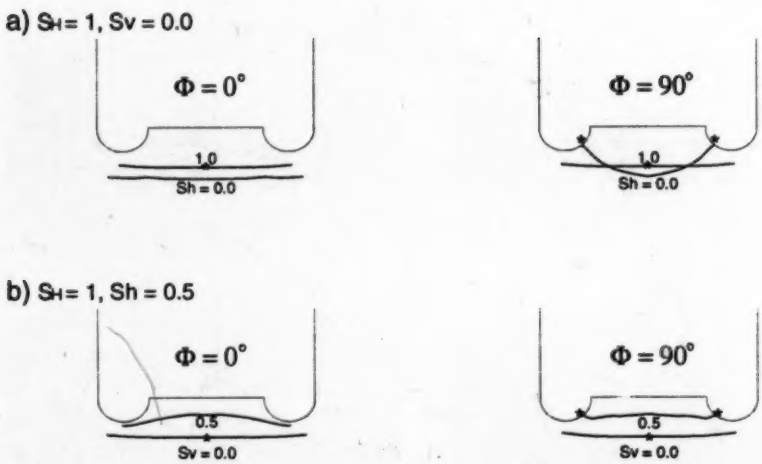

Figure 4.10. a) Predicted fracture trajectories in the thrust fault stress regime for $S_H = 1$, $S_v = 0$, and with $S_h = 0.0$ and 1.0 at $\Phi = 0°$ and 90°, and b) for $S_H = 1$, $S_h = 0.5$, with $S_v = 0.0$ and 0.5 at $\Phi = 0°$ and 90°.

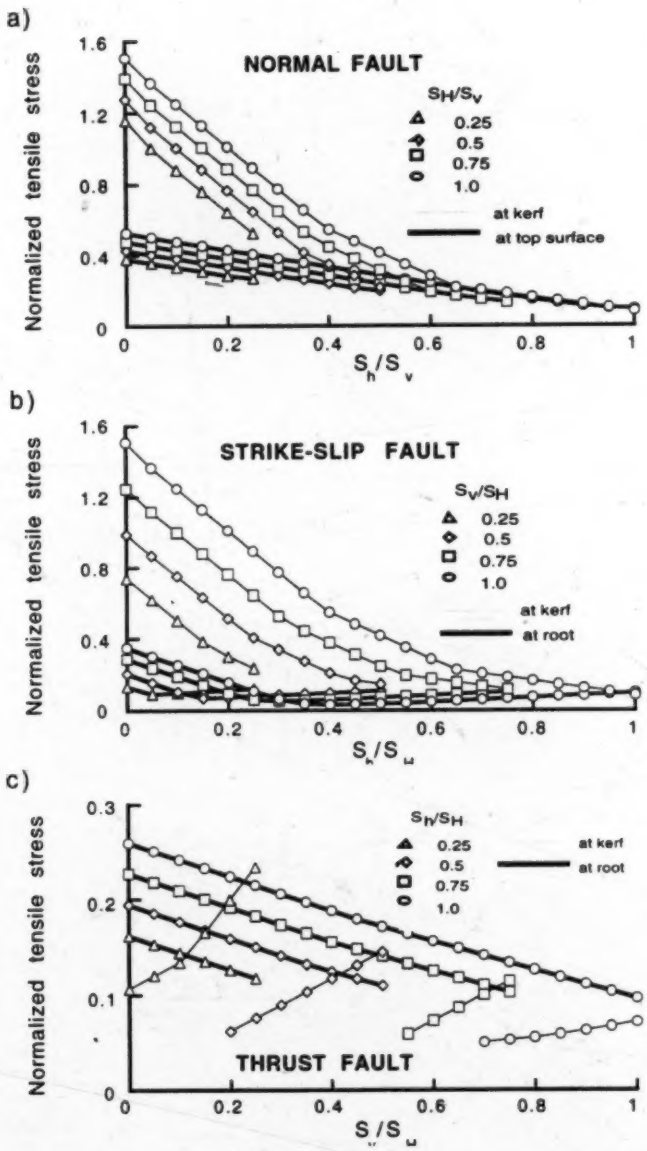

Figure 4.11. The greatest tensile stresses at the inner kerf area, the root and the top of core stub in a) the normal fault stress regime, b) the strike-slip fault stress regime and c) the thrust fault stress regime.

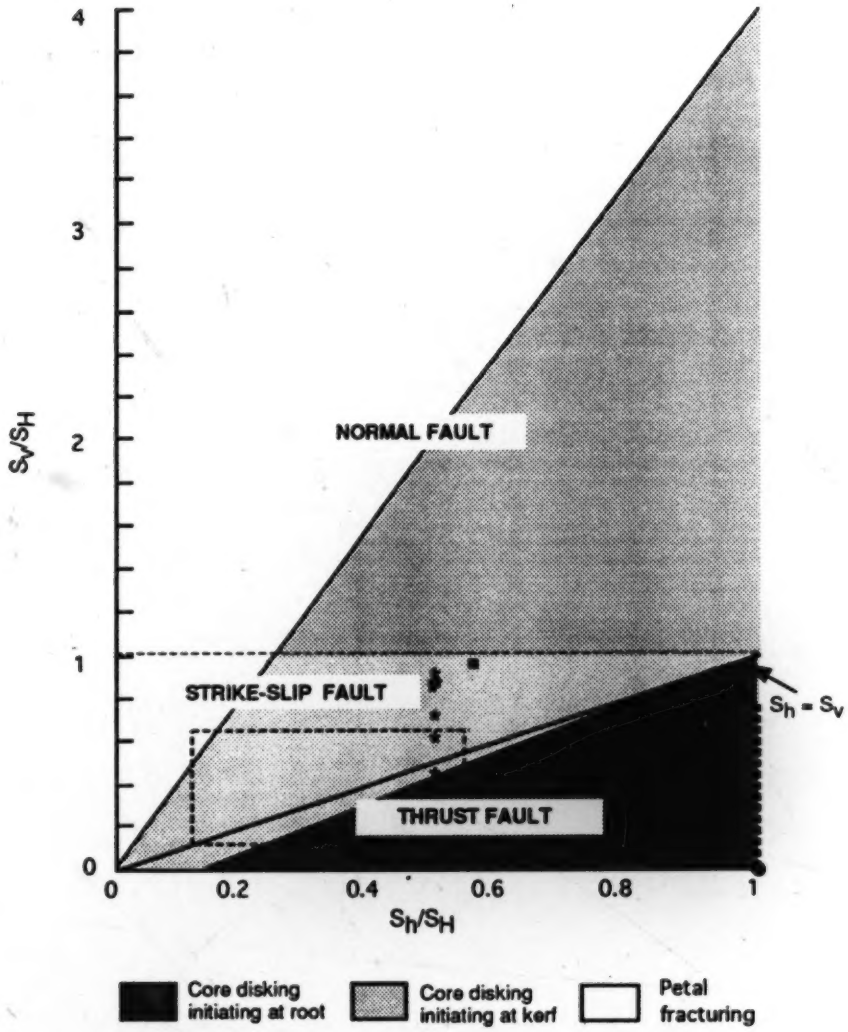

Figure 4.12. The relationship between coring induced fractures and in situ stresses. Thick dash line, solid circle and rectangular area formed by thin dash line represent the laboratory experimental data of core disking fractures from Jaeger and Cook (1963), Obert and Stephenson (1965), and Haimson and Lee (1995), respectively; Cross signs, solid square, asterisks represent the field data of core disking fractures from Paillet and Kim (1987), Röeckel and Natau (1991), and Brudy (1995), respectively.

CHAPTER 5

CONCLUSIONS AND FUTURE DIRECTIONS

5.1 CONCLUSIONS

In the preceding chapter, drilling-induced fractures were investigated from theoretical and practical perspectives. Three major topics related to drilling induced fractures and one topic related to microcrack damage in core were discussed: specifically these are concerned with the general characteristics of stress concentrations at the bottomhole, the determination of absolute magnitudes of in situ stresses for a special case, the determination of relative magnitudes of in situ stresses in various stress regimes, and the determination of the microcrack tensor in cores. It can be seen that although these topics were presented in an independent fashion, they are all related to the stress concentrations at the bottomhole or to the release of in situ stresses in rock.

In general, this investigation demonstrates that highly concentrated stresses exist at the bottomhole. These stresses may affect rock strength and consequently the drilling rate, wellbore stability, and the physical properties of core due to induced fractures and microcracks. Another important finding is that high tensions are produced in the vicinity of the bottomhole and their directions and distributions are in very good agreement with the observed morphologies of drilling induced fractures. Core stub length has a significant influence on the bottomhole stress concentrations and indicates that the uniform spacing of drilling induced fractures is controlled by rock strength and the magnitude of the in situ stresses. Drilling induced fractures may thus be used, in principal, to determine the magnitudes of in situ stresses although in practical terms this may not be so straightforward.

The analysis of the bottomhole stress concentrations under various stress conditions suggests that coring induced fractures result in tension because of the agreement between

the distribution of tensile stresses and the observed morphologies of the coring induced fractures. Uniaxial and biaxial horizontal stress states may produce saddle- and cup-shaped disk fractures, respectively. Drill bit weight and wellbore fluid pressure may aid in the initiation of coring induced fractures but place the interior of the core largely in compression and would not be expected to contribute to continued tensile fracture propagation. In addition, centerline fracturing may be produced for a short core stub under a high overburden.

Study of the bottomhole stress concentrations indicates that core disking, petal, petal-centerline, and centerline fractures are inherently related and are controlled by in situ stress conditions. The high tensile stress levels existing on the core surface or within the core suggests that if macroscopic fractures are not seen, subcritical microcracks may still be generated. The existence of this microscopic damage needs to be considered as a potentially important influence on what has broadly been characterized as stress relief phenomena. Indisputable evidence for this 'stress relief' includes the acoustic emissions and apparent viscoelastic strains observed in cores immediately upon removal from the earth and the elastic anisotropy in ultrasonic velocities and strain seen in laboratory experiments. How such damage within the cores superposes with other stress relief effects to produce a final observable signal is a topic in need of further investigation.

The relations among core disking fractures, rock physical properties, and in situ stress magnitudes for a special case with radial compression applied perpendicular to the wellbore axis and a compression directed parallel to the wellbore axis based on the core disking experiments conducted by Obert and Stephenson (1965) were developed. Hypothetical incipient failure curves derived from the modeling are in good agreement with early experimental results and further suggest that coring-induced fractures result from tensional failure. A Mohr-Coulomb shear mechanism could not explain the experimental observations. The length of the core stub influences the magnitudes of the concentrated stresses with tensions increasing to a maximum for 1/5 to l/4 of the core diameter. This is

consistent with the experimental results in which the core disks have the thickness of 1/5 to 1/4 of the core diameter.

Further, hypothetical relations between the thickness of core disks and the magnitudes of in situ stresses were developed. The applied radial stress is inversely proportional to the core disk thickness with an assumed rock tensional strength. The requirement for tensional failure increases dramatically for the core stub lengths shorter than 1/10 of the core diameter. This suggests that thinner core disks are less sensitive to the change of stress conditions but are a good indication of high stress magnitudes.

Poisson's ratio influences core disking substantially. The concentrated tensions are diminished with larger values of Poisson's ratio. Core disks are more easily produced in rocks with low values of Poisson's ratio. This suggests that the appearance of a core disk fracture may also indicate changes in rock properties under an otherwise uniform stress state along the wellbore. The developed relationship between the thickness of core disks, the magnitude of in situ stresses, and Poisson's ratio could be used to predict the magnitudes of in situ stresses

The relation between the morphologies of drilling induced fractures and in situ stresses was developed in a thorough investigation based on the Andersonian stress regime classifications. The calculated morphologies are in good agreement with those observed. There is a gradual, stress-state dependent evolution of fracture morphology from petal fractures to disking fractures. The modeling confirmed field observations that the strikes of petal and petal-centerline fractures align with the greatest horizontal compression and that the high points on saddle-shaped disking fractures indicate the direction of the least horizontal stress. Observed drilling induced fractures are in very good agreement with the shapes predicted here and we await future experimental tests.

The modeling here also suggests that the point of fracture initiation is an additional useful piece of information. In nearly all faulting regimes the core fractures will initiate near the bit cut except for most thrust faulting stress conditions where the fractures initiate

on the core axis. Further, under thrust faulting conditions only disking fractures appear possible. Both petal and disking fractures can be produced in strike-slip and normal faulting regimes depending upon the relative magnitudes between the least horizontal compressive stress and overburden. The relation of morphology of the drilling induced fractures to in situ stresses suggests that they may be used as independent and complementary indicators in identifying stress regimes.

The influence of the cut geometry on bottomhole stress concentrations were studied and the relations of core stub length against the greatest tensile stresses developed (Appendix 2). It indicates that the curved cut reduces stress concentration near the cutting surface substantially. The peak magnitudes of the greatest tensile stresses on the cutting surface is reduced nearly 100% relative to that for a flat cut. However, a reverse effect exists at the root of core stub where relatively minor changes of about 7 to 10% are seen. The change in geometry due to the relative widths of the cut to the core diameter has only a relatively small effect. On the cutting surface, small cut width generates high tension under in situ stress conditions but less tension under the weight of drill bit and the wellbore fluid pressure. In addition, a large cut width generates higher tension at the root of core stub. These results suggests that the cut geometry and especially the cut shape should not be ignored in analyzing the phenomena related to bottomhole stress concentrations.

The modeling method and finite element programs for studying stress concentrations in inclined borehole are developed. Preliminary calculations (Appendix 3) show that in general an inclined borehole results in asymmetry in the stress concentrations. The results indicate that the stress concentrations at the end of borehole differ significantly from those of a vertical borehole. It also suggests that the shear forces generate high tension at the bottomhole.

In addition, a high-pressure technique for determining the microcrack porosities in a core was developed (Appendix 1). This technique adapted the commonly known differential strain method to more correctly account for the fact that microcrack and mineral

compressibilities are nearly of the same order of magnitude; the component of the total strains due to mineral compression is removed to provide a better understanding of the microcrack distributions within the sample. In the 'tight' dolomitic rock studied, the microcrack porosity is substantial proportion of the total rock porosity, such microcrack porosity probably does not exist in situ and as a result estimates of porosity can be biased upwards by this damage.

5.2. FUTURE DIRECTIONS

5.2.1 Application in the Western Canadian Basin

The most important contributions to the description of in situ stress field in the Western Canadian Sedimentary Basin and the Alberta Basement have been given by Bell and Gough (1979), Gough and Bell (1981), and Bell and Babcock (1986) in the study of borehole breakouts. A recent summary of the studies of in situ stresses in the Western Canadian Sedimentary Basin has been published by Bell et al. (1994). These studies established a foundation for understanding the characteristics and the tectonic origin of the stress field in the Western Canadian Basin. The in situ stress field is basically characterized by a northeast -southwest compression which is considered either to result from mantle drag on the base of lithosphere by lithosphere sliding southwestward across the asthenosphere (Zoback and Zoback, 1980) or by northeastward sublithospheric mantle flow (Gough, 1984). A major, but to date unfullfilled, motivation for the work described in the body of the thesis was to study the stress states in the Alberta Basement using the existing basement cores. Time constraints did not allow for the resolution of this issue but it remains a priority for future work.

To date, the estimation of the in situ stress orientations and magnitudes in the Western Canadian Basin are mainly from the study of borehole breakouts (Bell and Gough, 1979; Gough and Bell, 1981; and Bell and Babcock, 1986) and hydraulic fractures (e.g., Wyman et al., 1980; Kry and Gronseth, 1983; McLellan, 1988; Talebi, et al., 1991;

McLellan et al., 1992). The data are limited, especially as regards the magnitudes of the in situ stresses. Only about 100 sets of magnitudes and 200 sets of orientations have been published (Bell et al., 1994). Even though the orientations of in situ stresses have been better covered, the lack of magnitude information results in difficulties in determining the stress regime and the stress variations (Bell et al, 1994) although this information is considered crucial in petroleum production. Consequently, more data especially the magnitudes are required in order to better understand the in situ stress regime in the Western Canadian Basin and Alberta basement, and to more efficiently enhance the production of oil and gas.

The information about in situ stresses contained in drilling induced core fractures has been largely ignored for lack of an interpretive framework. No estimate of in situ stresses from drilling induced fractures has been used in the analysis of the regional stress field (Adams and Bell, 1991; Zoback, 1992; and Bell et al., 1994, and Coblentz and Richardson, 1996). However, large numbers of cores retrieved from the Western Canadian Sedimentary Basin have a great potential to improve present knowledge about the stress field in this region. The low cost and on site information would be greatly beneficial to the petroleum industry.

5.2.2 Application to Inclined Boreholes

Inclined wells and directional drilling are becoming more and more common in the petroleum and other industries (Cooper, 1994). Along an inclined borehole, one of the principal far-field stress is generally no longer parallel to the borehole axis. The relationship between in situ stress field and the orientation of a long borehole is described by Equation 1.4. Because the inclined borehole has a new relation to the far-field stresses, different bottomhole stress concentrations are expected. A set of core disks given by Maury and Henry (1988) shows that the uniformly spaced core disks with relatively flat fractures surfaces have angles of 65 to 70° degrees to the core axis. This may indicate the

principal far-field stress may not be aligned with the borehole axis in this case. In addition to the application in analyzing drilling induced fractures, such information is also important in tunneling. Some researchers have realized the importance of the bottomhole stress concentrations for an inclined borehole but either gave no solution (Hocking, 1976) or only presented a limited result (Dyke, 1989). The preliminary modeling in this thesis suggests that the study of bottomhole stress concentrations of an inclined borehole may greatly improve the understanding in analyses of drilling induced damages, well bore stability, and the interaction between drilling and rock.

5.2.3 Application in Analysis of Wellbore Stability

Although this topic was to some degree avoided here, the stress concentrations at the bottomhole should also result in damage to the wellbore wall. All present analyses of these phenomena inherently assume that the wellbores exist within the rock mass and employ the equations reviewed in Chapter 1; in reality, however, the borehole must be drilled and the bottomhole must pass each point along the wellbore in this process. As a result it is important to determine how this might influence our interpretation of wellbore wall damage phenomena.

High shear stresses and high tension near the wellbore wall under certain stress conditions have been observed in this research. The studies on the influence of bottomhole stress concentrations may add valuable information to the analyses of wellbore stability and well-logging data. A future project will be to mine the existing data set for further information in this direction.

5.2.4 Application in Analysis of Drilling Rate

The decline of the rate of penetration (ROP) as the fluid pressure (hydrostatic head of the fluid column) or the well depth increases is an important phenomenon in drilling operations. This is often attributed to the increase of differential pressure (the differential

between the formation pore pressure and the hydrostatic pressure of the mud column) (Murray, 1955; Cunningham and Eenink, 1959; Garnier and Lingen, 1959; Rowley et al., 1961; Eckel, 1963; Vidrine and Benit, 1969; and Anderson and Azar, 1993). The explanation of the mechanism, however, is still not satisfactory. One of the reasons is that the existing photoelastic stress analyses (Deily and Durelli, 1958; Galle and Wilhoit, 1963) and finite element modeling (Warren and Smith, 1985) did not supply complete information of the stresses at the bottomhole. This includes the orientations of the stresses and the behaviour of the stress with a continuous increase of wellbore fluid pressure. A study of the relation between rock strength and bottomhole stress concentrations under in situ state of stresses and wellbore fluid pressure definitely would be beneficial to drilling engineering and is an additional work in progress leading from this thesis.

5.3 BIBLIOGRAPHY

Adams, J., and J.S. Bell, Crustal stresses in Canada, in Slemmons, D.B., E.R., Engdahl, M.D. Zoback, and D.D. Blackwell, eds., Neotectonics of North America, Decade Map, *Geological Society of America*, **1**, p. 367-386, 1991.

Anderson, E.E., and J.J. Azar, PDC-Bit performance under simulated borehole conditions, *SPE Drilling and Completion*, (Sept. 1993) 185-189.

Bell, J.S., and D.I. Gough, Northeast-Southwest compressive stress in Alberta: evidence from oil wells, *Earth and planetary Science Letters*, **45**, p. 475-482, 1979.

Bell, J.S., and E.A. Babcock, The stress regime of the Western Canadian Basin and implications for hydrocarbon production, *Bulletin of Canadian Petroleum Geology*, **34**, p. 364-378, 1986.

Bell, J.S., P.R. Price, and P.J. McLellan, In-situ stress in the Western Canada Sedimentary Basin, Geological Atlas of the Western Canada Sedimentary Basin, Canadian Society of Petroleum Geologists and Alberta Research Council, p. 439-446, 1994.

Coblentz, D.D., and R.M. Richardson, Analysis of the South American interplate stress field, *J. Geophys. Res.*, **101**, p. 8643-8657, 1996.

Cooper, G., Directional drilling, *Scientific American*, May, p. 82-87, 1994.

Cunningham, R.A., and J.G. Eenink, Laboratory study of effect of overburden, formation and mud column pressure on drilling rate of permeable formations, *J. Pet. Tech.*, Jan. 1959, *Trans.*, **216**, p. 9-15, 1959

Deily, F.H., and A.J. Durelli, Bottom-Hole stresses in a well bore, *SPE* 1095-G, 26 p., 1958.

Dyke, C.G., Core disking: its potential as an indicator of principal in-situ stress directions, *in* V. Maury, and D. Fourmaintraux eds., Rock at Great Depth: Balkema, Rotterdam, **2**, p. 1057-1064, 1989.

Eckel, J.R., Effect of pressure on rock drillability, *Petroleum Drilling*, Reprint Series, SPE, Rechardson, TX, **6**, p. 55-60, 1963

Galle, E.M., and J.C. Jr. Wilhoit, Stresses around a wellbore due to internal pressure and unequal principal geostatic stresses, *Drilling*, Reprint Series, SPE, Rechardson, TX, **6**, 12-22, 1963

Garnier, A.J., and N.H. van Lingen, Phenomena affecting drilling rates at depth, *J. Pet. Tech.*, Sept., *Trans.*, AIME, **217**, p. 232-239, 1959.

Gough, D.I., and J.S. Bell, Stress orientations from oil-well fractures in Alberta and Texas, *Can. J. Earth Sci.*, **18**, p. 639-645, 1981.

Gough, D.I., Mantle upflow under North America and plate dynamics, *Nature*, **311**, p. 428-433, 1984.

Hocking, G, Three-Dimensional elastic stress distribution around the flat end of a cylindrical cavity, *Int. J. Rock Mech. Min. Sci. & Geomech. Abstr.*, **13**, p. 331-337, 1976.

Kry, P.R., and J.M. Gronseth, In-situ stresses and hydraulic fracturing in the Deep Basin, *Journal of Canadian Petroleum Technology*, Nov.-Dec., p. 31-36, 1983.

Maury, V., F.J. Santarelli, and J.P. Henry, Core discing: a review, Sangorm Symposium: Rock Mechanics in Africa, Nov. p. 221-231, 1988.

McLellan P.J., K. Lawrence, and K. Cormier, 1992, A multiple zone acid stimulation treatment of a horizontal well. Midale, Saskatchewen, *Journal of Canadian Petroleum Technology*, **31**, no. 4, p. 71-82, 1992.

McLellan, P.J., In-situ stress prediction and measurement by hydraulic fracturing, Wapiti, Alberta, *Journal of Canadian Petroleum Technology*, 27, no. 2, p. 85-95, 1988.

Murray, A.S., Effect of mud column pressure on drilling rates, *J. Pet. Tech.*, Nov., *Trans.*, AIME, **204**, p. 232-239, 1955.

Obert, L., and D.E. Stephenson, Stress conditions under which core disking occurs, *SME Trans.*, **232**, p. 227-235, 1965.

Rowley, D.S., R.J. Howe, and F.H. Deily, Laboratory drilling performance of the full-scale rock bit, *J. Pet. Tech., Trans.*, AIME, Jan., **222**, p. 71-81, 1961.

Talebi, S., P.R. Young, L. Vandamme, and W.J. McGanghey, 1991, Microseismic mapping of a hydraulic fracture, In: Rock Mechanics as a Multidisciplinary Science, J.C. Roegiers ed., A.A. Balkema, Rotterdam, p.461-470, 1991.

Vidrine, D.J., and E.J. Benit,, Field variation of the effect of differential pressure on

drilling rate, *J. Pet. Tech.*, p. 676-682, 1969.

Warren, T.M., and M.B. Smith, Bottomhole stress factors affecting drilling rate at depth, *J. Pet. Tech.*, p. 1523-1533, 1985.

Wyman, R.E., S.A. Holdich, and P.L. Randolph, Analysis of an Elmworth hydraulic fracture in Alberta, *J. of Petro. Tech.*, **32**, p. 1621-1630, 1980.

Zoback, M.L., First- and secondary-order Patterns of stress in the lithosphere: the world stress map project, *J. Geophys. Res.*, **97**, p. 11703-11728, 1992.

Zoback, M.L., and M.D. Zoback, State of stress in the counterminous United States, *J. Geophys. Res.*, **85**, p. 6113-6156, 1980.

APPENDIX 1

A High-Pressure Technique For Determining The Microcrack Porosities of Damaged Brittle Materials

1.1 INTRODUCTION

Microcracks are produced in many polycrystalline brittle materials that have been damaged but have not completely failed (Simmons and Richter, 1974). They are defined as small crack-like voids with lengths typically on the order of 100 μm or less and aspect ratios (greatest aperture/length) less than 10^{-2}. They are most evident in shear failure of an initially intact material where the final failure surface, as evident from theoretical and acoustic emission studies, is the locus of numerous smaller microcracks linking together (Tapponier and Brace, 1976; Nemat-Nasser and Horii, 1982). In other materials, consisting of grains of two or more solid phases, microcracks may be produced by thermal stresses arising form differential thermal expansion of the minerals (Nur and Simmons, 1970). Stress-relief dilation in rocks emulates a viscoelastic process and appears to depend on the production of microcrack porosity in materials suddenly released from long-standing stress states (Voight, 1968; Teufel and Warpinski, 1984). Solids subject to lower pressure shock-loading conditions also display microcrack structures (Ahrens and Rubin, 1995). As a result the density and orientation of microcracks within a brittle material are indicative of the conditions the material was subject to during deformation.

The actual microcrack porosity of damaged materials is usually small typically being less than 1% of the total volume occupied by the medium. The microcracks are important,

---

A version of this chapter has been published, December, 1995, Canadian Journal of Physics, 73, 330- 337.

however, because they control many of the physical characteristics of the material at low confining pressures. For example, the strength of a microcrack-damaged material can be far less than that prior to deformation (He and Ahrens, 1994). Further, since the microcracks are easily compressed normal to their plane they can greatly influence both the velocity and attenuation of longitudinal and shear elastic waves that pass through them (O'Connell and Budiansky, 1974). If the microcracks are not randomly oriented within the material then there are both a directional dependence of the longitudinal wave velocity and a birefringence of the shear waves into fast and slow polarizations (Crampin, 1981). The intrinsic fluid permeabilities and electrical conductivity of some of these materials are effectively entirely dependent on the connectedness of the network of microcracks within, as these serve as pathways for conductive fluids or compounds (Walsh and Brace, 1984; Lockner et al., 1991) A final, but important, point to note here is that all of these properties are generally nonlinear functions of the confining pressure, the application of which changes the effective microcrack density due to the progressive closure of cracks at increasing pressures (Adams and Williamson, 1923; Brace, 1965). This is additionally complicated if a pressure exists within these pores that will further affect the property measured; indeed, these physical properties may be considered as state variables, which are functions of both the confining and pore pressures (Coyner, 1984).

Despite the fact that microcrack porosity is often the dominant factor controlling many of the above properties in damaged brittle materials and evaluating it has useful applications, it is difficult to quantify. This is because the microcrack porosities are usually of magnitudes similar to the accuracy of common porosity-measurement techniques, which require, for example, comparisons of mass differences between a known volume of a sample both dry and fully saturated with a liquid of a known density. To overcome these difficulties, highly sensitive strain-measuring techniques are used (Brace, 1965; Simmons and Richter, 1974; and Siegfried and Simmons, 1978). These techniques are often referred to as differential strain analysis or differential strain curve analysis (Strickland and Ren,

1980; Ren and Rogiers, 1983). In this appendix a modification to the analysis of strain data that accounts for the intrinsic mineral compressibilities is applied to measurements made on a dolomite-bearing rock sample damaged during coring operations. In particular, the technique allows determination of a complete microcrack strain tensor as a function of the hydrostatic confining pressure. At high pressures this tensor provides sufficient information to calculate that portion of the crack-related porosity that has closed at a given pressure. In the present study, knowledge of the microcrack porosity is important from the perspective of the petroleum explorationist who is concerned with determining that fraction of the porosity which resulted fromthe coring of the rock and which did not exist within the earth.

This appendix is primarily to describe the present experimental technique and the analysis procedures used in the crack-strain measurements. It concludes with a discussion of such strain observations with regards to the porosity structure and the source of damage in a rock sample studied. In particular, the observations of crack porosity are not in agreement with that expected if the crack porosity resulted solely from stress relief against the principal stresses that are aligned with the vertical and horizontal directions.

1.2 THEORETICAL BASIS

The theoretical bases of the microcrack measurements has been previously described (Siegfried and Simmons, 1978) and only a brief, phenomenological explanation is given here. The hypothetical linear or volumetric strain response with increasing confining pressure for a strain gauge mounted on the surface of the cracked material is shown in Figure A1.1a. Note that this curve is produced by application of a hydrostatic pressure to the external surface of the brittle material only if no traction or pressures act on any of the internal pore-well surfaces. This state is often referred to as either jacketed (Biot and Willis, 1957) or drained conditions (Jaeger and Cook, 1979). Siegfreid and Simmons (1978) point out that this observed linear strain ε_k is a superposition of the linear strains ε_k^m

and ε_k^c resulting from compression of the solid matrix material and the microcrack porosity, respectively. That is

$$\varepsilon_k = \varepsilon_k^m + \varepsilon_k^c \tag{A1.1}$$

where the subscript k indicates the strain gauge providing the measurement. Proof of (A1.1) relies on the application of Betti's reciprocal theorem in which it is shown that the average matrix solid dilation at any given confining pressure is the direct product of the pressure increment and the intrinsic matrix compressibility. Biot and Willis (1957), and Nur and Byerlee (1971) expressed the same concept through the parameter

$$\alpha = 1 - \frac{K}{K_m'} \tag{A1.2}$$

which is the ratio of the change in the pore volume to the total volumetric strain in where K is the bulk modulus of the rock and K_m' is the bulk modulus of the solid portion. For the purposes of the present study, the modulus K_m' may be dependent upon, but not necessarily exactly the same as, the intrinsic bulk modulus of the porosity-free solid compounds of which the material is constituted.

Here, we estimate those components of the total strains that represent the void space within the material due to microcracks. In many rocks, especially sedimentary rocks, the porosity may be composed of both these planar cracks and higher aspect ratio voids. These voids may take any shape, for example spherical voids might have been left by gas bubbles formed within the sediments as they were being deposited or within a volcanic rock as it was extruded near the surface. Angular voids would be expected in a sandstone constructed from the close packing of nearly spherical quartz grains. These high-aspect-ratio, three-dimensional voids will close only at very high pressures by an irreversible deformation due to plastic yield or crushing of the material (Cooper and Carlton, 1962;

Bhatt et al., 1975). For example, Zhang et al. (1990) observed the onset of crushing at hydrostatic pressures near 400 MPa in a quartz grain sandstone with a relatively high porosity of 21%. The present analysis assumes that these three-dimensional pores remain open and that the dilations produced are reversible (i.e., the brittle material is not further damaged) by application of the hydrostatic confining pressures used in the present experiments. Under these circumstances, the remainder of the observed strains result from closure of the microcrack porosity.

Two differing strain regimes are displayed by the hypothetical curve of Figure A1.1. At pressures below a critical confining pressure P_c, microcrack porosity remains open and the rock compressibility is still strongly influenced by the compliant microcracks. The compressibility of the cracked material is dependent upon the density and distributions of the apertures and length of the microcracks it contains (Walsh, 1965; Morlier, 1971; Mavko and Nur, 1978; and Doyen, 1987). At low confining pressures the microcracks have large lengths and apertures and as a result will be more compliant than at higher confining pressures where the applied tractions result in partial closure and shortening of the effective length of the cracks. The nonlinear shape of the strain curve is a consequence of the progressive closure of the cracks with increasing pressure. At these higher pressures the microcracks are less open, shorter, and less compliant, thus stiffening the cracked material. As an illustration of this effect, the theoretical effective bulk modulus of a medium containing randomly oriented penny-shaped crack according to the Reuss method of averaging stiffnesses (Walsh, 1965) is

$$K_{eff} = 1 - \frac{K_m'}{1 + \frac{16}{9}\frac{1 - \nu^2}{1 - 2\nu}\frac{N c^3}{V_0}} \qquad \text{(A1.3)}$$

where N is the number of penny-shaped cracks with average length c contained in a given volume V_0. Here K_m is the bulk modulus of the nonporous solid constituent. Since the

denominator in (A1.3) is always greater than unity, the effective bulk modulus of a cracked material is always less than that of its solid portion.

At the critical pressure, however, the microcrack porosity has been entirely closed and the strain response above this pressure parallels that expected for the solid matrix constituents only. Consequently, if intrinsic solid matrix strains are known, then the strain ε_k^c due to microcrack closure at a given pressure may be calculated using (1) by subtracting ε_{ij}^m from ε_{ij} as shown in Figure A1.1.

The maximum crack strain is observed when the confining pressure reaches P_c. At any confining pressure, the magnitude of these measured residual ε_k^c for pressures in excess of P_c may be used to determine a microcrack porosity tensor

$$\begin{bmatrix} \varepsilon_{xx}^c & \varepsilon_{xy}^c & \varepsilon_{xz}^c \\ \varepsilon_{yx}^c & \varepsilon_{yy}^c & \varepsilon_{yz}^c \\ \varepsilon_{zx}^c & \varepsilon_{zy}^c & \varepsilon_{zz}^c \end{bmatrix} \tag{A1.4}$$

the trace of which is equivalent to the microcrack porosity (the ratio of the void space due to microcracks to the total volume of the cracked medium) at any given pressure

$$\phi^c = \varepsilon_{xx}^c + \varepsilon_{yy}^c + \varepsilon_{zz}^c \tag{A1.5}$$

Although ϕ^c may itself be of interest, the microcrack porosity tensor provides additional insight into the orientation and the degree of microcrack damage within the material, which is useful for correlating with physical property anisotropies or for diagnosing the source of the damage.

In the data to be presented below, the intrinsic solid strains ε_k^m are estimated for each of the strain measurements on the sample by fitting a line to the last few data points observed in each strain curve. The slope of this line parallels that anticipated for ε_k^m slope which must intercept the origin of the strain-pressure curve (Figure A1.1). This procedure

assumes that the compressibility of the solid portion of the cracked material is linear and that the critical pressure for complete microcrack closure has been exceeded.

The first assumption is, strictly, not true as the compressibility of solids does not remain constant with pressure. Over the pressure range of the present experiments, however, this is a good practical approximation for rock-forming minerals whose compressibilities will typically vary by less than 1%. For example, the derivative of the adiabatic bulk modulus with pressure ($\partial K_S/\partial P$) has an empirically derived value near 4 for many of the rock-forming minerals (Anderson et al., 1968). That is , the bulk modulus of many of these materials increases at a rate of 4 to 5 times that of the confining pressure. Over the pressure range studied here (to 200 MPa) the increase in bulk modulus will be approximately 1 GPa as compared with the estimated zero-pressure bulk modulus for dolomite (Table A1.1) between 80 and 100 GPa.

The second assumption is less easily justified and care must be exercised by examining the linearity of the strain curves at high pressure and by comparisons of the observed slopes of independently measured linear compressibilities of the solid constituents.

1.3 EXPERIMENTAL PROCEDURE

Cubes of rock with dimensions of nearly 2.5 cm were machined from an unoriented core sample obtained by drilling into dolomitic rock. The core sample was obtained from a depth of 4783 m in the Foothills Region of the Rocky Mountains in Alberta, Canada. The local geologic structure consists of large, westward-dipping thrust faults. The lithostatic or overburden pressure expected at this depth is 120 ± 10 MPa as estimated from the density of the overlying sedimentary rocks. Otherwise, the local stresses are expected to include a NE-SW compression that was estimated from the preferred orientation of wellbore spalling (Bell and Gough, 1979). The least compressive horizontal stress magnitude is estimated to be approximately 80 MPa on the basis of other deep stress measurements in the area (Bell

and Babcock, 1986). The magnitude of the greatest compressive horizontal stress is unknown but Bell and Babcock (1986) suggest that it is less than that for the vertical stress at these depths. The rock itself was initially deposited as a limestone in a relatively deep-sea environment during the Mississippian period between 345 and 320 Ma (Press and Siever, 1978). The rock has since been altered with the mineral calcite, $CaCO_3$, being changed by substitution of Mg for Ca to form dolomite, $(Mg,Ca)CaO_3$, (Hurlburt and Klein, 1971), which is the principal solid constituent of the cubes.

Great care was taken during the cutting and surface preparation of these samples to avoid inadvertently producing further microcracks that would contaminated the observed signal. The surfaces of the cubes were flattened by slowly removing material on a surface grinder modified to include a continuous spray of water onto the sample whilst it was being ground to remove material and to keep the surfaces being ground cool. When finished, the sides of cubes were parallel to better than 25 μm and adjacent sides differed from perpendicular by no more than 0.1°. The bulk density (dry density/dry volume) of these rock samples was measured to be 2.695 ± 0.005 g cm^{-3}.

Strain gauges (Micro-Measurements CEA-06-250UR-350) were attached to the cube with a two-component epoxy in the configuration shown in Figure A1.2. Note that the z axis is aligned with the axis of core but the orientations of the horizontal axes of the block are unknown relative to any real world reference. In practice there are three independent gauges separated at 45° on a single substrate. Misalignment of the strain gauges at this point can be a source of uncertainty but for the case presented here the gauges differed from their intended directions by no more than 3°, which does not significantly affect the final results. Single-strand wires were soldered to takeouts on the strain gauges. The entire sample was then encased in a flexible castable urethane rubber (Devcon Flexane), which provided the impermeable jacket to isolate the cube from the confining pressure fluid. Each stain gauge was positively connected to the pressure vessel feed-through wires by soldering. Further, each strain gauge was attached to one arm of an

individual Wheatstone bridge outside the pressure vessel made from low-drift precision resistors (0.01%). With this configuration, each bridge was always activated with each strain gauge being at thermal equilibrium for the duration of the experiment. These Wheatstone bridges were activated by a voltage of 10.000 ± 0.003 V. The cube was then placed in the pressure vessel and slowly pressurized to maintain, as best possible, the thermal equilibrium of the system. Pressure was incremented in steps that increased from 2 to 10 MPa to account for the decreasing curvature of the strain-pressure plot with increasing confining pressure up to the 200 MPa capacity of the vessel. Confining pressure were measured with both an accurate (0.15%) pressure transducer and a calibrated Bourdon tube gauge, the measurement was taken only after a short time period to allow equilibration of the system due to adiabatic change in temperature of the pressure fluid. Once equilibration was achieved, the voltage responses of each Wheatstone bridge and the activating input voltage were manually recorded from a, 5(1/2) digit, digital voltmeter.

The linear strain recorded by each gauge was individually calculated using well-known formulas for an unbalanced Wheatstone bridge and the gauge factor ($2.095 \pm 0.5\%$ for the two perpendicular gauges and $2.105 \pm 0.5\%$ for the gauge at 45°). Additional corrections such as accounting for the effect of pressure on the strain gauges or reducing thermal effects by differential comparison of the sample to a known standard were not used. As noted above, the strain of the solid portion was estimated for each gauge by fitting a line to those data above approximately 140 MPa of the confining pressure and resulting estimated solid strain to yield the observed crack strains ε_k^c. The fitting process was conducted continuously by increasing the number of points fit from the highest pressure datum. The quality of the linear line fit to these data as measured by the Pearson's correlation co-efficient was found to noticeably change at the pressure of 140 MPa; the strain data taken above this pressure were used to estimate the intrinsic linear compressibilities. These observed strain ε_k^c are related to the presently unknown crack-strain tensor whose basis is the co-ordinate axis of the cube as shown in Figure A1.2 via

$$\varepsilon_k^c = l^2 \varepsilon_{xx}^c + m^2\varepsilon_{yy}^c + n^2\varepsilon_{zz}^c + 2lm\varepsilon_{xy}^c + 2ln\varepsilon_{xz}^c + 2mn\varepsilon_{yz}^c \quad \text{(A1.6)}$$

where l, m, and n are the direction cosines between a vector representing the direction of the strain gauge k and , respectively, the x, y and z axes (Malvern, 1969; Fung, 1965). As an example, the formula for strain gauge 2 in Figure A1.2 will be

$$\varepsilon_2^c = \frac{1}{2}\varepsilon_{xx}^c + \frac{1}{2}\varepsilon_{yy}^c + \frac{1}{2}\varepsilon_{xy}^c \quad \text{(A1.7)}$$

a similar formula may be written for each of the strain observations, In the present experiments, this allows nine different equations to be written that are in turn used together in a least-squares inversion routine (Press and Flannery, 1989) to determine the six components of the crack-strain tensor. This last procedure differs from that used by previous workers in which the effects of the solid-matrix strains were not removed in the derivation of a strain tensor (Strickland and Ren, 1980; Dey and Brown, 1986) or in the original application in which the derivatives of the experimental strain curves were taken (Simmons et al., 1974; Siegfried and Simmons, 1978; and Wang and Simmons, 1978).

1.4 RESULTS AND DISCUSSION

1.4.1 Compressibilities

Figure A1.3 contains plots of the observed raw strains and the residual crack strains versus pressure. The linear compressibility λ (Brace, 1965) is defined as

$$\lambda = -\frac{1}{L_o}\frac{\partial L}{\partial P} = -\frac{\partial \varepsilon_k}{\partial P} \quad \text{(A1.8)}$$

where L is the length at hydrostatic confining pressure P of an arbitrarily oriented line segment on the surface of the sample whose original length at zero pressure was L_o. The values of these linear compressibilities as measured from the slope of the strain-pressure

curves above confining pressures of 140 MPa for each of the nine independent strain gauges are given in Table A1.1, and these are assumed to provide a measure of the linear compressibility of the solid portion of the sample. The pressure of 140 MPa is arbitrary but in general the curvature of the observed strains is substantially diminished past this pressure on all the samples, suggesting that the microcrack porosity was essentially closed and the remaining response was primarily that due to the solid. Note that the calculated bulk compressibilities in Table A1.1 are assumed to be three times λ.

The presently measured compressibilities are also compared with the results of previous measurements on other dolomite bearing rocks (Brace, 1965; Coyner, 1984; and Zisman, 1933). The last value in Table A1.1 was determined indirectly from the ultrasonic longitudinal and transverse elastic wave velocities and the density measured in a dolomite sample at high pressure (Christensen, 1982). The observed compressibilities are substantially larger than those previously measured, that is, those that were previously measured are stiffer by nearly a factor of 2 or more. This indicates that some porosity remains within this sample. That additional porosity exists within the sample is consistent with the observed bulk density for the rock, which, when compared to the single-crystal density for dolomite of 2.85 g cm^{-3}, indicates a porosity of 5.3%.

Scanning electron microscopy of the sample was carried out to determine whether the porosity consists of damage-induced microcracks or includes higher aspect ratio pores that existed in the rock prior to its removal from the earth. Two images at magnifications of 1250 and 2620 times of the same region of a thin section of the rock are shown in Figure A1.4; these images are typical of the structure observed over the thin section with an area equal to approximately 4 cm by 2.5 cm. In Figure A1.4a number of pores with complex angular shapes and with dimensions typically from 5 to 20 μm may be seen. That these are pores, and are not the result of plucking of mineral grains during sample preparation, is supported by the image at the higher magnification. Here, well-developed dolomite crystals are seen to bound the void space of the pore; the angularity of these crystals

suggests that they would have formed by growth into a void. Regardless, the images in Figure A1.4 confirm that higher aspect ratio pores, which will remain open to high pressures within the sample, exist.

Some evidence from other workers exists to suggest that the damage-induced microcracks are indeed closed within this test piece at the higher pressures used in the experiment, although this assumption must be approached with care. The basis of this suggestion rests on two observations:

(i) that damage-induced microcracks appear to provide a record of the most severe stress state that the material had experienced, and

(ii) that these cracks will further close at a pressure nearly equal to the stress to which they were initially subject.

The first of these observations is based on the fact that the rate of acoustic emissions, which are the result of the growth of microcracks within the material under an increasing deformation, is very low while the material is at stress levels below an earlier maximum but increases substantially once the stress level is reattained. This is referred to as the Kaiser effect (Christensen, 1982) in which the previously applied maximum stress is determined from a plot of rate or number of acoustic emissions versus stress. Some authors have exploited the Kaiser effect as a technique to estimate the original in situ stress magnitudes to which a rock was subject (Yoshikawa and Mogi, 1989) although numerous drawbacks to the method have been noted (Yoshikawa and Mogi, 1981; Kurita and Fujii, 1979). The microcracks within this rock sample may contain some memory of the original stress magnitudes, estimated to be below 120 MPa on the basis of the depth from which the rock was retrieved.

Secondly, there is an empirical correlation between the confining pressure at which certain families of microcracks within the rock mass close in experiments similar to those described here and the expected magnitudes of the stress tensor acting on the rock mass from which the sample was removed (Dyke, 1989). There exists some theoretical basis for

this; as noted by Walsh (1965) the closure pressure P_c for an idealized penny-shaped crack with aspect ratio α (minor semi-axis/major semi-axis) is :

$$P_c = \frac{\pi E \alpha}{4(1 - \nu^2)}. \qquad \text{(A1.9)}$$

In a careful study using the differential strain analysis technique, Wang and Simmons (1978) observed that the majority of microcracks within two igneous rock samples obtained from depths near 5.3 km in the Michigan basin closed at a pressure near 145 MPa, which corresponded closely to the in situ stress magnitudes inferred using knowledge of the density of the overlying column of rock. In a separate study, Kowallis and Wang (1983) observed fresh microcracks with sharp tapered ends in scanning electron microscope images from granitic cores retrieved to depths of 1572 m in a wellbore drilled in Illinois, differential strain analysis on their cores yielded lower closure pressures of the predominant crack families of 15-22.5 MPa, which in this case is below the maximum expected stress levels for the deepest sample near 40 MPa. In an extensive series of tests on differing rock types, Dyke (1989) observed generally that the predominant crack-closure pressures were consistent with in situ stress magnitudes. By analogy to the present situation, it is likely that the damage-produced microcracks are mostly closed above pressures of 140 MPa as the expected in situ stresses are on the order of 100 MPa.

If, as suggested, the microcracks resulting from drilling or stress-relief damage are closed, then the observed compressibilities of the sample above 140 MPa are nearly those of the solid matrix modulus K_m'. Since these observed values are substantially less than that anticipated for porosity-free dolomite (Table A1.1) then lower aspect-ratio porosity must exist. Equation (A1.3) above provides an estimate of the effective bulk modulus of a sample containing a given porosity of spherical pores. However, using a mineral bulk modulus K_m of 100 GPa and a Poisson's ration v of 0.34 for nonporous dolomite, as estimated from the acoustic measurements in Table A1.1, suggests that porosities on the

order of 20% would be required to explain the observed compressibilities if the pores were all spherical. This discrepancy suggests that the porosity may take a different form within the sample. Due to difficulties at arriving at an analytic solution, there are few results that predict the effect of pore shapes different from cracks or spherical pores (Ferrari and Filipponi, 1991; Mori and Tanaka, 1983). However, Wu (1966) demonstrates that needle-shaped pores have a much greater effect in lowering the modulus of the material than spherical pores. Hence lower aspect-ratio porosity would be consistent with the observations of compressibility in the sample as is confirmed by the direct scanning electron microscope images of Figure A1.4 (Kowallis et al., 1982). The reason for the nearly 25% variance in these compressibilities with direction, however, is unknown but probably due to a preferential alignment of either the dolomite crystals or the pore voids within the rock.

1.4.2 Microcrack Strain Tensor

Figure A1.5a shows the three principal microcrack strains as a function of confining pressure. Taken together these indicate a crack porosity within the sample of 0.79%. The orientation of each of these principal crack-strain components is shown in an equal angle stereographic projection (Hobbs et al., 1976) in Figure A1.4b, which indicates that the largest strain magnitudes deviate from the vertical (z) direction by slightly more than 20° at the highest confining pressure of 200 MPa. Note further that the last two data points for the two greatest strains are clustered together, this means that any relative change between the crack strains is small at the higher pressures and further indicates that the majority of the microcracks must be closed.

Since the crack stains describe the closure of the microcrack porosity, a given principal strain will correspond to a family of microcracks with planes normal to the principal strain direction. Consequently, Figure A1.5a shows that the test piece contains either a greater number of subhorizontally aligned microcracks or that these microcracks

generally have a large aperture than those with other orientations. This observation has been made by other worker, who examined the microcrack distributions in core sample (Meglis et al., 1992), and suggests that coring operations result in such a state of damage. Indeed, under certain states of stress, there is a well known "disking" effect that results in incipient or complete rupture of the core along a saddle-shaped fracture the shaped of which appears to be related to the magnitudes and directions of the in situ stresses (Dyke, 1989). The observed microcrack distribution of Figure A1.5 and especially the result of the greatest strain magnitude being nearly vertical may be indicative of relatively low levels of damage produced by moderate stress states below those necessary to produce the core-disking effects.

1.5 CONCLUSIONS

Nine linear strains on the surface of a cube of a damaged rock were measured as a function of hydrostatic confining pressures of 200 MPa. To estimate that component of the observed strains due to the progressive closure of the microcrack porosity, the solid strains were determined by a linear fit to the strain curves at the highest confining pressures. An interesting observation in the dolomite sample studied was that the compressibility of the solid portion of this sample was substantially less than that expected for single crystal dolomite. This is possibly rationalized if the solid portion of the rock consists of dolomite containing high-aspect-ratio voids as was supported by scanning electron microscopic observations of the rock sample. These large voids could not be closed by confining pressure to 200 MPa. Despite this, the microcrack stain tensor for this sample indicated that the predominant microcrack family within the sample was oriented subhorizontally. This observation is consistent with those of earlier workers and is probably a consequence of the drilling and coring operations. Such observations are extremely important as in many rocks the microcrack distributions control many of the physical properties. As is well known, the physical properties such as permeability and

electrical conductivity measured under conditions of standard temperature and pressure may have little resemblance to those same properties in situ. But further and perhaps more importantly, such microcrack distributions will result in substantial anisotropies to these physical properties. Knowledge of these damage-induced microcracks as determined in the present testing procedure could, however, provide some indication of the degree of damage, which would be useful in the evaluation of any laboratory physical-property measurements for the estimation of in situ properties.

1.6 BIBLIOGRAPHY

Adams, L.H., and E.D. Williamson. *J. Franklin Inst.* **195**, 475 (1923).

Ahrens, T.J., and A.M. Rubin. *J. Geophys. Res.* **100**, 529 (1995).

Anderson, O.L., E. Schreiber, R.C. Liebermann, and N. Soga. Rev. *Geophys.* **6**, 491 (1968).

Bell, J.S., and D.I. Gough. Earth Planet. *Sci. Lett.* **45**, 475 (1979).

Bell, J.S., and E.A. Babcock. *Bull. Can. Pet. Geol.* **34**, 364 (1986).

Bhatt, J.J., M.M. Carrol, and J.F. Schatz. *J. Appl. Mech.* **42**, 363 (1975).

Biot, M.A., and D.G. Willis. *J. Appl. Mech.* **24**, 594 (1957).

Brace, W.F., *J. Geophys. Res.* **70**, 391 (1965).

Christensen, N.I., In Handbook of physical properties of rocks. Vol. II. *Edited by* R.S. Carmicheal. CRC Press, Boca Raton. 1982. pp.1-228.

Cooper, A.B., and L.E. Carlton. *J. Am. Cer. Soc.* **45**, 97 (1962).

Coyner, K.B., Ph. D. thesis, Massachusetts Institute of Technology, Cambridge, Mass. 1984. pp. 14-80.

Crampin, S., *Wave Motion.* **3**, 343 (1981).

Dey, T.N., and D.W. Brown. Proc. Int. Symp. on Rock Stress and Rock Stress Measurements. September 1-3, Stockholm. Centek, Lulea, Sweden. 1986. pp. 351-357.

Doyen, P.M., *J. Geophys. Res.* **92**, 8169 (1987).

Dyke, C.G., Ph. D. thesis, Imperial College of Science and Technology, University of London, London. 1988. pp. 22-66.

Ferrari, M., and M. Filipponi. *J. Am. Cer. Soc.* **74**, 229 (1991).

Fung, Y.C., Foundations of solid mechanics. Prentice-Hall, Englewd Cliffs, 1965. pp. 92-94.

He, H., and T.J. Ahrens. *Int. J. Rock Mech. Min. Sci. Geomech. Abstr.* 525 (1994).

Hobbs, B.E., W.D. Means, and P.F. Williams. An outline of structural geology. John Wiley and Sons, New York. 1976. pp. 483-495.

Hurlburt, C.S., and C. Klein. Manual of mineralogy. 19th ed. John Wiley & Sons, New York. 1971. pp. 307-309.

Jaeger, J.C., and N.G.W. Cook. Fundamentals of rock mechanics. 3rd ed. Chapman and Hall, London. 1979. pp. 211-214.

Kaiser, J., *Arch. Eisenhüttenwes.* **24**, 43 (1953).

Kowallis, B.J., and H.F. Wang. *J. Geophys. Res.* **88**, 7373 (1983).

Kowallis, B.J., E.A. Roeloffs, and H. F. Wang. *J. Geophys. Res.* **87**, 6650 (1982).

Kurita, K., and N. Fujii. *Geophys. Res. Lett.* **6**, 9 (1979).

Lockner, D., S. Hickman, V. Kuksenko, A. Ponomarev, A. Sidorin, J. Byerlee, and B. Khakaev. *Geophys. Res. Lett.* **18**, 881 (1991).

Malvern, L.E., Introduction to the mechanics of a continuous medium. Prentice-Hall, Englewood Cliffs, N. Y. 1969. pp. 132-134.

Mavko, G.M., and A. Nur. *J. Geophys. Res.* **83**, 6414 (1978).

Meglis, I.L, R.J. Greenfield, and T. Engelder. *EOS-Trans. Am. Geophys. Union.* **73**, 299 (1992).

Mori, T., and K. Tanaka. *Acta Metall.* **21**, 571 (1983).

Morlier, P., Rock Mech. **3**, 125 (1971).

Nemat-Nasser, S., and H. Horii, *J. Geophys. Res.*, **87**, 6805 (1982).

Nur, A., and G. Simmons, *Int. J. Rock Mech. Min. Sci. Geomech. Abstr.* **7**, 307 (1970).

Nur, A., and J.D. Byerlee. *J. Geophys. Res.* **76**, 6414 (1971).

O'Connell, R.J., and B. Budiansky. *J. Geophys. Res.* **79**, 5412 (1974).

Press, F., and R. Siever. Earth. W.H. Freeman, San Francisco. 1978. pp. 39-42.

Press, W.H., B.P. Flannery, S.A. Teukolsky, and W. T. Vetterling. Numerical recipies (Fortran version). Cambridge University Press, Cambridge. 1989. pp. 19-74.

Ren, N.K., and J.-C. Rogiers. Proc. Int. Congr. Rock Mech. 5th. 2, International Society of Rock Mechanics, Melborne (1983), pp. F117-F127.

Siegfried, R.W., and G. Simmons. *J. Geophys. Res.* **83**, 1269 (1978).

Simmons, G., and D. Richter, The Physics and Chemistry of Mineral and Rock, Edited by R.G.J. Strens, John Wiley and Sons, New York, pp. 105-137 (1974).

Simmons, G., R.W. Siegfried, and M. Feves. *J. Geophys. Res.* **79**, 4383 (1974).

Striekland, F.G., and N-K. Ren. In Proc. 21 st U.S. Symp. Rock Mech. 1980. pp. 523-532.

Tapponier, P., and W.F. Brace, *Int. J. Rock Mech. Min. Sci. Geomech. Abstr.* **13**, 103 (1976).

Teufel, L.W., and N.R. Warpinski, Proc. 25th U.S. Symp. Rock Mech. Illinois, June 25-27, 1984, Soc. Mining Engineers, N.Y., 1984, pp. 176-185.

Voight, B., *Felsmech. Ingenieurgeo.* **6**, 201 (1968).

Walsh, J.B., and W. F. Brace. *J. Geophys. Res.* **89**, 9425 (1984).

Walsh, J.B., *J. Geophys. Res.* **70**, 381 (1965).

Wang, H.F., and G. Simmons. *J. Geophys. Res.* **83**, 5849 (1978).

Wu, T.T., *Int. J. Solids Struct.* **2**, 1 (1966).

Yoshikawa, S., and K. Mogi. *J. Acoust. Emiss.* **8**, 113 (1989).

Yoshikawa, S., and K. Mogi. *Tectonophys.* **74**, 323 (1981).

Zhang, J., T-F. Wong, T. Yanagidani, and D. M. Davis. *Mech. Mater.* **9**, 1 (1990).

Zisman, W.A., *Proc. Natl. Acad. Sci. U.S.A.* **19**, 666 (1933).

Table A1.1. Observed linear and calculated bulk compressibility

Observation	Linear Compressibility ($GPa^{-1} \times 10^{-3}$)	Bulk Compressibility ($GPa^{-1} \times 10^{-3}$)
Gauge No. 1	8.18	24.5
Gauge No. 2	6.49	19.5
Gauge No. 3	7.82	23.5
Gauge No. 4	9.15	27.5
Gauge No. 5	7.91	23.7
Gauge No. 6	8.07	24.2
Gauge No. 7	7.26	21.8
Gauge No. 8	6.78	20.3
Gauge No. 9	7.34	22.0
Blair dolomite (Coyner, 1984)	—	12.3
Blair dolomite (Brace, 1965)	—	11.8
Wetabuck dolomite (Coyner, 1984)	—	10.3
Wetabuck dolomite (Coyner, 1984)	—	10.0
Wetabuck dolomite (Coyner, 1984)	—	11.8
Dolomate 72-4 (Acoustic)	—	9.6

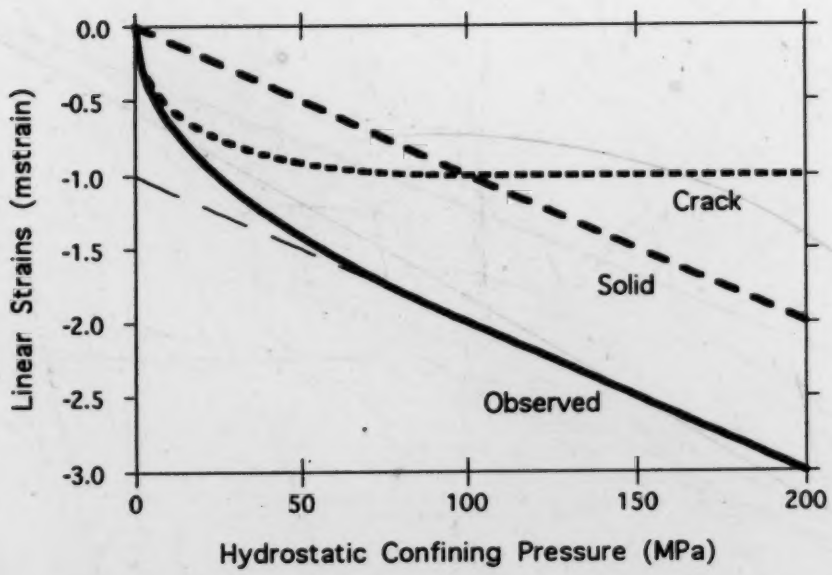

Figure A1.1. Hypothetical linear or volumeric strain curve versus hydrostatic-confining pressure for a cracked material. Contractional strains have negative sign. The crack strains (short dashes) is the difference between the observed strains (continuous line) and the solid matrix strains (long dashes). Best fit straight line (thin broken line) parallels solid strains.

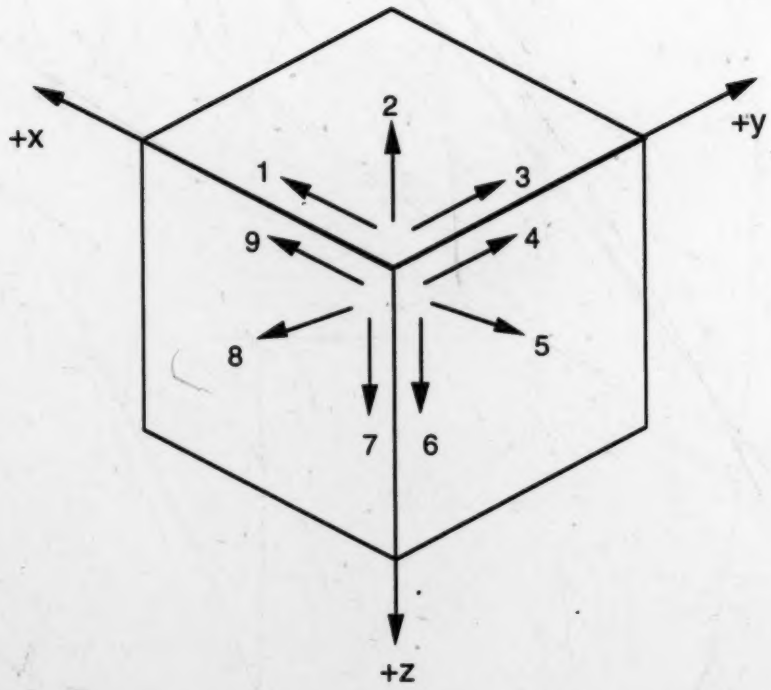

Figure A1.2. Placement of nine strain gauges on cubical sample. Note orientation of view. The z-axis coincides with the axis of the core. The horizontal x and y axes are arbitrarily aligned.

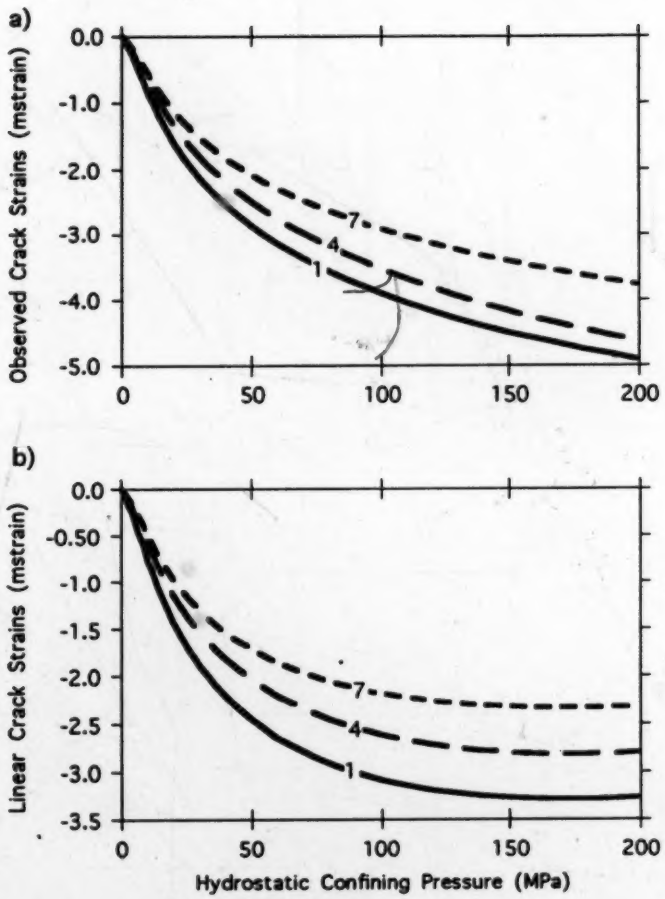

Figure A1.3. (a) Observed linear strains versus confining pressure for gauge 1, 4 and 7. (b) Linear crack strains calculated from the difference of those observed and the estimated solid strains for gauges, 1, 4, and 7.

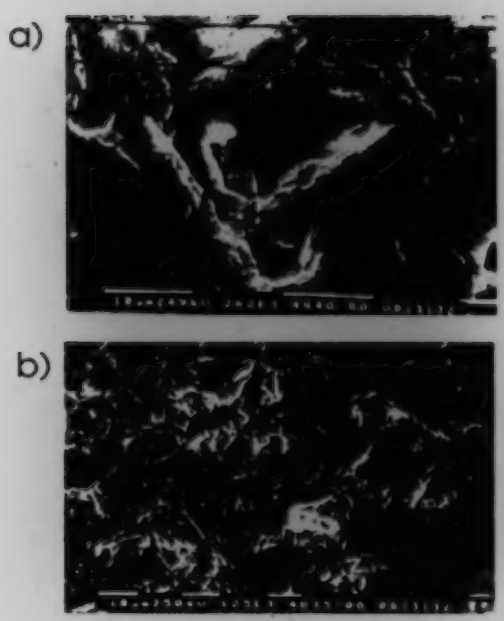

Figure A1.4. Scanning electron microscope images of a section of the rock studied at magnifications of (a) 2620 times and (b) 1250 times. The large pore in the center of (a) is a magnified view, rotated 180°, of the large pore slightly above the right-center of (b).

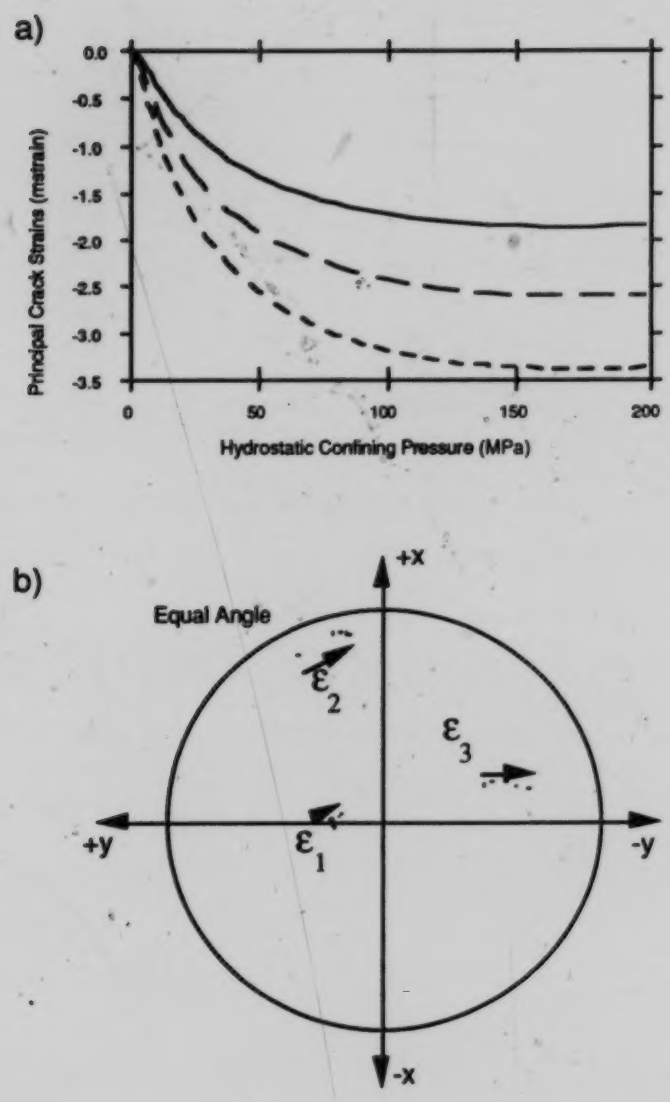

Figure A1.5. (a) Principal crack strains. (b) Orientations of principal crack strains on equal angle stereonet

APPENDIX 2

Influence of Core Bit Cut Geometry on Bottomhole Stress Concentrations

2.1 INTRODUCTION

The geometry of a cavity within a continuum medium influences the degree and the distribution of the stress concentration. This is an important and practical problem: texts on fracture mechanics in the engineering literature contain the anecdote about the WW II U.S. Liberty ships that failed catastrophically even while merely sitting in port. These ships sank because fractures grew rapidly from the poorly reinforced square holes in the hull. Two simple examples of analytic solutions are the stress concentration due to circular and elliptical cavities (Kirsch, 1898; Fenner, 1986; and Engelder, 1993). The stress concentrations due to a circular hole have been widely used in areas related to the analysis of wellbore stability, borehole breakouts (Bell and Gough, 1983; Zoback et al., 1985), hydraulic fracturing testing (Hubbert and Willis, 1957; Hamison and Fairhurst, 1967), and other borehole related techniques for in situ stress measurements (Leeman, 1964). A detailed study of the stress concentrations produced by many different cavity geometries in two dimensions has been published by Savin (1961). The stress concentration in the vicinity of a crack tip and the subsequent formation and propagation of fractures and microcracks are a fundamental basis of the field of fracture mechanics.

The end of borehole is a three dimensional cavity created by a drill bit within the rock mass. Many different drill bits are employed in engineering and petroleum recovery producing many kinds of bottomhole cavities. Geometry dependent variations in the bottomhole stress concentrations are expected. The stress concentrations for two often encountered bottomhole geometries, a flat cut as illustrated in Chapters 2 and 3, and a circular or curved cut as illustrated in Chapter 4, were studied using 3-D finite element

modeling. Here we hope to explore briefly the influence that core geometry has on the general character of the stress concentrations. In particular, we seek to evaluate the differing influences of the flat versus the circular kerf cut and the thin versus the thick kerfs.

The flat cut with the ratios of cut width/core radius (w/R) equal to 1/5, 2/5 and 1, and a curved cut with coring cut width/core radius ratio equal to 1 were studied in detail. The finite element meshes for the flat cut cases with w/R = 1/5, 2/5, and for the curved cut case were described in Chapters 2, 3, and 4, respectively. In all calculations, the medium has a Young's modulus of 20 GPa and Poisson's ratio of 0.25. Here only most tensional stress (σ_3) is discussed because of its importance in producing core disking fractures.

The bottomhole cut shape and the ratio of the cut (kerf) width relative to the core diameter are two important geometrical parameters in affecting bottomhole stress concentrations. The former is considered important in affecting stress distribution; and the latter mainly affects the peak magnitudes of the concentrated stresses. This analysis mainly focuses on the comparison of the difference between the stresses produced by different cut shapes and cut width/core radius ratios. It is important to evaluate this to see how general the solutions for the particular geometries in the previous chapters might apply to other, slightly different, geometries.

2.2 RESULTS

2.2.1 General Stress Characteristics

To evaluate the influence of the bottomhole cut shape, the stresses produced by the flat and curved cut with w/R = 1 are first compared. Figure A2.1 shows the most tensional stresses (σ_3) on these two different cut surfaces, where the radial distance from borehole axis r, and the distance from borehole bottom z are normalized by the core radius and diameter, respectively. Notice that r/R = 1 and 2 indicate the locations of the core side surface and the wellbore wall, respectively, and z/d = 0 represents the end of the borehole.

For the purpose of stress comparison, the curved cut surface is projected onto the flat one. The calculations were performed with a varying core stub length from zero to the core diameter, but only the cases with core stub lengths of zero and 1/4 the core diameter are presented.

For these geometries the stress concentrations produced by the loads of in situ uniaxial horizontal stress, S_H, overburden, S_v, uniaxial horizontal stress with overburden, $S_H = S_v$, biaxial horizontal stress condition, $S_H = S_h$, the wellbore fluid pressure, S_p, and the weight of drill bit, S_b were used.

Under the uniaxial horizontal stress condition, high tension exists at $\Phi = 90°$ (Figure A2.1a). With no core stub, the tensile stresses are low and both cut shapes result in similar magnitudes at the center of the cut surface but the difference becomes apparent towards the wellbore wall. With a core stub, the flat and the curved cut produces high tension at the inner corner (r/R =1) and away from the core stub, respectively. It shows that the normalized greatest tensile stress produced by the flat cut is twice (1.07) that of the curved one (0.5). This is expected as the flat case has flat square corners which serve as the locus of extreme stress concentration in analytic solutions.

The overburden produces a similar tensile stress distribution (Figure A2.1b). The greatest tensile stresses are almost doubled from the curved to the flat cut also.

As an example, the stresses under superposition the uniaxial horizontal and overburden stress conditions are used to demonstrate the local stress interaction (Figure A2.1c). It shows that the general characteristics of the stresses on the cut surface are similar to the former two cases as shown in Figure A2.1a and b. Notice that the magnitudes of the stresses basically are the sum of Figure A2.1a and b. This indicate the orientations of the tensile stresses for the cases under uniaxial horizontal and overburden stress conditions are in good agreement.

Most importantly, the tensile stresses along the borehole axis and removed as much as possible from the influence of the kerf geometry also were investigated under the biaxial

stress condition ($S_H = S_h$) (Figure A2.1d). There is no tension for the case with zero core stub length. The tension, however, appears at the root of core stub as the core stub grows. The largest tension is reached when core stub length is about 1/4 of the core diameter. It can be seen that for both cut geometries the magnitudes and distribution of the tensile stresses are similar. This suggests that the stress distributions at points removed from the kerf do not depend strongly on the kerf shape. Although we might expect this from St. Venant's principle, it is encouraging to see that the kerf shape should not unduly influence the final core fracture morphology if fracture initiates at the root of core stub.

Under the wellbore fluid pressure and the weight of drill bit, the greatest tension is located at the outer side of the kerf (Figure A2.1e-f). The core stub length has little influence on the greatest tensile stresses near the wellbore wall.

In a comparison of all these cases, the flat cut under fluid pressure produces the most tension with a normalized magnitude of approximately 3.0. In decreasing order are the overburden, the uniaxial horizontal stress, and the weight of the drill bit with the magnitudes of approximately 2.0, 1.06, and 1.25, respectively. In contrast, the corresponding curved cut cases results in lower peak concentrated magnitudes of 2.0, 1.1, 0.5, and 1.2. As might be expected, the core stub length influences the tension more significantly near the core stub with this influence diminishing near the wellbore wall. Assuming tensional failure, rupture may be expected at the inner side of the kerf under a uniaxial horizontal stress, an overburden stress, or their superposition. As previously described in Chapter 2, under wellbore fluid pressure and drill bit weight of drill bit, the failure may occur at the wellbore wall. The high tension at the root of core stub under biaxial stress condition is considered as responsible for initiating core disk fracture.

2.2.2 Concentrated Stress Magnitudes and Kerf Shape

The dependence of the normalized greatest tensile stresses at the cut surface versus core stub length l/d are of special of interest and shown in Figure A2.2 for a variety of

applied stress conditions. In Figure A2.2a, the peak tensions increase with core stub reaches a length slightly less than 40% the core diameter, remaining essentially constant for longer stubs. Notice that for these cases the peak tensions are all located at the inner corner of the kerf. An important characteristic here is that in a long core stub the magnitudes of the tensile stresses produced by the flat cut are nearly double those of the curved cut. This difference is reduced with diminishing core stub length, however.

Under biaxial conditions, the greatest tensile stresses are at the root of the core stub and these increase with core stub length while $l/d \leq 1/4$ and 1/3 for the flat and the curved cuts, respectively. As described in Chapter 3, these peak and then decline (Figure A2.2b). The peak tensile stress of the curved cut case is about 6% higher than that of the flat cut case although the core root stress rises more rapidly with stub length. Alternatively, however, the curved cut may produce slightly thicker core disks because the peak of its tensile stress curve occurs at a longer core stub. Consequently, quantitative magnitude interpretations of core disk thickness or spacings of core disk fractures may need to carefully account for the actual geometry.

Core stub length is of little importance on the magnitudes of the peak tensile stresses when the wellbore fluid pressure or the weight of drill bit are considered (Figure A2.2c) as these peak stresses are located near the wellbore wall, not in the vicinity of the core. Figure A2.2c is a bit deceptive in that the larger tensions produced by the drill bit weight result from changes in the contact area on the cut surface. Again, the stresses produced with the flat cut have the magnitudes approximately twice that of the curved cut.

The characteristics of the greatest tensile stresses above indicate that cut shape has a significant influence on the bottomhole stress concentrations. This result was not unexpected as, analytically, the stress concentrations at sharp points approach singularity. This influence may not be ignored if core disks are to be used as a quantitative stress magnitude determination tool but are of less important in the general interpretation of the core fracture shape in light of faulting environments.

2.2.3 Influence of Cut Width/Core Radius Ratio

Increasing values of cut width/core radius (w/R) ratio represent an increasingly wider cut relative to a given core diameter. For the same drill bit shape, if w/R remains constant for a series of bottomholes of different diameters then the concentrated stress magnitudes will be the same and the positions of the stress concentrations will map linearly. To investigate the influence of the w/R ratio, the calculations for three different w/R ratios (1/5, 2/5, and 1.0) all for a flat cut case were carried out. These three ratios represent two relative narrow cuts (w/R = 1/5 and 2/5) and a wide cut (w/R = 1). Detailed studies on the magnitudes and orientations of local stresses for the two cases with w/R = 1/5 and 2/5 have been described in Chapter 2 and 3, respectively. The normalized greatest tensile stresses under the same stress conditions as those in the previous section are shown in Figure A2.3. The analysis mainly focuses on the difference of the stress magnitudes resulted from changing the w/R ratio.

Under the stress conditions of S_H, S_V, and $S_H = S_V$, a smaller w/R ratio produces slightly greater tension (Figure A2.3a). This influence diminishes as the core stub shrinks. Because the tensile stress curves level off when the core stub length is greater than about 1/3 core diameter, the tension remains nearly constant.

The opposite effect is observed under biaxial stress conditions (Figure A2.3b). The tension slightly increases with increasing w/R ratio. The peak tensile stresses increase about 7% when w/R increases from 1/5 to 1.0. These variations are relatively minor and it is important to note that the curves for the different w/R ratios are not dramatically different.

A similar situation occurs when the wellbore fluid pressure and the weight of drill bit are considered (Figure A2.3c) For the wellbore fluid pressure, very slight increase of tension are seen with increasing w/R. When the larger of the rock-drill bit contact area under the constant drill bit pressure is accounted for, the curves for the drill bit weight also nearly coincide for different w/R ratios. The increase of the contact area gives a

proportional increase of the total weight of the drill string.

Based on these results, the influence of the ratio w/R on bottomhole stress concentrations are relatively small in comparison to those resulting from different cut shapes. Changes in this aspect of the bottomhole geometry are expected to have very little influence on the interpretations of drilling induced core fractures as might arise from Chapter 4.

2.3 CONCLUSIONS

The stress analyses of the dependence of stress concentrations at the wellbore bottom on cut geometry indicates:

1. As anticipated, the curved cut bottomhole reduces the stress concentrations substantially on the immediate cut surface. A 100% reduction of the greatest tensile stress magnitude is expected if a flat cut is replaced by a curved cut. At the root of core stub, the curved cut reduces tension for a short core stub but this trend reverses for a longer core stub. The other aspect is that the core stub length has significant influence on the stresses near a core stub but very little near the wellbore wall.

2. Increasing the cut width/core radius ratio reduces tension on the cut surface under in situ stress conditions but increases tension under wellbore fluid pressure drill bit weight. Furthermore, the tension at the root of core stub under biaxial stress condition increases with w/R.

3. There is a small dependence on the stresses at the root of core stub on both the cut shape and w/R ratio. In addition, significant variations of the stresses on the cut surface are not expected for small changes of the w/R ratio.

2.4 BIBLIOGRAPHY

Bell, J.S., and D.I. Gough, Northeast-Southwest compressive stress in Alberta: evidence from oil wells, *Earth and planetary Science Letters*, **45**, p. 475-482, 1979.

Engelder, T., Stress Regimes in the Lithosphere, Princeton University Press, p. 26-28, 1993.

Fenner, R.T., Engineering Elasticity, Application of Numerical and Analytical Techniques, Ellis Horwood, John Wiley, p. 228-235 & 241-259, 1986.

Haimson, B.C., and C. Fairhurst, Initiation and extension of hydraulic fractures in rock, *Society of petroleum Engineers Journal*, **7**, p. 310-18, 1967.

Hubbert, M.K. and D.G. Willis, Mechanics of hydraulic fracturing, *Trans. AIME*, **210**, p. 153-163, 1957.

Kirsch, G., Die theorie der elastizität und die bedürfnisse der festigkeitslehre, *Zeit. Ver. dt. Ingenieure*, **42**, p. 797-807, 1898.

Leeman, E.R., The measurement of stress in rock, Part I-III, *Journal of the South African Institute of Mining and Metallurgy*, **65**, p. 45-114 & p. 254-284, 1964.

Savin, G.N., Stress Concentration Around Holes, Pergamon Press, 1961.

Zoback, M.D., D. Moos, and L. Mastin, 1985, Well bore breakouts and in situ stress, *J. Geophys. Res.*, **90**, p. 5523-5530, 1985.

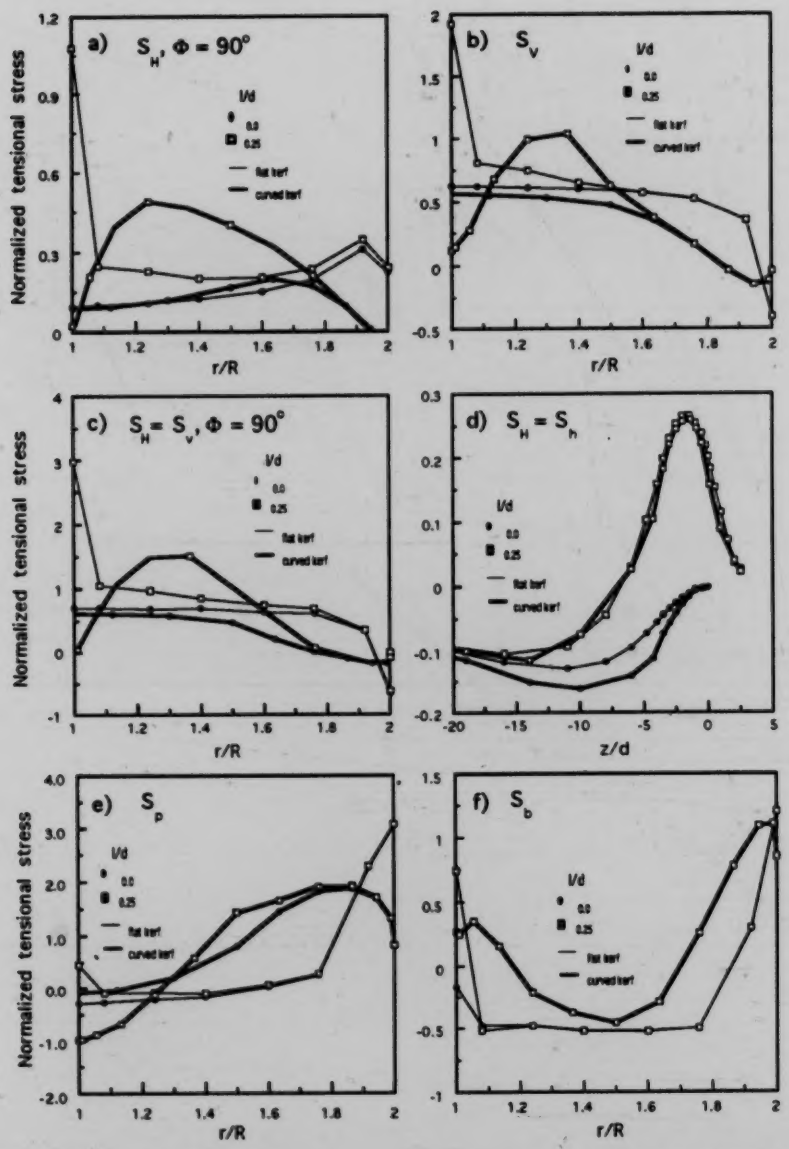

Figure A2.1. Normalized tensile stresses on the flat and curved cut surfaces and along borehole axis with the ratio of cut width/core radius equal to 1 under stress conditions of a) S_H, b) S_v, c) $S_H = S_v$, d) $S_H = S_h$, e) S_p, and f) S_b.

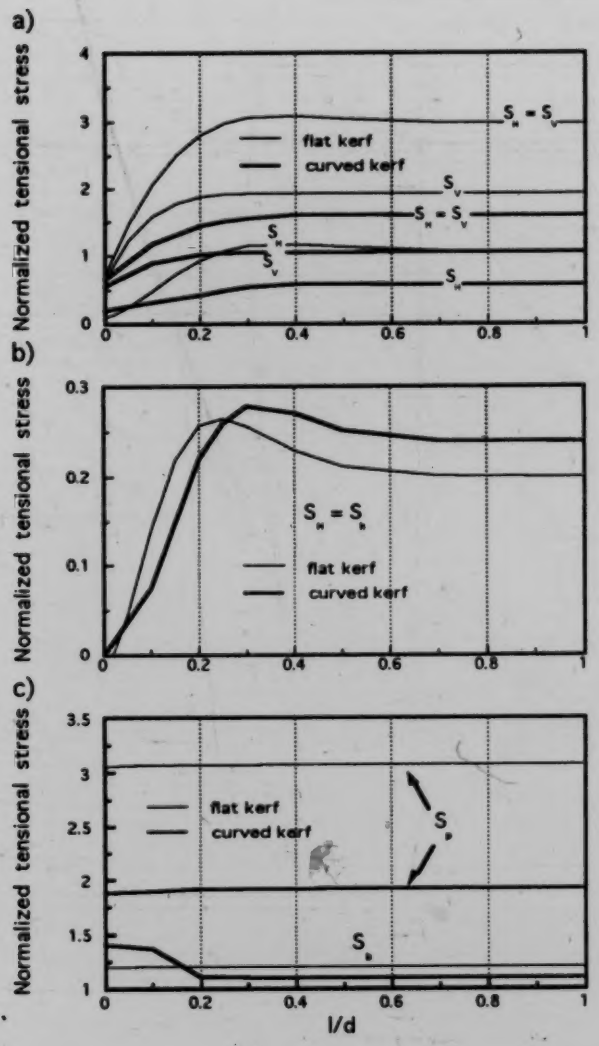

Figure A2.2. The normalized greatest tensile stresses on the flat and curved cutting surfaces versus core stub length with the ratio of cut width/core radius equal to 1 under stress conditions of a) S_H, S_v, and $S_H = S_v$, b) $S_H = S_h$, and c) S_p and S_b.

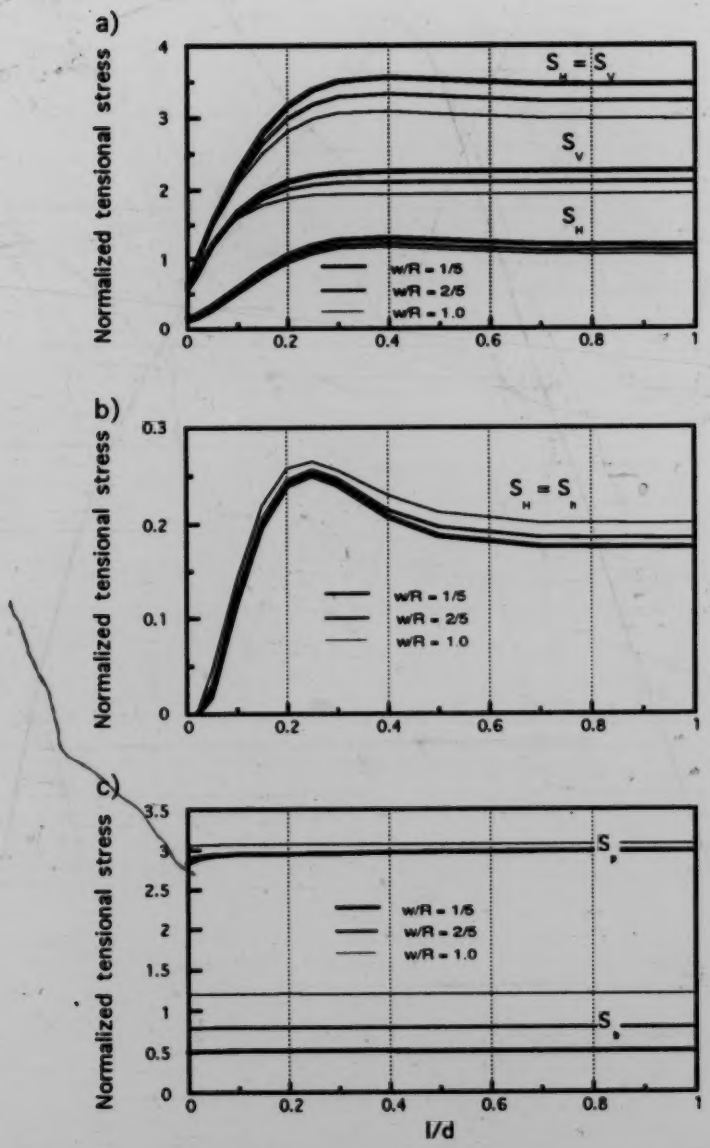

Figure A2.3. The normalized greatest tensile stresses on flat cut surfaces versus core stub length with the ratios of cut width/core radius equal to 1/5, 2/5 and 1 under stress conditions of a) S_H, S_v, and $S_H = S_v$, b) $S_H = S_h$, and c) S_p and S_b.

APPENDIX 3

Preliminary Modeling of Stress Concentrations in an Inclined Borehole

3.1 MODEL DESCRIPTION

It is usually assumed that one of the far-field principal stresses in the earth is vertical in regions of subtle topography. As a result, once a wellbore deviates from the vertical it is generally no longer parallel to a far-field principal stress; and from the wellbore's perspective a shear stress is seen. This loss of geometric symmetry increases the complexity of the stress concentration problem and requires that a much more detailed finite element analysis be carried out. We present here some initial results of finite element calculations of stresses in an inclined borehole.

The wellknown tensor co-ordinate transformation equation put in terms of a principal (S_1, S_2, S_3) and a nonprincipal (S_{xx}, S_{yy}, S_{zz}, S_{xy}, S_{xz}, S_{yz}) description is:

$$\begin{bmatrix} S_{xx} & S_{yx} & S_{zx} \\ S_{xy} & S_{yy} & S_{zy} \\ S_{xz} & S_{yz} & S_{zz} \end{bmatrix} = [A]^T \begin{bmatrix} S_1 & 0 & 0 \\ 0 & S_2 & 0 \\ 0 & 0 & S_3 \end{bmatrix} [A] \qquad \text{(A3.1)}$$

where (S_1, S_2, S_3) can represent (S_H, S_h, S_v) but arranged in terms of their magnitudes and

$$[A] = \begin{bmatrix} \cos\gamma\cos\beta\cos\alpha - \sin\gamma\sin\alpha & \cos\gamma\cos\beta\sin\alpha + \sin\gamma\sin\alpha & -\cos\gamma\sin\beta \\ -\sin\gamma\cos\beta\cos\alpha - \cos\gamma\sin\alpha & \sin\gamma\cos\beta\cos\alpha + \cos\gamma\sin\alpha & \sin\gamma\sin\beta \\ \sin\beta\cos\alpha & \cos\beta\cos\alpha & \cos\beta \end{bmatrix}$$

(A3.2).

The Eulerian angles, α, β, γ define a sequence of three rotations required in the co-ordinate transformation (Figure A3.1). As is well known, six independent stress terms are required

to describe the nonconcentratred stress state (i.e. that existing before the wellbore is drilled) in the (x, y, z) wellbore co-ordinate system (see Figure A3.2). Solutions for the stress concentrations due to the normal components of these (S_{xx}, S_{yy}, S_{zz}) are already provided in the body of the thesis. Preliminary solutions for the shear components relative to our 'deviated' wellbore (S_{xy}, S_{xz}, S_{yz}) are described here. As follows our earlier procedures and because we retain elastic linearity, the complete stress concentrations resulting from a complex stress field of normal and shear terms can still be found by the appropriate superposition of the individual solutions, a task for the future.

The loss of symmetry due to the inclusion of a shear stress relative to the wellbore is problematic from the perspective of a finite element solution. It is worth noting briefly that to eliminate the asymmetric effect in the z direction, one of the solutions will require that the wellbore is mirrored at the top and bottom of the model (Figure A3.2).

As noted, the assumption of linearly elastic and isotropic material properties allows simplification of the finite element model by decomposing nine components of far-field stresses into three normal tractions, S_{xx}, S_{yy} and S_{zz} and three sets of pure shear forces, S_{xy} , S_{yz}, and S_{xz}. Only one eighth of the entire volume of material around the wellbore as shown in Figure A3.2 was required in the modeling of the normal tractions described in the previous chapters. The boundary conditions and models needed to accommodate the loss of symmetry in modeling the shear stresses are shown in Figure A3.3; these require much larger models consisting of at least one half of the entire volume under each of three sets of shear forces.

Figure A3.3a shows the boundary conditions under the shear force S_{xy}. No displacements are allowed normal to the base at $z = 0$ and the surface normal to x or y axis. The boundary conditions under the shear forces S_{xz} and S_{yz} are shown in Figure A3.3b-c. Note that solution of this problem allowed symmetry considerations with respect to the wellbore axis to be exploited but the lack of symmetry with respect to the bottom of the wellbore required that a mirror approach with a virtual wellbore coming up from the bottom

of the model being required. For the S_{xz} problem, no normal displacements are allowed in the x-z plane and at the bottom surface, similar constraints exist for the S_{yz} solution. In Figure A3.3b-c the ends of the two mirrored cavities are separated by a distance of about ten times of borehole diameter. Preliminary tests indicated that there was negligible interference between the concentrated stress fields induced by each in accordance with St. Venant's principle.

Six sets of finite element programs corresponding to three normal tractions and three sets of shear forces with a varying core stub length and a curved cut bottomhole have been developed for the geometry of this wellbore. Near wellbore details of the finite element mesh for the normal stresses are shown in Figure A3.4 and this is similar to models used in the body of the thesis. Details of the meshes for the shear stress problems of S_{yz} (or S_{xz}) and of S_{xy} are given in Figures A3.5 and 6, respectively, for the case where the core stub has a length equal the core diameter and a half circle bottomhole kerf with the ratio of cut width and core ratio equal to 1.

The models for the normal tractions are the same as those used in previous chapters for a vertical borehole. For the shear forces, however, the models have a volume four times of that the normal tractions with 11948 nodes and 9616 elements even after optimization of the design. Because great numbers of the nodes and elements, the required computing time and hard-driver space were increased significantly. On a Sun workstation basis, about 550 MB hard-drive space is required for the calculations. The real computation time is about 1.5 hours as compared with about 20 min. on a Sun Ultra 1 workstation for the calculation of the model with normal tractions only.

3.2 STRESS CONCENTRATIONS UNDER APPLIED SHEAR STRESS

The stress concentrations induced under normal tractions are similar to those presented in Chapter 2 to 4 and Appendix 2 and need not be described here. The characteristics of the stresses induced by concentration of the shear stresses are more

complex and of correspondingly more interest. A preliminary calculations for the two unique cases of shear stresses with S_{xz} and S_{xy} all for a magnitude of 20 MPa in a material with a medium of Young's modulus of 20 GPa and Poisson's ratio of 0.25 are presented here.

Figure A3.7 show the three dimensional contours of the most tensional principal stress, σ_3, and maximum shear stress, $(\sigma_1 - \sigma_3)/2$, under the shear forces of S_{xz}, respectively, where the core stub has a length of 1/4 core diameter. In Figure A3.7a, very high tension with a magnitude of -85 MPa is produced at the outer side of the kerf. The magnitude of the tensile stresses are more than four times of the applied shear force. In contrast, at the opposite side of the wellbore the concentrated stresses are basically compressive. This asymmetry of stresses may result in different modes of wellbore wall failure at opposite azimuths. The concentrated stresses within the body of the core appear either compressive or slightly tensile for this case. In Figure A3.7b, the greatest induced shear is located at the outer side of the kerf and 90° from the x-z plane; the magnitude of the greatest shear stress is approximately 45 MPa. The core stub basically is subject to low shear stresses. In general, it appears that S_{xz} will have more influence on damage of the wellbore wall than on bringing the core towards fracture but the asymmetric stresses induced within the core might be expected to influence the growth and trajectories of the drilling induced fractures.

The wellbore and bottomhole stress concentrations under the shear forces of S_{xy} are shown in Figure A3.8. First, the wellbore wall stresses removed from the wellbore bottom agree with Kirsch's plane strain solution (1898) as might easily anticipated by decomposing the shear stress into two normal stresses at 45°; the tensile stresses have magnitudes of 0.0 and -80.0 MPa at Φ = -45° and 45°, respectively (Figure A3.8a). Note that the simple elastic solution no longer applies within approximately one core diameter from the wellbore bottom. In contrast, high tensions with a magnitude of -74.0 MPa at Φ = -45° are generated at the bottom of the borehole within material that would be removed

during drilling. High shear stresses are located at the bottom of the kerf and on the wellbore wall with magnitudes near 45 MPa and 40 MPa (Figure A3.8b), respectively. Referring back to Figure A3.8a, it can be seen that these shear stresses essentially result from the large least principal stresses.

These results are provided only to give an idea of work in progress and the complexities that will arise when more complex stress states are considered. These preliminary results suggest that the stress concentrations at the end of an inclined borehole differ significantly from a vertical borehole. Principally, deviation of the wellbore from a principal far field stress axis will result in substantial asymmetries in the stress concentrations in both the core and the wellbore wall with implications for the stress interpretation of both drilling induced core fractures and geophysical image logs.

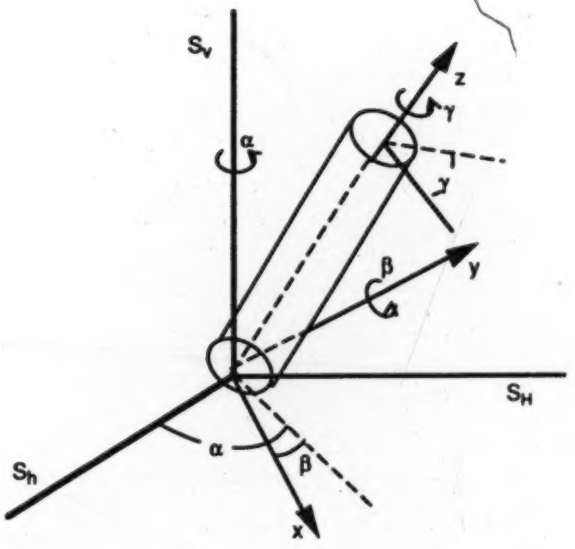

Figure A3.1. Inclined borehole with in situ stress field.

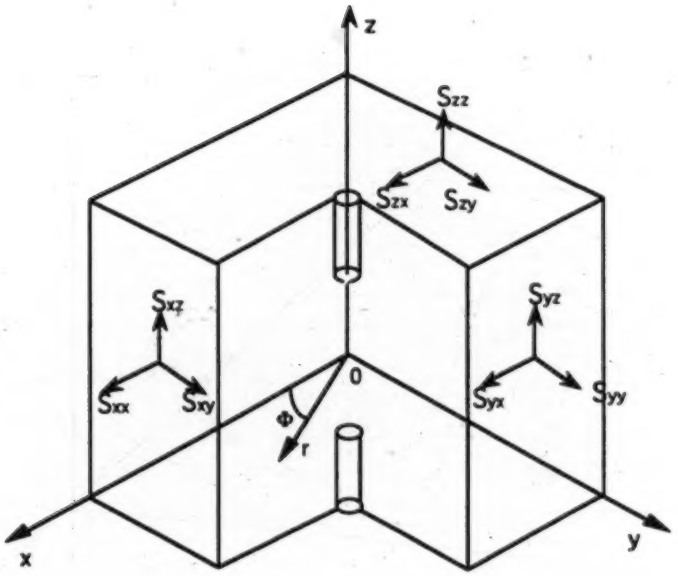

Figure A3.2. The stress conditions for an inclined borehole. A mirrored borehole in the -z direction is used for eliminate the asymmetric effect in finite element modeling under pure shear forces of S_{yz} and S_{xz}.

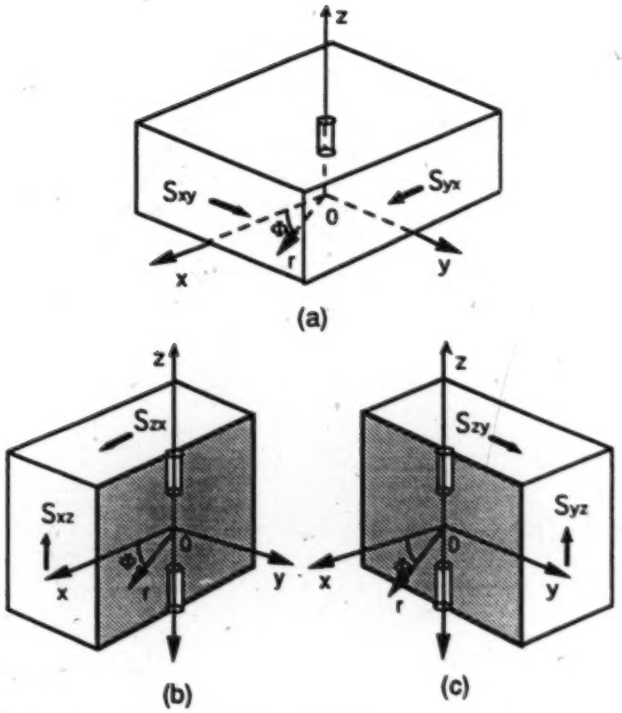

Figure A3.3. The decomposed pure shear models used for finite element modeling under (a) S_{xy} and S_{yx}, (b) S_{xz} and S_{zx}, and (c) S_{yz} and S_{zy}.

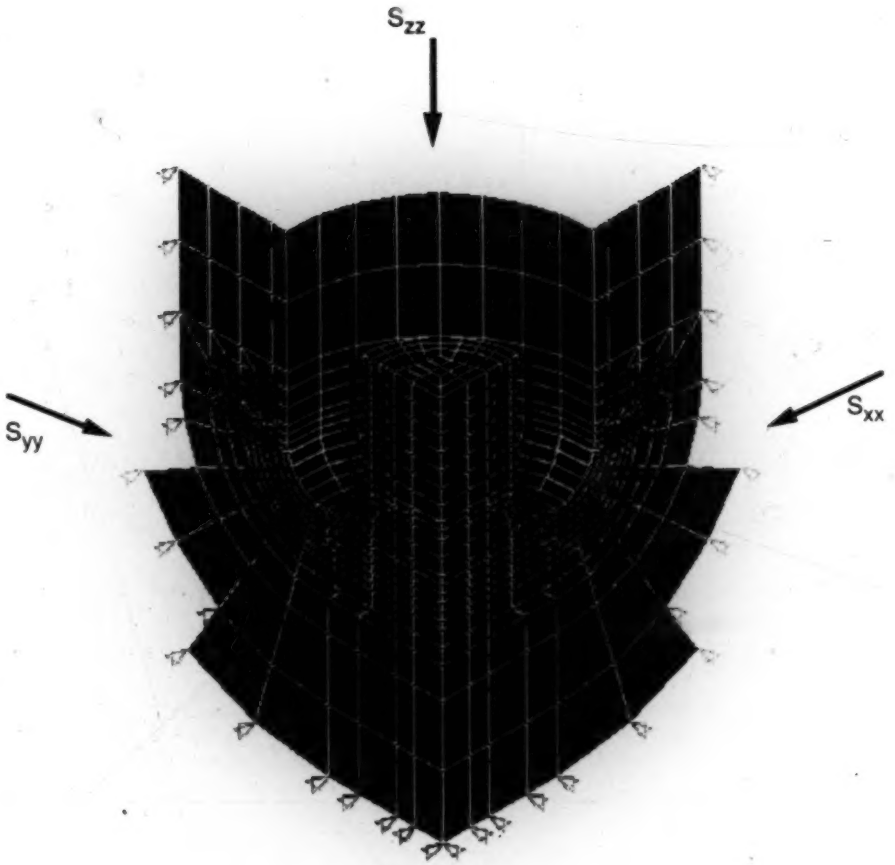

Figure A3.4. The finite element mesh in the vicinity of borehole bottom for the normal tractions, S_{xx}, S_{yy} and S_{zz}.

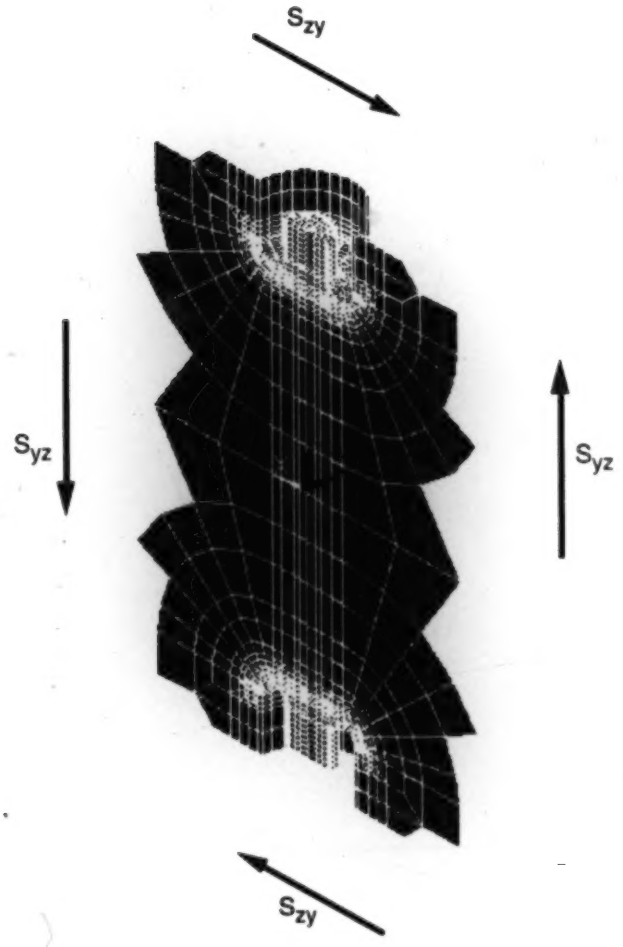

Figure A3.5. Finite element mesh in the vicinity of bottomhole for the shear forces of S_{yz} and S_{zy}. The mesh for the shear forces of S_{xz} with S_{zx} is the same except a 90° rotation subject to the z axis.

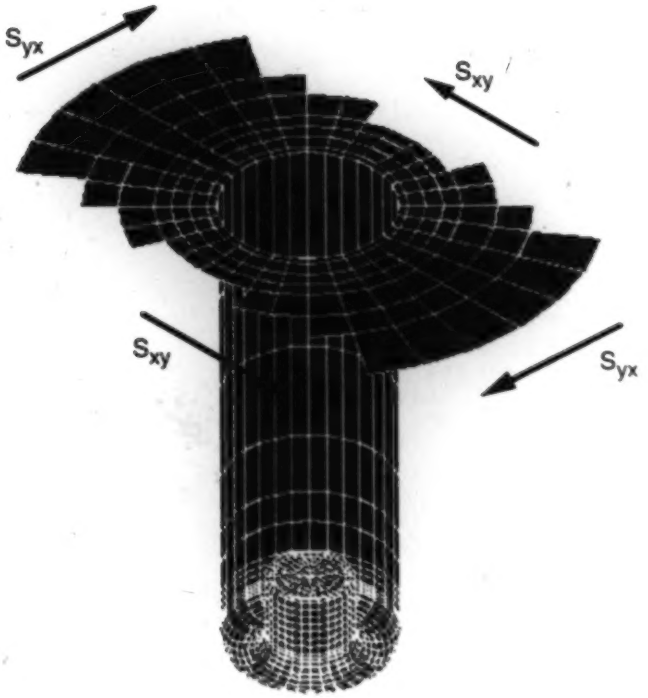

Figure A3.6. Finite element mesh in the vicinity of borehole for the shear forces of S_{xy} and S_{yx}.

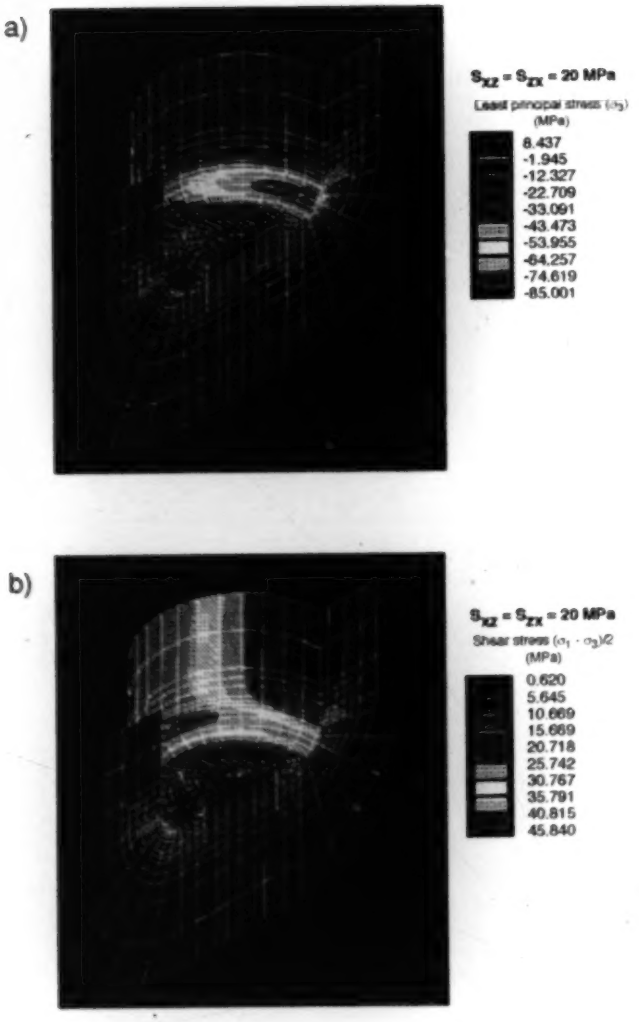

Figure A3.7. a) Least principal stresses (σ_3) and b) shear stresses (σ_1 - σ_3)/2 at the wellbore bottom under the shear forces of S_{XZ} and S_{ZX}.

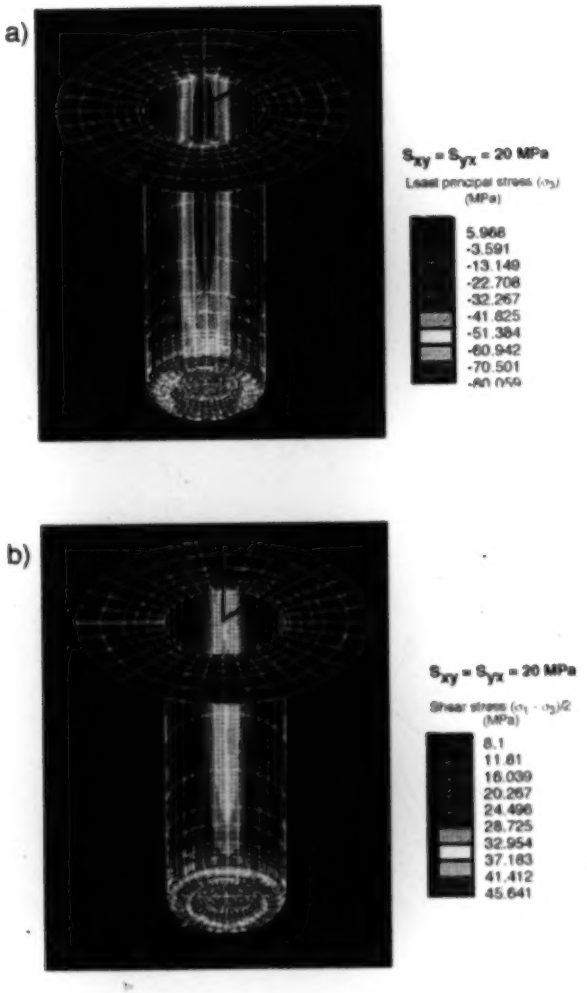

Figure A3.8. a) Least principal stresses (σ_3) and b) shear stresses (σ_1 - σ_3)/2 at the wellbore bottom under the shear forces of S_{xy} and S_{yx}.

APPENDIX 4.1

Fracture Trajectory Algorithm

The stresses calculated by finite element modeling are irregularly distributed with the nodes of the mesh of the finite element model. In the fracture trajectory determination procedure, the magnitudes and orientations of the most tensional principal stress (σ_3) within the two planes perpendicular and parallel to the greatest horizontal compression and intersecting at the wellbore axis were first interpolated into a finer grid. In each plane, the fracture was assumed to initiate at the grid point with the largest tension, opening of the fracture occurs parallel to the direction of σ_3 and the subsequent propagation of the fracture is perpendicular to this.

The determination of the fracture trajectories follows a procedure reminiscent of that employed in simple seismic ray tracing algorithms. Figure A4.1 illustrates the process of the fracture tracing, where Δx and Δy ($\Delta x = \Delta y$) are the spacings within the interpolated grid in the x (horizontal) and y (vertical) directions. They have a dimension about 1/100 of the core diameter. The fracture tracing starts at the grid node 1 also denoted as A; the line from A to B represents a small segment of the fracture trajectory across the cell and its orientation is dictated by the orientation of σ_3 at A. The segment intersects the boundary between two adjacent cells at point B which lies between the grid positions 2 and 3 where σ_3 is known. The magnitude and direction of σ_3 at B is then linearly interpolated from these two locations; the next segment of the fracture trajectory continues based on this orientation to point C. Point C lies on a horizontal boundary between two cells and here the new direction of the fracture tracing from C is determined by linear interpolation using the data at grid nodes 3 and 4. Continued propagation halts when the fracture trajectory either intersects the wellbore axis or when σ_3 is no longer tensional. The procedure is carried out in both planes only if the initial fracture trajectory leading from the point of the

greatest tension in both intersects the wellbore axis. The petal fracture like trajectories in Figures 4.6 and 4.8 are examples in which the calculations were only carried out in one plane.

We note that in the present analysis only the relationship between a potential fracture trajectory and the characteristics of the in situ stress field are of interest. These trajectories are independent of the material strength and as a result within the text the potential fracture paths have been referred to as fracture trajectories.

A drawback of the present arrangement is that cases of stable fracture propagation may not be adequately handled. For example, a stably growing fracture with a distinct opening and loss of cohesion (as opposed to a rupture as mentioned earlier) will of itself change the geometry of the situation and consequently also must influence the stress concentrations. Dealing with such situations from such a fracture mechanics perspective in relatively complicated geometries is not necessarily straightforward. Although such fracture mechanics approaches studies should remain a goal for the future, the good correspondence between the predicted fracture trajectories and suggests this simplified approach is valid.

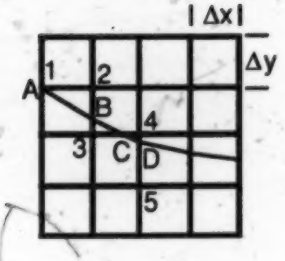

Figure A4.1. Illustration of fracture tracing process

APPENDIX 4.2

Example of Programs for Fracture Tracing

```
% ------------------------------------------------------------------------------------------------------------
%
% THIS MATLAB PROGRAM TJ_KERF.M CAN BE USED FOR FRACTURE
% TRACING
%
%------------------------------------------------------------------------------------------------------------
%
% Input core stub length and number of nodes for tracing
%
    num1 = 2.5;
    num2 = 196;
%
% Input fracture initiation location
%
    num3 = input( 'x coordinate of initiation location:  ','s');
    num4 = input( 'y coordinate of initiation location:  ','s');
    xs = str2num(num3);
    ys = str2num(num4);
%
% Input node coordinates
%
    fid1 = fopen('x1y?z1/s1_xy4.x1yqz1','r');
    a = fscanf(fid1,'%f %f %f\n',[3,num2]);
    fclose(fid1);
    a = a';
%
    x1 = a(:,1);
    y1 = a(:,2) + 10.0;
%
% Input orientation of principal stresses (cosine directions)
%
    fid2 = fopen('x1y?z3q_strikeb/spv4.x1y3.5_20z3q_s0','r');
    b = fscanf(fid2,'%f %f %f %f %f %f %f %f\n',[8,inf]);
    fclose(fid2);
    b = b';
%
    num3 = 3.*num2;
    k = 1;
    for i=1:3:num3
        b1(k,:) = b(i,:);
        k = k + 1;
    end
%
% Calculate orientation of principal stress in 360 degree
%
    for j = 1:num2
        if b1(j,4)/b1(j,3) < 0.0
            z1(j) = atan(b1(j,4)/b1(j,3)) + pi + pi/2;
```

```
        else
            z1(j) = atan(b1(j,4)/b1(j,3)) + pi/2;
        end
    end
%
    z1 = z1';
%
% Determine region to be interpolated
%
    k=0;
    for i = 1:num2
        if y1(i) >= -10.0
            k = k+1;
            x(k) = x1(i);
            y(k) = y1(i);
            z(k) = z1(i);
        end
    end
%
% Interpolate principal stress orientations
%
    tix = 0:.2:16;
    xn = 16/0.2 + 1;
    tiy = 0:.2:20;
    yn = 20/0.2 + 1;
    [xi1,yi1] = meshgrid(tix,tiy);
    zi1 = griddata(x,y,z,xi1,yi1);

%
% Clean up the inside of borehole
%
    xi1 = xi1';
    yi1 = yi1';
    zi1 = zi1';
    ai = 0.2;
    bi = 0.2;
%
    xi = xs/ai;
    yi = ys/bi;
    i0 = xi;
    j0 = yi;
    alpha = zi1(i0,j0);
    k1 = 0;
    k2 = 0;
    k = 1;
%
% Fracture tracing
%
%-------------------------------------------------------------------------------------------------------
    while xi >= 1 & yi >=1
%-------------------------------------------------------------------------------------------------------
%
% Case 1, when tracing intersects at horizontal boundary of a grid
%
```

```
    if (yi - round(yi)) == 0.0
        check1 = 1;
        xr = round(xi);
        xi = xi;
        yi = yi;
        yr = round(yi);
%
        if (xi - xr) <= 0.0
        deltx = 1 - (xr - xi);
        ix0 = xr;
        ix1 = ix0 - 1;
        iy0 = yr;
        iy1 = iy0;
        elseif (xi - xr) > 0.0
        deltx = xi - xr;
        ix1 = xr;
        ix0 = ix1 + 1;
        iy0 = yr;
        iy1 = iy0;
        end
%
        alpha1 = atan(deltx) + pi/2;
        alpha2 = pi;
        alpha3 = atan(1/deltx) + pi;
        alpha4 = 3*pi/2;
%
        if alpha >= pi/2 & alpha < alpha1
        xi = xi - tan(alpha - pi/2);
        yi = yi + 1;
        elseif alpha >= alpha1 & alpha <= alpha3;
        xi = xi - deltx;
        yi = yi - deltx*tan(alpha);
        elseif alpha > alpha3 & alpha <= 3*pi/2;
        xi = xi - tan(3*pi/2-alpha);
        yi = yi - 1;
        end
%
% Linear interpolation of principal stresses at two adjacent grid nodes
%
        if zi1(ix1,iy1) > zi1(ix0,iy0)
        alpha = zi1(ix0,iy0) + deltx*abs(zi1(ix1,iy1) - zi1(ix0,iy0));
        else
        alpha = zi1(ix0,iy0) - deltx*abs(zi1(ix1,iy1) - zi1(ix0,iy0));
        end
    k1 = k1 + 1;
    k = k1 + k2;
    XI(k) = xi;
    YI(k) = yi;
    ZI(k) = alpha;
%
    end
%
% Case 2, when tracing intersects at vertical boundary of a grid
%
```

```
    if (yi - round(yi)) ~= 0.0
        check2 = 2;
        xr = round(xi);
        xi = xi;
        yi = yi;
        yr = round(yi);

        if (yi - yr) > 0.0
        delty = 1 - (yi - yr);
        ix0 = xr;
        ix1 = ix0;
        iy0 = yr;
        iy1 = iy0 + 1;
        elseif (yi - yr) < 0.0
            delty = yr - yi;
        ix0 = xr;
        ix1 = ix0;
        iy0 = yr - 1;
        iy1 = yr;
        end
        alpha1 = atan(1/delty) + pi/2;
        alpha2 = pi;
        alpha3 = atan(1-delty) + pi;
        alpha4 = 3*pi/2;
%
        if alpha >= pi/2 & alpha < alpha1
        xi = xi - delty*tan(alpha - pi/2);
        yi = yi + delty;
        elseif alpha >= alpha1 & alpha <= alpha3;
        xi = xi - 1;
        yi = yi - tan(alpha);
        elseif alpha > alpha3 & alpha <= 3*pi/2.;
        xi = xi - (1-delty)*tan(3*pi/2-alpha);
        yi = yi - (1 - delty);
        end
%
% Linear interpolation of principal stresses at two adjacent grid nodes
%
        if zi1(ix1,iy1) > zi1(ix0,iy0)
        zi1(ix0,iy0)
        alpha = zi1(ix0,iy0) + (1 - delty)*abs(zi1(ix1,iy1) - zi1(ix0,iy0))
        else
        alpha = zi1(ix0,iy0) - delty*abs(zi1(ix1,iy1) - zi1(ix0,iy0));
        end
    k2 = k2 + 1;
    k = k1 + k2;
    XI(k) = xi;
    YI(k) = yi;
    ZI(k) = alpha;
%
    end
%-------------------------------------------------------------------------------------------------------
    end
%-------------------------------------------------------------------------------------------------------
```

```
% Plot the fracture trajectory
%
    XYZ = [XI*0.2-0.2;YI*0.2-0.2;ZI];
%
    xg1  = [9.8+2,9.8+2,18+2,18+2,2.0,2.0,7.2,7.2];
    yg1  = [2.5,12.0,12,-10,-10,2.7,2.7,2.5];
%
    alpha = -pi:pi/180.0:0.0;
    xg = 2.3*cos(alpha) + 7.5+2;
    yg = 2.3*sin(alpha) + 2.5;
    xx = [xg1 xg];
    yy = [yg1,yg];
    plot(xx,yy)
    cgray = [0.85,0.85,0.85];
    fill(xx,yy,cgray);
    hold on
%
% Plot borehole boundary
%
    x1 = [2.0,7.2];
    x2 = [11.8,11.8];
    x3 = [1.8,1.8];
    y1 = [2.7,2.7];
    y2 = [2.5,12.0];
    y3 = [-6.0,0.2];
    alpha = -(pi+3.0*pi/180):pi/2.0/90.0:0.0;
    x = 2.3*cos(alpha) + 9.5;
    y = 2.3*sin(alpha) + 2.5;
    h1 = plot(x1,y1);
    h2 = plot(x2,y2);
    %plot(x3,y3)
    hx = plot(x,y);
    set(h1,'LineWidth',[0.2])
    set(h2,'LineWidth',[0.2])
    set(hx,'LineWidth',[0.2])
%
    hold on
%
    plot(XI*0.2+2.0,YI*0.2-10.0)
    axis([0,30,-10,20]);
    axis('off');
%
% Output tracing data
%-------------------------------------------------------------------------------------------------------------
    outfile1 = input('Enter OUTFILE1 for trajectory:  ','s');
        fid2 = fopen(outfile1,'w');
        fprintf(fid2,' %10.4f %10.4f %10.4f\n',XYZ);
    status = fclose(fid2);
%-------------------------------------------------------------------------------------------------------------
%
% END OF PROGRAM
%
%-------------------------------------------------------------------------------------------------------------
```

APPENDIX 5.1

Stress Data Base Description

A large stress data base with a volume approximately 900 MB has been generated in this research. This appendix serves only to list the data available for potential collaborators For the sake of continuity, an example ANSYS program (Appendix 5.2), a MATLAB reading program (Appendix 5.3) and a MATLAB program for plotting stress orientations (Appendix 5.4) are also included. The bulk of this data base are the stress calculations of six primary stress components S_H, S_h, S_v, S_p, S_r and S_b for a growing core stub with a varying Poisson's ratio and different bottomhole cut geometries. The superposition of stress tensors, the calculations of stress orientations and stress contours, and the calculations for fracture tracing add additional data into this data base. Based on the bottomhole cut geometries, this data base is catalogued into two sub-data-bases corresponding to the curved cut with ratios of (kerf) width/core radius 1 (Chapter 4), and the flat cut (kerf) with ratios of cut width/core radius equal to 1/5 (Chapter 2), 2/5 (Chapter 3) and 1. The magnitudes of the applied primary stresses are 20 MPa and Young's modulus is 20 GPa in all generated data but these parameters and Poisson's ratio, can be changed in the finite element programs based on the requirement of a calculation.

The stress tensors can be superimposed by linear scaling. This is implemented by the program SOL_SOTT2.M (Appendix 5.3) which inputs the magnitudes of the applied stresses. Young's modulus and Poisson's ratio need to be defined before the finite element modeling is conducted.

Listing of main directories (start with slash) and files for the flat cut cases

Directory and File	Comments
Cut (kerf) width/ core radius = 2/5	
/Fsq.files	

/Fsq.x_p05	S_H, υ = 0.05
f169.b1 - f169.b12	finite element programs corresponding to core stub lengths 0.0, 0.02, 0.05, 0.1, 0.15, 0.2, 0.25, 0.3, 0.4, 0.5, 0.7, 1.0 of core diameter
/Unix.dat1 - /Unix.dat12	stress data corresponding each core stub length
sdat.all	stress for entire model
sdat.axi, sdat.b0, sdat.b9	stress along core axis, cutting surface at $\Phi = 0^\circ$ and 90°, respectively
sdat.c0, sdat c9	stress along core side surface at $\Phi = 0^\circ$ and 90°, respectively
sdat.eb, sdat.ec, sdat.ew	stress on entire cutting surface, entire core side surface, and entire wellbore wall
sdat.w0, sdat w9	stress along wellbore wall at $\Phi = 0^\circ$ and 90°, respectively
sdat.s0, sdat.s9, sdat.s45	stress in the sections across borehole axis at $\Phi = 0^\circ$, 45° and 90°, respectively

The content of the following directories is similar to the above except otherwise described

/Fsq.x_p15	S_H, υ = 0.15
/Uniy.dat1 - /Uniy.dat12	stress data corresponding to core stub lengths 0.0, 0.02, 0.05, 0.1, 0.15, 0.2, 0.25, 0.3, 0.4, 0.5, 0.7, 1.0 of core diameter
/Fsq.x	S_H, υ = 0.25
/Fsq.x_p35	S_H, υ = 0.35
/Fsq.x_p45	S_H, υ = 0.45
/Fsq.y_p05	S_h, υ = 0.05
/Uniy.dat1 - /Uniy.dat12	stress data corresponding to core stub lengths 0.0, 0.02, 0.05, 0.1, 0.15, 0.2, 0.25, 0.3, 0.4, 0.5, 0.7, 1.0 of core diameter
/Fsq.y_p15	S_h, υ = 0.15
/Fsq.y	S_h, υ = 0.25
/Fsq.y_p35	S_h, υ = 0.35
/Fsq.y_p45	S_h, υ = 0.45
/Fsq.z_p05	S_v, υ = 0.05
/Uniz.dat1 - /Uniz.dat12	stress data corresponding to core stub lengths 0.0, 0.02, 0.05, 0.1, 0.15, 0.2, 0.25, 0.3, 0.4, 0.5, 0.7, 1.0 of core diameter
/Fsq.z_p15	S_v, υ = 0.15
/Fsq.z	S_v, υ = 0.25
/Fsq.z_p35	S_v, υ = 0.35
/Fsq.z_p45	S_v, υ = 0.45
/Fsq.bit	bit weight, υ = 0.25
/b1 - /b12	stress data corresponding to core stub lengths 0.0, 0.02, 0.05, 0.1, 0.15, 0.2, 0.25, 0.3, 0.4, 0.5, 0.7, 1.0 of core diameter
/Fsq.pre	fluid pressure, υ = 0.25

/p1 - /p12	stress data corresponding to core stub lengths 0.0, 0.02, 0.05, 0.1, 0.15, 0.2, 0.25, 0.3, 0.4, 0.5, 0.7, 1.0 of core diameter

Cut (kerf) width/ core radius = 1/5 with "infinite block"

/Fos.files

/Fos.x_p05	S_H, $\upsilon = 0.05$
/x1 - /x12	stress data corresponding to core stub lengths 0.0, 0.02, 0.05, 0.1, 0.15, 0.2, 0.25, 0.3, 0.4, 0.5, 0.7, 1.0 of core diameter
/Fos.x_p15	S_H, $\upsilon = 0.15$
/Fos.x_p25	S_H, $\upsilon = 0.25$
/Fos.x_p35	S_H, $\upsilon = 0.35$
/Fos.x_p45	S_H, $\upsilon = 0.45$
/Fos.y_p05	S_h, $\upsilon = 0.05$
/y1 - /y12	stress data corresponding to core stub lengths 0.0, 0.02, 0.05, 0.1, 0.15, 0.2, 0.25, 0.3, 0.4, 0.5, 0.7, 1.0 of core diameter
/Fos.y_p15	S_h, $\upsilon = 0.15$
/Fos.y_p25	S_h, $\upsilon = 0.25$
/Fos.y_p35	S_h, $\upsilon = 0.35$
/Fos.y_p45	S_h, $\upsilon = 0.45$
Fos.z_p05	S_v, $\upsilon = 0.05$
/z1 - /z12	stress data corresponding to core stub lengths 0.0, 0.02, 0.05, 0.1, 0.15, 0.2, 0.25, 0.3, 0.4, 0.5, 0.7, 1.0 of core diameter
/Fos.z_p15	S_v, $\upsilon = 0.15$
/Fos.z_p25	S_v, $\upsilon = 0.25$
/Fos.z_p35	S_v, $\upsilon = 0.35$
/Fos.z_p45	S_v, $\upsilon = 0.45$

Cut (kerf) width/ core radius = 1/5 drilled within 4 in. cylindrical cores

/Fos.files

/Fos4.xy_p05	S_r, $\upsilon = 0.05$
/r1 - /r12	stress data corresponding to core stub lengths 0.0, 0.02, 0.05, 0.1, 0.15, 0.2, 0.25, 0.3, 0.4, 0.5, 0.7, 1.0 of core diameter
/Fos4.xy_p15	S_r, $\upsilon = 0.15$
/Fos4.xy_p25	S_r, $\upsilon = 0.25$
/Fos4.xy_p35	S_r, $\upsilon = 0.35$
/Fos4.xy_p45	S_r, $\upsilon = 0.45$
/Fos4.z_p05	S_v, $\upsilon = 0.05$
/Fos4.z_p15	S_v, $\upsilon = 0.15$
/Fos4.z_p25	S_v, $\upsilon = 0.25$
/Fos4.z_p35	S_v, $\upsilon = 0.35$
/Fos4.z_p45	S_v, $\upsilon = 0.45$

Cut (kerf) width/ core radius = 1/5 drilled within 5 in. cylindrical cores

Fos.files	
/Fos5.xy_p05	S_r, υ = 0.05
/r1 - /r12	stress data corresponding to core stub lengths 0.0, 0.02, 0.05, 0.1, 0.15, 0.2, 0.25, 0.3, 0.4, 0.5, 0.7, 1.0 of core diameter
/Fos5.xy_p15	S_r, υ = 0.15
/Fos5.xy_p25	S_r, υ = 0.25
/Fos5.xy_p35	S_r, υ = 0.35
/Fos5.xy_p45	S_r, υ = 0.45
/Fos5.z_p05	S_v, υ = 0.05
/Fos5.z_p15	S_v, υ = 0.15
/Fos5.z_p25	S_v, υ = 0.25
/Fos5.z_p35	S_v, υ = 0.35
/Fos5.z_p45	S_v, υ = 0.45

Cut (kerf) width/ core radius = 1

/F5.files	
/F5.x	S_H, υ = 0.05
/F5.y	S_h, υ = 0.15
/F5.z	S_v, υ = 0.25

Listing of main directories and files for the curved cut cases

Directory and File	Comments
Cut (kerf) width/ core radius = 1	
/Fcu.x_p25	S_H, υ = 0.25
fcu.b1 - fcu.b9	finite element programs corresponding to core stub lengths 0.0, 0.1, 0.2, 0.25, 0.3, 0.4, 0.5, 0.7, 1.0 of core diameter
/x1 - /x9	stress data corresponding to core stub lengths 0.0, 0.1, 0.2, 0.25, 0.3, 0.4, 0.5, 0.7, 1.0 of core diameter
/Fcu.y_p25	S_h, υ = 0.25
y1 - /y9	stress data corresponding to core stub lengths 0.0, 0.1, 0.2, 0.25, 0.3, 0.4, 0.5, 0.7, 1.0 of core diameter
/Fcu.z_p25	S_v, υ = 0.25
/z1 - /z9	stress data corresponding to core stub lengths 0.0, 0.1, 0.2, 0.25, 0.3, 0.4, 0.5, 0.7, 1.0 of core diameter

Listing of main directories and files for the inclined borehole with curved cut bottomhole

Directory and File	Comments
/F1s.x	far-field stress Sxx

fs.x1 - fs.x9	finite element programs corresponding to core stub lengths 0.0, 0.1, 0.2, 0.25, 0.3, 0.4, 0.5, 0.7, and 1.0 of core diameter
/F2s.y	far-field stress Syy
fs.y1 - fs.y9	finite element programs
/F3s.z	far-field stress Szz
fs.z1 - fs.z9	finite element programs
/F4s.yx	far-field stress Syx
fs.yx1 - fs.yx9	finite element programs
/F5so.yx	far-field stress Sxy
fso.yx1 - fso.yx9	finite element programs
/F6s.xz	far-field stress Sxz
fs.xz1 - fs.xz9	finite element programs
/F7so.xz	far-field stress Szx
fso.xz1 - fso.xz9	finite element programs
/F8s.yz	far-field stress Syz
fs.yz1 - fs.yz9	finite element programs
/F6so.yz	far-field stress Szy
fso.yz1 - fso.yz9	finite element programs

Listing of main directories and files for the related calculations

Directory and File	Comments
Fracture tracing	
/TJ.dat_normal	data and programs for fracture tracing in the normal faulting regime
/TJ.dat_strike	data and programs for fracture tracing in the strike-slip faulting regime
/TJ.dat_thrust	data and programs for fracture tracing in the thrust faulting regime

APPENDIX 5.2

Example of ANSYS Programs

```
C ---------------------------------------------------------------------------------------------------
C
C THIS ANSYS PROGRAM FCU.B9 GENERATES A FINITE ELEMENT MODEL
C WITH A CURVED CUT BOTTOMHOLE, AND 3505 NODES AND 3536
C ELEMENTS.
C
C ---------------------------------------------------------------------------------------------------
C
C PREPROCESSING FOR BUILDING THE MODEL
C
C ---------------------------------------------------------------------------------------------------
C
      /prep7
      /show,x11
      /view,,-0.2,0.2,-0.2
C
C Set coordinate systems by key points and change the vertical axis from y to z
C
      k,1
      k,2,1
      k,3,,,1
      cskp,11,0,1,3,2
      cskp,12,1,1,3,2
      local,15,1,0.0,77.5,7.5,180.0,,-90.0
      csys,11
C
C Define element types and input Young's modulus and Poisson's ratios
C
      et,1,45
      ex,1,1000.0
      nuxy,1,0.25
      et,2,95
      ex,2,1000.0
      nuxy,2,0.25
C
C Generate nodes
C
      n,1
      n,2,0.6,0.6
      n,3,1.2,1.2
      n,4,1.8
      n,5,1.8,0.6
      n,6,1.8,1.2
      n,7,1.8,1.8
      n,8,1.2,1.8
      n,9,0.6,1.8
      n,10,,1.8
      n,11,3.0
      n,12,2.9,0.6
```

```
n,13,2.7,1.2
n,14,2.5,1.8
n,15,2.4,2.4
n,16,1.8,2.5
n,17,1.2,2.7
n,18,0.6,2.9
n,19,,3.0
csys,12
n,20,4.5
n,28,4.5,90.0
fill
n,29,5.6
n,37,5.6,90.0
fill
ngen,2,9,29,37,1,0.9
ngen,3,9,38,46,1,1.0
ngen,2,9,56,64,1,0.9
n,74,10.5
n,82,10.5,90.0
fill
n,83,12.0
n,91,12.0,90.0
fill
n,92,16.0
n,100,16.0,90.0
fill
csys,11
n,101,20.0
n,102,19.91,3.91
n,103,19.45,7.91
n,104,18.27,12.27
n,105,16.36,16.36
n,106,12.27,18.27
n,107,7.91,19.45
n,108,3.91,19.91
n,109,,20.0
C
n,110,30
n,111,30,5.967
n,112,30,12.426
n,113,30,20.045
n,114,30;30
n,115,20.045,30
n,116,12.426,30
n,117,5.967,30
n,118,,30
C
n,119,45
n,123,45,30
fill,119,123
n,124,45,45
n,125,30,45
n,129,,45
fill, 125,129
```

```
C
      n,130,100
      n,134,100,30
      fill
      n,135,100,45
      n,136,100,100
      n,137,45,100
      n,138,30,100
      n,142,,100
      fill,138,142
C
      ngen,2,142,1,142,1,,,21.0
      ngen,2,284,1,142,1,,,38.0
      ngen,2,426,1,142,1,,,48.0
      ngen,2,568,1,142,1,,,56.0
      ngen,2,710,1,142,1,,,61.0
      ngen,2,852,1,142,1,,,65.0
      ngen,2,994,1,142,1,,,69.0
      ngen,2,1136,1,142,1,,,70.7
C
C Into the area of 20 node elements
C
      n,1279,0.0,0.0,71.1
      n,1281,0.0,0.0,71.5
      n,1282,0.3,0.3,71.5
      n,1283,0.6,0.6,71.5
      n,1284,0.9,0.0,71.5
      n,1285,1.2,0.6,71.5
      n,1286,1.2,1.2,71.5
      n,1287,0.6,1.2,71.5
      n,1288,0.0,0.9,71.5
      n,1289,1.8,0.0,71.5
      n,1290,1.8,0.3,71.5
      n,1291,1.8,0.6,71.5
      n,1292,1.8,1.2,71.5
      n,1293,1.8,1.8,71.5
      n,1295,0.6,1.8,71.5
      fill
      n,1297,0.0,1.8,71.5
      fill,1295,1297
      ngen,2,151,1147,1278,1,0.0,0.0,0.8
C
      n,1430,0.0,0.0,71.75
      n,1431,1.8,0.0,71.75
      n,1432,1.8,0.6,71.75
      n,1433,0.6,0.6,71.75
      n,1434,0.6,1.8,71.75
      n,1435,0.0,1.8,71.75
C
      ngen,4,155,1281,1429,1,0.0,0.0,0.5
      ngen,2,155,1746,1894,1,0.0,0.0,0.6
C
      ngen,3,155,1430,1435,1,0.0,0.0,0.5
      ngen,3,155,1740,1745,1,0.0,0.0,0.55
```

```
C
C Into the area of borehole bottom
C
C First layer
C
        ngen,2,155,1901,1944,1,0.0,0.0,0.5
        csys
        csys,15
        n,2100,3.5,105.69,0.0
        n,2109,3.5,90.0,0.0
        n,2118,3.5,74.31,0.0
        csys,12
        ngen,9,1,2100,2118,1,,11.25
        ngen,2,155,1972,2049,1,,,0.5
C
C Second layer
C
        n,2205,0.0,0.0,74.3
        ngen,2,2205,1,37,1,,,74.5
        csys
        csys,15
        n,2234,3.5,121.38,0.0
        n,2243,2.9,121.38,0.0
        n,2260,2.7,121.38
        n,2269,2.9,113.535
        n,2278,2.9,105.69,0.0
        n,2295,2.7,105.69
        n,2304,2.9,90.0,0.0
        n,2313,2.9,74.31,0.0
        n,2322,2.9,58.61,0.0
        n,2331,3.5,58.61,0.0
        csys,12
        ngen,9,1,2234,2234,1,,11.25
        ngen,17,1,2243,2243,1,,11.25/2
        ngen,9,1,2260,2269,1,,11.25
        ngen,17,1,2278,2278,1,,11.25/2
        ngen,9,1,2295,2331,1,,11.25
        ngen,2,204,2136,2204,1,,,0.4
C
C Third layer
C
        n,2409,,,74.8
        ngen,2,204,2206,2224,1,,,0.6
        csys
        csys,15
        n,2429,3.5,137.07,0.0
        n,2438,2.9,137.07,0.0
        n,2447,2.7,137.07,0.0
        n,2456,2.5,137.07,0.0
        n,2473,2.5,129.225,0.0
        n,2482,2.5,121.38,0.0
        n,2499,2.5,113.535,0.0
        n,2508,2.5,105.69,0.0
        n,2525,2.5,97.845,0.0
```

```
n,2534,2.5,90.0,0.0
n,2543,2.5,74.31,0.0
n,2552,2.5,58.61,0.0
n,2561,2.5,42.92,0.0
n,2570,2.9,42.92,0.0
n,2579,3.5,42.92,0.0
csys,12
ngen,9,1,2429,2447,1,,11.25
ngen,17,1,2456,2456,1,,11.25/2
ngen,9,1,2473,2473,1,,11.25
ngen,17,1,2482,2482,1,,11.25/2
ngen,9,1,2499,2499,1,,11.25
ngen,17,1,2508,2508,1,,11.25/2
ngen,9,1,2525,2579,1,,11.25
ngen,2,239,2349,2408,1,,,0.6
C
C Fourth layer
C
n,2648,,,75.5
ngen,2,239,2410,2428,1,,,0.8
csys
csys,15
n,2668,3.5,152.76,0.0
n,2677,2.9,152.76,0.0
n,2686,2.7,152.76,0.0
n,2695,2.5,152.76,0.0
n,2712,2.5,144.91,0.0
n,2721,2.5,27.228,0.0
n,2730,2.9,27.228,0.0
n,2739,3.5,27.228,0.0
csys,12
ngen,9,1,2668,2686,1,,11.25
ngen,17,1,2695,2695,1,,11.25/2
ngen,9,1,2712,2739,1,,11.25
ngen,2,160,2588,2647,1,,,0.8
C
C Fifth layer
C
n,2808,,,76.45
ngen,2,160,2649,2667,1,,,1.1
n,2828,4.0,,77.0
n,2837,4:6,0.0,77.0
n,2846,4.8,,77.0
ngen,9,1,2828,2846,1,,11.25
n,2855,5.05,,77.0
n,2871,5.05,90.0,77.0
fill
C
csys,15
n,2872,2.5,160.6
C
csys,12
ngen,9,1,2872,2872,1,,11.25
ngen,2,53,2828,2836,1,5.95
```

```
      ngen,2,9,2881,2889,1,0.40
      ngen,2,9,2890,2898,1,0.6
      ngen,2,160,2748,2807,1,,,1.1
C
C End of node generating at borehole bottom
C
      n,2968,,,77.25
      n,2969,5.0,,77.25
      n,2977,5.0,90.0,77.25
      fill
      ngen,2,169,2809,2827,1,,,0.5
      n,2997,4.0,,77.5
      n,3005,4.0,90.0,77.5
      fill
C
      ngen,2,9,2997,3005,1,0.6
      ngen,2,9,3006,3014,1,0.4
      ngen,2,9,3015,3023,1,5.0
      ngen,2,9,3024,3032,1,0.4
      ngen,2,9,3033,3041,1,0.6
C
      ngen,2,143,2908,2967,1,,,0.5
      ngen,2,133,2978,3110,1,,,0.5
      ngen,2,266,2978,3110,1,,,1.5
      ngen,2,399,2978,3110,1,,,2.5
      ngen,2,532,2978,3110,1,,,4.5
C
      ngen,2,665,2978,3110,1,,,7.5
      ngen,2,798,2978,3110,1,,,12.5
      ngen,2,931,2978,3110,1,,,22.5
      ngen,2,1064,2978,3110,1,,,42.5
      ngen,2,1197,2978,3110,1,,,72.5
C
C End of node generating
C
C Generate elements
C
      e,1,4,5,2,143,146,147,144
      e,2,5,6,3,144,147,148,145
      e,3,6,7,8,145,148,149,150
      e,3,8,9,2,145,150,151,144
      e,2,9,10,1,144,151,152,143
C
      e,4,11,12,5,146,153,154,147
      egen,3,1,6
      e,7,14,15,16,149,156,157,158
      e,7,16,17,8,149,158,159,150
      egen,3,1,10
C
      e,11,20,21,12,153,162,163,154
      egen,8,1,13
      egen,11,9,13,20,1
C
      e,110,119,120,111,252,261,262,253
```

```
      egen,4,1,101
      e,114,123,124,125,256,265,266,267
      e,114,125,126,115,256,267,268,257
      egen,4,1,106
C
      e,119,130,131,120,261,272,273,262
      egen,5,1,110
      e,124,135,136,137,266,277,278,279
      e,124,137,138,125,266,279,280,267
      egen,5,1,116
C
      egen,8,142,1,120,1
C
C Into the area of 20 node elements
C
      type,2
      mat,2
C
      e,1137,1140,1141,1138,1281,1289,1291,1283
      emore,,,,,1284,1290,1285,1282
      emore,1279
      e,1138,1141,1142,1139,1283,1291,1292,1286
      emore,,,,,1285
      e,1139,1142,1143,1144,1286,1292,1293,1294
      e,1138,1139,1144,1145,1283,1286,1294,1295
      emore,,,,,,,,1287
      e,1137,1138,1145,1146,1281,1283,1295,1297
      emore,,,,,1282,1287,1296,1288
      e,1140,1147,1148,1141,1289,1298,1299,1291
      emore,,,,,,,,1290
      e,1141,1148,1149,1142,1291,1299,1300,1292
      egen,2,1,967
      e,1143,1150,1151,1152,1293,1301,1302,1303
      e,1144,1143,1152,1153,1294,1293,1303,1304
      egen,2,1,970
      e,1146,1145,1154,1155,1297,1295,1305,1306
      emore,,,,,1296
C
      type,1
      mat,1
C
      e,1147,1156,1157,1148,1298,1307,1308,1299
      egen,8,1,973
      egen,11,9,973,980,1
C
      e,1246,1255,1256,1247,1397,1406,1407,1398
      egen,4,1,1061
      e,1250,1259,1260,1261,1401,1410,1411,1412
      e,1251,1250,1261,1262,1402,1401,1412,1413
      egen,4,1,1066
      e,1255,1266,1267,1256,1406,1417,1418,1407
      egen,5,1,1070
      e,1260,1271,1272,1273,1411,1422,1423,1424
      e,1261,1260,1273,1274,1412,1411,1424,1425
```

```
      egen,5,1,1076
C
C New layer
C
      type,2
      mat,2
C
      e,1281,1289,1291,1283,1436,1444,1446,1438
      emore,1284,1290,1285,1282,1439,1445,1440,1437
      emore,1430,1431,1432,1433
      e,1291,1292,1286,1283,1446,1447,1441,1438
      emore,,,,1285,,,,1440
      emore,1432,,,1433
      e,1286,1292,1293,1294,1441,1447,1448,1449
      e,1283,1286,1294,1295,1438,1441,1449,1450
      emore,,,,1287,,,,1442
      emore,1433,,,1434
      e,1281,1283,1295,1297,1436,1438,1450,1452
      emore,1282,1287,1296,1288,1437,1442,1451,1443
      emore,1430,1433,1434,1435
      e,1289,1298,1299,1291,1444,1453,1454,1446
      emore,,,,1290,,,,1445
      emore,1431,,,1432
      e,1291,1446,1447,1292,1299,1454,1455,1300
      emore,1432
      e,1292,1300,1301,1293,1447,1455,1456,1448
      e,1293,1301,1302,1303,1448,1456,1457,1458
      e,1294,1293,1303,1304,1449,1448,1458,1459
      e,1295,1450,1460,1305,1294,1449,1459,1304
      emore,1434
      e,1295,1305,1306,1297,1450,1460,1461,1452
      emore,,,,1296,,,,1451
      emore,1434,,,1435
C
      type,1
      mat,1
C
      e,1298,1307,1308,1299,1453,1462,1463,1454
      egen,8,1,1093
      egen,11,9,1093,1100
      e,1397,1406,1407,1398,1552,1561,1562,1553
      egen,4,1,1181
      e,1401,1410,1411,1412,1556,1565,1566,1567
      e,1402,1401,1412,1413,1557,1556,1567,1568
      egen,4,1,1186
      e,1406,1417,1418,1407,1561,1572,1573,1562
      egen,5,1,1190
      e,1411,1422,1423,1424,1566,1577,1578,1579
      e,1412,1411,1424,1425,1567,1566,1579,1580
      egen,5,1,1196
C
      egen,5,155,1081,1200,1
C
C New layer
```

```
C
      type,2
      mat,2
C
      e,2056,2064,2066,2058,2206,2209,2210,2207
      emore,2059,2065,2060,2057
      e,2058,2066,2067,2061,2207,2210,2211,2208
      emore,2060
      e,2061,2067,2068,2069,2208,2211,2212,2213
      e,2058,2061,2069,2070,2207,2208,2213,2214
      emore,,,,2062
      e,2056,2058,2070,2072,2206,2207,2214,2215
      emore,2057,2062,2071,2063
      e,2064,2073,2074,2066,2209,2216,2217,2210
      emore,,,,2065
      e,2066,2074,2075,2067,2210,2217,2218,2211
      egen,2,1,1687
      e,2068,2076,2077,2078,2212,2219,2220,2221
      e,2069,2068,2078,2079,2213,2212,2221,2222
      egen,2,1,1690
      e,2072,2070,2080,2081,2215,2214,2223,2224
      emore,2071
C
      type,1
      mat,1
C
      e,2073,2082,2083,2074,2216,2225,2226,2217
      egen,8,1,1693
      egen,2,9,1693,1700
      e,2091,2100,2234,2234,2092,2101,2235,2235
      egen,8,1,1709
C
      type,2
      mat,2
C
C Into the area of borehole bottom (area with curved surface)
C
C First layer
C
      e,2234,2100,2101,2235,2243,2278,2280,2245
      emore,,,,,2269,2279,2270,2244
      e,2235,2101,2102,2236,2245,2280,2282,2247
      emore,,,,,2270,2281,2271,2246
      e,2236,2102,2103,2237,2247,2282,2284,2249
      emore,,,,,2271,2283,2272,2248
      e,2237,2103,2104,2238,2249,2284,2286,2251
      emore,,,,,2272,2285,2273,2250
      e,2238,2104,2105,2239,2251,2286,2288,2253
      emore,,,,,2273,2287,2274,2252
      e,2239,2105,2106,2240,2253,2288,2290,2255
      emore,,,,,2274,2289,2275,2254
      e,2240,2106,2107,2241,2255,2290,2292,2257
      emore,,,,,2275,2291,2276,2256
      e,2241,2107,2108,2242,2257,2292,2294,2259
```

```
      emore,,,,,2276,2293,2277,2258
C
      e,2100,2109,2110,2101,2278,2304,2305,2280
      emore,,,,,,,,2279
      e,2101,2110,2111,2102,2280,2305,2306,2282
      emore,,,,,,,,2281
      e,2102,2111,2112,2103,2282,2306,2307,2284
      emore,,,,,,,,2283
      e,2103,2112,2113,2104,2284,2307,2308,2286
      emore,,,,,,,,2285
      e,2104,2113,2114,2105,2286,2308,2309,2288
      emore,,,,,,,,2287
      e,2105,2114,2115,2106,2288,2309,2310,2290
      emore,,,,,,,,2289
      e,2106,2115,2116,2107,2290,2310,2311,2292
      emore,,,,,,,,2291
      e,2107,2116,2117,2108,2292,2311,2312,2294
      emore,,,,,,,,2293
C
      type,1
      mat,1
C
      e,2109,2118,2119,2110,2304,2313,2314,2305
      egen,8,1,1733
      e,2118,2331,2332,2119,2313,2322,2323,2314
      egen,8,1,1741
      e,2118,2127,2331,2331,2119,2128,2332,2332
      egen,8,1,1749
      e,2127,2136,2137,2128,2331,2340,2341,2332
      egen,8,1,1757
      egen,5,9,1757,1764
C
      e,2172,2181,2182,2173,2376,2385,2386,2377
      egen,4,1,1797
      e,2176,2185,2186,2187,2380,2389,2390,2391
      e,2177,2176,2187,2188,2381,2380,2391,2392
      egen,4,1,1802
      e,2181,2192,2193,2182,2385,2396,2397,2386
      egen,5,1,1806
      e,2186,2197,2198,2199,2390,2401,2402,2403
      e,2187,2186,2199,2200,2391,2390,2403,2404
      egen,5,1,1812
C
C New layer
C
      type,2
      mat,2
      e,2206,2209,2210,2207,2410,2413,2414,2411
      e,2207,2210,2211,2208,2411,2414,2415,2412
      e,2208,2211,2212,2213,2412,2415,2416,2417
      e,2207,2208,2213,2214,2411,2412,2417,2418
      e,2206,2207,2214,2215,2410,2411,2418,2419
C
      type,1
```

```
mat,1
C
e,2209,2216,2217,2210,2413,2420,2421,2414
egen,3,1,1822
e,2212,2219,2220,2221,2416,2423,2424,2425
e,2213,2212,2221,2222,2417,2416,2425,2426
egen,3,1,1826
e,2216,2225,2226,2217,2420,2429,2430,2421
egen,8,1,1829
e,2225,2234,2429,2429,2226,2235,2430,2430
egen,8,1,1837
C
type,2
mat,2
C
e,2429,2234,2235,2430,2438,2243,2245,2439
emore,,,,,,2244
e,2430,2235,2236,2431,2439,2245,2247,2440
emore,,,,,,2246
e,2431,2236,2237,2432,2440,2247,2249,2441
emore,,,,,,2248
e,2432,2237,2238,2433,2441,2249,2251,2442
emore,,,,,,2250
e,2433,2238,2239,2434,2442,2251,2253,2443
emore,,,,,,2252
e,2434,2239,2240,2435,2443,2253,2255,2444
emore,,,,,,2254
e,2435,2240,2241,2436,2444,2255,2257,2445
emore,,,,,,2256
e,2436,2241,2242,2437,2445,2257,2259,2446
emore,,,,,,2258
C
e,2438,2243,2245,2439,2456,2482,2484,2458
emore,,2244,,,2473,2483,2474,2457
emore,2447,2260,2261,2448
e,2439,2245,2247,2440,2458,2484,2486,2460
emore,,2246,,,2474,2485,2475,2459
emore,2448,2261,2262,2449
e,2440,2247,2249,2441,2460,2486,2488,2462
emore,,2248,,,2475,2487,2476,2461
emore,2449,2262,2263,2450
e,2441,2249,2251,2442,2462,2488,2490,2464
emore,,2250,,,2476,2489,2477,2463
emore,2450,2263,2264,2451
e,2442,2251,2253,2443,2464,2490,2492,2466
emore,,2252,,,2477,2491,2478,2465
emore,2451,2264,2265,2452
e,2443,2253,2255,2444,2466,2492,2494,2468
emore,,2254,,,2478,2493,2479,2467
emore,2452,2265,2266,2453
e,2444,2255,2257,2445,2468,2494,2496,2470
emore,,2256,,,2479,2495,2480,2469
emore,2453,2266,2267,2454
e,2445,2257,2259,2446,2470,2496,2498,2472
```

```
      emore,,2258,,,2480,2497,2481,2471
      emore,2454,2267,2268,2455
C
      e,2243,2278,2280,2245,2482,2508,2510,2484
      emore,2269,2279,2270,2244,2499,2509,2500,2483
      emore,2260,2295,2296,2261
      e,2245,2280,2282,2247,2484,2510,2512,2486
      emore,2270,2281,2271,2246,2500,2511,2501,2485
      emore,2261,2296,2297,2262
      e,2247,2282,2284,2249,2486,2512,2514,2488
      emore,2271,2283,2272,2248,2501,2513,2502,2487
      emore,2262,2297,2298,2263
      e,2249,2284,2286,2251,2488,2514,2516,2490
      emore,2272,2285,2273,2250,2502,2515,2503,2489
      emore,2263,2298,2299,2264
      e,2251,2286,2288,2253,2490,2516,2518,2492
      emore,2273,2287,2274,2252,2503,2517,2504,2491
      emore,2264,2299,2300,2265
      e,2253,2288,2290,2255,2492,2518,2520,2494
      emore,2274,2289,2275,2254,2504,2519,2505,2493
      emore,2265,2300,2301,2266
      e,2255,2290,2292,2257,2494,2520,2522,2496
      emore,2275,2291,2276,2256,2505,2521,2506,2495
      emore,2266,2301,2302,2267
      e,2257,2292,2294,2259,2496,2522,2524,2498
      emore,2276,2293,2277,2258,2506,2523,2507,2497
      emore,2267,2302,2303,2268
C
C Element 1869 - 1876
C
      e,2278,2304,2305,2280,2508,2534,2535,2510
      emore,,,,2279,2525,,2526,2509
      emore,2295,,,2296
      e,2280,2305,2306,2282,2510,2535,2536,2512
      emore,,,,2281,2526,,2527,2511
      emore,2296,,,2297
      e,2282,2306,2307,2284,2512,2536,2537,2514
      emore,,,,2283,2527,,2528,2513
      emore,2297,,,2298
      e,2284,2307,2308,2286,2514,2537,2538,2516
      emore,,,,2285,2528,,2529,2515
      emore,2298,,,2299
      e,2286,2308,2309,2288,2516,2538,2539,2518
      emore,,,,2287,2529,,2530,2517
      emore,2299,,,2300
      e,2288,2309,2310,2290,2518,2539,2540,2520
      emore,,,,2289,2530,,2531,2519
      emore,2300,,,2301
      e,2290,2310,2311,2292,2520,2540,2541,2522
      emore,,,,2291,2531,,2532,2521
      emore,2301,,,2302
      e,2292,2311,2312,2294,2522,2541,2542,2524
      emore,,,,2293,2532,,2533,2523
      emore,2302,,,2303
```

```
C
C Element 1877 - 1884
C
      type,1
      mat,1
C
      e,2304,2313,2314,2305,2534,2543,2544,2535
      egen,8,1,1877
      egen,2,9,1877,1884
      e,2322,2570,2571,2323,2552,2561,2562,2553
      egen,8,1,1893
      e,2331,2579,2580,2332,2322,2570,2571,2323
      egen,8,1,1901
      e,2331,2340,2579,2579,2332,2341,2580,2580
      egen,8,1,1909
      e,2340,2349,2350,2341,2579,2588,2589,2580
      egen,8,1,1917
      egen,4,9,1917,1924
C
C Element 1949 - 1968
C
      e,2376,2385,2386,2377,2615,2624,2625,2616
      egen,4,1,1949
      e,2380,2389,2390,2391,2619,2628,2629,2630
      e,2381,2380,2391,2392,2620,2619,2630,2631
      egen,4,1,1954
      e,2385,2396,2397,2386,2624,2635,2636,2625
      egen,5,1,1958
      e,2390,2401,2402,2403,2629,2640,2641,2642
      e,2391,2390,2403,2404,2630,2629,2642,2643
      egen,5,1,1964
C
C Element 1969 - 1973
C
      type,2
      mat,2
C
      e,2410,2413,2414,2411,2649,2652,2653,2650
      e,2411,2414,2415,2412,2650,2653,2654,2651
      e,2412,2415,2416,2417,2651,2654,2655,2656
      e,2411,2412,2417,2418,2650,2651,2656,2657
      e,2410,2411,2418,2419,2649,2650,2657,2658
C
      type,1
      mat,1
      e,2413,2420,2421,2414,2652,2659,2660,2653
      egen,3,1,1974
      e,2416,2423,2424,2425,2655,2662,2663,2664
      e,2417,2416,2425,2426,2656,2655,2664,2665
      egen,3,1,1978
      e,2420,2429,2430,2421,2659,2668,2669,2660
      egen,8,1,1981
      e,2668,2429,2430,2669,2677,2438,2439,2678
      egen,8,1,1989
```

```
C
        type,2
        mat,2
C
C Element 1997 - 2004
C
        e,2677,2438,2439,2678,2695,2456,2458,2697
        emore,,,,,2712,2457,2713,2696
        emore,2686,2447,2448,2687
        e,2678,2439,2440,2679,2697,2458,2460,2699
        emore,,,,,2713,2459,2714,2698
        emore,2687,2448,2449,2688
        e,2679,2440,2441,2680,2699,2460,2462,2701
        emore,,,,,2714,2461,2715,2700
        emore,2688,2449,2450,2689
        e,2680,2441,2442,2681,2701,2462,2464,2703
        emore,,,,,2715,2463,2716,2702
        emore,2689,2450,2451,2690
        e,2681,2442,2443,2682,2703,2464,2466,2705
        emore,,,,,2716,2465,2717,2704
        emore,2690,2451,2452,2691
        e,2682,2443,2444,2683,2705,2466,2468,2707
        emore,,,,,2717,2467,2718,2706
        emore,2691,2452,2453,2692
        e,2683,2444,2445,2684,2707,2468,2470,2709
        emore,,,,,2718,2469,2719,2708
        emore,2692,2453,2454,2693
        e,2684,2445,2446,2685,2709,2470,2472,2711
        emore,,,,,2719,2471,2720,2710
        emore,2693,2454,2455,2694
C
C Element 2005 - 2052
C
        type,1
        mat,1
C
        e,2561,2570,2571,2562,2721,2730,2731,2722
        egen,8,1,2005
        egen,6,9,2005,2012
C
        e,2615,2624,2625,2616,2775,2784,2785,2776
        egen,4,1,2053
        e,2619,2628,2629,2630,2779,2788,2789,2790
        e,2620,2619,2630,2631,2780,2779,2790,2791
        egen,4,1,2058
        e,2624,2635,2636,2625,2784,2795,2796,2785
        egen,5,1,2062
        e,2629,2640,2641,2642,2789,2800,2801,2802
        e,2630,2629,2642,2643,2790,2789,2802,2803
        egen,5,1,2068
C
C New layer
C
        type,2
```

```
      mat,2
      e,2649,2652,2653,2650,2809,2812,2813,2810
      e,2650,2653,2654,2651,2810,2813,2814,2811
      e,2651,2654,2655,2656,2811,2814,2815,2816
      e,2650,2651,2656,2657,2810,2811,2816,2817
      e,2649,2650,2657,2658,2809,2810,2817,2818
C
      type,1
      mat,1
      e,2652,2659,2660,2653,2812,2819,2820,2813
      egen,3,1,2078
      e,2655,2662,2663,2664,2815,2822,2823,2824
      e,2656,2655,2664,2665,2816,2815,2824,2825
      egen,3,1,2082
      e,2659,2668,2669,2660,2819,2828,2829,2820
      egen,8,1,2085
      egen,2,9,2085,2092
C
      type,2
      mat,2
      e,2837,2677,2678,2838,2855,2695,2697,2857
      emore,,,,,2872,2696,2873,2856
      emore,2846,2686,2687,2847
      e,2838,2678,2679,2839,2857,2697,2699,2859
      emore,,,,,2873,2698,2874,2858
      emore,2847,2687,2688,2848
      e,2839,2679,2680,2840,2859,2699,2701,2861
      emore,,,,,2874,2700,2875,2860
      emore,2848,2688,2689,2849
      e,2840,2680,2681,2841,2861,2701,2703,2863
      emore,,,,,2875,2702,2876,2862
      emore,2849,2689,2690,2850
      e,2841,2681,2682,2842,2863,2703,2705,2865
      emore,,,,,2876,2704,2877,2864
      emore,2850,2690,2691,2851
      e,2842,2682,2683,2843,2865,2705,2707,2867
      emore,,,,,2877,2706,2878,2866
      emore,2851,2691,2692,2852
      e,2843,2683,2684,2844,2867,2707,2709,2869
      emore,,,,,2878,2708,2879,2868
      emore,2852,2692,2693,2853
      e,2844,2684,2685,2845,2869,2709,2711,2871
      emore,,,,,2879,2710,2880,2870
      emore,2853,2693,2694,2854
C
      type,1
      mat,1
      e,2721,2730,2731,2722,2881,2890,2891,2882
      egen,8,1,2109
      egen,6,9,2109,2116
      egen,2,160,2053,2072
C
C New layer
C
```

```
C Element 2177 - 2212
C
        type,2
        mat,2
        e,2809,2812,2813,2810,2978,2981,2982,2979
        e,2810,2813,2814,2811,2979,2982,2983,2980
        e,2811,2814,2815,2816,2980,2983,2984,2985
        e,2810,2811,2816,2817,2979,2980,2985,2986
        e,2809,2810,2817,2818,2978,2979,2986,2987
C
        type,1
        mat,1
        e,2812,2819,2820,2813,2981,2988,2989,2982
        egen,3,1,2182
        e,2815,2822,2823,2824,2984,2991,2992,2993
        e,2816,2815,2824,2825,2985,2984,2993,2994
        egen,3,1,2186
        e,2819,2828,2829,2820,2988,2997,2998,2989
        egen,8,1,2189
        egen,2,9,2189,2196
C
        type,2
        mat,2
C
        e,2837,3006,3007,2838,2855,3015,3016,2857
        emore,,,,,2969,,2970,2856
        emore,2846,,,2847
        e,2838,3007,3008,2839,2857,3016,3017,2859
        emore,,,,,2970,,2971,2858
        emore,2847,,,2848
        e,2839,3008,3009,2840,2859,3017,3018,2861
        emore,,,,,2971,,2972,2860
        emore,2848,,,2849
        e,2840,3009,3010,2841,2861,3018,3019,2863
        emore,,,,,2972,,2973,2862
        emore,2849,,,2850
        e,2841,3010,3011,2842,2863,3019,3020,2865
        emore,,,,,2973,,2974,2864
        emore,2850,,,2851
        e,2842,3011,3012,2843,2865,3020,3021,2867
        emore,,,,,2974,,2975,2866
        emore,2851,,,2852
        e,2843,3012,3013,2844,2867,3021,3022,2869
        emore,,,,,2975,,2976,2868
        emore,2852,,,2853
        e,2844,3013,3014,2845,2869,3022,3023,2871
        emore,,,,,2976,,2977,2870
        emore,2853,,,2854
C
        type,1
        mat,1
C
        e,2881,2890,2891,2882,3024,3033,3034,3025
        egen,8,1,2213
```

```
      egen,6,9,2213,2220
      e,2935,2944,2945,2936,3078,3087,3088,3079
      egen,4,1,2261
      e,2939,2948,2949,2950,3082,3091,3092,3093
      e,2940,2939,2950,2951,3083,3082,3093,3094
      egen,4,1,2266
      e,2944,2955,2956,2945,3087,3098,3099,3088
      egen,5,1,2270
      e,2949,2960,2961,2962,3092,3103,3104,3105
      e,2950,2949,2962,2963,3093,3092,3105,3106
      egen,5,1,2276
C
C Layer above borehole bottom
C
C Element 2245 - 2292
C
      e,2978,2981,2982,2979,3111,3114,3115,3112
      egen,2,1,2281
      e,2980,2983,2984,2985,3113,3116,3117,3118
      e,2979,2980,2985,2986,3112,3113,3118,3119
      e,2978,2979,2986,2987,3111,3112,3119,3120
      e,2981,2988,2989,2982,3114,3121,3122,3115
      egen,3,1,2286
      e,2984,2991,2992,2993,3117,3124,3125,3126
      e,2985,2984,2993,2994,3118,3117,3126,3127
      egen,3,1,2290
C
      e,2988,2997,2998,2989,3121,3130,3131,3122
      egen,8,1,2293
      egen,3,9,2293,2300
C
      e,3024,3033,3034,3025,3157,3166,3167,3158
      egen,8,1,2317
      egen,6,9,2317,2324
C
C Element 2293 - 2312
C
      e,3078,3087,3088,3079,3211,3220,3221,3212
      egen,4,1,2365
      e,3082,3091,3092,3093,3215,3224,3225,3226
      e,3083,3082,3093,3094,3216,3215,3226,3227
      egen,4,1,2370
      e,3087,3098,3099,3088,3220,3231,3232,3221
      egen,5,1,2374
      e,3092,3103,3104,3105,3225,3236,3237,3238
      e,3093,3092,3105,3106,3226,3225,3238,3239
      egen,5,1,2380
C
      egen,9,133,2281,2384

C
C End of element generating
C
C Delete elements to form a required core length
```

```
C
        edele,3113,3148
        edele,3009,3044
        edele,2905,2940
        edele,2801,2836
C
C Delete loads and nodes not attached to elements
C
        nelem
        ninv
        ddele,all
        ndele,all
C
C Applying loads
C
        /type,,2
        csys,11
        nall
        nsel,y,0,0
        d,all,ux
        nall
        nsel,x,0,0
        d,all,uz
        nall
        nsel,z,0,0
        d,all,uy
C
        nall
        nsel,x,100,100
        psf,all,,,20.0
        nall
        /pbc,all,1
        /psf,pres,,1
        nplot
C
        eplot
        csys,12
        save
        finish

C------------------------------------------------------------------------------------------------------
C End of generating model
C------------------------------------------------------------------------------------------------------
C
C SOLUSION FOR MODEL CALCULATION
C
C------------------------------------------------------------------------------------------------------
        /solu
        solve
        yes
        yes
        finish
```

```
C--------------------------------------------------------------------------------
C
C POSTPROCESSING FOR DATA OUTPUT
C
C--------------------------------------------------------------------------------
        /post1
        set,1
C
C Output start
C
        nall
        csys,12
        /format,,F,10,4
        /output,sdat.all
        prnstr,all
        /output
C1
        nsel,x,0,0
        /output,sdat.axi
        prnstr,all
        /output
C2
        nsel,y,0,0
        nrsel,x,0,16.1
        nrsel,z,64.9,85.1
        /output,sdat.s9
        prnstr,all
        /output
C3
        /output,vdat.s9
        prvect,pdir
        /output
C4
        csys,11
        nsel,x,0,0
        nrsel,y,0,16.1
        nrsel,z,64.9,85.1
        csys,12
        /output,sdat.s0
        prnstr,all
        /output
C5
        /output,vdat.s0
        prvect,pdir
        /output
C6
        csys,12
        nsel,x,0,25
        nrsel,y,44.9,45.1
        nrsel,z,64.9,85.1
        /output,sdat.s45
        prnstr,all
        /output
```

```
C
        /output,vdat.s45
        prvect,pdir
        /output
C7
        nsel,node,3680
        nasel,node,3547
        nasel,node,3414
        nasel,node,3281
        nasel,node,3148
        nasel,node,3015
        nasel,node,2855
        nasel,node,2695
        nasel,node,2456
        nasel,node,2482
        nasel,node,2508
        nasel,node,2534
        nasel,node,2543
        nasel,node,2552
        nasel,node,2561
        nasel,node,2721
        nasel,node,2881
        nasel,node,3024
        nasel,node,3157
        nasel,node,3290
        nasel,node,3423
        nasel,node,3556
        nasel,node,3689
        /output,sdat.sc9
        prnstr,all
        /output
C
        /output,vdat.sc9
        prvect,pdir
        /output
C8
        nsel,node,3688
        nasel,node,3555
        nasel,node,3422
        nasel,node,3289
        nasel,node,3156
        nasel,node,3023
        nasel,node,2871
        nasel,node,2711
        nasel,node,2472
        nasel,node,2498
        nasel,node,2524
        nasel,node,2542
        nasel,node,2551
        nasel,node,2560
        nasel,node,2569
        nasel,node,2729
        nasel,node,2889
        nasel,node,3032
```

```
      nasel,node,3165
      nasel,node,3298
      nasel,node,3431
      nasel,node,3564
      nasel,node,3697
      /output,sdat.sc0
      prnstr,all
      /output
C
      /output,vdat.sc0
      prvect,pdir
      /output
C
      nall
      finish
      /eof
C------------------------------------------------------------------------------
C
C  END OF PROGRAM
C
C------------------------------------------------------------------------------
```

APPENDIX 5.3

Example of Programs for Stress Superposition

```
% ------------------------------------------------------------------------------------------------
%
% THIS MATLAB PROGRAM SOL_SOTT2.M CAN BE USED TO SUPERPOSE
% STRESSES
%
% ------------------------------------------------------------------------------------------------
%
% Input parameters
%
        n1 = input('Number of nodes:  ','s');
        n2 = input('Number of input_files for fixed stresses:  ','s');
        n3 = input('Magnitude of fixed_stress #1:  ','s');
        n4 = input('Magnitude of fixed_stress #2:  ','s');
        n5 = input('Magnitude of varing_apply_stress:  ','s');
%
        num1 = str2num(n1);
        num2 = str2num(n2);
        num3 = str2num(n3);
        num4 = str2num(n4);
        num5 = str2num(n5);
%
% Input the names of output files
%
        outfile1 = input('Enter OUTFILE1 for principal stresses:  ','s');
        outfile2 = input('Enter OUTFILE2 for principal stress orientations:  ','s');
        outfile3 = input('Enter OUTFILE3 for contouing principal stresses:  ','s');
        outfile4 = input('Enter OUTFILE4 for contouring maximum shear stresses  ','s');
%
        fid6 = fopen(outfile1,'w');
        fid7 = fopen(outfile2,'w');
        fid8 = fopen(outfile3,'w');
        fid9 = fopen(outfile4,'w');
%
% Input stresses with fixed magnitudes
%
        c = 0;
%
        for finnum = 1:num2;
                fprintf(' \n INPUTING  FIXED file:  Number %1.0f \n',finnum);
                inputfile1 = input('Enter INPUTFILES(for FIXED stresses):  ','s');
                fprintf(fid6,'-----FIXED STRESS FILES: \n');
                fprintf(fid6,inputfile1);
                fprintf(fid6,'\n');
                fprintf(fid7,'-----FIXED STRESS FILES: \n');
                fprintf(fid7,inputfile1);
                fprintf(fid7,'\n');
                fprintf(fid8,'-----FIXED STRESS FILES: \n');
                fprintf(fid8,inputfile1);
                fprintf(fid8,'\n');
```

```
            fprintf(fid9,'-----FIXED STRESS FILES: \n');
            fprintf(fid9,inputfile1);
            fprintf(fid9,'\n');
%
            fid1 = fopen(inputfile1,'r');
            c1 = fscanf(fid1,'%f %f %f %f %f %f %f %f %f %f %f %f\n',[12,num1]);
            fclose(fid1);
%
            if finnum == 1
                  c1 = c1*(num3/20.0);
            else
                  c1 = c1*(num4/20.0);
            end
            c = c + c1;
      end
            c2 = c(1,1:num1)/((num3+num4)/20.0);
%
% Input stresses with a varing magnitude
%
      fprintf(' \n INPUTING  VARING file: \n');
      inputfile2 = input('Enter INPUTFILE(for VARING stress):  ','s');
      fprintf(fid6,'-----VARING STRESS FILE: \n');
      fprintf(fid6,inputfile2);
      fprintf(fid6,'\n');
      fprintf(fid7,'-----VARING STRESS FILE: \n');
      fprintf(fid7,inputfile2);
      fprintf(fid7,'\n');
      fprintf(fid8,'-----VARING STRESS FILE: \n');
      fprintf(fid8,inputfile2);
      fprintf(fid8,'\n');
      fprintf(fid9,'-----VARING STRESS FILE: \n');
      fprintf(fid9,inputfile2);
      fprintf(fid9,'\n');
%
      fid2 = fopen(inputfile2,'r');
      b1 = fscanf(fid2,'%f %f %f %f %f %f %f %f %f %f %f %f\n',[12,num1]);
      fclose(fid2);
%
      ratio = num5/20.0;
      b = ratio*b1;
%
% Input coordinate of nodes
%
      fprintf(' \n INPUTING  NODE-COORDINATE file: \n');
      inputfile3 = input('Enter NODE_COORDINATE file ../node_f5.??:  ','s');
      fid3 = fopen(inputfile3,'r');
%
      bb = fscanf(fid3,'%f %f %f %f %f %f %f \n',[7,num1]);
      b2 = bb(2:3,1:num1);
      b2(2,1:num1) = b2(2,1:num1) - 75.0;
      fclose(fid3);
%
% Superposing stresses and solving principal stresses
%
```

```
a = c + b;
a = a';
%
for i = 1:num1
        tensor(1,1) = a(i,2);
        tensor(1,2) = a(i,5);
        tensor(1,3) = a(i,7);
        tensor(2,1) = a(i,5);
        tensor(2,2) = a(i,3);
        tensor(2,3) = a(i,6);
        tensor(3,1) = a(i,7);
        tensor(3,2) = a(i,6);
        tensor(3,3) = a(i,4);
        [v,d] = eig(tensor);
%
        s1(i,1) = d(1,1);
        s1(i,2) = d(2,2);
        s1(i,3) = d(3,3);
        [Y,I] = sort(s1');
%
        s2(i,1) = c2(i);
        s2(i,2) = Y(3,i)';
        s2(i,3) = Y(2,i)';
        s2(i,4) = Y(1,i)';
        s2(i,5) = max(s1(i,:)) - min(s1(i,:));
        I = I';
%
        for ij = 1:3
          if I(i,ij) == 3
          II(ij) = 1;
        elseif I(i,ij) == 1
          II(ij) = 3;
        else
          II(ij) = 2;
        end
end
%
II = II';
%
j = (i-1)*3;
        sv(1+j,1) = c2(i);
        sv(2+j,1) = c2(i);
        sv(3+j,1) = c2(i);
        sv(1+j,2) = s2(i,2);
        sv(2+j,2) = s2(i,3);
        sv(3+j,2) = s2(i,4);
        sv(1+j,3) = v(1,I(i,3));
        sv(1+j,4) = v(2,I(i,3));
        sv(1+j,5) = v(3,I(i,3));
        sv(2+j,3) = v(1,I(i,2));
        sv(2+j,4) = v(2,I(i,2));
        sv(2+j,5) = v(3,I(i,2));
        sv(3+j,3) = v(1,I(i,1));
        sv(3+j,4) = v(2,I(i,1));
```

```
                sv(3+j,5) = v(3,I(i,1));
%
                sv(1+j,6) = acos(sv(1+j,3))*180.0/pi;
                sv(1+j,7) = acos(sv(1+j,4))*180.0/pi;
                sv(1+j,8) = acos(sv(1+j,5))*180.0/pi;
                sv(2+j,6) = acos(sv(2+j,3))*180.0/pi;
                sv(2+j,7) = acos(sv(2+j,4))*180.0/pi;
                sv(2+j,8) = acos(sv(2+j,5))*180.0/pi;
                sv(3+j,6) = acos(sv(3+j,3))*180.0/pi;
                sv(3+j,7) = acos(sv(3+j,4))*180.0/pi;
                sv(3+j,8) = acos(sv(3+j,5))*180.0/pi;
%
        end
%
                sig1 = [b2' s2(1:num1,2)];
                sint1 = [b2' s2(1:num1,5)/2];

                  b3(1:num1,1) = b2(1,1:num1)'*(-1);
                  b3(1:num1,2) = b2(2,1:num1)';
                sig2 = [b3 s2(1:num1,2)];
                sint2 = [b3 s2(1:num1,5)/2];
                sig1 = [sig1;sig2];
                sint = [sint1;sint2];
                sig1 = sig1';
                sint = sint';
%
% Output data
%
        fprintf(fid6,'\n      NODE\t s1\t s2\t s3\t s1 - s3\n\n');
        fprintf(fid6,' %10.0f  %10.4f  %10.4f  %10.4f %10.4f\n',s2');
        status = fclose(fid6);
%
        fprintf(fid7,'\n\t NODE\t s_1_2_3\t consx\t consy\t consz\t sita_gamma_beta\n\n');
        for k = 1:num1
        for l = 3*k - 2:3*k
                fprintf(fid7,'%10.0f %10.4f %10.4f %10.4f %10.4f %10.4f %10.4f
                        10.4f\n',sv(l,1:8));
        end
        end
        status = fclose(fid7);
%
        fprintf(fid8,'\n  X\t Y\t SIG1 \n\n');
        fprintf(fid8,' %10.4f %10.4f %10.4f\n',sig1);
        status = fclose(fid8);
%
        fprintf(fid9,'\n  X\t Y\t (S1 - S3)/2\n\n');
        fprintf(fid9,' %10.4f %10.4f %10.4f\n',sint);
        status = fclose(fid9);
%
%-------------------------------------------------------------------------------------------------------------
%
% END OF PROGRAM
%
%-------------------------------------------------------------------------------------------------------------
```

APPENDIX 5.4

Example of Programs for Plotting Stress Orientation

```
% ------------------------------------------------------------------------------------------------------
%
% THIS MATLAB PROGRAM V_S0TTT.M CAN BE USED TO PLOT
% ORIENTATIONS WITH MAGNITUDES OF PRINCIPAL STRESSES
%
%------------------------------------------------------------------------------------------------------
%
% Input number of input nodes, number of nodes used to plot principal stress sticks, and
% plotting ratio.

                num1 = 3*175;
                num2 = 10;
                num3 = 72;
                num4 = 3*72;
%
%------------------------------------------------------------------------------------------------------
%
% Input principal stresses with orientations
%
%
        fid1 = fopen('spv_s0.x1_ed','r');
        a = fscanf(fid1,'%f %f %f %f %f \n',[8,num1]);
        fclose(fid1);
%
% Input node coordinates
%
        fid2 = fopen('node0v.cu','r');
        b1 = fscanf(fid2,'%f %f %f %f %f %f %f \n',[7,num3]);
        b2 = bb1(2:3,1:num3);
        b2(2,1:num3) = bb2(2,1:num3) - 75.0;
        c2 = bb1(1,1:num3);
        fclose(fid2);
%
        b3(2,num4) = 0.0;
        b = b3;
%
        for k = 1:num3
        for l = 3*k-2:3*k
                b3(1:2,l) = b2(1:2,k);
                c3(1,l) = c2(1,k);
        end
        end
%
        b(1,:) = b3(2,:);
        b(2,:) = b3(1,:);
%
% Plot background
%
        xg1 = [9.8+2,9.8+2,18+2,18+2,0.+2,0.+2];
```

```
        yg1 = [2.5,12.0,12,-8,-8,0.2];
        alpha = -pi/2.0:pi/2.0/90.0:0.0;
        xg = 2.3*cos(alpha) + 7.5+2;
        yg = 2.3*sin(alpha) + 2.5;
        xx = [xg1 xg];
        yy = [yg1,yg];
        plot(xx,yy)
        cgray = [0.85,0.85,0.85];
        fill(xx,yy,cgray);
%
% Plot principal stresses
%
        for i = 1:num1
        for j = 1:num4
%
            if a(1,i) == c3(1,j)
            if a(2,i) <= 0.0
%
                X = [ ((b(2,j) + a(2,i)*a(3,i)/num2/2)+2.0)  ((b(2,j) -
                        a(2,i)*a(3,i)/num2/2)+2.0) ];
                Y = [ (b(1,j) + a(2,i)*a(4,i)/num2/2)  (b(1,j) - a(2,i)*a(4,i)/num2/2) ];
                h = line(X,Y);
                set(h,'LineStyle','-','Color','g','LineWidth',[0.5])
        else
%
                X = [ ((b(2,j) + a(2,i)*a(3,i)/num2/2)+2.0)  ((b(2,j) -
                        a(2,i)*a(3,i)/num2/2)+2.0) ];
                Y = [ (b(1,j) + a(2,i)*a(4,i)/num2/2 ) (b(1,j) - a(2,i)*a(4,i)/num2/2) ];
                h = line(X,Y);
                set(h,'LineStyle','-','Color','r','LineWidth',[2.0])
%
            end
            end
%
        end
        end
%
        hold on
%
% Plot boundary
%
        x1 = [2.0,9.5];
        x2 = [11.8,11.8];
        x3 = [1.8,1.8];
        y1 = [0.2,0.2];
        y2 = [2.5,12.0];
        y3 = [-6.0,0.2];
        alpha = -pi/2.0:pi/2.0/90.0:0.0;
        x = 2.3*cos(alpha) + 9.5;
        y = 2.3*sin(alpha) + 2.5;
        h1 = plot(x1,y1);
        h2 = plot(x2,y2);
        hx = plot(x,y);
        set(h1,'LineWidth',[0.2])
```

```
        set(h2,'LineWidth',[0.2])
        set(hx,'LineWidth',[0.2])
%
% Labling
%
        axis([-34,34,-45,20]);
        axis('off');
        xx = [-2.0,2.0];
        yy = [-40.0,-40.0];
        h1 = plot(xx,yy);
        set(h1,'Color','g')
        h2=text(0.0,-41.5,'40  MPa','FontSize',12,'Color','green',
                'HorizontalAlignment','center');
        h3=text(-5,5.0,'F = 0');
        h4=text(5,5,'F = 90');
%
        set(h3,'FontSize',12,'Color','green','HorizontalAlignment','center','FontName',
                'Symbol')

        set(h4,'FontSize',12,'Color','green','HorizontalAlignment','center','FontName',
                'Symbol')
%
        h5=text(-2.6,6.0,'o');
        h6=text(7.8,6.0,'o');
        set(h5,'FontSize',6,'Color','green','HorizontalAlignment','center')
        set(h6,'FontSize',6,'Color','green','HorizontalAlignment','center')
        text(-20,14,'a)')
        text(-20,-11.5,'b)')
%
%-------------------------------------------------------------------------------------------------
        clear all
%-------------------------------------------------------------------------------------------------
%
% END OF PROGRAM
%
%-------------------------------------------------------------------------------------------------
```